OBSERVATION OF THE DALITZ DECAY OF THE FIRST EXCITED STATE OF THE CHARMED-STRANGE MESON

A Dissertation

Presented to the Faculty of the Graduate School

of Cornell University

in Partial Fulfillment of the Requirements for the Degree of

Doctor of Philosophy

by

Souvik Das

January 2011

© 2011 Souvik Das

ALL RIGHTS RESERVED

OBSERVATION OF THE DALITZ DECAY OF THE FIRST EXCITED STATE OF THE CHARMED-STRANGE MESON

Souvik Das, Ph.D.

Cornell University 2011

The branching fraction for a previously unobserved decay $D_s^{*+} \to D_s^+ e^+ e^-$ is predicted theoretically in this dissertation to be 0.65% of the branching fraction for the decay $D_s^{*+} \to D_s^+ \gamma$. We conduct a search for the $D_s^{*+} \to D_s^+ e^+ e^-$ in 586 pb^{-1} of $e^+ e^-$ collision data collected with the CLEO-c detector at the Cornell Electron Storage Ring (CESR) operating at a center of mass energy of 4170 MeV and observe it with a significance of 6.4 σ over estimated backgrounds. The ratio of branching fractions $B(D_s^{*+} \to D_s^+ e^+ e^-)/B(D_s^{*+} \to D_s^+ \gamma)$ is measured to be $(0.72 \pm 0.14(\text{stat}) \pm 0.06(\text{syst}))\%$, which is within one standard deviation of uncertainty from the predicted value.

BIOGRAPHICAL SKETCH

Souvik Das was born to Tapan and Tanusri Das on August 20, 1982 in Kolkata, India. Bred on an abundance of books, toys and love in a family of humble means, he was soon convinced in spite of the stagnant life of Kolkata that the world, in the larger scheme of things, is a magical place that bears investigation. He gravitated towards physics and at 14 declared to his father that he had to be a physicist.

In 2000, he graduated from Don Bosco School Park Circus in Kolkata and enrolled in the undergraduate physics program at St. Stephen's College in Delhi. There his interest in physics blossomed and besides curricular studies he worked with physicists across the country on a variety of projects ranging from condensed matter physics to complex systems and biophysics.

He joined Cornell University as a graduate student in 2003 and continued his tradition of wandering between physics groups till he converged on experimental high energy physics for his Ph.D. research in 2006. He worked on the pixel detector for the Compact Muon Solenoid (CMS) experiment at the Large Hadron Collider (LHC), sometimes living for months at Fermilab, Illinois where a part of it was being fabricated. In early 2007, he along with parts of the pixel detector was shipped out to CERN, Geneva. He worked on various aspects of the CMS experiment till the LHC suffered a breakdown in September 2008. Thereafter, he switched to the CLEO-c experiment where he worked on the electromagnetic Dalitz decay of the D_s^{*+} meson, which is the content of this dissertation.

Souvik looks forward to resuming work at the LHC where he hopes to occupy himself with searching for the mechanism of electroweak symmetry breaking.

To my parents, Tapan and Tanusri,

and my grandparents, Phalguni and Haripada,

who taught me to value knowledge above all else

ACKNOWLEDGEMENTS

I must acknowledge that any result in contemporary high energy physics, especially from large collaborations like CLEO, owes a lot to many people. This analysis is no different and sits at the end of decades of effort, drawing on the labor and expertise of hundreds who built, maintained, and operated the CLEO-c detector and the CESR collider. I must also acknowledge the efforts that went into making sense of the data, in particular the efforts of those who measured the hadronic branching fractions of the D_s^+ meson that this analysis explicitly depends on.

Onto more personal acknowledgements, I must first thank my advisor, Anders Ryd, for guiding me through this and many other projects in the course of my graduate career in high energy physics with exceptional involvement. This document would not exist were it not for his patient guidance and encouragement. I have learned much from him in the fields of particle phenomenology, detector hardware, software development, statistics and collaboration politics, and I hope to learn more in the years ahead.

I thank David Cassel and Jim Alexander for following the progress of this analysis with so much interest and offering very helpful advice at various junctures of the effort. I am grateful to Werner Sun for helping me familiarize myself with CLEO-c software. Werner, Dan Riley, David Kreinick and Brian Heltsley must be thanked for helping me reprocess large CLEO-c datasets. I thank Peter Onyisi for lending us his expertise on the hadronic decay of D_s^+ mesons. Brian, Matthew Shepherd and Richard Ehrlich were tasked with reviewing this analysis internally within the CLEO collaboration and for that I thank them. Brian must also be thanked for answering my questions regarding CLEO-c calorimetry and offering great suggestions for improving the analysis. I also thank Paras

Naik for fielding random questions about the detector and software at equally random times of the day or night. I am grateful to Pattie Place, the Thesis Advisor of the Graduate School at Cornell University, for weeding out typesetting errors from this document.

Finally, I thank Cornell University, the Department of Physics and the Laboratory for Elementary Particle Physics for accepting my candidacy and giving me such an extraordinary opportunity to work at the very frontiers of physics.

TABLE OF CONTENTS

Biographical Sketch . . . iii
Dedication . . . iv
Acknowledgements . . . v
Table of Contents . . . vii
List of Tables . . . x
List of Figures . . . xvii

1 Introduction **1**

2 A Theoretical Prediction for the Ratio of Branching Fractions $B(D_s^{*+} \to D_s^+ e^+ e^-)/B(D_s^{*+} \to D_s^+ \gamma)$ **6**
2.1 Rate for $D_s^{*+} \to D_s^+ \gamma$ . . . 8
2.2 Rate for $D_s^{*+} \to D_s^+ e^+ e^-$ . . . 10

3 The CLEO-c Detector **16**
3.1 The Tracking System . . . 21
3.2 The Calorimeter . . . 24

4 Analysis Method to Search for the $D_s^{*+} \to D_s^+ e^+ e^-$ and Measure the Ratio of Branching Fractions $B(D_s^{*+} \to D_s^+ e^+ e^-)/B(D_s^{*+} \to D_s^+ \gamma)$ **26**
4.1 Backgrounds for $D_s^{*+} \to D_s^+ e^+ e^-$ . . . 31
4.2 Selection Criteria for Reconstructing $D_s^{*+} \to D_s^+ e^+ e^-$ . . . 33
4.2.1 Track Quality Requirements for the Soft e^+e^- Pair . . . 33
4.2.2 Mass of the D_s^+ Meson, $m_{D_s^+}$ . . . 34
4.2.3 Beam Constrained Mass of the D_s^{*+} Meson, m_{BC} . . . 34
4.2.4 Mass Difference between the D_s^{*+} and the D_s^+ Mesons, δm . . . 35
4.2.5 Δd_0 between the e^+ and e^- Tracks . . . 36
4.2.6 $\Delta\phi_0$ between the e^+ and e^- Tracks . . . 37
4.3 Selection Criteria for Reconstructing $D_s^{*+} \to D_s^+ \gamma$ . . . 38
4.3.1 Shower Criteria for the Photon . . . 39
4.4 Datasets Used . . . 40
4.4.1 Generic Monte Carlo . . . 41
4.4.2 Continuum Monte Carlo . . . 42
4.5 Reprocessing Data to Fit Tracks with the Electron Mass Hypothesis 43
4.6 Monte Carlo Generation and Validation . . . 45
4.7 Optimization of Selection Criteria for the $D_s^{*+} \to D_s^+ e^+ e^-$ . . . 47
4.7.1 $D_s^+ \to K^+K^-\pi^+$ . . . 50
4.7.2 $D_s^+ \to K_S K^+$ . . . 62
4.7.3 $D_s^+ \to \eta\pi^+; \eta \to \gamma\gamma$ . . . 64
4.7.4 $D_s^+ \to \eta'\pi^+; \eta' \to \pi^+\pi^-\eta; \eta \to \gamma\gamma$ . . . 66
4.7.5 $D_s^+ \to K^+K^-\pi^+\pi^0$ . . . 68
4.7.6 $D_s^+ \to \pi^+\pi^-\pi^+$ . . . 70

4.7.7 $D_s^+ \to K^{*+}K^{*0}; K^{*+} \to K_S^0\pi^+, K^{*0} \to K^-\pi^+$ . . . 72
4.7.8 $D_s^+ \to \eta\rho^+; \eta \to \gamma\gamma; \rho^+ \to \pi^+\pi^0$ . . . 74
4.7.9 $D_s^+ \to \eta'\pi^+; \eta' \to \rho^0\gamma$ . . . 76
4.8 Efficiency of Selection Criteria for the Reconstruction of $D_s^{*+} \to D_s^+e^+e^-$ . . . 78
4.9 Estimation of Background in the Signal Region of $D_s^{*+} \to D_s^+e^+e^-$. 84
4.9.1 Determining the Shape of the m_{BC} Distribution . . . 86
4.9.2 Determining the Shape of the δm Distribution . . . 88
4.9.3 Estimating the Background in the $D_s^+ \to K^+K^-\pi^+$ Mode . . 90
4.9.4 Estimating the Background in the $D_s^+ \to K_SK^+$ Mode . . . 93
4.9.5 Estimating the Background in the $D_s^+ \to \eta\pi^+; \eta \to \gamma\gamma$ Mode 95
4.9.6 Estimating the Background in the $D_s^+ \to \eta'\pi^+; \eta' \to \pi^+\pi^-\eta; \eta \to \gamma\gamma$ Mode . . . 97
4.9.7 Estimating the Background in the $D_s^+ \to K^+K^-\pi^+\pi^0$ Mode . 99
4.9.8 Estimating the Background in the $D_s^+ \to \pi^+\pi^-\pi^+$ Mode . . . 102
4.9.9 Estimating the Background in the $D_s^+ \to K^{*+}K^{*0}; K^{*+} \to K_S^0\pi^+; K^{*0} \to K^-\pi^+$ Mode . . . 104
4.9.10 Estimating the Background in the $D_s^+ \to \eta\rho^+; \eta \to \gamma\gamma; \rho^+ \to \pi^+\pi^0$ Mode . . . 107
4.9.11 Estimating the Background in the $D_s^+ \to \eta'\pi^+; \eta' \to \rho^0\gamma$ Mode 110
4.9.12 Summary of Estimated Background in the Various Modes 113
4.9.13 Predicted Signal Significances . . . 113
4.10 Signal Yields and Selection Efficiencies for $D_s^{*+} \to D_s^+\gamma$ . . . 117
4.10.1 $D_s^+ \to K^+K^-\pi^+$ . . . 120
4.10.2 $D_s^+ \to K_SK^+$ . . . 129
4.10.3 $D_s^+ \to \eta\pi^+; \eta \to \gamma\gamma$ . . . 135
4.10.4 $D_s^+ \to \eta'\pi^+; \eta' \to \pi^+\pi^-\eta; \eta \to \gamma\gamma$ . . . 141
4.10.5 $D_s^+ \to K^+K^-\pi^+\pi^0$ . . . 147
4.10.6 $D_s^+ \to \pi^+\pi^-\pi^+$ . . . 153
4.10.7 $D_s^+ \to K^{*+}K^{*0}; K^{*+} \to K_S^0\pi^+; K^{*0} \to K^-\pi^+$ . . . 159
4.10.8 $D_s^+ \to \eta\rho^+; \eta \to \gamma\gamma; \rho^+ \to \pi^+\pi^0$ . . . 165
4.10.9 $D_s^+ \to \eta'\pi^+; \eta' \to \rho^0\gamma$ . . . 171
4.11 Un-blinding Data and Results . . . 177
4.11.1 $D_s^+ \to K^+K^-\pi^+$ . . . 184
4.11.2 $D_s^+ \to K_SK^+$ . . . 185
4.11.3 $D_s^+ \to \eta\pi^+; \eta \to \gamma\gamma$ . . . 186
4.11.4 $D_s^+ \to \eta'\pi^+; \eta' \to \pi^+\pi^-\eta; \eta \to \gamma\gamma$ . . . 187
4.11.5 $D_s^+ \to K^+K^-\pi^+\pi^0$ . . . 188
4.11.6 $D_s^+ \to \pi^+\pi^-\pi^+$ . . . 189
4.11.7 $D_s^+ \to K^{*+}K^{*0}; K^{*+} \to K_S^0\pi^+; K^{*0} \to K^-\pi^+$ . . . 190
4.11.8 $D_s^+ \to \eta\rho^+; \eta \to \gamma\gamma; \rho^+ \to \pi^+\pi^0$ . . . 191
4.11.9 $D_s^+ \to \eta'\pi^+; \eta' \to \rho^0\gamma$ . . . 192
4.11.10 Comparison of $m_{e^+e^-}$ between Data and Monte Carlo Simulation . . . 193

4.11.11 A Re-evaluation of All D_s^{*+} Branching Fractions 194
4.12 Systematic Uncertainties from the Tracking of Soft Electrons and Photons 196
4.12.1 Method 1 199
4.12.2 Method 2 210

5 Results and Conclusion **213**

A Plots Used to Optimize Selection Criteria for $D_s^{*+} \to D_s^+ e^+ e^-$ **215**
A.1 $D_s^+ \to K_S K^+$ 216
A.2 $D_s^+ \to \eta\pi^+; \eta \to \gamma\gamma$ 222
A.3 $D_s^+ \to \eta'\pi^+; \eta' \to \pi^+\pi^-\eta; \eta \to \gamma\gamma$ 228
A.4 $D_s^+ \to K^+K^-\pi^+\pi^0$ 234
A.5 $D_s^+ \to \pi^+\pi^-\pi^+$ 240
A.6 $D_s^+ \to\to K^{*+}K^{*0}; K^{*+} \to K_S^0\pi^+, K^{*0} \to K^-\pi^+$ 246
A.7 $D_s^+ \to \eta\rho^+; \eta \to \gamma\gamma; \rho^+ \to \pi^+\pi^0$ 252
A.8 $D_s^+ \to \eta'\pi^+; \eta' \to \rho^0\gamma$ 258

Bibliography **264**

LIST OF TABLES

1.1 Branching fractions of the known decays of the D_s^{*+}. 4

4.1 Integrated luminosity corresponding to the CLEO-c datasets used in this analysis. The statistical uncertainties are added in quadrature, while the systematic uncertainties are added linearly. Thereafter, these two forms of uncertainties are added in quadrature to give us the total uncertainty we use for the analysis and the remainder of this document. 40

4.2 Numbers of signal and background events retained by optimized selection criteria in signal and background Monte Carlo simulations where electron tracks have been fitted to the pion mass hypothesis. The numbers are normalized to 586 pb^{-1} of integrated luminosity. 49

4.3 Numbers of signal and background events retained by optimized selection criteria in signal and background Monte Carlo simulations where electron tracks have been fitted to the electron mass hypothesis. The numbers are normalized to 586 pb^{-1} of integrated luminosity. 50

4.4 Selection criteria for data with electron tracks fitted to the pion and electron mass hypotheses in the $D_s^+ \to K^+K^-\pi^+$ decay mode. 61

4.5 Numbers of signal and background events left in 586 pb^{-1} of pion and electron-fitted simulation samples in the $D_s^+ \to K^+K^-\pi^+$ decay mode. 61

4.6 Selection criteria for data with electron tracks fitted to the pion and electron mass hypotheses in the $D_s^+ \to K_S K^+$ decay mode. . . 62

4.7 Numbers of signal and background events expected in pion and electron-fitted data in the $D_s^+ \to K_S K^+$ decay mode. 63

4.8 Selection criteria for data with electron tracks fitted to the pion and electron mass hypotheses in the $D_s^+ \to \eta\pi^+; \eta \to \gamma\gamma$ decay mode. 64

4.9 Numbers of signal and background events expected in pion and electron-fitted data in the $D_s^+ \to \eta\pi^+; \eta \to \gamma\gamma$ decay mode. 65

4.10 Selection criteria for data with electron tracks fitted to the pion and electron mass hypotheses in the $D_s^+ \to \eta'\pi^+; \eta' \to \pi^+\pi^-\eta; \eta \to \gamma\gamma$ decay mode. 66

4.11 Numbers of signal and background events expected in pion and electron-fitted data in the $D_s^+ \to \eta'\pi^+; \eta' \to \pi^+\pi^-\eta; \eta \to \gamma\gamma$ decay mode. 67

4.12 Selection criteria for data with electron tracks fitted to the pion and electron mass hypotheses in the $D_s^+ \to K^+K^-\pi^+\pi^0$ decay mode. 68

4.13 Numbers of signal and background events expected in pion and electron-fitted data in the $D_s^+ \to K^+K^-\pi^+\pi^0$ decay mode. 69

4.14 Selection criteria for data with electron tracks fitted to the pion and electron mass hypotheses in the $D_s^+ \to \pi^+\pi^-\pi^+$ decay mode. . 70
4.15 Numbers of signal and background events expected in pion and electron-fitted data in the $D_s^+ \to \pi^+\pi^-\pi^+$ decay mode. 71
4.16 Selection criteria for data with electron tracks fitted to the pion and electron mass hypotheses in the $D_s^+ \to K^{*+}K^{*0}$ decay mode. . 72
4.17 Numbers of signal and background events expected in pion and electron-fitted data in the $D_s^+ \to K^{*+}K^{*0}$ decay mode. 73
4.18 Selection criteria for data with electron tracks fitted to the pion and electron mass hypotheses in the $D_s^+ \to \eta\rho^+; \eta \to \gamma\gamma; \rho^+ \to \pi^+\pi^0$ decay mode. 74
4.19 Numbers of signal and background events expected in pion and electron-fitted data in the $D_s^+ \to \eta\rho^+; \eta \to \gamma\gamma; \rho^+ \to \pi^+\pi^0$ decay mode. 75
4.20 Selection criteria for data with electron tracks fitted to the pion and electron mass hypotheses in the $D_s^+ \to \eta'\pi^+; \eta' \to \rho^0\gamma$ decay mode. 76
4.21 Numbers of signal and background events expected in pion and electron-fitted data in the $D_s^+ \to \eta'\pi^+; \eta' \to \rho^0\gamma$ decay mode. 77
4.22 Selection efficiencies for reconstructing the $D_s^{*+} \to D_s^+e^+e^-$ signal in each of the hadronic decay modes of the D_s^+ that this analysis deals with. 79
4.23 Maximum likelihood fit parameters for the MC shape in m_{BC} distribution. 86
4.24 Maximum likelihood fit parameters for the data shape in m_{BC} distribution. 86
4.25 Maximum likelihood fit parameters for the MC shape in δm distribution. 88
4.26 Maximum likelihood fit parameters for the *Data shape* in δm distribution. 89
4.27 Maximum likelihood fit parameters to estimate background in the $D_s^+ \to K^+K^-\pi^+$ mode 91
4.28 Estimates of the background in the signal region of the $D_s^+ \to K^+K^-\pi^+$ mode using four fits outlined above. 92
4.29 Maximum likelihood fit parameters to estimate background in the $D_s^+ \to K_S K^+$ mode 94
4.30 Estimates of the background in the signal region of the $D_s^+ \to K_S K^+$ mode using four fits outlined above. 94
4.31 Maximum likelihood fit parameters to estimate background in the $D_s^+ \to \eta\pi^+; \eta \to \gamma\gamma$ mode 96
4.32 Estimates of the background in the signal region of the $D_s^+ \to \eta\pi^+; \eta \to \gamma\gamma$ mode using four fits outlined above. 96
4.33 Estimates of the background in the signal region of the $D_s^+ \to \eta'\pi^+; \eta' \to \pi^+\pi^-\eta; \eta \to \gamma\gamma$ mode using four fits outlined above. . . 98

4.34 Maximum likelihood fit parameters to estimate background in the $D_s^+ \to K^+K^-\pi^+\pi^0$ mode 99
4.35 Estimates of the background in the signal region of the $D_s^+ \to K^+K^-\pi^+\pi^0$ mode using four fits outlined above. 100
4.36 Maximum likelihood fit parameters to estimate background in the $D_s^+ \to \pi^+\pi^-\pi^+$ mode 103
4.37 Estimates of the background in the signal region of the $D_s^+ \to \pi^+\pi^-\pi^+$ mode using four fits outlined above. 103
4.38 Maximum likelihood fit parameters to estimate background in the $D_s^+ \to K^{*+}K^{*0}$ mode 105
4.39 Estimates of the background in the signal region of the $D_s^+ \to K^{*+}K^{*0}$ mode using four fits outlined above. 106
4.40 Maximum likelihood fit parameters to estimate background in the $D_s^+ \to \eta\rho^+; \eta \to \gamma\gamma; \rho^+ \to \pi^+\pi^0$ mode 108
4.41 Estimates of the background in the signal region of the $D_s^+ \to \eta\rho^+; \eta \to \gamma\gamma; \rho^+ \to \pi^+\pi^0$ mode using four fits outlined above. . . . 109
4.42 Maximum likelihood fit parameters to estimate background in the $D_s^+ \to \eta'\pi^+; \eta' \to \rho^0\gamma$ mode 111
4.43 Estimates of the background in the signal region of the $D_s^+ \to \eta'\pi^+; \eta' \to \rho^0\gamma$ mode using four fits outlined above. 112
4.44 Summary of the estimates for the background in the signal region for all the modes we have studied. 114
4.45 The projected signal significance expected for each individual hadronic decay mode of the D_s^+, as well as modes combined. . . . 116
4.46 Signal yields and efficiencies for $D_s^{*+} \to D_s^+\gamma$ from all the modes of decay of the D_s^+ relevant for our measurement of the ratio $B(D_s^{*+} \to D_s^+e^+e^-)/B(D_s^{*+} \to D_s^+\gamma)$. $B(D_s^+ \to i)$ is the known branching fraction for D_s^+ to decay via the i^{th} hadronic mode we are studying. $\epsilon^i_{D_s\gamma}$ is the efficiency of our selection criteria for the mode. $N^i_{D_s\gamma}$ is the signal yield observed for this mode. 118
4.47 Signal yields and efficiencies for $D_s^{*+} \to D_s^+\gamma$ from all the modes of decay of the D_s^+ relevant for our measurement of the ratio $B(D_s^{*+} \to D_s^+e^+e^-)/B(D_s^{*+} \to D_s^+\gamma)$ in Generic Monte Carlo. $B(D_s^+ \to i)$ is the known branching fraction for D_s^+ to decay via the i^{th} hadronic mode we are studying. $\epsilon^i_{D_s\gamma}$ is the efficiency of our selection criteria for the mode. $N^i_{D_s\gamma}$ is the signal yield observed for this mode. $B(D_s^{*+} \to D_s^+\gamma)$ is the branching fraction for $D_s^{*+} \to D_s^+e^+e^-$ inferred from this mode. Error [1] on the inferred branching fraction is the statistical error from the final fit. Error [2] encapsulates the systematic uncertainties from the signal efficiency and the uncertainty in the number of produced generic MC events as described in Section 4.4.1. 119

4.48 Selection criteria for $D_s^{*+} \to D_s^+\gamma$ events where $D_s^+ \to K^+K^-\pi^+$. The δm cut has been widened to accommodate the wider peak for the signal in this distribution. 120
4.49 $\epsilon^i_{D_s\gamma}$ is the efficiency of our selection criteria for the mode. $N^i_{D_s\gamma}$ is the signal yield observed in generic Monte Carlo for this mode. $B(D_s^{*+} \to D_s^+\gamma)$ is the branching fraction for $D_s^{*+} \to D_s^+e^+e^-$ inferred from this mode. Error [1] on the inferred branching fraction is the statistical error from the final fit. Error [2] encapsulates the systematic uncertainties from the signal efficiency and the uncertainty in the number of produced generic MC events. . 127
4.50 $\epsilon^i_{D_s\gamma}$ is the efficiency of our selection criteria for the mode. $N^i_{D_s\gamma}$ is the signal yield in data observed for this mode. 128
4.51 Selection criteria for $D_s^{*+} \to D_s^+\gamma$ events where $D_s^+ \to K_SK^+$. The δm cut has been widened to accomodate the wider peak for the signal in this distribution. 129
4.52 $\epsilon^i_{D_s\gamma}$ is the efficiency of our selection criteria for the mode. $N^i_{D_s\gamma}$ is the signal yield in generic Monte Carlo observed for this mode. $B(D_s^{*+} \to D_s^+\gamma)$ is the branching fraction for $D_s^{*+} \to D_s^+e^+e^-$ inferred from this mode. Error [1] on the inferred branching fraction is the statistical error from the final fit. Error [2] encapsulates the systematic uncertainties from the signal efficiency and the uncertainty in the number of produced generic MC events. . 131
4.53 $\epsilon^i_{D_s\gamma}$ is the efficiency of our selection criteria for the mode. $N^i_{D_s\gamma}$ is the signal yield in data observed for this mode. 132
4.54 Selection criteria for $D_s^{*+} \to D_s^+\gamma$ events where $D_s^+ \to \eta\pi^+; \eta \to \gamma\gamma$. The δm cut has been widened to accomodate the wider peak for the signal in this distribution. 135
4.55 $\epsilon^i_{D_s\gamma}$ is the efficiency of our selection criteria for the mode. $N^i_{D_s\gamma}$ is the signal yield in generic Monte Carlo observed for this mode. $B(D_s^{*+} \to D_s^+\gamma)$ is the branching fraction for $D_s^{*+} \to D_s^+e^+e^-$ inferred from this mode. Error [1] on the inferred branching fraction is the statistical error from the final fit. Error [2] encapsulates the systematic uncertainties from the signal efficiency, the integrated luminosity and the production cross section for $D_s^{*\pm}D_s^{\mp}$. . . 137
4.56 $\epsilon^i_{D_s\gamma}$ is the efficiency of our selection criteria for the mode. $N^i_{D_s\gamma}$ is the signal yield observed in data for this mode. $B(D_s^{*+} \to D_s^+\gamma)$ is the branching fraction for $D_s^{*+} \to D_s^+e^+e^-$ inferred from this mode. Error [1] on the inferred branching fraction is the statistical error from the final fit. Error [2] arises from the uncertainty in the branching fraction for $D_s^+ \to i$. Error [3] encapsulates the systematic uncertainties from the signal efficiency, the integrated luminosity and the production cross section for $D_s^{*\pm}D_s^{\mp}$. Error [4] encapsulates the systematic error arising from the fit. 140

4.57 Selection criteria for $D_s^{*+} \to D_s^+\gamma$ events where $D_s^+ \to \eta'\pi^+; \eta' \to \pi^+\pi^-\eta; \eta \to \gamma\gamma$. The δm cut has been widened to accomodate the wider peak for the signal in this distribution. 141
4.58 $\epsilon^i_{D_s\gamma}$ is the efficiency of our selection criteria for the mode. $N^i_{D_s\gamma}$ is the signal yield observed in generic Monte Carlo for this mode. $B(D_s^{*+} \to D_s^+\gamma)$ is the branching fraction for $D_s^{*+} \to D_s^+e^+e^-$ inferred from this mode. Error [1] on the inferred branching fraction is the statistical error from the final fit. Error [2] encapsulates the systematic uncertainties from the signal efficiency, the integrated luminosity and the production cross section for $D_s^{*\pm}D_s^{\mp}$. . . 143
4.59 $\epsilon^i_{D_s\gamma}$ is the efficiency of our selection criteria for the mode. $N^i_{D_s\gamma}$ is the signal yield in data observed for this mode. $B(D_s^{*+} \to D_s^+\gamma)$ is the branching fraction for $D_s^{*+} \to D_s^+e^+e^-$ inferred from this mode. Error [1] on the inferred branching fraction is the statistical error from the final fit. Error [2] arises from the uncertainty in the branching fraction for $D_s^+ \to i$. Error [3] encapsulates the systematic uncertainties from the signal efficiency, the integrated luminosity and the production cross section for $D_s^{*\pm}D_s^{\mp}$. Error [4] encapsulates the systematic error arising from the fit. 146
4.60 Selection criteria for $D_s^{*+} \to D_s^+\gamma$ events where $D_s^+ \to K^+K^-\pi^+\pi^0$. The δm cut has been widened to accomodate the wider peak for the signal in this distribution. 147
4.61 $\epsilon^i_{D_s\gamma}$ is the efficiency of our selection criteria for the mode. $N^i_{D_s\gamma}$ is the signal yield observed in generic Monte Carlo for this mode. $B(D_s^{*+} \to D_s^+\gamma)$ is the branching fraction for $D_s^{*+} \to D_s^+e^+e^-$ inferred from this mode. Error [1] on the inferred branching fraction is the statistical error from the final fit. Error [2] encapsulates the systematic uncertainties from the signal efficiency, the integrated luminosity and the production cross section for $D_s^{*\pm}D_s^{\mp}$. . . 149
4.62 $\epsilon^i_{D_s\gamma}$ is the efficiency of our selection criteria for the mode. $N^i_{D_s\gamma}$ is the signal yield observed in data for this mode. $B(D_s^{*+} \to D_s^+\gamma)$ is the branching fraction for $D_s^{*+} \to D_s^+e^+e^-$ inferred from this mode. Error [1] on the inferred branching fraction is the statistical error from the final fit. Error [2] arises from the uncertainty in the branching fraction for $D_s^+ \to i$. Error [3] encapsulates the systematic uncertainties from the signal efficiency, the integrated luminosity and the production cross section for $D_s^{*\pm}D_s^{\mp}$. Error [4] encapsulates the systematic error arising from the fit. 152
4.63 Selection criteria for $D_s^{*+} \to D_s^+\gamma$ events where $D_s^+ \to \pi^+\pi^-\pi^+$. The δm cut has been widened to accomodate the wider peak for the signal in this distribution. 153

4.64 $\epsilon^i_{D_s\gamma}$ is the efficiency of our selection criteria for the mode. $N^i_{D_s\gamma}$ is the signal yield observed in generic Monte Carlo for this mode. $B(D_s^{*+} \to D_s^+\gamma)$ is the branching fraction for $D_s^{*+} \to D_s^+e^+e^-$ inferred from this mode. Error [1] on the inferred branching fraction is the statistical error from the final fit. Error [2] encapsulates the systematic uncertainties from the signal efficiency, the integrated luminosity and the production cross section for $D_s^{*\pm}D_s^{\mp}$. . . 155
4.65 $\epsilon^i_{D_s\gamma}$ is the efficiency of our selection criteria for the mode. $N^i_{D_s\gamma}$ is the signal yield observed in data for this mode. $B(D_s^{*+} \to D_s^+\gamma)$ is the branching fraction for $D_s^{*+} \to D_s^+e^+e^-$ inferred from this mode. Error [1] on the inferred branching fraction is the statistical error from the final fit. Error [2] arises from the uncertainty in the branching fraction for $D_s^+ \to i$. Error [3] encapsulates the systematic uncertainties from the signal efficiency, the integrated luminosity and the production cross section for $D_s^{*\pm}D_s^{\mp}$. Error [4] encapsulates the systematic error arising from the fit. 158
4.66 Selection criteria for $D_s^{*+} \to D_s^+\gamma$ events where $D_s^+ \to K^{*+}K^{*0}$. The δm cut has been widened to accomodate the wider peak for the signal in this distribution. 159
4.67 $\epsilon^i_{D_s\gamma}$ is the efficiency of our selection criteria for the mode. $N^i_{D_s\gamma}$ is the signal yield observed in generic Monte Carlo for this mode. $B(D_s^{*+} \to D_s^+\gamma)$ is the branching fraction for $D_s^{*+} \to D_s^+e^+e^-$ inferred from this mode. Error [1] on the inferred branching fraction is the statistical error from the final fit. Error [2] encapsulates the systematic uncertainties from the signal efficiency, the integrated luminosity and the production cross section for $D_s^{*\pm}D_s^{\mp}$. . . 161
4.68 $\epsilon^i_{D_s\gamma}$ is the efficiency of our selection criteria for the mode. $N^i_{D_s\gamma}$ is the signal yield observed in data for this mode. $B(D_s^{*+} \to D_s^+\gamma)$ is the branching fraction for $D_s^{*+} \to D_s^+e^+e^-$ inferred from this mode. Error [1] on the inferred branching fraction is the statistical error from the final fit. Error [2] arises from the uncertainty in the branching fraction for $D_s^+ \to i$. Error [3] encapsulates the systematic uncertainties from the signal efficiency, the integrated luminosity and the production cross section for $D_s^{*\pm}D_s^{\mp}$. Error [4] encapsulates the systematic error arising from the fit. 164
4.69 Selection criteria for $D_s^{*+} \to D_s^+\gamma$ events where $D_s^+ \to \eta\rho^+$. The δm cut has been widened to accomodate the wider peak for the signal in this distribution. 165

4.70 $\epsilon^i_{D_s\gamma}$ is the efficiency of our selection criteria for the mode. $N^i_{D_s\gamma}$ is the signal yield observed in generic Monte Carlo for this mode. $B(D_s^{*+} \to D_s^+\gamma)$ is the branching fraction for $D_s^{*+} \to D_s^+e^+e^-$ inferred from this mode. Error [1] on the inferred branching fraction is the statistical error from the final fit. Error [2] encapsulates the systematic uncertainties from the signal efficiency, the integrated luminosity and the production cross section for $D_s^{*\pm}D_s^{\mp}$. . . 167
4.71 $\epsilon^i_{D_s\gamma}$ is the efficiency of our selection criteria for the mode. $N^i_{D_s\gamma}$ is the signal yield observed in data for this mode. $B(D_s^{*+} \to D_s^+\gamma)$ is the branching fraction for $D_s^{*+} \to D_s^+e^+e^-$ inferred from this mode. Error [1] on the inferred branching fraction is the statistical error from the final fit. Error [2] arises from the uncertainty in the branching fraction for $D_s^+ \to i$. Error [3] encapsulates the systematic uncertainties from the signal efficiency, the integrated luminosity and the production cross section for $D_s^{*\pm}D_s^{\mp}$. Error [4] encapsulates the systematic error arising from the fit. 170
4.72 Selection criteria for $D_s^{*+} \to D_s^+\gamma$ events where $D_s^+ \to \eta'\pi^+; \eta' \to \rho^0\gamma$. The δm cut has been widened to accomodate the wider peak for the signal in this distribution. 171
4.73 $\epsilon^i_{D_s\gamma}$ is the efficiency of our selection criteria for the mode. $N^i_{D_s\gamma}$ is the signal yield observed in generic Monte Carlo for this mode. $B(D_s^{*+} \to D_s^+\gamma)$ is the branching fraction for $D_s^{*+} \to D_s^+e^+e^-$ inferred from this mode. Error [1] on the inferred branching fraction is the statistical error from the final fit. Error [2] encapsulates the systematic uncertainties from the signal efficiency, the integrated luminosity and the production cross section for $D_s^{*\pm}D_s^{\mp}$. . . 173
4.74 $\epsilon^i_{D_s\gamma}$ is the efficiency of our selection criteria for the mode. $N^i_{D_s\gamma}$ is the signal yield observed in data for this mode. $B(D_s^{*+} \to D_s^+\gamma)$ is the branching fraction for $D_s^{*+} \to D_s^+e^+e^-$ inferred from this mode. Error [1] on the inferred branching fraction is the statistical error from the final fit. Error [2] arises from the uncertainty in the branching fraction for $D_s^+ \to i$. Error [3] encapsulates the systematic uncertainties from the signal efficiency, the integrated luminosity and the production cross section for $D_s^{*\pm}D_s^{\mp}$. Error [4] encapsulates the systematic error arising from the fit. 176
4.75 Data and estimated backgrounds in the signal region used to estimate the numbers of signal events found in each mode and the corresponding significance of the signal. Expected numbers of signal events from Monte Carlo simulations also listed. 178
4.76 The ratio of branching fractions $B(D_s^{*+} \to D_s^+e^+e^-)/B(D_s^{*+} \to D_s^+\gamma)$ inferred from the signal yields and efficiencies of each and all modes. 180

LIST OF FIGURES

2.1 A Feynman diagram for the $D_s^{*+} \to D_s^+ \gamma$ process. 8
2.2 A Feynman diagram for the $D_s^{*+} \to D_s^+ e^+ e^-$ process. 10

3.1 Cutaway schematic of the CLEO-c detector. 17
3.2 Quarter-view schematic of the CLEO-c detector. 18
3.3 The inner drift chamber. 20
3.4 Stereo angles in the outer drift chamber. 20

4.1 A schematic showing a e^+e^- collision producing a $D_s^{*+}D_s^-$ pair where the D_s^{*+} decays to a D_s^+ and a e^+e^- via the decay we are searching for in this dissertation. 28
4.2 An illustration of Δd_0 between the soft e^+e^- tracks of the signal and conversion events. 37
4.3 An illustration of $\Delta\phi_0$ between the soft e^+e^- tracks of the signal and conversion events. 38
4.4 (Left) The difference between the reconstructed and Monte Carlo generated electron energy plotted against the generated electron energy when the electrons have been fitted to tracks using the pion mass hypothesis. (Right) The difference when the electrons are fitted to tracks using the electron mass hypothesis. 44
4.5 (a) The analytical expression for the distribution of k^2 overlaid with the distribution of the corrected m_{ee}^2 from the Monte Carlo. (b) A zoom into the region betweeen 0 GeV and $20m_e^2$ to illustrate the close match near the peak. 46
4.6 Optimization plots for the $m_{D_s^+}$ selection criterion in the $D_s^+ \to K^+K^-\pi^+$ mode using pion-fitted tracks in the simulated samples. The top left plot is the distribution of $m_{D_s^+}$ in the signal Monte Carlo sample. The top right plot graphs the number of signal MC sample events accepted by the criterion as we increase the cut width plotted on the x-axis. The plots in the second and third rows correspond to the generic and continuum MC samples. The bottom left shows the significance of the signal over background. The bottom right plot shows the precision of the signal. 51
4.7 Optimization plots for the m_{BC} selection criterion in the $D_s^+ \to K^+K^-\pi^+$ mode using pion-fitted tracks in the simulated samples. The top left plot is the distribution of m_{BC} in the signal Monte Carlo sample. The top right plot graphs the number of signal MC sample events accepted by the criterion as we increase the cut width plotted on the x-axis. The plots in the second and third rows correspond to the generic and continuum MC samples. The bottom left shows the significance of the signal over background. The bottom right plot shows the precision of the signal. 52

4.8 Optimization plots for the δm selection criterion in the $D_s^+ \to K^+K^-\pi^+$ mode using pion-fitted tracks in the simulated samples. The top left plot is the distribution of δm in the signal Monte Carlo sample. The top right plot graphs the number of signal MC sample events accepted by the criterion as we increase the cut width plotted on the x-axis. The plots in the second and third rows correspond to the generic and continuum MC samples. The bottom left shows the significance of the signal over background. The bottom right plot shows the precision of the signal. 53
4.9 Optimization plots for the Δd_0 selection criterion in the $D_s^+ \to K^+K^-\pi^+$ mode using pion-fitted tracks in the simulated samples. The top left plot is the distribution of Δd_0 between the e^+e^- tracks in the signal Monte Carlo sample. The top right plot graphs the number of signal MC sample events accepted by the criterion as we vary the cut on the x-axis. The plots in the second and third rows correspond to the generic and continuum MC samples. The bottom left shows the significance of the signal over background. The bottom right plot shows the precision of the signal. 54
4.10 Optimization plots for the $\Delta\phi_0$ selection criterion in the $D_s^+ \to K^+K^-\pi^+$ mode using pion-fitted tracks in the simulated samples. The top left plot is the distribution of $\Delta\phi_0$ between the e^+e^- tracks in the signal Monte Carlo sample. The top right plot graphs the number of signal MC sample events accepted by the criterion as we vary the cut on the x-axis. The plots in the second and third rows correspond to the generic and continuum MC samples. The bottom left shows the significance of the signal over background. The bottom right plot shows the precision of the signal. 55
4.11 Optimization plots for the $m_{D_s^+}$ selection criterion in the $D_s^+ \to K^+K^-\pi^+$ mode using electron-fitted tracks in the simulated samples. The top left plot is the distribution of $m_{D_s^+}$ in the signal Monte Carlo sample. The top right plot graphs the number of signal MC sample events accepted by the criterion as we increase the cut width plotted on the x-axis. The plots in the second, third and fourth rows correspond to the $D_s^{*+} \to D_s^+\gamma$, generic and continuum MC samples. The bottom left shows the significance of the signal over background. The bottom right plot shows the precision of the signal. 56

4.12 Optimization plots for the m_{BC} selection criterion in the $D_s^+ \to K^+K^-\pi^+$ mode using electron-fitted tracks in the simulated samples. The top left plot is the distribution of m_{BC} in the signal Monte Carlo sample. The top right plot graphs the number of signal MC sample events accepted by the criterion as we increase the cut width plotted on the x-axis. The plots in the second, third and fourth rows correspond to the $D_s^{*+} \to D_s^+\gamma$, generic and continuum MC samples. The bottom left shows the significance of the signal over background. The bottom right plot shows the precision of the signal. 57
4.13 Optimization plots for the δm selection criterion in the $D_s^+ \to K^+K^-\pi^+$ mode using electron-fitted tracks in the simulated samples. The top left plot is the distribution of δm in the signal Monte Carlo sample. The top right plot graphs the number of signal MC sample events accepted by the criterion as we increase the cut width plotted on the x-axis. The plots in the second, third and fourth rows correspond to the $D_s^{*+} \to D_s^+\gamma$, generic and continuum MC samples. The bottom left shows the significance of the signal over background. The bottom right plot shows the precision of the signal. 58
4.14 Optimization plots for the Δd_0 selection criterion in the $D_s^+ \to K^+K^-\pi^+$ mode using electron-fitted tracks in the simulated samples. The top left plot is the distribution of Δd_0 between the e^+e^- tracks in the signal Monte Carlo sample. The top right plot graphs the number of signal MC sample events accepted by the criterion as we vary the cut on the x-axis. The plots in the second, third and fourth rows correspond to the $D_s^{*+} \to D_s^+\gamma$, generic and continuum MC samples. The bottom left shows the significance of the signal over background. The bottom right plot shows the precision of the signal. 59
4.15 Optimization plots for the $\Delta\phi_0$ selection criterion in the $D_s^+ \to K^+K^-\pi^+$ mode using electron-fitted tracks in the simulated samples. The top left plot is the distribution of $\Delta\phi_0$ between the e^+e^- tracks in the signal Monte Carlo sample. The top right plot graphs the number of signal MC sample events accepted by the criterion as we vary the cut on the x-axis. The plots in the second, third and fourth rows correspond to the $D_s^{*+} \to D_s^+\gamma$, generic and continuum MC samples. The bottom left shows the significance of the signal over background. The bottom right plot shows the precision of the signal. 60
4.16 Signal efficiency for reconstructing $D_s^{*+} \to D_s^+e^+e^-$ in $D_s^+ \to K^+K^-\pi^+$ as represented in the m_{BC} distribution. 78
4.17 Signal efficiency for reconstructing $D_s^{*+} \to D_s^+e^+e^-$ in $D_s^+ \to K_S K^+$ as represented in the m_{BC} distribution. 79

4.18 Signal efficiency for reconstructing $D_s^{*+} \to D_s^+ e^+ e^-$ in $D_s^+ \to \eta\pi^+$ as represented in the m_{BC} distribution. 80
4.19 Signal efficiency for reconstructing $D_s^{*+} \to D_s^+ e^+ e^-$ in $D_s^+ \to \eta'\pi^+; \eta' \to \pi^+\pi^-\eta; \eta \to \gamma\gamma$ as represented in the m_{BC} distribution. . 80
4.20 Signal efficiency for reconstructing $D_s^{*+} \to D_s^+ e^+ e^-$ in $D_s^+ \to K^+K^-\pi^+\pi^0$ as represented in the m_{BC} distribution. 81
4.21 Signal efficiency for reconstructing $D_s^{*+} \to D_s^+ e^+ e^-$ in $D_s^+ \to \pi^+\pi^-\pi^+$ as represented in the m_{BC} distribution. 81
4.22 Signal efficiency for reconstructing $D_s^{*+} \to D_s^+ e^+ e^-$ in $D_s^+ \to K^{*+}K^{*0}$ as represented in the m_{BC} distribution. 82
4.23 Signal efficiency for reconstructing $D_s^{*+} \to D_s^+ e^+ e^-$ in $D_s^+ \to \eta\rho^+; \eta \to \gamma\gamma; \rho^+ \to \pi^+\pi^0$ as represented in the m_{BC} distribution. . . 82
4.24 Signal efficiency for reconstructing $D_s^{*+} \to D_s^+ e^+ e^-$ in $D_s^+ \to \eta'\pi^+; \eta' \to \rho^0\gamma$ as represented in the m_{BC} distribution. 83
4.25 Distributions of m_{BC} in Monte Carlo and data. The blue region is distribution of m_{BC} in Continuum MC. On top of that, in green, is stacked the Generic MC with Conversion type events excluded. The Conversion MC is stacked on top of that in red. The black curve is fitted to the sum of the aforementioned background distributions. The Signal MC is stacked on top of the background MC to show roughly what expect to see when we unblind data. Data points, blinded in the signal region, are overlaid in magenta. The magenta curve is fitted to the data in the sideband regions, as described in the text. 87
4.26 Distributions of δm in Monte Carlo and data. The blue region is distribution of δm in Continuum MC. On top of that, in green, is stacked the Generic MC with Conversion type events excluded. The Conversion MC is stacked on top of that in red. The black curve is fitted to the sum of the aforementioned background distributions. The Signal MC is stacked on top of the background MC to show roughly what expect to see when we unblind data. Data points, blinded in the signal region, are overlaid in magenta. The magenta curve is fitted to the data in the sideband regions, as described in the text. 89
4.27 The various backgrounds and signal MC expected in the vicinity of the signal region in m_{BC} distribution of the $D_s^+ \to K^+K^-\pi^+$ mode. The data, blinded in the signal region, is overlaid in magenta points. The black and magenta curves are *MC* and *data shapes* scaled by maximum likelihood to the points of data in the sideband regions. 90

4.28 The various backgrounds and signal MC expected in the vicinity of the signal region in δm distribution of the $D_s^+ \to K^+K^-\pi^+$ mode. The data, blinded in the signal region, is overlaid in magenta points. The black and magenta curves are *MC* and *data shapes* scaled by maximum likelihood to the points of data in the sideband regions. 91
4.29 The various backgrounds and signal MC expected in the vicinity of the signal region in m_{BC} distribution of the $D_s^+ \to K_S K^+$ mode. The data, blinded in the signal region, is overlaid in magenta points. The black and magenta curves are *MC* and *data shapes* scaled by maximum likelihood to the points of data in the sideband regions. 93
4.30 The various backgrounds and signal MC expected in the vicinity of the signal region in δm distribution of the $D_s^+ \to K_S K^+$ mode. The data, blinded in the signal region, is overlaid in magenta points. The black and magenta curves are *MC* and *data shapes* scaled by maximum likelihood to the points of data in the sideband regions. 94
4.31 The various backgrounds and signal MC expected in the vicinity of the signal region in m_{BC} distribution of the $D_s^+ \to \eta\pi^+; \eta \to \gamma\gamma$ mode. The data, blinded in the signal region, is overlaid in magenta points. The black and magenta curves are *MC* and *data shapes* scaled by maximum likelihood to the points of data in the sideband regions. 95
4.32 The various backgrounds and signal MC expected in the vicinity of the signal region in δm distribution of the $D_s^+ \to \eta\pi^+; \eta \to \gamma\gamma$ mode. The data, blinded in the signal region, is overlaid in magenta points. The black and magenta curves are *MC* and *data shapes* scaled by maximum likelihood to the points of data in the sideband regions. 96
4.33 The various backgrounds and signal MC expected in the vicinity of the signal region in m_{BC} distribution of the $D_s^+ \to \eta'\pi^+; \eta' \to \pi^+\pi^-\eta; \eta \to \gamma\gamma$ mode. The data, blinded in the signal region, is overlaid in magenta points. The black and magenta curves are *MC* and *data shapes* scaled by maximum likelihood to the points of data in the sideband regions. 97
4.34 The various backgrounds and signal MC expected in the vicinity of the signal region in δm distribution of the $D_s^+ \to \eta'\pi^+; \eta' \to \pi^+\pi^-\eta; \eta \to \gamma\gamma$ mode. The data, blinded in the signal region, is overlaid in magenta points. The black and magenta curves are *MC* and *data shapes* scaled by maximum likelihood to the points of data in the sideband regions. 98

4.35 The various backgrounds and signal MC expected in the vicinity of the signal region in m_{BC} distribution of the $D_s^+ \to K^+K^-\pi^+\pi^0$ mode. The data, blinded in the signal region, is overlaid in magenta points. The black and magenta curves are *MC* and *data shapes* scaled by maximum likelihood to the points of data in the sideband regions. 100
4.36 The various backgrounds and signal MC expected in the vicinity of the signal region in δm distribution of the $D_s^+ \to K^+K^-\pi^+\pi^0$ mode. The data, blinded in the signal region, is overlaid in magenta points. The black and magenta curves are *MC* and *data shapes* scaled by maximum likelihood to the points of data in the sideband regions. 101
4.37 The various backgrounds and signal MC expected in the vicinity of the signal region in m_{BC} distribution of the $D_s^+ \to \pi^+\pi^-\pi^+$ mode. The data, blinded in the signal region, is overlaid in magenta points. The black and magenta curves are *MC* and *data shapes* scaled by maximum likelihood to the points of data in the sideband regions. 102
4.38 The various backgrounds and signal MC expected in the vicinity of the signal region in δm distribution of the $D_s^+ \to \pi^+\pi^-\pi^+$ mode. The data, blinded in the signal region, is overlaid in magenta points. The black and magenta curves are *MC* and *data shapes* scaled by maximum likelihood to the points of data in the sideband regions. 103
4.39 The various backgrounds and signal MC expected in the vicinity of the signal region in m_{BC} distribution of the $D_s^+ \to K^{*+}K^{*0}$ mode. The data, blinded in the signal region, is overlaid in magenta points. The black and magenta curves are *MC* and *data shapes* scaled by maximum likelihood to the points of data in the sideband regions. 104
4.40 The various backgrounds and signal MC expected in the vicinity of the signal region in δm distribution of the $D_s^+ \to K^{*+}K^{*0}$ mode. The data, blinded in the signal region, is overlaid in magenta points. The black and magenta curves are *MC* and *data shapes* scaled by maximum likelihood to the points of data in the sideband regions. 105
4.41 The various backgrounds and signal MC expected in the vicinity of the signal region in m_{BC} distribution of the $D_s^+ \to \eta\rho^+; \eta \to \gamma\gamma; \rho^+ \to \pi^+\pi^0$ mode. The data, blinded in the signal region, is overlaid in magenta points. The black and magenta curves are *MC* and *data shapes* scaled by maximum likelihood to the points of data in the sideband regions. 107

4.42 The various backgrounds and signal MC expected in the vicinity of the signal region in δm distribution of the $D_s^+ \to \eta\rho^+; \eta \to \gamma\gamma; \rho^+ \to \pi^+\pi^0$ mode. The data, blinded in the signal region, is overlaid in magenta points. The black and magenta curves are *MC* and *data shapes* scaled by maximum likelihood to the points of data in the sideband regions. 108
4.43 The various backgrounds and signal MC expected in the vicinity of the signal region in m_{BC} distribution of the $D_s^+ \to \eta'\pi^+; \eta' \to \rho^0\gamma$ mode. The data, blinded in the signal region, is overlaid in magenta points. The black and magenta curves are *MC* and *data shapes* scaled by maximum likelihood to the points of data in the sideband regions. 110
4.44 The various backgrounds and signal MC expected in the vicinity of the signal region in δm distribution of the $D_s^+ \to \eta'\pi^+; \eta' \to \rho^0\gamma$ mode. The data, blinded in the signal region, is overlaid in magenta points. The black and magenta curves are *MC* and *data shapes* scaled by maximum likelihood to the points of data in the sideband regions. 111
4.45 Distribution of δm in the signal Monte Carlo sample of $D_s^{*+} \to D_s^+\gamma$ events where $D_s^+ \to K^+K^-\pi^+$. The plot is normalized so as to directly read out the efficiency of the δm selection criterion. . . . 121
4.46 Distribution of m_{BC} in the signal Monte Carlo sample of $D_s^{*+} \to D_s^+\gamma$ events where $D_s^+ \to K^+K^-\pi^+$. The plot is normalized so as to directly read out the efficiency of the m_{BC} selection criterion. . . . 122
4.47 Distribution of m_{BC} in the signal Monte Carlo sample of $D_s^{*+} \to D_s^+\gamma$ events where $D_s^+ \to K^+K^-\pi^+$. 123
4.48 Combinatorial background structured in the m_{BC} distribution consisting of events where the D_s^{*+} has been reconstructed out of the D_s^- and the γ, and where both the D_s^- and the γ have been matched to their generated counterparts in the Monte Carlo simulation. This distribution has been fitted to a shape described by Eq. 4.24. 124
4.49 Combinatorial background structured in the m_{BC} distribution consisting of events where the D_s^{*+} has been reconstructed out of the D_s^- and the γ, and the D_s^- has been matched to its generated counterpart but the γ has failed to match the photon from the D_s^{*+} decay at the generator level of the Monte Carlo simulation. This distribution has been fitted to a shape described by Eq. 4.25. 125
4.50 Distribution of m_{BC} of $D_s^{*+} \to D_s^+\gamma$ events where $D_s^+ \to K^+K^-\pi^+$ in 586 pb^{-1} of Generic Monte Carlo. 127
4.51 Distribution of m_{BC} of $D_s^{*+} \to D_s^+\gamma$ events where $D_s^+ \to K^+K^-\pi^+$ in 586 pb^{-1} of data. 128

4.52 Distribution of δm in the signal Monte Carlo sample of $D_s^{*+} \to D_s^+\gamma$ events where $D_s^+ \to K_S K^+$. The plot is normalized so as to directly read out the efficiency of the δm selection criterion. . . . 129
4.53 Distribution of m_{BC} in the signal Monte Carlo sample of $D_s^{*+} \to D_s^+\gamma$ events where $D_s^+ \to K_S K^+$. The plot is normalized so as to directly read out the efficiency of the m_{BC} selection criterion. . . . 130
4.54 Distribution of m_{BC} in the signal Monte Carlo sample of $D_s^{*+} \to D_s^+\gamma$ events where $D_s^+ \to K_S K^+$. 131
4.55 Combinatorial background in the m_{BC} distribution consisting of events where the D_s^{*+} has been reconstructed out of the D_s^- and the γ, and where both the D_s^- and the γ have been matched to their generated counterparts in the Monte Carlo simulation. This distribution has been fitted to a shape described by Eq. 4.24. . . . 132
4.56 Combinatorial background structured in the m_{BC} distribution consisting of events where the D_s^{*+} has been reconstructed out of the D_s^- and the γ, and the D_s^- has been matched to its generated counterpart but the γ has failed to match the photon from the D_s^{*+} decay at the generator level of the Monte Carlo simulation. This distribution has been fitted to a shape described by Eq. 4.25. 133
4.57 Distribution of m_{BC} of $D_s^{*+} \to D_s^+\gamma$ events where $D_s^+ \to K_S K^+$ in 586 pb^{-1} of Generic Monte Carlo. 133
4.58 Distribution of m_{BC} of $D_s^{*+} \to D_s^+\gamma$ events where $D_s^+ \to K_S K^+$ in 586 pb^{-1} of data. 134
4.59 Distribution of δm in the signal Monte Carlo sample of $D_s^{*+} \to D_s^+\gamma$ events where $D_s^+ \to \eta\pi^+; \eta \to \gamma\gamma$. The plot is normalized so as to directly read out the efficiency of the δm selection criterion. 135
4.60 Distribution of m_{BC} in the signal Monte Carlo sample of $D_s^{*+} \to D_s^+\gamma$ events where $D_s^+ \to \eta\pi^+; \eta \to \gamma\gamma$. The plot is normalized so as to directly read out the efficiency of the m_{BC} selection criterion from the area under the fit within the signal region. 136
4.61 Distribution of m_{BC} in the signal Monte Carlo sample of $D_s^{*+} \to D_s^+\gamma$ events where $D_s^+ \to \eta\pi^+; \eta \to \gamma\gamma$. 137
4.62 Combinatorial background in the m_{BC} distribution consisting of events where the D_s^{*+} has been reconstructed out of the D_s^- and the γ, and where both the D_s^- and the γ have been matched to their generated counterparts in the Monte Carlo simulation. This distribution has been fitted to a shape described by Eq. 4.24. . . . 138

4.63 Combinatorial background structured in the m_{BC} distribution consisting of events where the D_s^{*+} has been reconstructed out of the D_s^- and the γ, and the D_s^- has been matched to its generated counterpart but the γ has failed to match the photon from the D_s^{*+} decay at the generator level of the Monte Carlo simulation. This distribution has been fitted to a shape described by Eq. 4.25. 139
4.64 Distribution of m_{BC} of $D_s^{*+} \to D_s^+\gamma$ events where $D_s^+ \to \eta\pi^+; \eta \to \gamma\gamma$ in 586 pb^{-1} of Generic Monte Carlo. 139
4.65 Distribution of m_{BC} of $D_s^{*+} \to D_s^+\gamma$ events where $D_s^+ \to \eta\pi^+; \eta \to \gamma\gamma$ in 586 pb^{-1} of data. 140
4.66 Distribution of δm in the signal Monte Carlo sample of $D_s^{*+} \to D_s^+\gamma$ events where $D_s^+ \to \eta'\pi^+; \eta' \to \pi^+\pi^-\eta; \eta \to \gamma\gamma$. The plot is normalized so as to directly read out the efficiency of the δm selection criterion. 141
4.67 Distribution of m_{BC} in the signal Monte Carlo sample of $D_s^{*+} \to D_s^+\gamma$ events where $D_s^+ \to \eta'\pi^+; \eta' \to \pi^+\pi^-\eta; \eta \to \gamma\gamma$. The plot is normalized so as to directly read out the efficiency of the m_{BC} selection criterion from the area under the fit within the signal region. 142
4.68 Distribution of m_{BC} in the signal Monte Carlo sample of $D_s^{*+} \to D_s^+\gamma$ events where $D_s^+ \to \eta'\pi^+; \eta' \to \pi^+\pi^-\eta; \eta \to \gamma\gamma$. 143
4.69 Combinatorial background in the m_{BC} distribution consisting of events where the D_s^{*+} has been reconstructed out of the D_s^- and the γ, and where both the D_s^- and the γ have been matched to their generated counterparts in the Monte Carlo simulation. This distribution has been fitted to a shape described by Eq. 4.24. . . . 144
4.70 Combinatorial background structured in the m_{BC} distribution consisting of events where the D_s^{*+} has been reconstructed out of the D_s^- and the γ, and the D_s^- has been matched to its generated counterpart but the γ has failed to match the photon from the D_s^{*+} decay at the generator level of the Monte Carlo simulation. This distribution has been fitted to a shape described by Eq. 4.25. 145
4.71 Distribution of m_{BC} of $D_s^{*+} \to D_s^+\gamma$ events where $D_s^+ \to \eta'\pi^+; \eta' \to \pi^+\pi^-\eta; \eta \to \gamma\gamma$ in 586 pb^{-1} of Generic Monte Carlo. 145
4.72 Distribution of m_{BC} of $D_s^{*+} \to D_s^+\gamma$ events where $D_s^+ \to \eta'\pi^+; \eta' \to \pi^+\pi^-\eta; \eta \to \gamma\gamma$ in 586 pb^{-1} of data. 146
4.73 Distribution of δm in the signal Monte Carlo sample of $D_s^{*+} \to D_s^+\gamma$ events where $D_s^+ \to K^+K^-\pi^+\pi^0$. The plot is normalized so as to directly read out the efficiency of the δm selection criterion. . . 147

4.74 Distribution of m_{BC} in the signal Monte Carlo sample of $D_s^{*+} \to D_s^+\gamma$ events where $D_s^+ \to K^+K^-\pi^+\pi^0$. The plot is normalized so as to directly read out the efficiency of the m_{BC} selection criterion from the area under the fit within the signal region. 148
4.75 Distribution of m_{BC} in the signal Monte Carlo sample of $D_s^{*+} \to D_s^+\gamma$ events where $D_s^+ \to K^+K^-\pi^+\pi^0$. 149
4.76 Combinatorial background in the m_{BC} distribution consisting of events where the D_s^{*+} has been reconstructed out of the D_s^- and the γ, and where both the D_s^- and the γ have been matched to their generated counterparts in the Monte Carlo simulation. This distribution has been fitted to a shape described by Eq. 4.24. . . . 150
4.77 Combinatorial background structured in the m_{BC} distribution consisting of events where the D_s^{*+} has been reconstructed out of the D_s^- and the γ, and the D_s^- has been matched to its generated counterpart but the γ has failed to match the photon from the D_s^{*+} decay at the generator level of the Monte Carlo simulation. This distribution has been fitted to a shape described by Eq. 4.25. 151
4.78 Distribution of m_{BC} of $D_s^{*+} \to D_s^+\gamma$ events where $D_s^+ \to K^+K^-\pi^+\pi^0$ in 586 pb^{-1} of Generic Monte Carlo. 151
4.79 Distribution of m_{BC} of $D_s^{*+} \to D_s^+\gamma$ events where $D_s^+ \to K^+K^-\pi^+\pi^0$ in 586 pb^{-1} of data. 152
4.80 Distribution of δm in the signal Monte Carlo sample of $D_s^{*+} \to D_s^+\gamma$ events where $D_s^+ \to \pi^+\pi^-\pi^+$. The plot is normalized so as to directly read out the efficiency of the δm selection criterion. . . . 153
4.81 Distribution of m_{BC} in the signal Monte Carlo sample of $D_s^{*+} \to D_s^+\gamma$ events where $D_s^+ \to \pi^+\pi^-\pi^+$. The plot is normalized so as to directly read out the efficiency of the m_{BC} selection criterion from the area under the fit within the signal region. 154
4.82 Distribution of m_{BC} in the signal Monte Carlo sample of $D_s^{*+} \to D_s^+\gamma$ events where $D_s^+ \to \pi^+\pi^-\pi^+$. 155
4.83 Combinatorial background in the m_{BC} distribution consisting of events where the D_s^{*+} has been reconstructed out of the D_s^- and the γ, and where both the D_s^- and the γ have been matched to their generated counterparts in the Monte Carlo simulation. This distribution has been fitted to a shape described by Eq. 4.24. . . . 156
4.84 Combinatorial background structured in the m_{BC} distribution consisting of events where the D_s^{*+} has been reconstructed out of the D_s^- and the γ, and the D_s^- has been matched to its generated counterpart but the γ has failed to match the photon from the D_s^{*+} decay at the generator level of the Monte Carlo simulation. This distribution has been fitted to a shape described by Eq. 4.25. 157

4.85 Distribution of m_{BC} of $D_s^{*+} \to D_s^+\gamma$ events where $D_s^+ \to \pi^+\pi^-\pi^+$ in 586 pb^{-1} of Generic Monte Carlo. 157
4.86 Distribution of m_{BC} of $D_s^{*+} \to D_s^+\gamma$ events where $D_s^+ \to \pi^+\pi^-\pi^+$ in 586 pb^{-1} of data. 158
4.87 Distribution of δm in the signal Monte Carlo sample of $D_s^{*+} \to D_s^+\gamma$ events where $D_s^+ \to K^{*+}K^{*0}$. The plot is normalized so as to directly read out the efficiency of the δm selection criterion. . . . 159
4.88 Distribution of m_{BC} in the signal Monte Carlo sample of $D_s^{*+} \to D_s^+\gamma$ events where $D_s^+ \to K^{*+}K^{*0}$. The plot is normalized so as to directly read out the efficiency of the m_{BC} selection criterion from the area under the fit within the signal region. 160
4.89 Distribution of m_{BC} in the signal Monte Carlo sample of $D_s^{*+} \to D_s^+\gamma$ events where $D_s^+ \to K^{*+}K^{*0}$. 161
4.90 Combinatorial background in the m_{BC} distribution consisting of events where the D_s^{*+} has been reconstructed out of the D_s^- and the γ, and where both the D_s^- and the γ have been matched to their generated counterparts in the Monte Carlo simulation. This distribution has been fitted to a shape described by Eq. 4.24. . . . 162
4.91 Combinatorial background structured in the m_{BC} distribution consisting of events where the D_s^{*+} has been reconstructed out of the D_s^- and the γ, and the D_s^- has been matched to its generated counterpart but the γ has failed to match the photon from the D_s^{*+} decay at the generator level of the Monte Carlo simulation. This distribution has been fitted to a shape described by Eq. 4.25. 163
4.92 Distribution of m_{BC} of $D_s^{*+} \to D_s^+\gamma$ events where $D_s^+ \to K^{*+}K^{*0}$ in 586 pb^{-1} of Generic Monte Carlo. 163
4.93 Distribution of m_{BC} of $D_s^{*+} \to D_s^+\gamma$ events where $D_s^+ \to K^{*+}K^{*0}$ in 586 pb^{-1} of data. 164
4.94 Distribution of δm in the signal Monte Carlo sample of $D_s^{*+} \to D_s^+\gamma$ events where $D_s^+ \to \eta\rho^+$. The plot is normalized so as to directly read out the efficiency of the δm selection criterion. . . . 165
4.95 Distribution of m_{BC} in the signal Monte Carlo sample of $D_s^{*+} \to D_s^+\gamma$ events where $D_s^+ \to \eta\rho^+; \eta \to \gamma\gamma; \rho^+ \to \pi^+\pi^0$. The plot is normalized so as to directly read out the efficiency of the m_{BC} selection criterion from the area under the fit within the signal region. 166
4.96 Distribution of m_{BC} in the signal Monte Carlo sample of $D_s^{*+} \to D_s^+\gamma$ events where $D_s^{*+} \to D_s^+\gamma$ events where $D_s^+ \to \eta\rho^+; \eta \to \gamma\gamma; \rho^+ \to \pi^+\pi^0$. 167

4.97 Combinatorial background in the m_{BC} distribution consisting of events where the D_s^{*+} has been reconstructed out of the D_s^- and the γ, and where both the D_s^- and the γ have been matched to their generated counterparts in the Monte Carlo simulation. This distribution has been fitted to a shape described by Eq. 4.24. . . . 168
4.98 Combinatorial background structured in the m_{BC} distribution consisting of events where the D_s^{*+} has been reconstructed out of the D_s^- and the γ, and the D_s^- has been matched to its generated counterpart but the γ has failed to match the photon from the D_s^{*+} decay at the generator level of the Monte Carlo simulation. This distribution has been fitted to a shape described by Eq. 4.25. . . . 169
4.99 Distribution of m_{BC} of $D_s^{*+} \to D_s^+\gamma$ events where $D_s^+ \to \eta\rho^+; \eta \to \gamma\gamma; \rho^+ \to \pi^+\pi^0$ in 586 pb^{-1} of Generic Monte Carlo. . . . 169
4.100 Distribution of m_{BC} of $D_s^{*+} \to D_s^+\gamma$ events where $D_s^+ \to \eta\rho^+; \eta \to \gamma\gamma; \rho^+ \to \pi^+\pi^0$ in 586 pb^{-1} of data. . . . 170
4.101 Distribution of δm in the signal Monte Carlo sample of $D_s^{*+} \to D_s^+\gamma$ events where $D_s^+ \to \eta'\pi^+; \eta' \to \rho^0\gamma$. The plot is normalized so as to directly read out the efficiency of the δm selection criterion. 171
4.102 Distribution of m_{BC} in the signal Monte Carlo sample of $D_s^{*+} \to D_s^+\gamma$ events where $D_s^+ \to \eta'\pi^+; \eta' \to \rho^0\gamma$. The plot is normalized so as to directly read out the efficiency of the m_{BC} selection criterion from the area under the fit within the signal region. . . . 172
4.103 Distribution of m_{BC} in the signal Monte Carlo sample of $D_s^{*+} \to D_s^+\gamma$ events where $D_s^{*+} \to D_s^+\gamma$ events where $D_s^+ \to \eta'\pi^+; \eta' \to \rho^0\gamma$. . 173
4.104 Combinatorial background in the m_{BC} distribution consisting of events where the D_s^{*+} has been reconstructed out of the D_s^- and the γ, and where both the D_s^- and the γ have been matched to their generated counterparts in the Monte Carlo simulation. This distribution has been fitted to a shape described by Eq. 4.24. . . . 174
4.105 Combinatorial background structured in the m_{BC} distribution consisting of events where the D_s^{*+} has been reconstructed out of the D_s^- and the γ, and the D_s^- has been matched to its generated counterpart but the γ has failed to match the photon from the D_s^{*+} decay at the generator level of the Monte Carlo simulation. This distribution has been fitted to a shape described by Eq. 4.25. . . . 175
4.106 Distribution of m_{BC} of $D_s^{*+} \to D_s^+\gamma$ events where $D_s^+ \to \eta'\pi^+; \eta' \to \rho^0\gamma$ in 586 pb^{-1} of Generic Monte Carlo. . . . 175
4.107 Distribution of m_{BC} of $D_s^{*+} \to D_s^+\gamma$ events where $D_s^+ \to \eta'\pi^+; \eta' \to \rho^0\gamma$ in 586 pb^{-1} of data. . . . 176
4.108 Distribution of m_{BC} in data after unblinding. . . . 183
4.109 Distribution of δm in data after unblinding. . . . 183

4.110 Distribution of m_{BC} in data after unblinding overlaid with prediction from Monte Carlo. 184
4.111 Distribution of δm in data after unblinding overlaid with prediction from Monte Carlo. 184
4.112 Distribution of m_{BC} in data after unblinding overlaid with prediction from Monte Carlo. 185
4.113 Distribution of δm in data after unblinding overlaid with prediction from Monte Carlo. 185
4.114 Distribution of m_{BC} in data after unblinding overlaid with prediction from Monte Carlo. 186
4.115 Distribution of δm in data after unblinding overlaid with prediction from Monte Carlo. 186
4.116 Distribution of m_{BC} in data after unblinding overlaid with prediction from Monte Carlo. 187
4.117 Distribution of δm in data after unblinding overlaid with prediction from Monte Carlo. 187
4.118 Distribution of m_{BC} in data after unblinding overlaid with prediction from Monte Carlo. 188
4.119 Distribution of δm in data after unblinding overlaid with prediction from Monte Carlo. 188
4.120 Distribution of m_{BC} in data after unblinding overlaid with prediction from Monte Carlo. 189
4.121 Distribution of δm in data after unblinding overlaid with prediction from Monte Carlo. 189
4.122 Distribution of m_{BC} in data after unblinding overlaid with prediction from Monte Carlo. 190
4.123 Distribution of δm in data after unblinding overlaid with prediction from Monte Carlo. 190
4.124 Distribution of m_{BC} in data after unblinding overlaid with prediction from Monte Carlo. 191
4.125 Distribution of δm in data after unblinding overlaid with prediction from Monte Carlo. 191
4.126 Distribution of m_{BC} in data after unblinding overlaid with prediction from Monte Carlo. 192
4.127 Distribution of δm in data after unblinding overlaid with prediction from Monte Carlo. 192
4.128 Distribution of $m_{e^+e^-}$ in data after unblinding overlaid with prediction from Monte Carlo. 193
4.129 Invariant mass of the J/ψ reconstructed from its decay to e^+e^- (top plots) and $\mu^+\mu^-$ (bottom plots). The column on the left is from signal MC of Type I events. The column at the center is from signal MC of Type II events. The column on the right is from data. 200

4.130 The invariant mass of the first π^0. The column on the left is from signal MC of Type I events. The column at the center is from MC of Type II events. The column on the right is from data. 201
4.131 The invariant mass of the second π^0. The column on the left is from signal MC of Type I events. The column at the center is from MC of Type II events. The column on the right is from data. 201
4.132 The distribution of energy of the positron and the electron from the Dalitz decay of the π^0 in the MC. Events containing positron and electrons with energy less than 144 MeV, as indicated, are accepted. 202
4.133 Four momenta of $\psi(2S)$ relative to the e^+e^- collision four momenta. The column on the left is from signal MC of Type I events. The column at the center is from MC of Type II events. The column on the right is from data. 203
4.134 Difference between the invariant masses of the $\psi(2S)$ and the J/ψ. The column on the left is from signal MC of Type I events. The column at the center is from MC of Type II events. The column on the right is from data. 204
4.135 The Δd_0 between the e^+e^- pair from the second π^0. The column on the left is from signal MC of Type I events. The column at the center is from MC of Type II events. The column on the right is from data. 204
4.136 The $\Delta\phi_0$ between the e^+e^- pair from the second π^0. The column on the left is from signal MC of Type I events. The column at the center is from MC of Type II events. The column on the right is from data. 204
4.137 Invariant mass of the J/ψ reconstructed from its decay to e^+e^- (top plots) and $\mu^+\mu^-$ (bottom plots). The column on the left is from signal MC of Type II events. The column on the right is from data. 206
4.138 The invariant mass of the first π^0. The column on the left is from signal MC of Type II events. The column on the right is from data. 207
4.139 The invariant mass of the second π^0. The column on the left is from signal MC of Type II events. The column on the right is from data. 207
4.140 Four momenta of $\psi(2S)$ relative to the e^+e^- collision four momenta. The column on the left is from signal MC of Type II events. The column on the right is from data. 208
4.141 Difference between the invariant masses of the $\psi(2S)$ and the J/ψ. The column on the left is from signal MC of Type II events. The column on the right is from data. 209

4.142 The $\Delta\phi_0$ between the e^+e^- pair. Now we accept events with $\Delta\phi_0$ greater than 0.12. These were previously rejected as likely to be conversion-type events. The column on the left is from signal MC of Type I events. The column at the center is from MC of Type II events. The column on the right is from data. 210

A.1 $m_{D_s^+}$, $K_S K^+$, pion-fit 217
A.2 $m_{D_s^+}$, $K_S K^+$, electron-fit 217
A.3 m_{BC}, $K_S K^+$, pion-fit 218
A.4 m_{BC}, $K_S K^+$, electron-fit 218
A.5 δm, $K_S K^+$, pion-fit 219
A.6 δm, $K_S K^+$, electron-fit 219
A.7 Δd_0, $K_S K^+$, pion-fit 220
A.8 Δd_0, $K_S K^+$, electron-fit 220
A.9 $\Delta\phi_0$, $K_S K^+$, pion-fit 221
A.10 $\Delta\phi_0$, $K_S K^+$, electron-fit 221
A.11 $m_{D_s^+}$, $\eta\pi^+$, pion-fit 223
A.12 $m_{D_s^+}$, $\eta\pi^+$, electron-fit 223
A.13 m_{BC}, $\eta\pi^+$, pion-fit 224
A.14 m_{BC}, $\eta\pi^+$, electron-fit 224
A.15 δm, $\eta\pi^+$, pion-fit 225
A.16 δm, $\eta\pi^+$, electron-fit 225
A.17 Δd_0, $\eta\pi^+$, pion-fit 226
A.18 Δd_0, $\eta\pi^+$, electron-fit 226
A.19 $\Delta\phi_0$, $\eta\pi^+$, pion-fit 227
A.20 $\Delta\phi_0$, $\eta\pi^+$, electron-fit 227
A.21 $m_{D_s^+}$, $\eta'\pi^+; \eta' \to \pi^+\pi^-\eta$, pion-fit 229
A.22 $m_{D_s^+}$, $\eta'\pi^+; \eta' \to \pi^+\pi^-\eta$, e-fit 229
A.23 m_{BC}, $\eta'\pi^+; \eta' \to \pi^+\pi^-\eta$, pion-fit 230
A.24 m_{BC}, $\eta'\pi^+; \eta' \to \pi^+\pi^-\eta$, e-fit 230
A.25 δm, $\eta'\pi^+; \eta' \to \pi^+\pi^-\eta$, pion-fit 231
A.26 δm, $\eta'\pi^+; \eta' \to \pi^+\pi^-\eta$, e-fit 231
A.27 Δd_0, $\eta'\pi^+; \eta' \to \pi^+\pi^-\eta$, pion-fit 232
A.28 Δd_0, $\eta'\pi^+; \eta' \to \pi^+\pi^-\eta$, e-fit 232
A.29 $\Delta\phi_0$, $\eta'\pi^+; \eta' \to \pi^+\pi^-\eta$, pion-fit 233
A.30 $\Delta\phi_0$, $\eta'\pi^+; \eta' \to \pi^+\pi^-\eta$, e-fit 233
A.31 $m_{D_s^+}$, $K^+K^-\pi^+\pi^0$, pion-fit 235
A.32 $m_{D_s^+}$, $K^+K^-\pi^+\pi^0$, electron-fit 235
A.33 m_{BC}, $K^+K^-\pi^+\pi^0$, pion-fit 236
A.34 m_{BC}, $K^+K^-\pi^+\pi^0$, electron-fit 236
A.35 δm, $K^+K^-\pi^+\pi^0$, pion-fit 237
A.36 δm, $K^+K^-\pi^+\pi^0$, electron-fit 237
A.37 Δd_0, $K^+K^-\pi^+\pi^0$, pion-fit 238
A.38 Δd_0, $K^+K^-\pi^+\pi^0$, electron-fit 238

A.39 $\Delta\phi_0$, $K^+K^-\pi^+\pi^0$, pion-fit 239
A.40 $\Delta\phi_0$, $K^+K^-\pi^+\pi^0$, electron-fit 239
A.41 $m_{D_s^+}$, $\pi^+\pi^-\pi^+$, pion-fit 241
A.42 $m_{D_s^+}$, $\pi^+\pi^-\pi^+$, electron-fit 241
A.43 m_{BC}, $\pi^+\pi^-\pi^+$, pion-fit 242
A.44 m_{BC}, $\pi^+\pi^-\pi^+$, electron-fit 242
A.45 δm, $\pi^+\pi^-\pi^+$, pion-fit 243
A.46 δm, $\pi^+\pi^-\pi^+$, electron-fit 243
A.47 Δd_0, $\pi^+\pi^-\pi^+$, pion-fit 244
A.48 Δd_0, $\pi^+\pi^-\pi^+$, electron-fit 244
A.49 $\Delta\phi_0$, $\pi^+\pi^-\pi^+$, pion-fit 245
A.50 $\Delta\phi_0$, $\pi^+\pi^-\pi^+$, electron-fit 245
A.51 $m_{D_s^+}$, $K^{*+}K^{*0}$, pion-fit 247
A.52 $m_{D_s^+}$, $K^{*+}K^{*0}$, electron-fit 247
A.53 m_{BC}, $K^{*+}K^{*0}$, pion-fit 248
A.54 m_{BC}, $K^{*+}K^{*0}$, electron-fit 248
A.55 δm, $K^{*+}K^{*0}$, pion-fit 249
A.56 δm, $K^{*+}K^{*0}$, electron-fit 249
A.57 Δd_0, $K^{*+}K^{*0}$, pion-fit 250
A.58 Δd_0, $K^{*+}K^{*0}$, electron-fit 250
A.59 $\Delta\phi_0$, $K^{*+}K^{*0}$, pion-fit 251
A.60 $\Delta\phi_0$, $K^{*+}K^{*0}$, electron-fit 251
A.61 $m_{D_s^+}$, $\eta\rho^+$, pion-fit 253
A.62 $m_{D_s^+}$, $\eta\rho^+$, electron-fit 253
A.63 m_{BC}, $\eta\rho^+$, pion-fit 254
A.64 m_{BC}, $\eta\rho^+$, electron-fit 254
A.65 δm, $\eta\rho^+$, pion-fit 255
A.66 δm, $\eta\rho^+$, electron-fit 255
A.67 Δd_0, $\eta\rho^+$, pion-fit 256
A.68 Δd_0, $\eta\rho^+$, electron-fit 256
A.69 $\Delta\phi_0$, $\eta\rho^+$, pion-fit 257
A.70 $\Delta\phi_0$, $\eta\rho^+$, electron-fit 257
A.71 $m_{D_s^+}$, $\eta'\pi^+; \eta' \to \rho^0\gamma$, pion-fit 259
A.72 $m_{D_s^+}$, $\eta'\pi^+; \eta' \to \rho^0\gamma$, e-fit 259
A.73 m_{BC}, $\eta'\pi^+; \eta' \to \rho^0\gamma$, pion-fit 260
A.74 m_{BC}, $\eta'\pi^+; \eta' \to \rho^0\gamma$, e-fit 260
A.75 δm, $\eta'\pi^+; \eta' \to \rho^0\gamma$, pion-fit 261
A.76 δm, $\eta'\pi^+; \eta' \to \rho^0\gamma$, e-fit 261
A.77 Δd_0, $\eta'\pi^+; \eta' \to \rho^0\gamma$, pion-fit 262
A.78 Δd_0, $\eta'\pi^+; \eta' \to \rho^0\gamma$, e-fit 262
A.79 $\Delta\phi_0$, $\eta'\pi^+; \eta' \to \rho^0\gamma$, pion-fit 263
A.80 $\Delta\phi_0$, $\eta'\pi^+; \eta' \to \rho^0\gamma$, e-fit 263

CHAPTER 1

INTRODUCTION

What is the world made of?

What holds it together?

The tale of human civilization is a testament to the gullibility of a pattern seeking social species, challenged perhaps only by its insatiable curiosity. Contemporary particle physics represents the culmination and cutting-edge of our most organized and ambitious attempt at answering some of our biggest questions, becoming at once a signature of and remedy to this curiosity. Recorded history is littered with attempts at coming to an understanding of what the world is made of, from the ancient patterns of classification of the world into fundamental elements to the atomic hypotheses of the Ionian Greeks and the Vaisheshika and Jain schools of India in the 5th century BC. However, it is difficult to associate the thrust of empiricism and the scientific method with any atomic understanding of the fundamental constituents of matter prior to the works of John Dalton between 1800 and 1805, which in turn paved the way for the periodic table of elements. The patterns in the properties of the elements compiled by Dmitri Mendeleev in the late 1860s was a powerful suggestion of sub-atomic structure. Thereafter, a series of experiments and insights lead not only to our archetypical image of the atom with a nucleus at the center and electrons in orbit, but also to some understanding of the nature of the electron and the nucleus itself.

A similar train of events occurred in the 1960s. A menagerie of new and short-lived particles were discovered by experiments on cosmic rays and with particle accelerators designed to probe the sub-nuclear structure of matter. The first sense of order emerged with the realization that there are two distinct types of matter. There are particles like the electron that do not experience the strong

nuclear force; they were named *leptons* from the Greek for lightweight. There exist 6 of them and they appear to be truly fundamental. Then there are *hadrons* (Greek for bulky) that do feel the strong nuclear force, and we have discovered well over 200 of them. Hadrons may be usefully divided into *baryons* and *mesons*. Baryons are particles of spin 1/2 that are unstable and decay, ultimately returning to a proton. Mesons are particles with integer spin that ultimately decay to electrons, photons and neutrinos. This proliferation of hadrons eventually gave hint of an underlying pattern called the *Eightfold Way*. Identification of such patterns lead to the proposal that hadrons are not fundamental but are composed of at least three varieties of quarks; the up (u), the down (d) and the strange (s).

This served to explain most thus far observed hadronic phenomena except for a few, among which was the observed rate of $K_L^0 \rightarrow \mu^+\mu^-$ that was lower than expected. Introducing a fourth quark, the charm c, within the Glashow-Iliopoulos-Maiani (GIM) mechanism produced the required interference with the u being exchanged between the d and s quarks of the K_L^0 meson to lower the theoretical rate [13]. The mass of the charm quark required to lower this theoretical rate to the observed value was calculated to be in the range of a few GeVs. Bound states of the charm quark were subsequently discovered, the almost simultaneous discovery of the J/ψ ($c\bar{c}$) meson at SLAC and BNL in November 1974 being among the most prominent. This was followed by discoveries of the $D_0(c\bar{u})$ and the $D^+(c\bar{d})$. The $D_s^+(c\bar{s})$ bound state was discovered at CLEO in 1983 [8].

A D_s^+ meson is the 0^- (L=0, S=0) bound state of a charm and strange quark system, while a D_s^{*+} is the 1^- (L=0, S=1) excited state of the same. While the

Table 1.1: Branching fractions of the known decays of the D_s^{*+}.

Mode	Branching Fraction
$B(D_s^{*+} \to D_s^+\gamma)$	$(94.2 \pm 0.7)\%$
$B(D_s^{*+} \to D_s^+\pi^0)$	$(5.8 \pm 0.7)\%$

D_s^+ decays via the weak interaction into a rich spectrum of particles, the D_s^{*+} is known to decay via an electromagnetic and an isospin-suppressed strong decay as recorded by the Review of Particle Physics 2008 [4] and listed in Table 1.1.

It is important to note that the branching fractions listed in the table are derived from the ratio

$$\frac{\Gamma(D_s^{*+} \to D_s^+\pi^0)}{\Gamma(D_s^{*+} \to D_s^+\gamma)} = 0.062 \pm 0.008$$

assuming that the branching fractions of $D_s^{*+} \to D_s^+\gamma$ and $D_s^{*+} \to D_s^+\pi^0$ decays sum to 100% [5].

In this dissertation, we propose a new electromagnetic decay of the D_s^{*+}, the $D_s^{*+} \to D_s^+e^+e^-$, and search for it using data collected by the CLEO-c detector. Since this decay does not violate any rigorous or semi-rigorous conservation principle, it is expected to occur at the rate of $D_s^{*+} \to D_s^+\gamma$ suppressed by approximately a factor of the electromagnetic structure constant, α. Such decays where a virtual photon is internally converted to a e^+e^- pair are known in high energy physics as Dalitz decays [11]. Dalitz decays have not been observed in the electromagnetic decays of mesons containing the heavy charm or bottom quark. This dissertation documents the first observation of such a decay.

A theoretical derivation of the ratio of branching fractions

$$\frac{B(D_s^{*+} \to D_s^+e^+e^-)}{B(D_s^{*+} \to D_s^+\gamma)} \tag{1.1}$$

is presented in Chapter 2. Chapter 3 presents a description of the components of the CLEO-c detector relevant for following the analysis technique outlined in Chapter 4 towards making an observation of the $D_s^{*+} \to D_s^+ e^+ e^-$ decay and measuring the ratio of branching fractions in Eq. 1.1. An observation of this decay and a measurement of the ratio of branching fractions would lead to a re-evaluation of the fractions listed in Table 1.1.

CHAPTER 2

A THEORETICAL PREDICTION FOR THE RATIO OF BRANCHING FRACTIONS $B(D_s^{*+} \to D_s^+ e^+ e^-)/B(D_s^{*+} \to D_s^+ \gamma)$

The electromagnetic decay $D_s^{*+} \to D_s^+\gamma$ supercedes the strong decay $D_s^{*+} \to D_s^+\pi^0$ in rate because the latter is suppressed by isospin violation of the strong interaction. The currently known branching fractions of the D_s^{*+} are listed in Table 1.1 of the Introduction. In this section, we propose the existence of a hitherto unobserved electromagnetic decay, the $D_s^{*+} \to D_s^+e^+e^-$. It is separated from the $D_s^{*+} \to D_s^+\gamma$ process by one vertex of the electromagnetic interaction, as can be seen by comparing Fig. 2.1 and 2.2, and does not violate any known symmetry.

In this section, we estimate the ratio of branching fractions $B(D_s^{*+} \to D_s^+e^+e^-)/B(D_s^{*+} \to D_s^+\gamma)$ through a prediction of the ratio of rates for the $D_s^{*+} \to D_s^+e^+e^-$ and $D_s^{*+} \to D_s^+\gamma$ processes.

$$\frac{B(D_s^{*+} \to D_s^+e^+e^-)}{B(D_s^{*+} \to D_s^+\gamma)} = \frac{\Gamma(D_s^{*+} \to D_s^+e^+e^-)}{\Gamma(D_s^{*+} \to D_s^+\gamma)} \tag{2.1}$$

With reference to Fig. 2.1, the quantum mechanical amplitude for the $D_s^{*+} \to D_s^+\gamma$ decay may be written schematically as

$$\mathcal{M}(D_s^{*+} \to D_s^+\gamma) = \varepsilon^{\mu}_{D_s^*}\varepsilon^{*\nu}_{\gamma}T_{\mu\nu}(P,k), \tag{2.2}$$

where $\varepsilon^{\mu}_{D_s^*}$ is the polarization vector of the decaying D_s^{*+} meson with three degrees of freedom indexed by μ, $\varepsilon^{*\nu}_{\gamma}$ is the polarization vector of the photon with two degrees of freedom indexed by ν, P is the four-momentum of the D_s^{*+}, k is the four-momentum of the photon and $T_{\mu\nu}(P,k)$ encodes the coupling between the meson and the photon.

$T_{\mu\nu}(P,k)$ may be expressed, most generally, in the form:

$$T_{\mu\nu}(P,k) = Ag_{\mu\nu} + Bk_{\mu}P_{\nu} + C\epsilon_{\mu\nu\alpha\beta}P^{\alpha}k^{\beta}. \tag{2.3}$$

The D_s^{*+} meson has $J^P = 1^-$, the D_s^+ has $J^P = 0^-$ and the emitted γ has spin

$s = 1$ with intrinsic odd parity. The angular momentum of the $D_s^+\gamma$ state, L, could be $0, 1$ or 2 depending on the projection of the spin of the photon on the J_z of the D_s^{*+}. If $s_z = J_z$, then $L = 0$. If $s_z = 0$ then $L = 1, L_z = J_z$. And if $s_z = -J_z$, then $L = 2, L_z = 2J_z$. However, in order to conserve the odd parity of the initial state, given $P = -1$ for both the D_s^+ and the γ, L must be equal to 1. This narrows down the kind of terms that may constitute $T_{\mu\nu}(P, k)$ to

$$T_{\mu\nu}(P, k) = C\epsilon_{\mu\nu\alpha\beta}P^\alpha k^\beta, \tag{2.4}$$

where α and β keep track of the four-momentum components of the D_s^{*+} and photon respectively. We consider C to be a constant as the range of k^2 is small compared to the ρ mass.

In order to model the $D_s^{*+} \to D_s^+e^+e^-$ process, we change the final state photon to a virtual photon and couple it to a e^+e^- pair as depicted in Fig. 2.2. We may then write the invariant amplitude as

$$\mathcal{M}(D_s^{*+} \to D_s^+e^+e^-) = \varepsilon^\mu_{D_s^*} T_{\mu\nu}(P, k)\frac{-ig^{\nu\alpha}}{k^2}\langle\bar{u}(p)|ie\gamma_\alpha|v(p')\rangle, \tag{2.5}$$

where $u(p)$ and $v(p')$ are the spinors of the electron and positron respectively as functions of their four-momenta, k is the four-momentum of the virtual photon and $g^{\nu\alpha}$ is the metric tensor of flat spacetime.

2.1 Rate for $D_s^{*+} \to D_s^+\gamma$

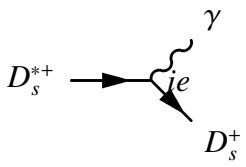

Figure 2.1: A Feynman diagram for the $D_s^{*+} \to D_s^+\gamma$ process.

We now proceed to express the rate for $D_s^{*+} \to D_s^+ \gamma$ in terms of the normalization constant C used to express $T_{\mu\nu}(P,k)$ in Eq. 2.4 and other constants in this process such as the masses of the D_s^{*+} and D_s^+ which we denote by $m_{D_s^{*+}}$ and $m_{D_s^+}$ respectively.

Inserting the expression for the coupling in Eq. 2.4 into the expression for the invariant amplitude in Eq. 2.2, we may write

$$\mathcal{M} = \varepsilon^{\mu}_{D_s^*} \varepsilon^{*\nu}_{\gamma} C \epsilon_{\mu\nu\alpha\beta} P^{\alpha} k^{\beta}. \tag{2.6}$$

This may be squared to get

$$|\mathcal{M}^2| = |C^2| \varepsilon^{\mu}_{D_s^*} \varepsilon^{*\nu}_{\gamma} \epsilon_{\mu\nu\alpha\beta} P^{\alpha} k^{\beta} \varepsilon^{*\mu'}_{D_s^*} \varepsilon^{\nu'}_{\gamma} \epsilon_{\mu'\nu'\alpha'\beta'} P^{\alpha'} k^{\beta'}, \tag{2.7}$$

where μ', ν', α' and β' are indices of four momentum distinguished from their un-primed cousins.

We now sum over final state polarizations and average over initial state polarizations, recalling for photons that

$$\sum_{\lambda=1,2} \varepsilon^{*\nu}_{\gamma_\lambda} \varepsilon^{\nu'}_{\gamma_\lambda} = -g^{\nu\nu'}, \tag{2.8}$$

and for massive vector bosons that

$$\frac{1}{3} \sum_{\lambda=1,3} \varepsilon^{*\nu}_{D_{s\lambda}^*} \varepsilon^{\nu'}_{D_{s\lambda}^*} = \frac{1}{3} \left(-g^{\nu\nu'} + \frac{P^{\mu} P^{\mu'}}{m^2_{D_s^*}} \right). \tag{2.9}$$

Thus, we get

$$\overline{|\mathcal{M}^2|} = \frac{|C^2|}{3} g^{\nu\nu'} \left(g^{\mu\mu'} - \frac{P^{\mu} P^{\mu'}}{m^2_{D_s^*}} \right) \epsilon_{\mu\nu\alpha\beta} P^{\alpha} k^{\beta} \epsilon_{\mu'\nu'\alpha'\beta'} P^{\alpha'} k^{\beta'} \tag{2.10}$$

which may be simplified to

$$\overline{|\mathcal{M}^2|} = \frac{2|C^2|}{3} (P \cdot k)^2 = \frac{2|C^2|}{3} m^2_{D_s^*} E^2_{\gamma} \tag{2.11}$$

where we have used the tensorial relationship $\epsilon^{\mu\nu}{}_{\alpha\beta}\epsilon_{\mu\nu\alpha'\beta'} = -2g_{\alpha\alpha'}g_{\beta\beta'} + 2g_{\alpha\beta'}g_{\alpha'\beta'}$ and E_γ is the energy component of the photon in the rest frame of the D_s^{*+}.

For a two-body decay, we may write the differential decay rate as

$$d\Gamma = \frac{1}{32\pi^2}\overline{|\mathcal{M}^2|}\frac{E_\gamma}{m_{D_s^*}^2}d\Omega \tag{2.12}$$

where $d\Omega$ is the differential element of the solid angle subtended from the point of decay of the D_s^{*+} in its rest frame. Since the invariant amplitude in the simplified expression of Eq. 2.11 does not have any angular dependence, our expression for the rate of $D_s^{*+} \to D_s^+\gamma$ simplifies to

$$\Gamma = \frac{|C^2|}{12\pi}E_\gamma^3. \tag{2.13}$$

2.2 Rate for $D_s^{*+} \to D_s^+e^+e^-$

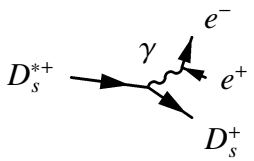

Figure 2.2: A Feynman diagram for the $D_s^{*+} \to D_s^+e^+e^-$ process.

The rate for the $D_s^{*+} \to D_s^+e^+e^-$ is a bit more involved as it is a three-body decay. The amplitude for this process may be expressed by what we had for $D_s^{*+} \to D_s^+e^+e^-$ except now with the photon coupled to a e^+e^- pair. We express it as presented in Eq. 2.14.

$$\mathcal{M}(D_s^{*+} \to D_s^+e^+e^-) = \varepsilon_{D_s^*}^\mu C\epsilon_{\mu\nu\alpha\beta}P^\alpha k^\beta\frac{-ig^{\nu\rho}}{k^2}\bar{u}(p)ie\gamma_\rho v(p'). \tag{2.14}$$

We square this to get:

$$|\mathcal{M}^2| = |C^2|\varepsilon^{\mu}_{D_s^*}\varepsilon^{*\mu'}_{D_s^*}\epsilon_{\mu\nu\alpha\beta}P^{\alpha}k^{\beta}\epsilon_{\mu'\nu'\alpha'\beta'}P^{\alpha'}k^{\beta'}\frac{g^{\nu\rho}g^{\nu'\rho'}}{k^4}\bar{u}(p)e\gamma_{\rho}v(p')\bar{v}(p')e\gamma_{\rho'}u(p). \tag{2.15}$$

Summing over final state spins of the e^+e^- and averaging over initial state polarizations of the D_s^{*+}, we may write

$$\overline{|\mathcal{M}^2|} = -\frac{4e^2|C^2|}{3k^4}\epsilon^{\mu}_{\ \nu\alpha\beta}\epsilon_{\mu\nu'\alpha'\beta'}P^{\alpha}k^{\beta}P^{\alpha'}k^{\beta'}\left[p^{\nu}p'^{\nu'} + p'^{\nu}p^{\nu'} - g^{\nu\nu'}(p\cdot p' + m^2)\right] \tag{2.16}$$

which may then be expressed succinctly as

$$\overline{|\mathcal{M}^2|} = \frac{4e^2|C^2|}{3k^4}\left[k^2(P\cdot k)^2 + 2X^2 - m_{D_s^*}^2k^4\right], \tag{2.17}$$

where

$$X^{\mu} \equiv \epsilon^{\mu}_{\ \nu\alpha\beta}P^{\alpha}p'^{\beta}p^{\nu}$$

Using the following contraction of the Levi Civita tensor,

$$\begin{aligned}\epsilon^{\mu\alpha\beta\gamma}\epsilon_{\mu\alpha'\beta'\gamma'} &= -g^{\alpha}_{\alpha'}g^{\beta}_{\beta'}g^{\gamma}_{\gamma'} - g^{\alpha}_{\beta'}g^{\beta}_{\gamma'}g^{\gamma}_{\alpha'} - g^{\alpha}_{\gamma'}g^{\beta}_{\alpha'}g^{\gamma}_{\beta'} \\ &\quad + g^{\alpha}_{\alpha'}g^{\beta}_{\gamma'}g^{\gamma}_{\beta'} + g^{\alpha}_{\gamma'}g^{\beta}_{\beta'}g^{\gamma}_{\alpha'} + g^{\alpha}_{\beta'}g^{\beta}_{\alpha'}g^{\gamma}_{\gamma'},\end{aligned} \tag{2.18}$$

X^2 evaluates to

$$X^2 = -k^2(P\cdot p')(P\cdot p) + m_{D_s^*}^2\left(\frac{k^4}{4} - k^2m^2\right) + \frac{m^2}{4}\left(m_{D_s^*}^2 - m_{D_s}^2 + k^2\right)^2, \tag{2.19}$$

where m represents the mass of the electron, m_{D_s} the mass of the D_s^+ meson and $m_{D_s^*}$ the mass of the D_s^{*+}. The physical relationships

$$p\cdot p' = \frac{k^2}{2} - m^2 \tag{2.20}$$

and

$$P\cdot k = \frac{(m_{D_s^*}^2 - m_{D_s}^2 + k^2)}{2}. \tag{2.21}$$

have also been used to obtain the aforementioned expression for X^2.

Now, $P\cdot p'$ and $P\cdot p$ may be expressed in a more convenient form for the phase space integral by boosting our inertial frame of reference to the rest frame of the center of mass of the e^+e^-. Quantities marked by an asterix (*) in the following equations are those evaluated in the e^+e^- center of mass frame. We define θ^* to be the angle that the electron makes with the direction of the D_s^+ in the e^+e^- center of mass frame. Thus, we may write:

$$P \cdot p = P^* \cdot p^* = E^*_{D_s^*} E^*_e - |\mathbf{P}^*_{D_s^*}||\mathbf{p}^*_e| \cos\theta^*, \tag{2.22}$$

$$P \cdot p' = P^* \cdot p'^* = E^*_{D_s^*} E^*_e + |\mathbf{P}^*_{D_s^*}||\mathbf{p}^*_e| \cos\theta^*. \tag{2.23}$$

The energies of the D_s^+ and e^- in the center of mass frame of the e^+e^- may be expressed simply by recognizing that in this frame, $k^\mu = \left(\sqrt{k^2}, 0, 0, 0\right)$. Thus, they are

$$E^*_{D_s^*} = \frac{P\cdot k}{\sqrt{k^2}} \tag{2.24}$$

$$E^*_e = \frac{p\cdot k}{\sqrt{k^2}}. \tag{2.25}$$

Using this and

$$p \cdot k = \frac{k^2}{2}, \tag{2.26}$$

we may rewrite Eq. 2.22 and 2.23 as follows.

$$P \cdot p = \frac{P\cdot k}{2} + \sqrt{\frac{(P\cdot k)^2}{k^2} - m^2_{D_s^*}}\sqrt{\frac{k^2}{4} - m^2}\cos\theta^* \tag{2.27}$$

$$P \cdot p' = \frac{P\cdot k}{2} - \sqrt{\frac{(P\cdot k)^2}{k^2} - m^2_{D_s^*}}\sqrt{\frac{k^2}{4} - m^2}\cos\theta^*. \tag{2.28}$$

and thus arrive at the expression for $(P\cdot p)(P\cdot p')$:

$$(P\cdot p)(P\cdot p') = \frac{(P\cdot k)^2}{4} - \left(\frac{(P\cdot k)^2}{k^2} - m^2_{D_s^*}\right)\left(\frac{k^2}{4} - m^2\right)\cos^2\theta^*. \tag{2.29}$$

We may insert this into the expression for X in Eq. 2.19 to obtain:

$$X^2 = -k^2\frac{(P\cdot k)^2}{4} + \left((P\cdot k)^2 - k^2 m^2_{D_s^*}\right)\left(\frac{k^2}{4} - m^2\right)\cos^2\theta^* + m^2_{D_s^*}\left(\frac{k^4}{4} - k^2 m^2\right) \tag{2.30}$$

$$+ \quad \frac{m^2}{4}\left(m_{D_s^*}^2 - m_{D_s}^2 + k^2\right)^2 .$$

This may be inserted into the expression for the invariant amplitude $\overline{|\mathcal{M}|^2}$ obtained in Eq. 2.16 to give us

$$\overline{|\mathcal{M}^2|} = \frac{4e^2|C^2|}{3k^4}\left[\frac{A^2k^2}{8} - m_{D_s^*}^2\left(\frac{k^4}{2} + 2k^2m^2\right) + \frac{m^2}{2}A^2 + \left(\frac{A^2}{4} - k^2m_{D_s^*}^2\right)\left(\frac{k^2}{2} - 2m^2\right)\cos^2\theta^*\right], \tag{2.31}$$

which can be simplified to

$$\overline{|\mathcal{M}^2|} = \frac{4e^2|C^2|}{3k^4}\left[\left\{\frac{A^2}{4} - k^2m_{D_s^*}^2\right\}\left\{\frac{k^2}{2}\left(1 + \cos^2\theta^*\right) + 2m^2\left(1 - \cos^2\theta^*\right)\right\}\right] \tag{2.32}$$

where we define

$$A \equiv m_{D_s^*}^2 - m_{D_s}^2 + k^2. \tag{2.33}$$

Having thus obtained the averaged invariant amplitude for our process, we must now set up the integral over the available phase space. This being a three-body decay, we may write the decay rate in terms of the $\overline{|\mathcal{M}|^2}$ thus:

$$d\Gamma = \frac{1}{(2\pi)^3}\frac{1}{16m_{D_s^*}^2}\overline{|\mathcal{M}^2|}dE_e dk^2. \tag{2.34}$$

where dE_e is evaluated in the rest frame of the D_s^*.

Now we need to express the differential of the energy of the electron, dE_e, in terms of $d(\cos\theta^*)$. Using the relationship expressed in Eq. 2.22 and recognizing that $P \cdot p = m_{D_s^*}E_{e^-}$ in the rest frame of the D_s^*, we may write

$$E_e = \frac{P \cdot p}{m_{D_s^*}} = \frac{E_{D_s^*}^* E_e^*}{m_{D_s^*}} - \frac{|\mathbf{P}_{D_s^*}^*||\mathbf{p}_e^*|}{m_{D_s^*}}\cos\theta^*. \tag{2.35}$$

We note that the quantities $E_{D_s^*}^*$, E_e^*, $|\mathbf{P}_{D_s^*}^*|$, and $|\mathbf{p}_e^*|$ depend only on k^2 and not on $\cos\theta^*$. Therefore, we can differentiate the above expression to obtain

$$dE_e = -\frac{|\mathbf{P}_{D_s^*}^*||\mathbf{p}_e^*|}{m_{D_s^*}}d(\cos\theta^*). \tag{2.36}$$

In the center of mass frame of the e^+e^-, $P \cdot k = E^*_{D_s^*} k^*_0$. Therefore, we may write

$$E^*_{D_s^*} = \frac{P \cdot k}{k^*_0} = \frac{P \cdot k}{2E^*_e}. \tag{2.37}$$

Using this expression for the energy of the D_s^* in the center of mass frame of the e^+e^-, we may write its momentum thus:

$$|\mathbf{P}^*_{D_s^*}| = \sqrt{E^{*2}_{D_s^*} - m^2_{D_s^*}} = \sqrt{\frac{(P \cdot k)^2}{4E^{*2}_e} - m^2_{D_s^*}}. \tag{2.38}$$

Thus we may simplify the Jacobian of the differential,

$$\begin{aligned}
\frac{|\mathbf{P}^*_{D_s^*}||\mathbf{p}^*_e|}{m_{D_s^*}} &= \frac{|\mathbf{P}^*_{D_s^*}|E^*_e}{m_{D_s^*}} \sqrt{1 - \frac{4m^2}{k^2}} && (2.39)\\
&= \sqrt{\frac{(P \cdot k)^2}{4m^2_{D_s^*}} - E^{*2}_e} \sqrt{1 - \frac{4m^2}{k^2}} && (2.40)\\
&= \frac{1}{2}\sqrt{k_0^2 - k^2} \sqrt{1 - \frac{4m^2}{k^2}} && (2.41)\\
&= \frac{|\mathbf{P}_{D_s}|}{2} \sqrt{1 - \frac{4m^2}{k^2}} && (2.42)
\end{aligned}$$

Using this in Eq. 2.36, we arrive at a simple expression for dE_e:

$$dE_e = \frac{|\mathbf{P}_{D_s}|}{2} \sqrt{1 - \frac{4m^2}{k^2}} d(\cos\theta^*). \tag{2.43}$$

Now we substitute our expression for $\overline{|\mathcal{M}|^2}$ in Eq. 2.32 and dE_e in Eq. 2.43 into Eq. 2.34 and integrate over $d(\cos\theta^*)$ from -1 to +1 to obtain the differential rate of decay

$$\frac{d\Gamma}{dk^2} = \frac{|\mathbf{P}_{D_s}|\alpha|C^2|}{144\pi^2 m^2_{D_s^*} k^4} \left(A^2 - 4k^2 m^2_{D_s^*}\right)\left(k^2 + 2m^2\right) \sqrt{1 - \frac{4m^2}{k^2}} \tag{2.44}$$

where A is defined in Eq. 2.33. α is the fine structure constant.

We integrate this numerically with k^2 ranging from $4m^2$ to $\left(m_{D_s^{*+}} - m_{D_s^+}\right)^2$ to obtain our prediction for the ratio of branching fractions:

$$\frac{\Gamma(D_s^{*+} \to D_s^+ e^+ e^-)}{\Gamma(D_s^{*+} \to D_s^+ \gamma)} = \frac{B(D_s^{*+} \to D_s^+ e^+ e^-)}{B(D_s^{*+} \to D_s^+ \gamma)} = 0.89\alpha = 0.65\%. \tag{2.45}$$

The following chapters deal with an experimental observation of the $D_s^{*+} \rightarrow D_s^+ e^+ e^-$ process and a measurement of this ratio at the CLEO-c experiment.

CHAPTER 3

THE CLEO-C DETECTOR

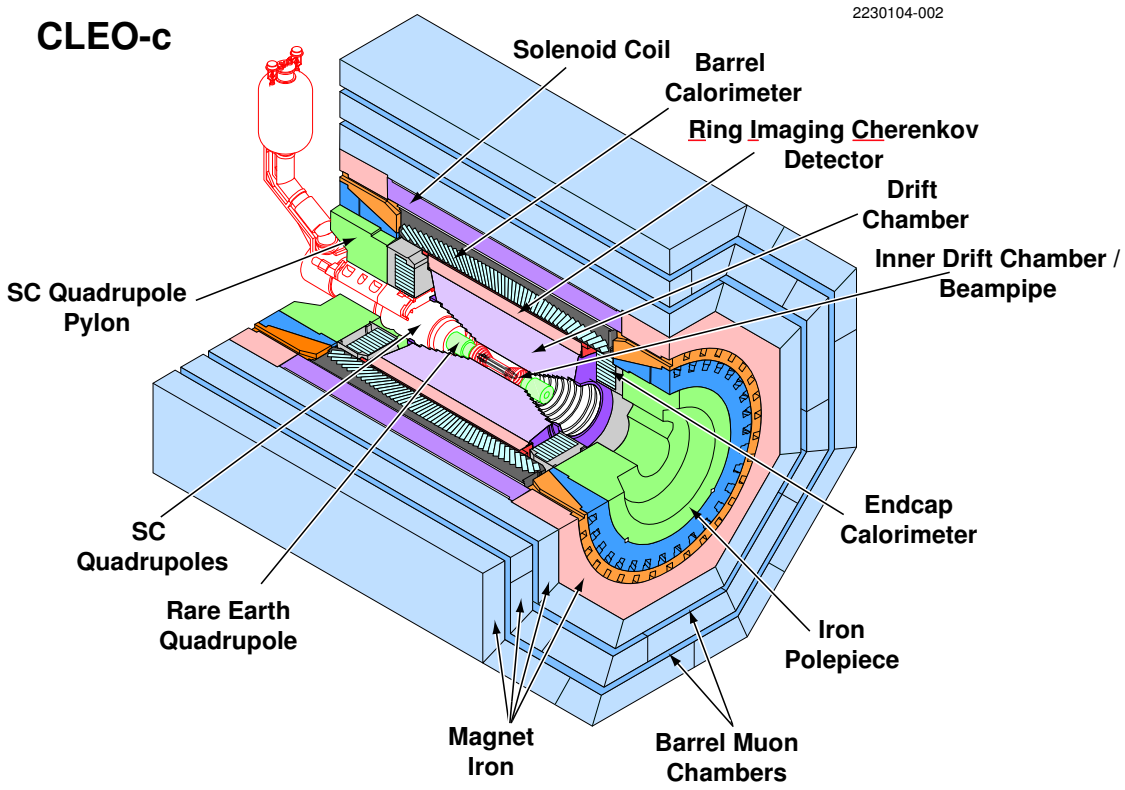

Figure 3.1: Cutaway schematic of the CLEO-c detector.

CLEO-c was the last upgrade to CLEO, a general purpose particle detector for high energy physics used to collect data on electron-positron collisions at the Cornell Electron Storage Ring (CESR) facility. The name CLEO is not an acronym and was derived from Cleopatra, to go with CESR which is pronounced as Caesar. The iteration of the collider used for studying the charm quark was called CESR-c. Counter-rotating beams of positrons and electrons in CESR-c were made to collide at the center of the CLEO-c detector with center of mass energies between 3 and 5 GeV that are required for studies of the charm quark. The nearly hermetic CLEO-c detector with several layers of subdetectors tracked and measured the energy and momenta of particles produced at these collisions.

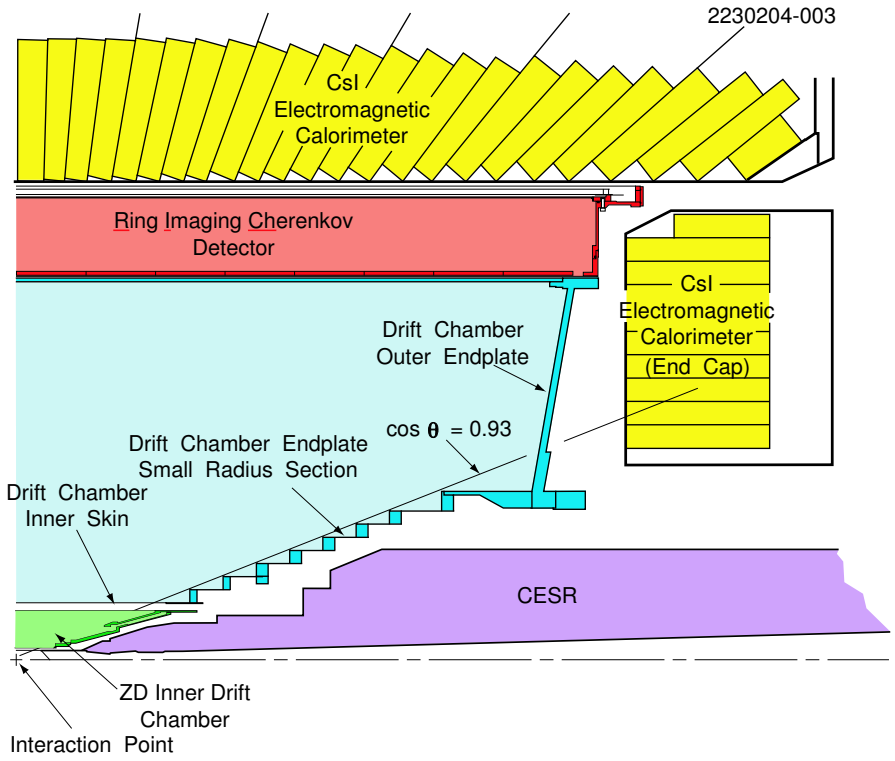

Figure 3.2: Quarter-view schematic of the CLEO-c detector.

A cutaway schematic of the CLEO-c detector is presented in Fig. 3.1. The sub-detectors closest to the interaction point were the inner drift chamber and the main drift chamber which were used together to reconstruct the 3 dimensional trajectories of charged particles. A solenoidal magnetic field of 1 T in the direction of the beampipe curved these trajectories and enabled us to deduce the momenta and charges of these particles. Outside the drift chamber lay the Ring Imaging Cerenkov (RICH) subdetector dedicated to particle identification. It used the Cerenkov radiation left in the wake of a charged particle traveling through a medium of high refractive index (LiF) to measure the velocity of the particle. This velocity combined with the momentum measured by the drift chambers allowed us to determine the mass, and hence the identity of the particle. Surrounding the RICH was the electromagnetic calorimeter made out of

CsI crystals arranged in the central barrel region and endcap regions flanking the drift chamber. It measured the energy of electromagnetic showers, thus allowing the reconstruction of photons and the identification of electrons. The superconducting solenoid used to maintain the 1 T magnetic field was located external to these subdetectors. All of this was encased in iron yokes to return the magnetic field, also known as the magnet iron. Interlaced within the magnet iron lay the muon drift chambers.

The following sections describe the sub-detectors that were used in the analysis presented in this dissertation.

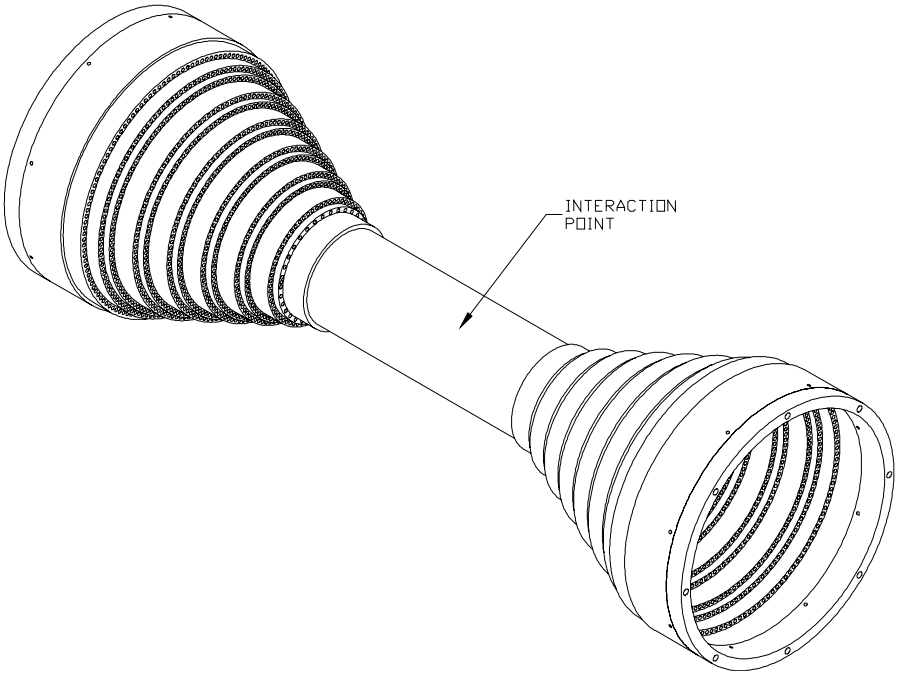

Figure 3.3: The inner drift chamber.

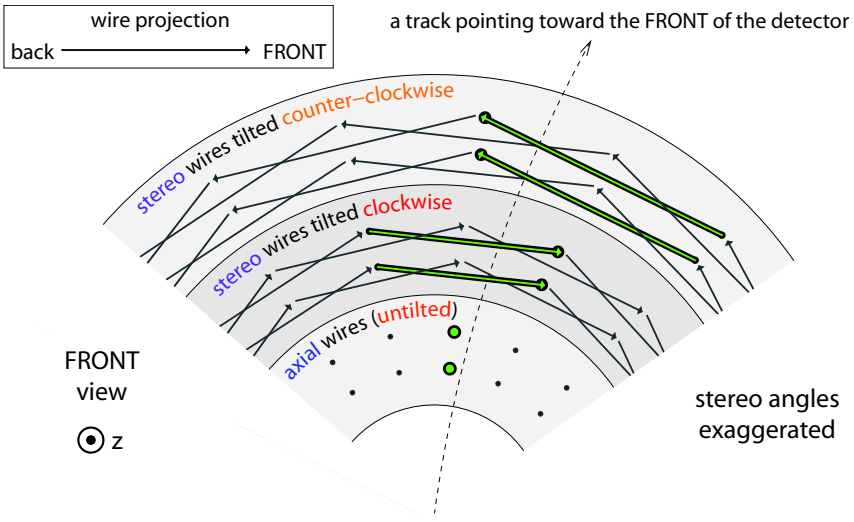

Figure 3.4: Stereo angles in the outer drift chamber.

3.1 The Tracking System

The CLEO-c tracking system consisted of two cylindrical, concentric drift chambers – an inner drift chamber between the radii of 5.3 cm and 10.5 cm, and an outer drift chamber between 12 cm and 82 cm. Longitudinally, they extended to cover the region in polar angle $|\cos\theta| < 0.93$ subtended from the interaction point as depicted in Fig. 3.2. A 3:2 mixture of He and C_3H_8 gas, chosen for its long radiation length, filled the volume of the detector. Tens of thousands of wires were strung along the length of the sub-detector as shown in Fig. 3.2, arranged in 6 layers within the inner chamber and 47 layers in the outer chamber. Sense wires were maintained at a 2,000 V positive electric potential relative to the field wires which were grounded. The sense wires were 20 μm in diameter made of gold-plated tungsten. The field wires were 130 μm in diameter and made of gold-plated aluminum. The minimum distance between sense and field wires were 5 mm for the inner chamber and 7 mm for the outer chamber. A detailed physical description of the tracking system may be found in Sections 2.1.1 and 2.2.2 of the *Yellow Book* [9].

An energetic charged particle traversing the chamber would ionize a track of gas and electrons liberated thus would be accelerated towards the sense wires. In the vicinity of the sense wires, the electrons would be energetic enough to induce local ionization in the gas, thereby releasing more electrons and amplifying the total charge deposited on the wires. The precise time of each such deposition event and the total charge collected would be recorded by the apparatus.

The temporal information was used to measure the distance of closest ap-

proach of the energetic particle to each sense wire. This could be done because the exact time of the electron-positron collisions at the center of CLEO-c was well known from the CESR-c machine and the drift velocities of the liberated electrons well understood. The distances of closest approach from multiple sense wires were fitted with a minimum χ^2-fit as well as Kalman-fits encoding physical models of various particles in a 1 T magnetic field to reconstruct the particle's 3-dimensional trajectory through the sub-detector. The curvature of the fitted track in the magnetic field allowed us to measure the momentum of the charged particle. This procedure is especially relevant for our analysis because we rely on an accurate reconstruction of electron-positron pairs that test the low-energy limits of this procedure. CLEO-c had decided not to store tracks reconstructed using the physical model of electrons, under the assumption that electron tracks reconstructed using the physical model of charged pions would do fine for most analyses and the fact that doing so would save some disk-space. As described in our analysis, the accuracy of pion-fitted tracks did not suffice and a campaign to reconstruct tracks to the physical model of electrons had to be undertaken.

The charge collected by the sense wire at each deposition event corresponds to the energy lost by the charged particle in ionizing a segment of the track, the dE/dx. We know from the Bethe-Bloch equation that this dE/dx varies with the mass and momentum of the incident particle. Thus, informed with the track's momentum and dE/dx we may deduce the particle's mass and hence its identity.

If the wires of the drift chamber were all aligned strictly parallel to the beam-axis, only dimensions of the track perpendicular to this axis, i.e. the azimuthal and radial directions, could be reconstructed. To enable reconstruction of the

longitudinal dimension, all 6 layers of sense wires in the inner drift chamber and 16 out of the 47 layers in the outer drift chamber were oriented at a small "stereo" angle to the beam-axis. The 16 layers were divided into groups of 4 and alternated in stereo angle. The timing pattern from such wires staggered in stereo angle allowed us to determine the longitudinal parameters of tracks. This afforded the tracker a spatial resolution of 85 μm for 2.5 GeV tracks in the dimensions perpendicular to the beam-axis and 5-7 mm in the dimension parallel.

3.2 The Calorimeter

The CLEO-c calorimeter, located outside the drift chambers and the RICH, was divided into a barrel section and two encap sections together covering 95% of the solid angle subtended from the interaction point. Thallium-doped cesium iodide crystals were used for showering and scintillation material in this calorimeter. CsI (Tl) crystals have a density of $4,510\ \mathrm{kg/m^3}$, a radiation length χ_0 of 1.83 cm and a Moliere radius of 3.8 cm, and this provided excellent showering material for the experiment. Each crystal was 30 cm (16.4 radiation lengths) long in the direction away from interaction point with a 5 cm $\times$ 5 cm face pointing inwards. Four photodiodes mounted at the back of each crystal measured the scintillation light.

The barrel consisted of an array of 6,144 CsI crystals, 128 along the azimuthal direction and 48 along the longitudinal. The crystals were tilted to point a few centimeters away from the interaction point so as to minimize the loss of particles in the cracks between crystals. The barrel calorimeter extended from a radius of 1.02 m to 1.32 m, and was 3.26 m long at the inner radius. This covers the region in polar angle $|\cos\theta| < 0.85$.

The two endcaps consisted of 820 crystals each, aligned parallel to the beampipe. The front faces of each endcap lay 1.308 m along the beam-line from the interaction point, and the back faces extended to 1.748 m. Each endcap extended from 43.3 cm to 95.8 cm in radius. Together, they covered the region in polar angle $0.83 < |\cos\theta| < 0.95$.

The energy of a typical electromagnetic shower produced by a photon, as used in our analysis, is spread over multiple adjacent crystals. Interpolating the

"center-of-mass" of this energy deposit offers us a much better resolution for the shower position and hence the direction of the photon than could be naively expected from the 5 cm face width of an individual crystal. A small fraction of crystals are known to be noisy and their contributions have been ignored in this analysis. The pattern of energy deposits in the crystals was used to distinguish between showers from electrons, hadrons and photons.

CHAPTER 4

ANALYSIS METHOD TO SEARCH FOR THE $D_s^{*+} \to D_s^+ e^+ e^-$ AND MEASURE THE RATIO OF BRANCHING FRACTIONS $B(D_s^{*+} \to D_s^+ e^+ e^-)/B(D_s^{*+} \to D_s^+ \gamma)$

As described in the Introduction, this chapter documents a search for and observation of the decay $D_s^{*+} \to D_s^+ e^+ e^-$ along with a measurement of the ratio of branching fractions

$$\frac{B(D_s^{*+} \to D_s^+ e^+ e^-)}{B(D_s^{*+} \to D_s^+ \gamma)}$$

at the CLEO-c experiment. We choose to measure and present this ratio of branching fractions instead of an absolute branching fraction for the $D_s^{*+} \to D_s^+ e^+ e^-$ in order to minimize systematic uncertainties arising from the reconstruction and selection of D_s^+ mesons. When we refer to the positively charged D_s^{*+} or the D_s^+ in this document, we imply the negatively charged particle or the charge-conjugate process unless otherwise specified. This search and measurement was conducted in 586 pb^{-1} of e^+e^- collision data collected by the CLEO-c experiment at a center of mass energy of 4,170 MeV. At this energy, the total charm cross section is known to be $\simeq$ 9 nb, of which about 10% produces $D_s^{\pm} D_s^{*\mp}$ events. More accurately, the cross section for producing $D_s^{\pm} D_s^{*\mp}$ at this energy has been experimentally measured in two papers, [10] and [3], that we average to quote 948 ± 36 pb. How we arrive at this number is covered in more detail in Section 4.4 where we discuss the datasets used. Using the quoted values of integrated luminosity and production cross section we conclude that approximately 556 thousand events were at our disposal for this analysis.

In our search and measurement we employ a blind-analysis technique to search for our signal process, the $D_s^{*+} \to D_s^+ e^+ e^-$, where we reconstruct the D_s^{*+} through the D_s^+ on the same side as the D_s^{*+} and the soft e^+e^- pair. The D_s^+ is reconstructed exclusively through the nine hadronic decay channels outlined in Eqs. 4.1 - 4.9. Selection criteria are optimized, their efficiencies noted and the background levels estimated from data outside the signal region before we proceed to unblind data within the signal region.

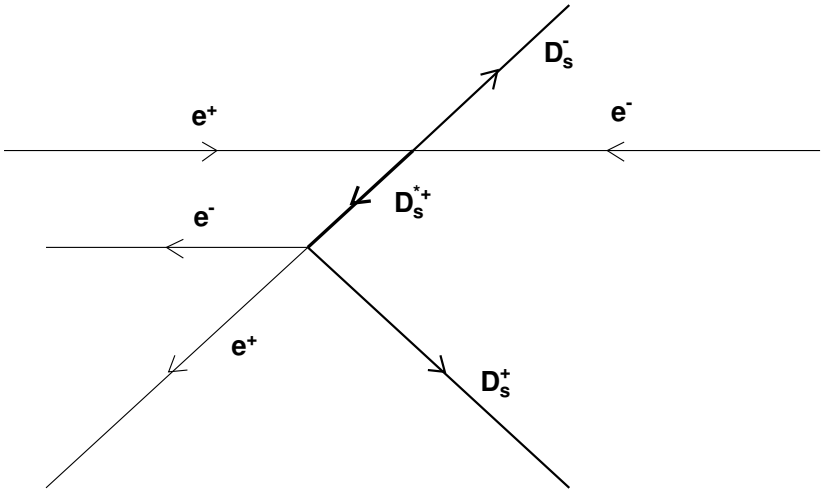

Figure 4.1: A schematic showing a e^+e^- collision producing a $D_s^{*+}D_s^-$ pair where the D_s^{*+} decays to a D_s^+ and a e^+e^- via the decay we are searching for in this dissertation.

$$D_s^+ \to K^+K^-\pi^+ \tag{4.1}$$

$$D_s^+ \to K_S K^+ \tag{4.2}$$

$$D_s^+ \to \eta\pi^+; \eta \to \gamma\gamma \tag{4.3}$$

$$D_s^+ \to \eta'\pi^+; \eta' \to \pi^+\pi^-\eta; \eta \to \gamma\gamma \tag{4.4}$$

$$D_s^+ \to K^+K^-\pi^+\pi^0 \tag{4.5}$$

$$D_s^+ \to K^{*+}K^{*0}; K^{*+} \to K_S^0\pi^+, K^{*0} \to K^-\pi^+ \tag{4.6}$$

$$D_s^+ \to \pi^+\pi^-\pi^+ \tag{4.7}$$

$$D_s^+ \to \eta\rho^+; \eta \to \gamma\gamma; \rho^+ \to \pi^+\pi^0 \tag{4.8}$$

$$D_s^+ \to \eta'\pi^+; \eta' \to \rho^0\gamma \tag{4.9}$$

Selection criteria on the reconstructed D_s^{*+}, D_s^+ and soft e^+e^- candidates are designed to reject background events described in Section 4.1. These selection

criteria are described in Section 4.2. Of note are the criteria on the helix parameters of the soft e^+e^- tracks that are used to discriminate our signal against backgrounds that come from $D_s^{*+} \to D_s^+\gamma$ where the γ converted to an e^+e^- pair in material. These selection criteria are optimized for each of the nine hadronic decay modes of the D_s^+ using Monte Carlo simulations of the signal and backgrounds as described in Section 4.7.

The e^+e^- pair from the D_s^{*+} decay share ~ 144 MeV of energy and are hence anticipated to be very soft. The Kalman-filter based track fitter used in CLEO-c did not, by default, store track fits with the electron mass hypothesis, storing tracks fitted to the charged pion mass hypothesis instead. Section 4.7 that documents our effort to converge on optimal sets of parameters for our selection criteria also documents our realization that tracks fitted to the electron mass hypothesis offers us considerably higher signal significances for observing the $D_s^{*+} \to D_s^+e^+e^-$ than tracks fitted to the pion mass hypothesis. Therefore, a campaign to reprocess several datasets to include track fits with the electron mass hypothesis was launched and this is described in Section 4.5. Henceforth, the analysis focuses on data with electron tracks fitted to the electron mass hypothesis in searching for the $D_s^{*+} \to D_s^+e^+e^-$.

Having narrowed down on a signal region for each of the hadronic decay modes of the D_s^+ in the course of our optimization procedure, we estimate the expected number of background events within this region for each mode by extrapolating Monte Carlo simulation and data points from the sideband regions. This is described in Section 4.9. Before we unblind data within the signal regions, we establish that our predicted signal and estimated background levels are adequate to obtain maximal signal significance if we are to unblind data in

all the modes.

Thereafter, we measure the efficiencies of our selection criteria for $D_s^{*+} \to D_s^+ e^+ e^-$ reconstruction in each of the hadronic decay channels in Section 4.8. We could at this point proceed to unblind data and use the number of observed events in conjunction with the selection efficiencies to present a measurement for the absolute branching fraction of $D_s^{*+} \to D_s^+ e^+ e^-$. Such a measurement, however, would have large unquantified systematic errors from the reconstruction of the D_s^+ and we choose not to present such a measurement.

Using criteria similar to those used to select $D_s^{*+} \to D_s^+ e^+ e^-$ events, except without the track helix criteria for the $e^+ e^-$ and including criteria on the photon from the D_s^{*+}, we reconstruct $D_s^{*+} \to D_s^+ \gamma$ events where the D_s^+ decays through the hadronic modes specified in Eq. 4.1 - 4.9. The efficiency of our selection criteria is noted, as is our signal yield for each of the channels. This is described in Section 4.10.

We then unblind data in the signal regions of the $D_s^{*+} \to D_s^+ e^+ e^-$ reconstruction in each of the chosen decay modes of the D_s^+ taking into account the background for each mode estimated in Section 4.9. Using the numbers of observed signal events, the efficiencies for our selection criteria and the signal yields and efficiencies for the $D_s^{*+} \to D_s^+ \gamma$ reconstruction, we proceed to compute the ratio of branching fractions we set out to measure. This is described in Section 4.11 of the document. Also motivated in this section is the requirement for quantifying systematic uncertainties in the selection efficiencies that stem from deviations between data and Monte Carlo in the reconstruction of soft $e^+ e^-$ pairs in $D_s^{*+} \to D_s^+ e^+ e^-$ and the photon in $D_s^{*+} \to D_s^+ \gamma$.

The systematic uncertainties associated with the selection and reconstruction efficiencies of soft e^+e^- pairs in $D_s^{*+} \to D_s^+ e^+ e^-$ and the photon in $D_s^{*+} \to D_s^+ \gamma$ is measured in Section 4.12. We estimate the systematic deviation between reconstruction efficiencies in Monte Carlo simulation and data by measuring the ratio of the numbers of events where one of the π^0 Dalitz decays to $\gamma e^+ e^-$ to the number of events where both π^0 decay to $\gamma\gamma$ and comparing this to the ratio expected from currently accepted branching fractions for $\pi^0 \to \gamma e^+ e^-$ and $\pi^0 \to \gamma\gamma$. This uncertainty is propagated into the ratio of branching fractions reported in Section 4.11.

4.1 Backgrounds for $D_s^{*+} \to D_s^+ e^+ e^-$

A significant background to the observation of this decay is expected from $D_s^{*+} \to D_s^+ \gamma$ events where the γ converts in the material of the apparatus or the beam-pipe to form an e^+e^- pair. The material of the beam-pipe is known to have been approximately 1% of a radiation length thick for photons incident on it closest to the interaction region and higher for photons incident at steeper angles. If we accept the theoretical estimate of the rate of the $D_s^{*+} \to D_s^+ e^+ e^-$ process with respect to the $D_s^{*+} \to D_s^+ \gamma$ as described in Section 2, we conclude that this conversion process occurred at roughly the same rate as the signal. This background is called the *conversion background* in this document. The electrons from such conversions will have the same range of energies as those from signal processes. However, their tracks would appear to originate at a distance away from the primary interaction point. Selection criteria for selecting and reconstructing the $D_s^{*+} \to D_s^+ e^+ e^-$ are designed to exploit this fact.

Another source of background, also seen to be significant from Monte Carlo simulation studies, arises from π^0 mesons that were produced at the primary interaction point which then decayed through the Dalitz channel: $\pi^0 \to \gamma e^+ e^-$ [11]. Such e^+e^- pairs would typically have had the same range of energies as those expected from the signal process and their tracks would seem to have originated from the primary interaction point. Though the rate of Dalitz decays of the π^0 is $\sim 1.2\%$ [4], the prodigious production of π^0 mesons makes this a significant background to our rare signal. We recognize that such a combinatorial background would not peak in the variables of any of our selection criteria and estimate the frequency of its occurrence from the sidebands of the signal region in our data. We call this the *Dalitz decay background* in the rest of the document.

Combinatorial backgrounds necessarily result from combining candidate daughters of the D_s^+ and candidate e^-s and e^+s. Such backgrounds are not expected to be structured in the kinematic variables used to select signal events and we estimate them from the sidebands around the signal region in our data.

We also account for backgrounds that arise from light quark (u, d, s) production at the interaction point. These backgrounds are seen, from Monte Carlo simulations, to dominate, though not peak, in the $\pi^+\pi^-\pi^+$ and $\eta'\pi^+$; $\eta' \to \rho^0\gamma$ decay channels of the D_s^+ after applying our selection criteria. Therefore, we choose to estimate their contributions from the sidebands of the signal region in our data. They are collectively called the *continuum background* in the rest of this document.

4.2 Selection Criteria for Reconstructing $D_s^{*+} \to D_s^+ e^+ e^-$

The entities directly measured by the CLEO-c detector that is relevant for our analysis are charged tracks and electromagnetic showers. The sub-detectors used for their detection have been described in Sections 3.1 and 3.2 respectively. Relatively stable particles like the soft e^+ and e^- in the final state of our signal process or the π^+, K^+ and γ from decays of the D_s^+ could be detected directly by the detector. Short-lived particles like the D_s^+ and the D_s^{*+} must be reconstructed by analyzing the signatures of their decays into particles that left tracks or shower in the detector. As we have mentioned earlier, we choose to reconstruct the D_s^+ through 9 hadronic final states as listed in Eq. 4.1 - 4.9, and the D_s^{*+} through the D_s^+ and the soft e^+e^- pair.

We construct three kinematic variables from reconstructed D_s^+ and D_s^{*+} candidates based on which we select events most likely to contain our signal. We also construct two combinations of track parameters of the e^+ and e^- which gives us criteria to powerfully reject conversion backgrounds.

4.2.1 Track Quality Requirements for the Soft e^+e^- Pair

Quality requirements are imposed on the soft e^+e^- tracks in order to reject poorly reconstructed tracks and tracks that cannot correspond to our signal process. These tracks are required to fit hits in the drift chambers with χ^2 less than 100,000. The measured energy, which is derived from the momentum, that in turn is inferred from the curvature of the track's helix in the 1 T magnetic field, is required to be between 10 MeV and 150 MeV. The upper limit is set by consider-

ing the mass difference between the D_s^{*+} and D_s^+ mesons, which is approximately 144 MeV. A single electron cannot carry more than that amount of energy. Below 10 MeV, electron tracks curl in a way that cannot be well reconstructed by the drift chamber. Next, we require tracks to pass within 5 cm of the interaction point in the dimension parallel to the beam-axis and within 5 mm of the beam-axis in the transverse dimensions. Finally, in order to reject particles that are not electrons, we require the dE/dx as computed from the track fit to be within 3σ of that expected for electrons.

These criteria remain identical for all the hadronic decay modes of the D_s^+ as the e^+e^- pair is independent of the D_s^+.

4.2.2 Mass of the D_s^+ Meson, $m_{D_s^+}$

The D_s^+ meson is reconstructed using the tight D_s-tagging criteria outlined in the document "Developments in $D_{(s)}$-Tagging" [18]. We select events which contain D_s^+ candidates with invariant mass within tens of MeV from 1.969 GeV. The current world standard for the D_s^+ mass as recorded in the Review of Particle Physics 2008 is 1.96849 ± 0.00034 GeV [4]. This criterion rejects most false combinations of D_s^+ daughters. The exact width of this criterion was optimized individually for each mode.

4.2.3 Beam Constrained Mass of the D_s^{*+} Meson, m_{BC}

The energy of a D_s^{*+} meson produced from the e^+e^- collisions in CESR may be determined with higher precision from the measured energy of the beam than

from the sum of the energies of its decay constituents as measured by the CLEO-c detector. It may be calculated from:

$$E_{D_s^{*+}}(\text{beam}) = \frac{4s - m^2_{D_s^+}(\text{RPP}) + m^2_{D_s^{*+}}(\text{RPP})}{4\sqrt{s}}, \tag{4.10}$$

where $E_{D_s^{*+}}(\text{beam})$ is the energy of the D_s^{*+} we calculate from the beam energy, s is the square of the center of mass energy of the beam, and $m_{D_s^+}(\text{RPP})$ and $m_{D_s^{*+}}(\text{RPP})$ are the current world standards for the D_s^+ and D_s^{*+} masses respectively as recorded in the Review of Particle Physics 2008 [4].

Having thus calculated the energy of the D_s^{*+} meson, we can now define a more precise variant of the invariant mass of the D_s^{*+} as follows:

$$m_{BC} = \sqrt{E^2_{D_s^{*+}}(\text{beam}) - p^2_{D_s^{*+}}(\text{constituents})} \tag{4.11}$$

where $p_{D_s^{*+}}(\text{constituents})$ is the momentum of the D_s^{*+} calculated from the momenta of the daughters of its decay. m_{BC} is called the *beam constrained mass* in CLEO literature.

For this selection criterion, we accept events with candidates having m_{BC} within tens of MeV from 2.112 GeV. The current world standard for the D_s^{*+} mass as recorded in the Review of Particle Physics 2008 is 2.1123 ± 0.0005 GeV [4]. This criterion is meant to reject most false combinations of D_s^{*+} daughters.

4.2.4 Mass Difference between the D_s^{*+} and the D_s^+ Mesons, δm

We define δm as the mass difference between the reconstructed D_s^{*+} and D_s^+ mesons.

$$\delta m = m_{D_s^{*+}} - m_{D_s^+} \tag{4.12}$$

This mass difference is known to be 143.8 MeV [4]. By accepting events with δm within a narrow range of these values around 143.8 MeV we reject most combinations where the e^- or e^+ that are used to reconstruct the D_s^{*+} did not, in fact, come from decays of the D_s^{*+}.

4.2.5 Δd_0 between the e^+ and e^- Tracks

In CLEO, the d_0 of a track is defined as the distance of closest approach of the track to the z-axis. It is a signed quantity, whose sign depends on the charge of the track (inferred from the sense of the track helix) and whether the origin of the $x-y$ plane falls within the circle made by the track in that plane. For more details, one may see Section 6 of the "How and Why Wonder Book of CLEO Tracking Conventions" [14].

Now, for e^+ and e^- tracks that come from the origin, as they do for our signal, it may be seen from Fig. 4.2 that $d_0^{e^-} - d_0^{e^+}$ is 0. Hence, in data, our signal will have Δd_0 centered around 0.

However, for e^+ and e^- tracks that come from a point away from the origin, as they do for the conversion background, it is clear from Fig. 4.2 that $d_0^{e^-} - d_0^{e^+}$ will be negative.

For our selection criterion, we define:

$$\Delta d_0 = d_0^{e^-} - d_0^{e^+} \tag{4.13}$$

and require Δd_0 to be greater than -5 mm. This criterion efficiently rejects conversion background events.

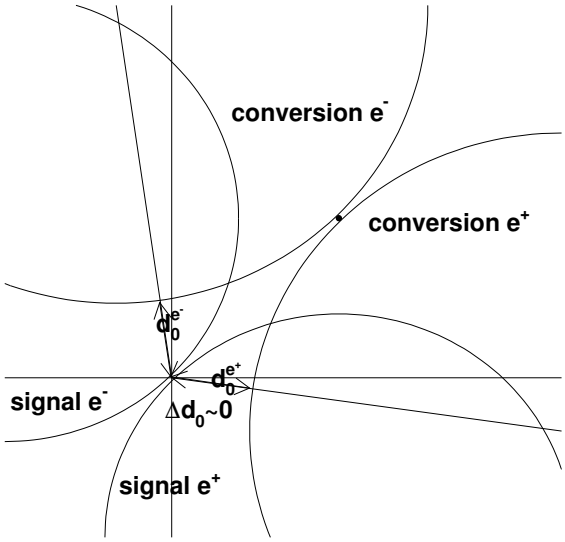

Figure 4.2: An illustration of Δd_0 between the soft e^+e^- tracks of the signal and conversion events.

4.2.6 $\Delta\phi_0$ between the e^+ and e^- Tracks

The azimuthal angle of the e^+ and e^- tracks measured at the point of closest approach of the track to the z-axis, denoted by ϕ_0, appears to be very effective in rejecting conversion background events.

For events where the e^+ and e^- tracks come from the origin, as they do for our signal, it may be noted from Fig. 4.3 that if we define:

$$\Delta\phi_0 = \phi_0^{e^-} - \phi_0^{e^+}, \tag{4.14}$$

$\Delta\phi_0$ will be centered around 0 for the signal. However, for conversion events where the tracks do not emanate from the origin, it may be inferred from Fig. 4.3 that $\Delta\phi_0$ will always be positive.

Requiring $\Delta\phi_0$ to be less than 0.12 in this selection criterion rejects a significant portion of our conversion background events.

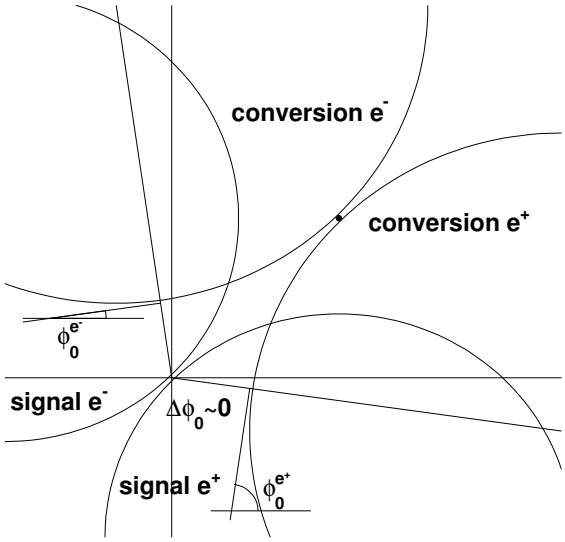

Figure 4.3: An illustration of $\Delta\phi_0$ between the soft e^+e^- tracks of the signal and conversion events.

4.3 Selection Criteria for Reconstructing $D_s^{*+} \to D_s^+\gamma$

As mentioned earlier, we seek to measure the ratio of branching fractions $B(D_s^{*+} \to D_s^+e^+e^-)/B(D_s^{*+} \to D_s^+\gamma)$ in order to minimize systematics arising from the reconstructing of D_s^+ mesons, and therefore we must have a way to measure yields and efficiencies for a $B(D_s^{*+} \to D_s^+\gamma)$ measurement. We do this, again, by reconstructing the D_s^{*+} through the D_s^+ and the γ. The D_s^+ is reconstructed exclusively through the nine hadronic decay channels listed in Eq. 4.1 - 4.9.

Selection criteria used to separate the $D_s^{*+} \to D_s^+\gamma$ signal from backgrounds are similar to those used for the $D_s^{*+} \to D_s^+e^+e^-$. The kinematic variables $m_{D_s^+}$, m_{BC} and δm retain their definitions from the previous section, except the four-momenta of the e^+e^- pair is replaced by that of the γ. Selection criteria on the e^+e^- pair are obviously inapplicable and are replaced by criteria on the γ. These are described in the following section. Furthermore, we plot the distribution of m_{BC} after applying all other criteria, and the large rate of this channel that

translates to a large number of data points allows us to compute the signal yields and efficiencies from a fit instead of cutting and counting within a range. The procedure is described in detail for the $K^+K^-\pi^+$ decay mode of the D_s^+ in Section 4.10.

4.3.1 Shower Criteria for the Photon

As described briefly in Section 3.2, photons are reconstructed from electromagnetic showers in the calorimeter that distribute their energies over multiple crystals. The direction of the photon is determined by interpolating between crystals and the total energy is determined by summing the energy deposited in the region identified as part of an electromagnetic shower. The shower is required to have total energy between 10 MeV and 2 GeV. No part of the shower may deposit its energy in a known noisy, i.e. "hot", crystal or an under-performing one. The shower may not lie in the path of a track since such a shower would almost certainly have been produced by a charged particle and therefore cannot be a photon candidate. Electromagnetic showers tend to deposit a narrower distribution of energy than a hadronic shower. The collimation of energy deposition is measured by a quantity known as $E9/E25$. It is the ratio of energy in the 3×3 block of crystal surrounding the cluster-center of the shower energy to the energy deposited in the 5×5 block. $E9/E25$ is required to be close to 1 for a photon shower. We also require that energies in this 5×5 block that are associated with any other photon be subtracted. We select on a range for this unfolded $E9/E25$ variable, limited by 1, such that 99% of showers are accepted. And finally, the shower is required to be from a region of the barrel or endcap calorimeter known to be good.

Table 4.1: Integrated luminosity corresponding to the CLEO-c datasets used in this analysis. The statistical uncertainties are added in quadrature, while the systematic uncertainties are added linearly. Thereafter, these two forms of uncertainties are added in quadrature to give us the total uncertainty we use for the analysis and the remainder of this document.

Dataset	Integrated Luminosity ± stat ± syst (pb^{-1})
39	55.1 ± 0.03 ± 0.56
40	123.9 ± 0.05 ± 1.3
41	119.1 ± 0.05 ± 1.3
47	109.8 ± 0.05 ± 1.1
48	178.3 ± 0.06 ± 1.9
Total	586.2 ± 0.11 ± 6.1

4.4 Datasets Used

Data taken by the CLEO-c detector at e^+e^- center of mass collision energy of 4,170 MeV that is used for this analysis correspond to the datasets enumerated in Table 4.1. The center of mass collision energy is usually represented in high energy physics as $\sqrt{s}$. We add the integrated luminosities of each of the datasets to converge on the value of 586 ± 6 pb^{-1} as the total luminosity of our data. This value is used for the rest of this dissertation.

Electron-positron collisions at a center of mass energy of $\sqrt{s}$= 4,170 MeV have been measured to produce $D_s^{\pm}D_s^{*\mp}$ pairs with a cross section of 916 ± 11(statistical) ± 49(systematic) pb in [10] and 983 ± 46(statistical) ± 21(systematics of measurement) ± 10 (systematics of luminosity) in [3]. These being independent measurements, we use the uncertainty-weighted average value of 948 ± 36 pb for the cross section in this analysis.

Dataset 42 containing 48.1 pb^{-1} of data collected at the $\psi(2S)$ resonance energy was used to measure the systematic uncertainty in the reconstruction efficiencies of soft e^+e^- and γ in this analysis.

Monte Carlo samples modeling known physical processes expected in these datasets had been produced and are available as the *Generic* and *Continuum* samples described in the following sections.

4.4.1 Generic Monte Carlo

By *Generic Monte Carlo*, we mean a Monte Carlo (MC) simulation of all known physics processes that follow from the production of charm quarks at 4,170 MeV e^+e^- collisions. The $D_s^{*+} \rightarrow D_s^+e^+e^-$ process which we are searching for, consequently, is not a part of this simulation. In order to decrease statistical uncertainties, the Generic MC was created with approximately 20 events for every 1 event of data. This scale factor of 20 was aimed for, but not necessarily achieved due to computational errors. We re-evaluate the scale factor achieved as follows:

According to

`https://www.lepp.cornell.edu/~c3mc/private/genmc_decs/20080404_MCGEN_1/ddmix_4170_isr.dec`

which is the EVTGEN decay file used to set the branching fractions of the various charm quark states possible at 4,170 MeV, the branching fraction of producing $D_s^{\pm}D_s^{*\mp}$ is 0.1014. Also, from the "Samples" section of

`https://wiki.lepp.cornell.edu/lepp/bin/view/CLEO/Private/SW/CLEOcMCstatus`

we see that the total number of produced events is 105.2 million. Therefore, we may write:

$$\frac{(586 \pm 3)\text{pb}^{-1} \times (948 \pm 36)\text{pb}}{0.1014} \times \text{scale} = (105.2 \pm 0.1) \times 10^6 \qquad (4.15)$$

From this, we deduce that the achieved scale factor for the Generic MC sample has been 19.2 ± 0.8. The uncertainty in the luminosity contributes most to the uncertainty in this scale. Since we will be mostly dividing the number of events in Generic MC by this scale factor, it is useful to record the inverse of this scale: 0.052 ± 0.002.

4.4.2 Continuum Monte Carlo

By *Continuum Monte Carlo*, we mean a Monte Carlo simulation of all physics processes that follow from the production of up, down and strange quarks at $\sqrt{s}$ = 4,170 MeV e^+e^- collisions. The scale factor for this MC sample is read off as 5 from the website:

`https://wiki.lepp.cornell.edu/lepp/bin/view/CLEO/Private/SW/CLEOcMCstatus`

4.5 Reprocessing Data to Fit Tracks with the Electron Mass Hypothesis

Tracks in CLEO-c are fitted to various particle mass hypotheses with a Kalman filter as described in [20]. In order to conserve disk-space, however, CLEO-c had chosen to not store track fits made with the electron mass hypothesis in the reconstruction process. Electrons tracks were stored with fits made with the charged pion mass hypothesis. This is found to work fine for energies above a few hundred MeVs, but not in our analysis which deals with average electron energies of 70 MeV and goes down to 40 MeV. A plot of the difference between the reconstructed and generated electron energy as a function of the generated energy for electron tracks fitted with the pion mass hypothesis is presented in Fig. 4.4(Left). We find a systematic and significant over-estimation of the electron energy with lower generated energies. This is directly related to the significantly larger mass of the charged pion being used to model the energy loss for an electron in the Kalman filter used to fit the tracks.

This systematic deviation disappears when we switch to the electron mass hypothesis for our track fits as presented in Fig. 4.4(Right). Simply re-parameterizing the energy of the tracks using a fit to Fig. 4.4(Left) was found to not improve our results as significantly as reconstructing tracks with the electron mass fit.

All datasets listed in Table 4.1 and dataset 42, which is used for computing systematic uncertainties in the low-energy electron tracking efficiency, were reprocessed to have events with D_s^+ candidates decaying to one of the nine hadronic modes specified in Eq. 4.1 - 4.9 also contain tracks fitted to the electron

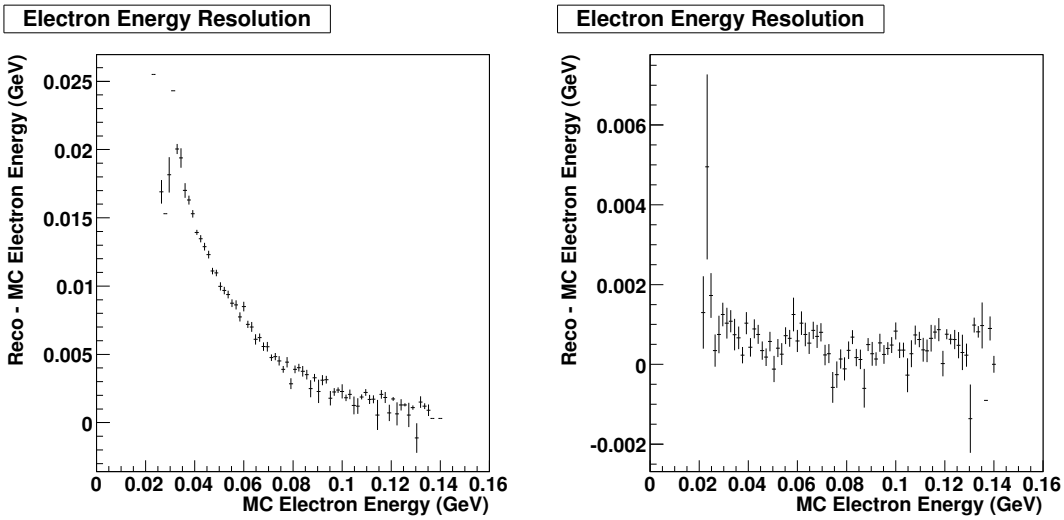

Figure 4.4: (Left) The difference between the reconstructed and Monte Carlo generated electron energy plotted against the generated electron energy when the electrons have been fitted to tracks using the pion mass hypothesis. (Right) The difference when the electrons are fitted to tracks using the electron mass hypothesis.

mass hypothesis. The execution of this procedure was a major technical challenge, given the sheer volume of data that had to be sifted through, and failed to reproduce 0.2% of the D_s^+ candidates while producing 0.1% new D_s^+ candidates in the reprocessed datasets. This was attributed to virtually intractable changes in software since the first processing of this data and is incorporated in our final measurement as a source of uncertainty.

4.6 Monte Carlo Generation and Validation

In order to calibrate our selection criteria for selecting $D_s^{*+} \to D_s^+ e^+ e^-$ and $D_s^{*+} \to D_s^+ \gamma$ events over background processes, we produce Monte Carlo simulations of these events. Monte Carlo simulations also help us estimate the efficiencies for our thus tuned selection criteria in retaining such events in data.

These simulations begin by modeling the physics of e^+e^- collisions which produces intermediate particles, which in turn decay to $D_s^{*+}D_s^-$ pairs and ultimately down to known stable particles. The invariant quantum mechanical amplitude which captures the essential dynamics of this process is programmed into the `EvtGen` [15] software package. The package uses this information along with the Lorentz-invariant phase space factor which encodes the kinematics of the process to populate the available phase space. Thus, distributions of final state particles in momenta are generated. The behavior and detection of these final state particles in CLEO-c are computed by another software package known as `GEANT` [12]. It accounts for the decay of short lived particles in flight, the interaction of particles with the material of the detector and energy loss due to bremsstrahlung.

The decay of a vector boson (D_s^{*+}) to a scalar boson (D_s^+ and two leptons (e^+e^-) had not previously been modeled in the `EvtGen` package. A software plug-in to accomplish this within `EvtGen`, based on the invariant amplitude computed in Eq. 2.14, was implemented. This was used to generate signal Monte Carlo samples for the $D_s^{*+} \to D_s^+ e^+ e^-$ process, and this included accounting for all angular correlations. However, it remained for us to ensure that the form for $d\Gamma/dk^2$ of the $D_s^{*+} \to D_s^+ e^+ e^-$ process which we arrived at analytically in Eq.

2.44 that was used in the computation of $\Gamma(D_s^{*+} \to D_s^+ e^+ e^-)/\Gamma(D_s^{*+} \to D_s^+ \gamma)$ in Eq. 2.45 matched with that produced by the Monte Carlo simulation of `EvtGen`. k^2 represents the invariant mass squared of the e^+e^- pair as it did in Chapter 2. To do this, we plotted the $d\Gamma/dk^2$ as a function of k^2 that was written down in Eq. 2.44 overlaid with an appropriately normalized histogram of the k^2 from `EvtGen` as presented in Fig. 4.5. The match is found to be satisfactory with discrepancies well beyond the capacity for our detector to resolve.

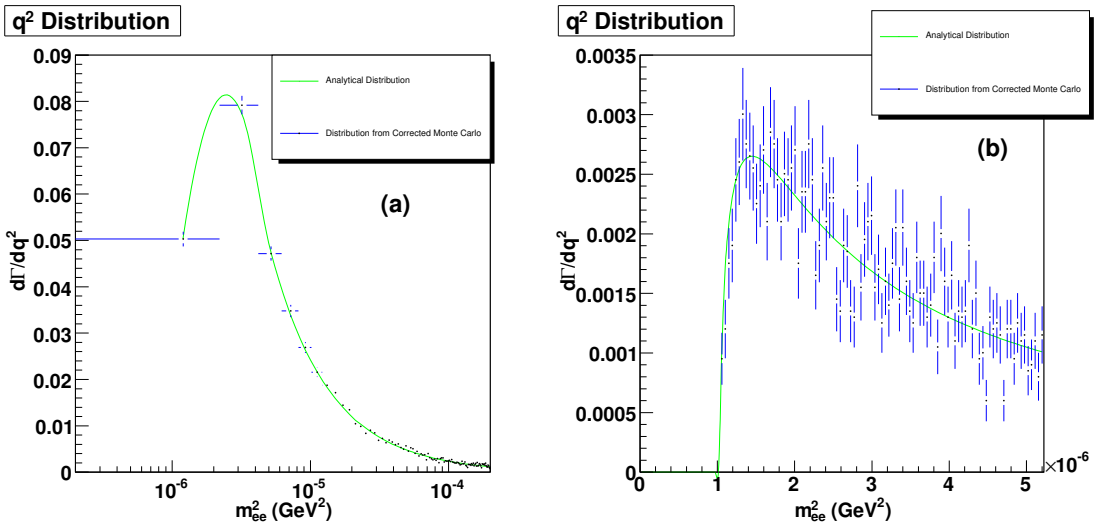

Figure 4.5: (a) The analytical expression for the distribution of k^2 overlaid with the distribution of the corrected m_{ee}^2 from the Monte Carlo. (b) A zoom into the region betweeen 0 GeV and $20m_e^2$ to illustrate the close match near the peak.

Monte Carlo samples were generated for both $D_s^{*+} \to D_s^+ e^+ e^-$ and $D_s^{*+} \to D_s^+ \gamma$ processes. The former served as the signal sample for the $D_s^{*+} \to D_s^+ e^+ e^-$ reconstruction. The latter served as one of the background samples for the $D_s^{*+} \to D_s^+ e^+ e^-$ reconstruction (where the γ converted to e^+e^- pairs in the material of the detector) and as the signal sample for reconstruction of the $D_s^{*+} \to D_s^+ \gamma$ itself. Separate samples were generated for the D_s^+ decaying to each of the 9 hadronic decay modes listed between Eq. 4.1 and 4.9.

4.7 Optimization of Selection Criteria for the $D_s^{*+} \to D_s^+ e^+ e^-$

In this section, we describe our method of calibrating the selection criteria outlined in Section 4.2 to optimally select $D_s^{*+} \to D_s^+ e^+ e^-$ events in data while rejecting background events. This is done using Monte Carlo samples for both the signal and background events. The various kinds of expected background events, as described in Section 4.1, had been simulated as part of the Generic and Continuum Monte Carlo samples accompanying each dataset as described in Section 4.4. A crude measure of signal significance, defined as:

$$\sigma_{\text{crude}} = \frac{s}{\sqrt{b}} \tag{4.16}$$

where s and b are the numbers of signal and background events observed after all selection criteria have been applied, is maximized in the course of our optimization effort. We optimize the selection criteria for each of the 9 hadronic decay modes of the D_s^+ separately using Monte Carlo samples that contain electron tracks fitted to both the charged pion and electron mass hypotheses. Improvements in the signal yields (observed number of signal events after selection criteria) and significances (as defined crudely above) are noted as we go from the pion-fitted to the electron-fitted samples, and this is summarized in Tables 4.2 and 4.3. They are a compilation of results obtained in the following sub-sections that deals with the optimization of the modes individually. The numbers in these tables are not used as final expectations of the background in data. A data driven method is used to achieve that in Section 4.9 and summarized in Section 4.9.12. The numbers here are merely representative and were used to converge on an optimized set of parameters for our selection criteria.

A problem arises in making optimization plots for the electron-fitted samples because the generic and the continuum Monte Carlo samples do not contain

tracks that are electron-fitted. To get around this, we recognize that electron-fitting tracks is most important for separating conversion events from signal. It does not change distributions of the Dalitz decay or other combinatoric backgrounds appreciably for the purposes of this analysis. Therefore, we privately produce electron-fitted Monte Carlo samples of $D_s^{*+} \to D_s^+\gamma$ events where the D_s^+ decays generically, and use them in place of Generic Monte Carlo events which have $D_s^{*+} \to D_s^+\gamma$ excluded at the generator (`EvtGen`) level.

To create the plots for optimization in the following sub-sections for each hadronic decay of the D_s^+, it is assumed that $D_s^{\pm}D_s^{*\mp}$ pairs are produced at $\sqrt{s}$= 4170 MeV with a cross section of 948 ± 36 pb, the branching fraction of $D_s^{*+} \to D_s^+\gamma$ is 94.2%, the branching fraction of $D_s^{*+} \to D_s^+e^+e^-$ is 0.65%, the scale of generic Monte Carlo is 1/19.2, and the scale of continuum Monte Caro is 1/5. The plots for a particular selection criterion are made having applied all other selection criteria. This allows us to assess the performance of a particular criterion when applied in conjunction with all other criteria. We may take the set of plots in Fig. 4.6 as an illustration of our procedure. We plot the distribution of the variable that we are selecting on, the mass of the D_s^+ in this example, for the signal on the top left plot in each set of plots. The plot on the right in the same row graphs the increase in accepted signal as we increase the width of our selection criterion in $m_{D_s^+}$. The number of produced signal events are normalized to what we expect in 586 pb^{-1} of data. The second row displays the same for a generic MC sample. The third row displays the same for the continuum MC sample. They too are normalized to a luminosity of 586 pb^{-1}. The first column on the last row plots the crude significance as defined in Eq. 4.16 against an increasing acceptance of the selection criterion. The second column on the last row plots a crude precision, as defined in Eq. 4.17 against an increasing accep-

tance of the selection criterion. For each selection criterion we try to maximize the crude significance while ensuring that we are not too far from the maximum in the crude precision.

$$p_{\text{crude}} = \frac{s}{\sqrt{s+b}} \tag{4.17}$$

Optimization of the selection criteria for each hadronic decay mode of the D_s^+ is described separately in the following sub-sections. In the interest of reading clarity, the plots used to converge on optimized parameters are only presented for the $D_s^+ \to K^+K^-\pi^+$ mode in this section. Plots for all other modes are relegated to Appendix A. The parameters converged upon for the selection criteria and their performances against signal and background Monte Carlo samples, however, are presented in the sub-sections corresponding to each of the modes.

Table 4.2: Numbers of signal and background events retained by optimized selection criteria in signal and background Monte Carlo simulations where electron tracks have been fitted to the pion mass hypothesis. The numbers are normalized to 586 pb^{-1} of integrated luminosity.

Mode	Signal	Generic Background	Continuum Background	Total Background	$s/\sqrt{b}$
$K^+K^-\pi^+$	11.7	2.03	0.00	2.03	8.2
$K_S K^+$	3.12	0.78	0.00	0.78	3.5
$\eta\pi^+$	1.57	0.21	0.20	0.41	6.3
$\eta'\pi^+; \eta' \to \pi^+\pi^-\eta$	1.02	0.47	0.00	0.47	1.5
$K^+K^-\pi^+\pi^0$	4.62	3.49	0.40	3.89	2.3
$\pi^+\pi^-\pi^+$	2.99	0.73	0.60	1.33	2.6
$K^{*+}K^{*0}$	1.78	1.35	0.00	1.35	1.5
$\eta\rho^+$	5.54	2.40	3.60	6.00	2.3
$\eta'\pi^+; \eta' \to \rho^0\gamma$	2.17	0.83	1.60	2.43	1.4
Total	36.94	12.29	6.4	18.69	8.6

Table 4.3: Numbers of signal and background events retained by optimized selection criteria in signal and background Monte Carlo simulations where electron tracks have been fitted to the electron mass hypothesis. The numbers are normalized to 586 pb^{-1} of integrated luminosity.

Mode	Signal	Conversion Background	Generic Background	Continuum Background	Total Background	$s/\sqrt{b}$
			Conversions Vetoed			
$K^+K^-\pi^+$	13.36	1.04	0.42	0.00	1.45	11.1
$K_S K^+$	3.05	0.34	0.21	0.00	0.54	4.13
$\eta\pi^+$	1.79	0.17	0.10	0.20	0.47	6.6
$\eta'\pi^+; \eta' \to \pi^+\pi^-\eta$	0.74	0.00	0.00	0.00	0.00	∞
$K^+K^-\pi^+\pi^0$	4.86	0.63	1.46	0.20	2.29	3.2
$\pi^+\pi^-\pi^+$	3.67	0.28	0.21	1.60	2.09	2.5
$K^{*+}K^{*0}$	2.02	0.23	0.63	0.20	1.05	2.0
$\eta\rho^+$	5.71	0.85	0.99	1.00	2.84	3.4
$\eta'\pi^+; \eta' \to \rho^0\gamma$	2.41	0.34	0.21	1.80	2.35	1.6
Total	40.36	3.88	4.23	5.00	13.08	11.2

4.7.1 $D_s^+ \to K^+K^-\pi^+$

Given that the branching fraction of $D_s^+ \to K^+K^-\pi^+$ is 0.055 ± 0.0028 [3, 4], we study the plots in 4.6, 4.7, 4.8, 4.9 and 4.10 to arrive at the selection criteria for data with electron tracks fitted to the pion mass hypothesis, and the plots in 4.11, 4.12, 4.13, 4.14 and 4.15 to arrive at the selection criteria for data with electron tracks fitted to the electron mass hypothesis. These are summarized in Table 4.4. The optimization plots for any given selection criteria are produced after having applied all other criteria on the simulated samples. All plots correspond to 586 pb^{-1} of integrated luminosity.

When the selection criteria outlined in Table 4.4 are applied to Monte Carlo simulation samples corresponding to 586 pb^{-1} of integrated luminosity, with the pion mass hypothesis and the electron mass hypothesis for electron tracks, we are left with signal and background yields as presented in Table 4.5.

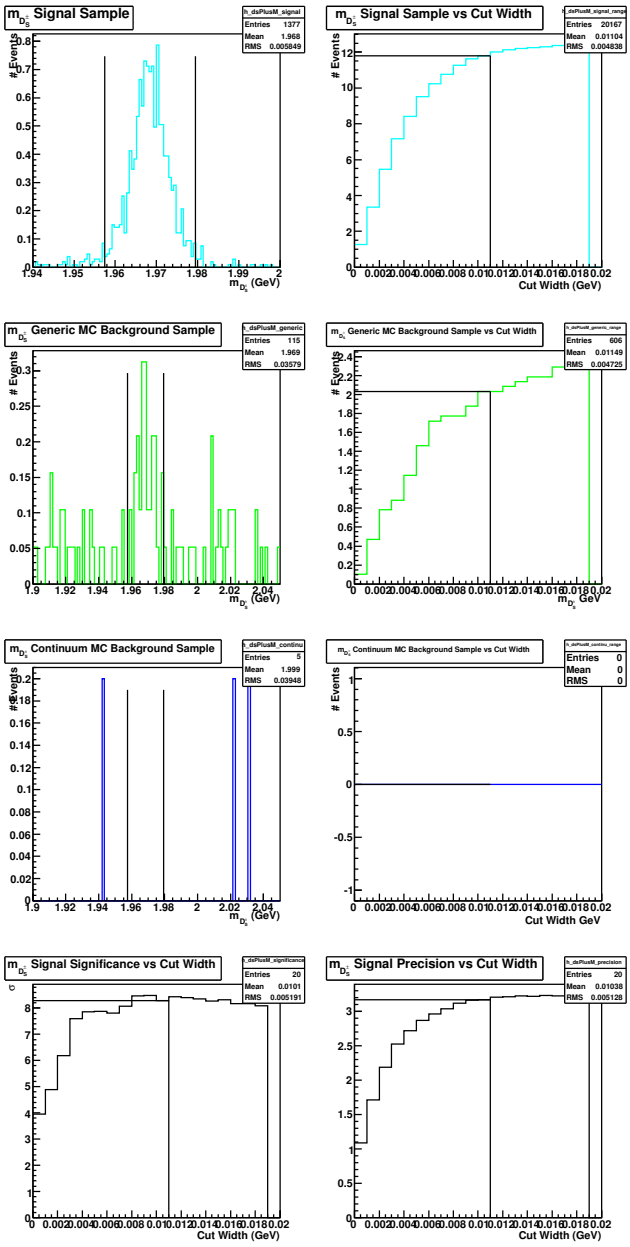

Figure 4.6: Optimization plots for the $m_{D_s^+}$ selection criterion in the $D_s^+ \to K^+K^-\pi^+$ mode using pion-fitted tracks in the simulated samples. The top left plot is the distribution of $m_{D_s^+}$ in the signal Monte Carlo sample. The top right plot graphs the number of signal MC sample events accepted by the criterion as we increase the cut width plotted on the x-axis. The plots in the second and third rows correspond to the generic and continuum MC samples. The bottom left shows the significance of the signal over background. The bottom right plot shows the precision of the signal.

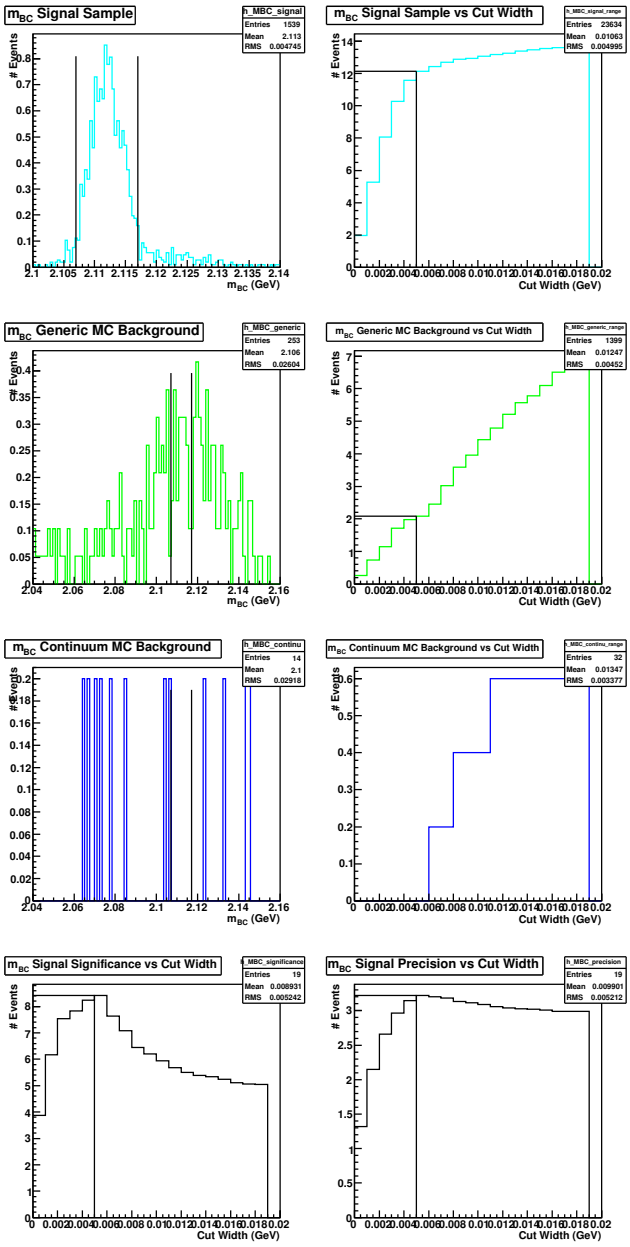

Figure 4.7: Optimization plots for the m_{BC} selection criterion in the $D_s^+ \to K^+K^-\pi^+$ mode using pion-fitted tracks in the simulated samples. The top left plot is the distribution of m_{BC} in the signal Monte Carlo sample. The top right plot graphs the number of signal MC sample events accepted by the criterion as we increase the cut width plotted on the x-axis. The plots in the second and third rows correspond to the generic and continuum MC samples. The bottom left shows the significance of the signal over background. The bottom right plot shows the precision of the signal.

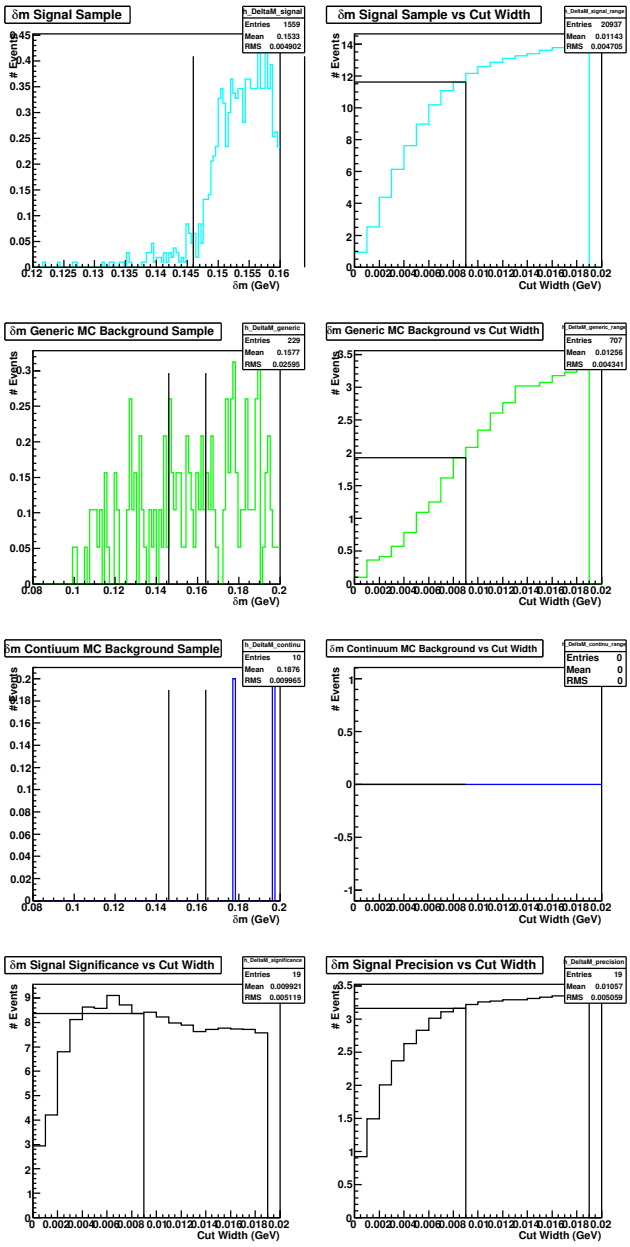

Figure 4.8: Optimization plots for the δm selection criterion in the $D_s^+ \to K^+K^-\pi^+$ mode using pion-fitted tracks in the simulated samples. The top left plot is the distribution of δm in the signal Monte Carlo sample. The top right plot graphs the number of signal MC sample events accepted by the criterion as we increase the cut width plotted on the x-axis. The plots in the second and third rows correspond to the generic and continuum MC samples. The bottom left shows the significance of the signal over background. The bottom right plot shows the precision of the signal.

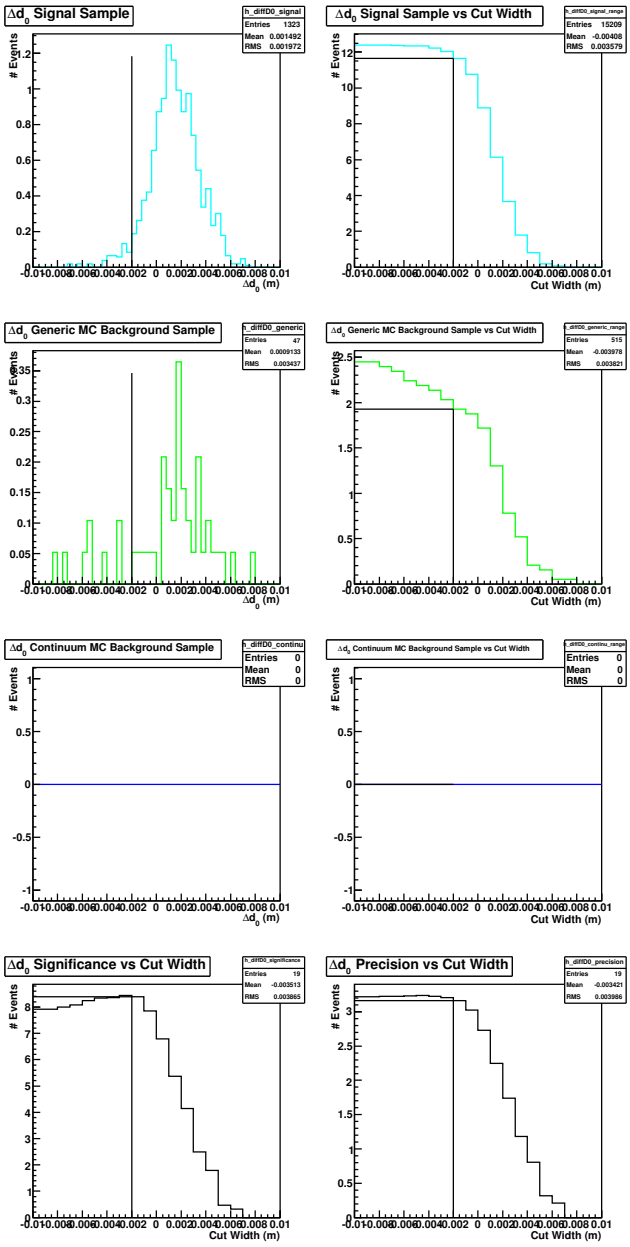

Figure 4.9: Optimization plots for the Δd_0 selection criterion in the $D_s^+ \to K^+K^-\pi^+$ mode using pion-fitted tracks in the simulated samples. The top left plot is the distribution of Δd_0 between the e^+e^- tracks in the signal Monte Carlo sample. The top right plot graphs the number of signal MC sample events accepted by the criterion as we vary the cut on the x-axis. The plots in the second and third rows correspond to the generic and continuum MC samples. The bottom left shows the significance of the signal over background. The bottom right plot shows the precision of the signal.

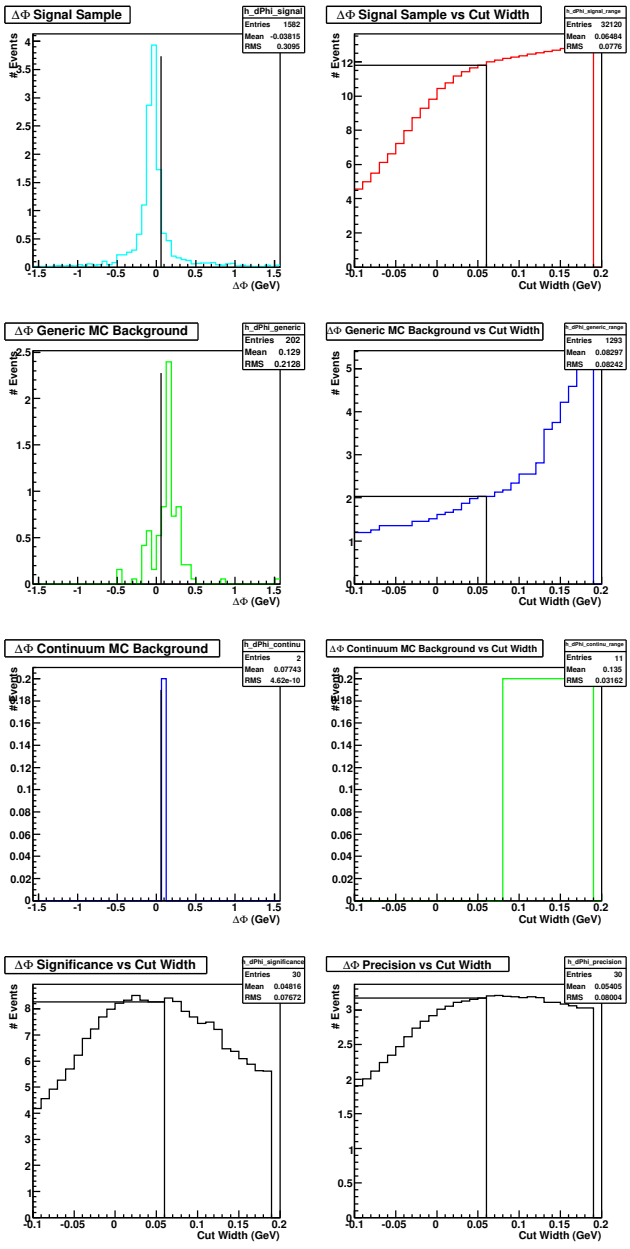

Figure 4.10: Optimization plots for the $\Delta\phi_0$ selection criterion in the $D_s^+ \to K^+K^-\pi^+$ mode using pion-fitted tracks in the simulated samples. The top left plot is the distribution of $\Delta\phi_0$ between the e^+e^- tracks in the signal Monte Carlo sample. The top right plot graphs the number of signal MC sample events accepted by the criterion as we vary the cut on the x-axis. The plots in the second and third rows correspond to the generic and continuum MC samples. The bottom left shows the significance of the signal over background. The bottom right plot shows the precision of the signal.

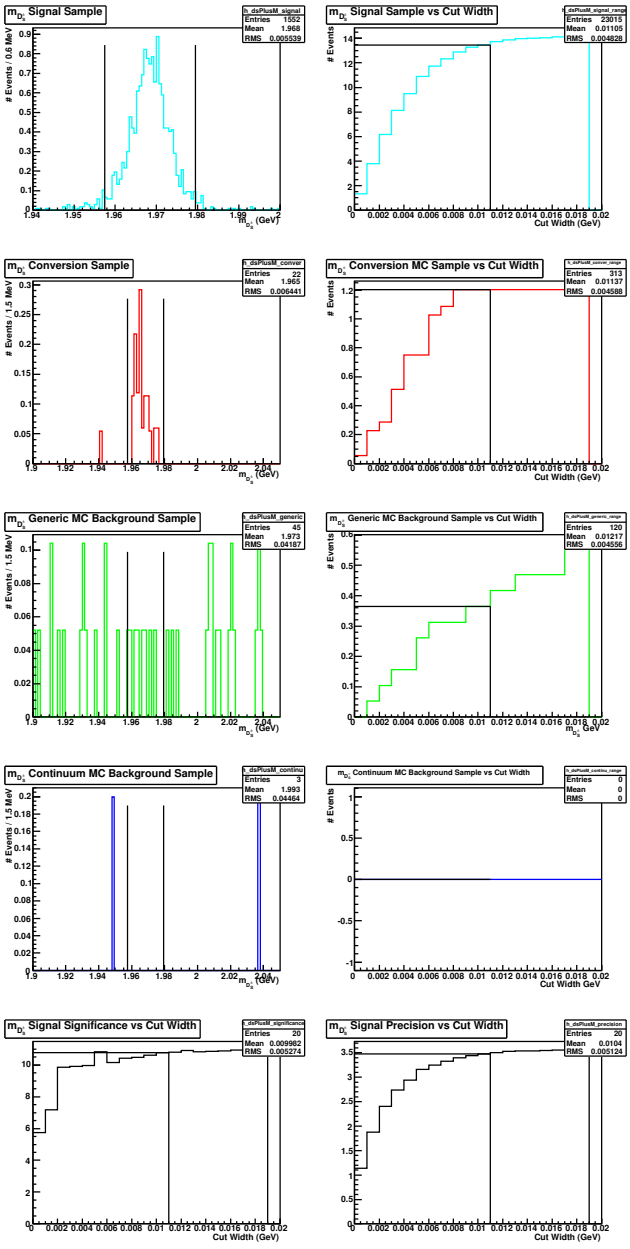

Figure 4.11: Optimization plots for the $m_{D_s^+}$ selection criterion in the $D_s^+ \to K^+K^-\pi^+$ mode using electron-fitted tracks in the simulated samples. The top left plot is the distribution of $m_{D_s^+}$ in the signal Monte Carlo sample. The top right plot graphs the number of signal MC sample events accepted by the criterion as we increase the cut width plotted on the x-axis. The plots in the second, third and fourth rows correspond to the $D_s^{*+} \to D_s^+\gamma$, generic and continuum MC samples. The bottom left shows the significance of the signal over background. The bottom right plot shows the precision of the signal.

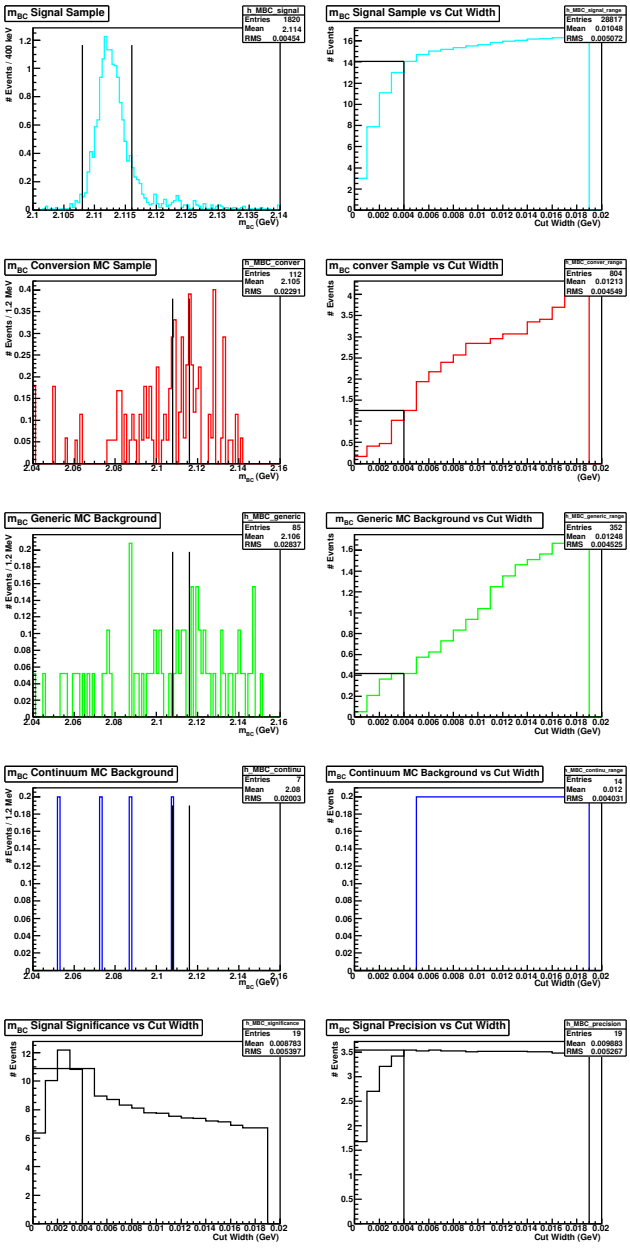

Figure 4.12: Optimization plots for the m_{BC} selection criterion in the $D_s^+ \to K^+K^-\pi^+$ mode using electron-fitted tracks in the simulated samples. The top left plot is the distribution of m_{BC} in the signal Monte Carlo sample. The top right plot graphs the number of signal MC sample events accepted by the criterion as we increase the cut width plotted on the x-axis. The plots in the second, third and fourth rows correspond to the $D_s^{*+} \to D_s^+\gamma$, generic and continuum MC samples. The bottom left shows the significance of the signal over background. The bottom right plot shows the precision of the signal.

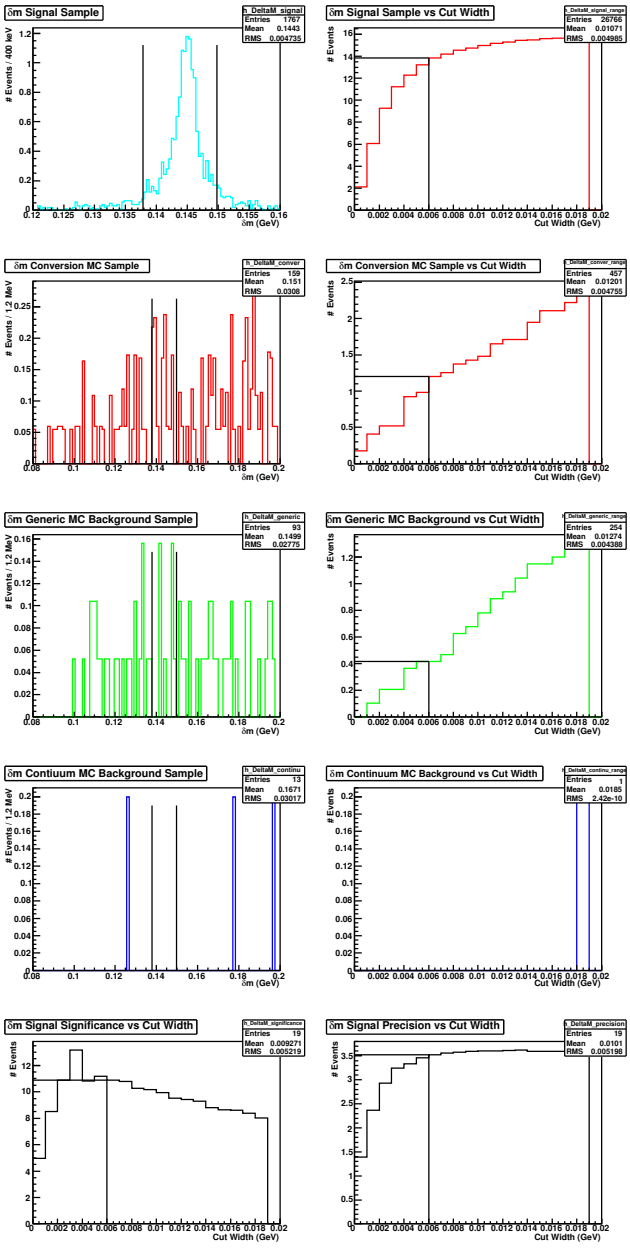

Figure 4.13: Optimization plots for the δm selection criterion in the $D_s^+ \to K^+K^-\pi^+$ mode using electron-fitted tracks in the simulated samples. The top left plot is the distribution of δm in the signal Monte Carlo sample. The top right plot graphs the number of signal MC sample events accepted by the criterion as we increase the cut width plotted on the x-axis. The plots in the second, third and fourth rows correspond to the $D_s^{*+} \to D_s^+\gamma$, generic and continuum MC samples. The bottom left shows the significance of the signal over background. The bottom right plot shows the precision of the signal.

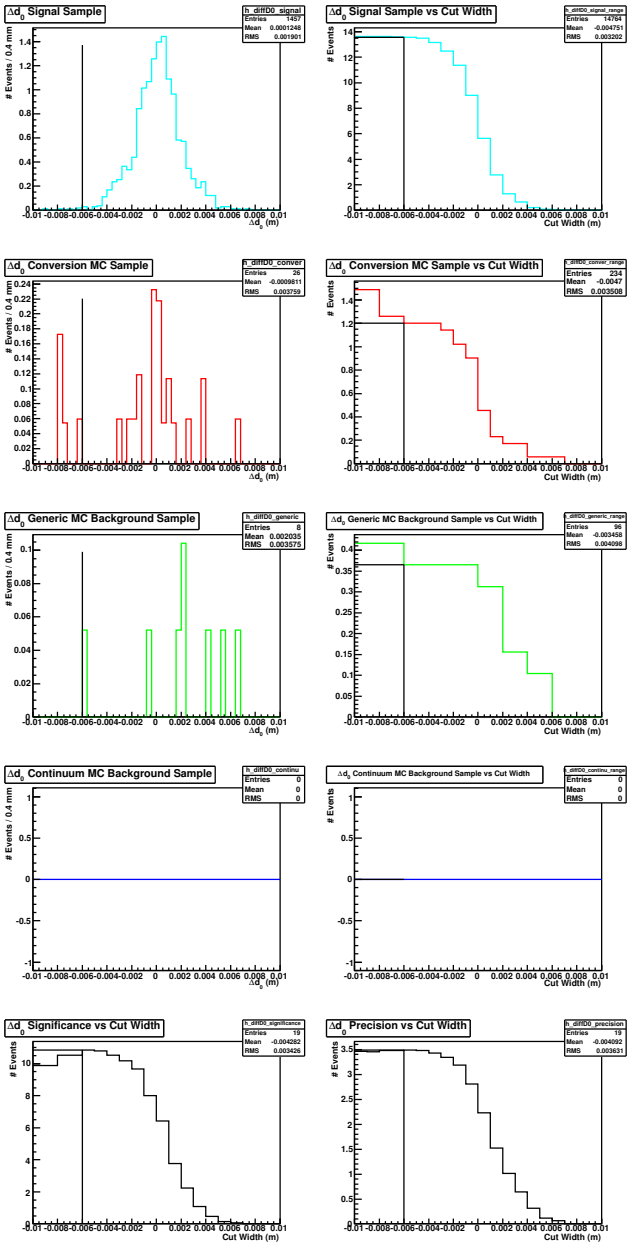

Figure 4.14: Optimization plots for the Δd_0 selection criterion in the $D_s^+ \to K^+K^-\pi^+$ mode using electron-fitted tracks in the simulated samples. The top left plot is the distribution of Δd_0 between the e^+e^- tracks in the signal Monte Carlo sample. The top right plot graphs the number of signal MC sample events accepted by the criterion as we vary the cut on the x-axis. The plots in the second, third and fourth rows correspond to the $D_s^{*+} \to D_s^+\gamma$, generic and continuum MC samples. The bottom left shows the significance of the signal over background. The bottom right plot shows the precision of the signal.

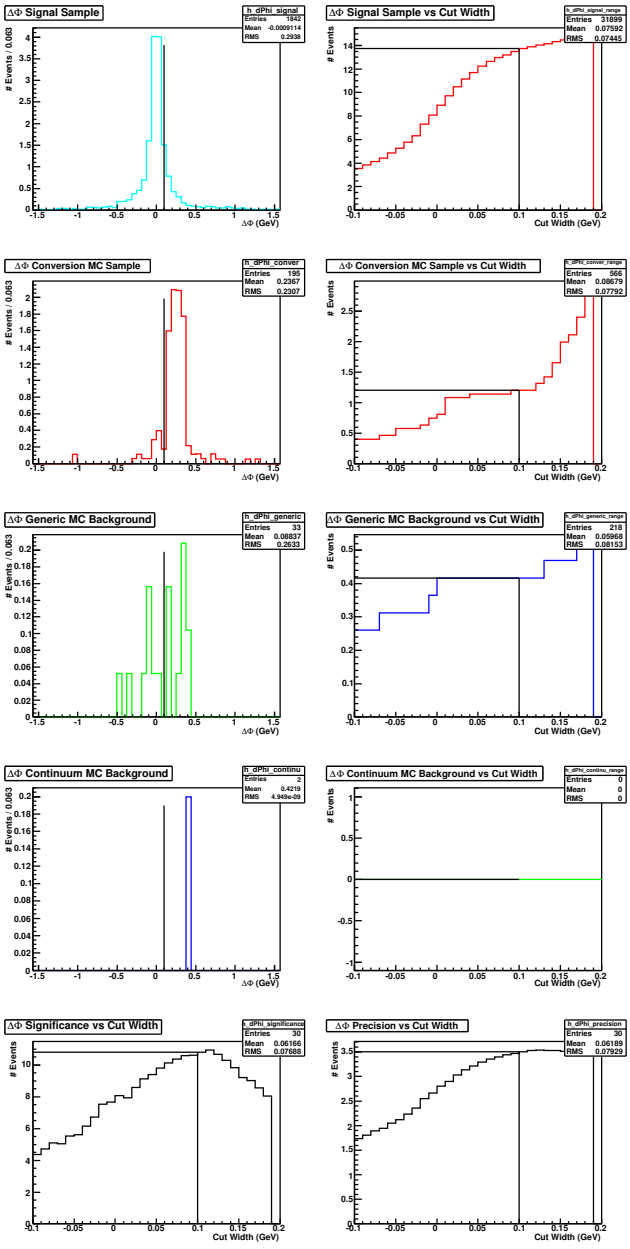

Figure 4.15: Optimization plots for the $\Delta\phi_0$ selection criterion in the $D_s^+ \to K^+K^-\pi^+$ mode using electron-fitted tracks in the simulated samples. The top left plot is the distribution of $\Delta\phi_0$ between the e^+e^- tracks in the signal Monte Carlo sample. The top right plot graphs the number of signal MC sample events accepted by the criterion as we vary the cut on the x-axis. The plots in the second, third and fourth rows correspond to the $D_s^{*+} \to D_s^+\gamma$, generic and continuum MC samples. The bottom left shows the significance of the signal over background. The bottom right plot shows the precision of the signal.

Table 4.4: Selection criteria for data with electron tracks fitted to the pion and electron mass hypotheses in the $D_s^+ \to K^+K^-\pi^+$ decay mode.

Selection Criterion	Pion-Fitted Data	Electron-Fitted Data
	Cut Center ± Width	Cut Center ± Width
$m_{D_s^+}$	1.969 ± 0.011 GeV	1.969 ± 0.011 GeV
m_{BC}	2.112 ± 0.005 GeV	2.112 ± 0.004 GeV
δm	0.155 ± 0.009 GeV	0.144 ± 0.006 GeV
Δd_0	-0.002 m	-0.006 m
$\Delta\phi_0$	0.06	0.1

Table 4.5: Numbers of signal and background events left in 586 pb^{-1} of pion and electron-fitted simulation samples in the $D_s^+ \to K^+K^-\pi^+$ decay mode.

Expected Number of Events in 586 pb^{-1}	Pion-Fitted Samples and Criteria	Electron-Fitted Samples and Criteria
Signal (s)	11.7	13.36
Conversion Background	-	1.04
Generic Background (without Conversions in e-fit)	2.03	0.42
Continuum Background	0.00	0.00
Total Background (b)	2.03	1.45
$s/\sqrt{b}$	8.2	11.1

4.7.2 $D_s^+ \to K_S K^+$

The optimization plots for this decay mode may be found in Appendix A.1. Given that the branching fraction of $D_s^+ \to K_S K^+$ is 0.0149 ± 0.0009 [3, 4], we study the plots in A.1, A.3, A.5, A.7 and A.9 to arrive at the selection criteria for data with electron tracks fitted to the pion mass hypothesis, and the plots in A.2, A.4, A.6, A.8 and A.10 to arrive at the selection criteria for data with electron tracks fitted to the electron mass hypothesis. These are summarized in Table 4.6.

Table 4.6: Selection criteria for data with electron tracks fitted to the pion and electron mass hypotheses in the $D_s^+ \to K_S K^+$ decay mode.

Selection Criterion	Pion-Fitted Data	Electron-Fitted Data
	Cut Center ± Width	Cut Center ± Width
$m_{D_s^+}$	1.969 ± 0.012 GeV	1.969 ± 0.008 GeV
m_{BC}	2.112 ± 0.006 GeV	2.112 ± 0.007 GeV
δm	0.158 ± 0.010 GeV	0.144 ± 0.006 GeV
Δd_0	-0.002 m	-0.004 m
$\Delta\phi_0$	0.09	0.14

When the selection criteria outlined in Table 4.6 are applied to Monte Carlo simulation samples corresponding to 586 pb^{-1} of integrated luminosity, with the pion mass hypothesis and the electron mass hypothesis for electron tracks, we are left with signal and background yields as presented in Table 4.7.

Table 4.7: Numbers of signal and background events expected in pion and electron-fitted data in the $D_s^+ \to K_S K^+$ decay mode.

Expected Number of Events in 586 pb^{-1}	Pion-Fitted Samples and Criteria	Electron-Fitted Samples and Criteria
Signal (s)	3.12	3.05
Conversion Background	-	0.34
Generic Background (without Conversions in e-fit)	0.78	0.21
Continuum Background	0.00	0.00
Total Background (b)	0.78	0.54
$s/\sqrt{b}$	3.5	4.13

4.7.3 $D_s^+ \to \eta\pi^+; \eta \to \gamma\gamma$

The optimization plots for this decay mode may be found in Appendix A.2. Given that the branching fraction of $D_s^+ \to \eta\pi^+$ is 0.0158 ± 0.0021 [3, 4] and $\eta \to \gamma\gamma$ is 0.3931 ± 0.0020 [1, 16, 4], we study the plots in A.11, A.13, A.15, A.17 and A.19 to arrive at the selection criteria for data with electron tracks fitted to the pion mass hypothesis, and the plots in A.12, A.14, A.16, A.18 and A.20 to arrive at the selection criteria for data with electron tracks fitted to the electron mass hypothesis. These are summarized in Table 4.8.

Table 4.8: Selection criteria for data with electron tracks fitted to the pion and electron mass hypotheses in the $D_s^+ \to \eta\pi^+; \eta \to \gamma\gamma$ decay mode.

Selection Criterion	Pion-Fitted Data	Electron-Fitted Data
	Cut Center ± Width	Cut Center ± Width
$m_{D_s^+}$	1.969 ± 0.015 GeV	1.969 ± 0.016 GeV
m_{BC}	2.112 ± 0.007 GeV	2.112 ± 0.008 GeV
δm	0.155 ± 0.013 GeV	0.144 ± 0.008 GeV
Δd_0	-0.007 m	-0.004 m
$\Delta\phi_0$	0.07	0.12

When the selection criteria outlined in Table 4.8 are applied to Monte Carlo simulation samples corresponding to 586 pb^{-1} of integrated luminosity, with the pion mass hypothesis and the electron mass hypothesis for electron tracks, we are left with signal and background yields as presented in Table 4.9.

Table 4.9: Numbers of signal and background events expected in pion and electron-fitted data in the $D_s^+ \to \eta\pi^+; \eta \to \gamma\gamma$ decay mode.

Expected Number of Events in 586 pb^{-1}	Pion-Fitted Samples and Criteria	Electron-Fitted Samples and Criteria
Signal (s)	1.57	1.79
Conversion Background	-	0.17
Generic Background (without Conversions in e-fit)	0.21	0.10
Continuum Background	0.20	0.20
Total Background (b)	0.41	0.47
$s/\sqrt{b}$	6.3	6.6

4.7.4 $D_s^+ \to \eta'\pi^+; \eta' \to \pi^+\pi^-\eta; \eta \to \gamma\gamma$

The optimization plots for this decay mode may be found in Appendix A.3. Given that the branching fraction of $D_s^+ \to \eta'\pi^+$ is 0.038 ± 0.004 [3, 4], the branching fraction of $\eta' \to \pi^+\pi^-\eta$ is 0.446 ± 0.0014 [19, 4], and the branching fraction of $\eta \to \gamma\gamma$ is 0.3931 ± 0.0020 [1, 16, 4], we studied the plots in A.21, A.23, A.25, A.27 and A.29 to arrive at the selection criteria for data with electron tracks fitted to the pion mass hypothesis, and the plots in A.22, A.24, A.26, A.28 and A.30 to arrive at the selection criteria for data with electron tracks fitted to the electron mass hypothesis. These are tabulated in Table 4.10

Table 4.10: Selection criteria for data with electron tracks fitted to the pion and electron mass hypotheses in the $D_s^+ \to \eta'\pi^+; \eta' \to \pi^+\pi^-\eta; \eta \to \gamma\gamma$ decay mode.

Selection Criterion	Pion-Fitted Data	Electron-Fitted Data
	Cut Center ± Width	Cut Center ± Width
$m_{D_s^+}$	1.969 ± 0.011 GeV	1.969 ± 0.008 GeV
m_{BC}	2.112 ± 0.011 GeV	2.112 ± 0.004 GeV
δm	0.155 ± 0.013 GeV	0.144 ± 0.008 GeV
Δd_0	-0.003 m	-0.004 m
$\Delta\phi_0$	0.07	0.1

When the selection criteria outlined in Table 4.10 are applied to Monte Carlo simulation samples corresponding to 586 pb^{-1} of integrated luminosity, with the pion mass hypothesis and the electron mass hypothesis for electron tracks, we are left with signal and background yields as presented in Table 4.11.

Table 4.11: Numbers of signal and background events expected in pion and electron-fitted data in the $D_s^+ \to \eta'\pi^+; \eta' \to \pi^+\pi^-\eta; \eta \to \gamma\gamma$ decay mode.

Expected Number of Events in 586 pb^{-1}	Pion-Fitted Samples and Criteria	Electron-Fitted Samples and Criteria
Signal (s)	1.02	0.74
Conversion Background	-	0.00
Generic Background (without Conversions in e-fit)	0.47	0.00
Continuum Background	0.00	0.00
Total Background (b)	0.47	0.00
$s/\sqrt{b}$	1.50	∞

4.7.5 $D_s^+ \to K^+K^-\pi^+\pi^0$

The optimization plots for this decay mode may be found in Appendix A.4. Given that the branching fraction of $D_s^+ \to K^+K^-\pi^+\pi^0$ is 0.056 ± 0.005 [3, 4], we study the plots in A.31, A.33, A.35, A.37 and A.39 to arrive at the selection criteria for data with electron tracks fitted to the pion mass hypothesis, and the plots in A.32, A.34, A.36, A.38 and A.40 to arrive at the selection criteria for data with electron tracks fitted to the electron mass hypothesis. These are tabulated in Table 4.12

Table 4.12: Selection criteria for data with electron tracks fitted to the pion and electron mass hypotheses in the $D_s^+ \to K^+K^-\pi^+\pi^0$ decay mode.

Selection Criterion	Pion-Fitted Data	Electron-Fitted Data
	Cut Center ± Width	Cut Center ± Width
$m_{D_s^+}$	1.969 ± 0.009 GeV	1.969 ± 0.010 GeV
m_{BC}	2.112 ± 0.007 GeV	2.112 ± 0.004 GeV
δm	0.155 ± 0.011 GeV	0.144 ± 0.006 GeV
Δd_0	-0.002 m	-0.006 m
$\Delta\phi_0$	0.07	0.12

When the selection criteria outlined in Table 4.12 are applied to Monte Carlo simulation samples corresponding to 586 pb^{-1} of integrated luminosity, with the pion mass hypothesis and the electron mass hypothesis for electron tracks, we are left with signal and background yields as presented in Table 4.13.

Table 4.13: Numbers of signal and background events expected in pion and electron-fitted data in the $D_s^+ \to K^+K^-\pi^+\pi^0$ decay mode.

Expected Number of Events in 586 pb^{-1}	Pion-Fitted Samples and Criteria	Electron-Fitted Samples and Criteria
Signal (s)	4.62	4.86
Conversion Background	-	0.63
Generic Background (without Conversions in e-fit)	3.49	1.46
Continuum Background	0.40	0.20
Total Background (b)	3.89	2.29
$s/\sqrt{b}$	2.3	3.2

4.7.6 $D_s^+ \to \pi^+\pi^-\pi^+$

The optimization plots for this decay mode may be found in Appendix A.5. Given that the branching fraction of $D_s^+ \to \pi^+\pi^-\pi^+$ is 0.0111 ± 0.0008 [4], we study the plots in A.41, A.43, A.45, A.47 and A.49 to arrive at the selection criteria for data with electron tracks fitted to the pion mass hypothesis, and the plots in A.42, A.44, A.46, A.48 and A.50 to arrive at the selection criteria for data with electron tracks fitted to the electron mass hypothesis. These are tabulated in Table 4.14.

Table 4.14: Selection criteria for data with electron tracks fitted to the pion and electron mass hypotheses in the $D_s^+ \to \pi^+\pi^-\pi^+$ decay mode.

Selection Criterion	Pion-Fitted Data	Electron-Fitted Data
	Cut Center ± Width	Cut Center ± Width
$m_{D_s^+}$	1.969 ± 0.013 GeV	1.969 ± 0.012 GeV
m_{BC}	2.112 ± 0.005 GeV	2.112 ± 0.004 GeV
δm	0.155 ± 0.009 GeV	0.144 ± 0.006 GeV
Δd_0	-0.001 m	-0.006 m
$\Delta\phi_0$	0.06	0.1

When the selection criteria outlined in Table 4.14 are applied to Monte Carlo simulation samples corresponding to 586 pb^{-1} of integrated luminosity, with the pion mass hypothesis and the electron mass hypothesis for electron tracks, we are left with signal and background yields as presented in Table 4.15.

Table 4.15: Numbers of signal and background events expected in pion and electron-fitted data in the $D_s^+ \to \pi^+\pi^-\pi^+$ decay mode.

Expected Number of Events in 586 pb^{-1}	Pion-Fitted Samples and Criteria	Electron-Fitted Samples and Criteria
Signal (s)	2.99	3.67
Conversion Background	-	0.28
Generic Background (without Conversions in e-fit)	0.73	0.21
Continuum Background	0.60	1.60
Total Background (b)	1.33	2.09
$s/\sqrt{b}$	2.6	2.5

4.7.7 $D_s^+ \to K^{*+}K^{*0}; K^{*+} \to K_S^0\pi^+, K^{*0} \to K^-\pi^+$

The optimization plots for this decay mode may be found in Appendix A.6. Given that the branching fraction of $D_s^+ \to K^{*+}K^{*0}; K^{*+} \to K_S^0\pi^+, K^{*0} \to K^-\pi^+$ is 0.0164 ± 0.0012 [2, 4], we study the plots in A.51, A.53, A.55, A.57 and A.59 to arrive at the selection criteria for data with electron tracks fitted to the pion mass hypothesis, and the plots in A.52, A.54, A.56, A.58 and A.60 to arrive at the selection criteria for data with electron tracks fitted to the electron mass hypothesis. These are tabulated in Table 4.16.

Table 4.16: Selection criteria for data with electron tracks fitted to the pion and electron mass hypotheses in the $D_s^+ \to K^{*+}K^{*0}$ decay mode.

Selection Criterion	Pion-Fitted Data	Electron-Fitted Data
	Cut Center ± Width	Cut Center ± Width
$m_{D_s^+}$	1.969 ± 0.007 GeV	1.969 ± 0.006 GeV
m_{BC}	2.112 ± 0.007 GeV	2.112 ± 0.005 GeV
δm	0.155 ± 0.009 GeV	0.144 ± 0.008 GeV
Δd_0	-0.004 m	-0.005 m
$\Delta\phi_0$	0.07	0.13

When the selection criteria outlined in Table 4.16 are applied to Monte Carlo simulation samples corresponding to 586 pb^{-1} of integrated luminosity, with the pion mass hypothesis and the electron mass hypothesis for electron tracks, we are left with signal and background yields as presented in Table 4.17.

Table 4.17: Numbers of signal and background events expected in pion and electron-fitted data in the $D_s^+ \to K^{*+}K^{*0}$ decay mode.

Expected Number of Events in 586 pb^{-1}	Pion-Fitted Samples and Criteria	Electron-Fitted Samples and Criteria
Signal (s)	1.78	2.02
Conversion Background	-	0.23
Generic Background (without Conversions in e-fit)	1.35	0.63
Continuum Background	0.00	0.20
Total Background (b)	1.35	1.05
$s/\sqrt{b}$	1.5	2.0

4.7.8 $D_s^+ \to \eta\rho^+; \eta \to \gamma\gamma; \rho^+ \to \pi^+\pi^0$

The optimization plots for this decay mode may be found in Appendix A.7. Given that the branching fraction of $D_s^+ \to \eta\rho^+$ is 0.130 ± 0.022 [17, 4], and the branching fraction of $\eta \to \gamma\gamma$ is 0.3931 ± 0.0020 [1, 16, 4], we study the plots in A.61, A.63, A.65, A.67 and A.69 to arrive at the selection criteria for data with electron tracks fitted to the pion mass hypothesis, and the plots in A.62, A.64, A.66, A.68 and A.70 to arrive at the selection criteria for data with electron tracks fitted to the electron mass hypothesis. These are tabulated in Table 4.18.

Table 4.18: Selection criteria for data with electron tracks fitted to the pion and electron mass hypotheses in the $D_s^+ \to \eta\rho^+; \eta \to \gamma\gamma; \rho^+ \to \pi^+\pi^0$ decay mode.

Selection Criterion	Pion-Fitted Data	Electron-Fitted Data
	Cut Center ± Width	Cut Center ± Width
$m_{D_s^+}$	1.969 ± 0.014 GeV	1.969 ± 0.015 GeV
m_{BC}	2.112 ± 0.006 GeV	2.112 ± 0.004 GeV
δm	0.155 ± 0.009 GeV	0.144 ± 0.005 GeV
Δd_0	-0.003 m	-0.007 m
$\Delta\phi_0$	0.07	0.13

When the selection criteria outlined in Table 4.18 are applied to Monte Carlo simulation samples corresponding to 586 pb^{-1} of integrated luminosity, with the pion mass hypothesis and the electron mass hypothesis for electron tracks, we are left with signal and background yields as presented in Table 4.19.

Table 4.19: Numbers of signal and background events expected in pion and electron-fitted data in the $D_s^+ \to \eta\rho^+; \eta \to \gamma\gamma; \rho^+ \to \pi^+\pi^0$ decay mode.

Expected Number of Events in 586 pb^{-1}	Pion-Fitted Samples and Criteria	Electron-Fitted Samples and Criteria
Signal (s)	5.54	5.71
Conversion Background	-	0.85
Generic Background (without Conversions in e-fit)	2.40	0.99
Continuum Background	3.60	1.00
Total Background (b)	6.00	2.84
$s/\sqrt{b}$	2.3	3.4

4.7.9 $D_s^+ \to \eta'\pi^+; \eta' \to \rho^0\gamma$

The optimization plots for this decay mode may be found in Appendix A.8. Given that the branching fraction of $D_s^+ \to \eta'\pi^+$ is 0.038 ± 0.004 [3, 4], and the branching fraction of $\eta' \to \rho^0\gamma$ is 0.294 ± 0.009 [19, 4], we study the plots in A.71, A.73, A.75, A.77 and A.79 to arrive at the selection criteria for data with electron tracks fitted to the pion mass hypothesis, and we studied the plots in A.72, A.74, A.76, A.78 and A.80 to arrive at the selection criteria for data with electron tracks fitted to the electron mass hypothesis. These are tabulated in Table 4.20.

Table 4.20: Selection criteria for data with electron tracks fitted to the pion and electron mass hypotheses in the $D_s^+ \to \eta'\pi^+; \eta' \to \rho^0\gamma$ decay mode.

Selection Criterion	Pion-Fitted Data	Electron-Fitted Data
	Cut Center ± Width	Cut Center ± Width
$m_{D_s^+}$	1.969 ± 0.018 GeV	1.969 ± 0.012 GeV
m_{BC}	2.112 ± 0.004 GeV	2.112 ± 0.004 GeV
δm	0.155 ± 0.008 GeV	0.144 ± 0.007 GeV
Δd_0	-0.004 m	-0.006 m
$\Delta\phi_0$	0.09	0.11

When the selection criteria outlined in Table 4.20 are applied to Monte Carlo simulation samples corresponding to 586 pb^{-1} of integrated luminosity, with the pion mass hypothesis and the electron mass hypothesis for electron tracks, we are left with signal and background yields as presented in Table 4.21.

Table 4.21: Numbers of signal and background events expected in pion and electron-fitted data in the $D_s^+ \to \eta'\pi^+; \eta' \to \rho^0\gamma$ decay mode.

Expected Number of Events in 586 pb^{-1}	Pion-Fitted Samples and Criteria	Electron-Fitted Samples and Criteria
Signal (s)	2.17	2.41
Conversion Background	-	0.34
Generic Background (without Conversions in e-fit)	0.83	0.21
Continuum Background	1.60	1.80
Total Background (b)	2.43	2.35
$s/\sqrt{b}$	1.4	1.6

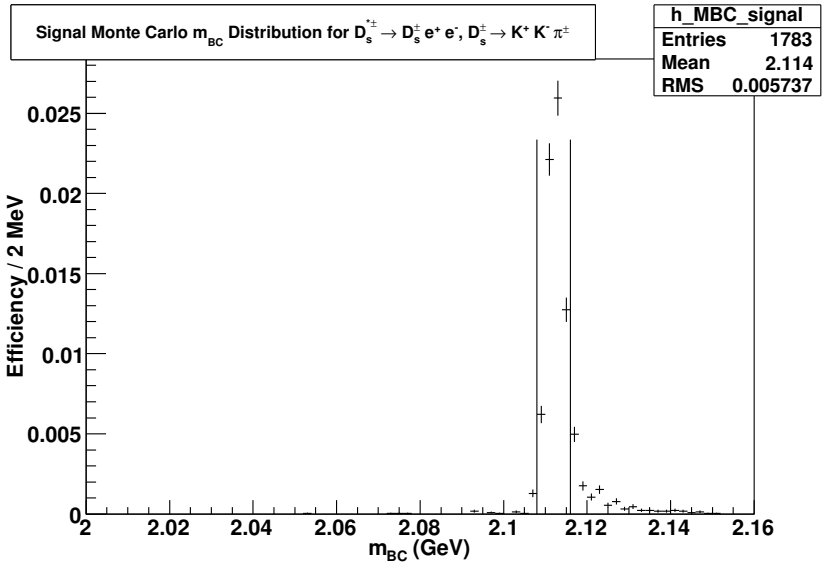

Figure 4.16: Signal efficiency for reconstructing $D_s^{*+} \rightarrow D_s^+ e^+ e^-$ in $D_s^+ \rightarrow K^+K^-\pi^+$ as represented in the m_{BC} distribution.

4.8 Efficiency of Selection Criteria for the Reconstruction of $D_s^{*+} \rightarrow D_s^+ e^+ e^-$

In order to estimate the ratio of branching fractions $B(D_s^{*+} \rightarrow D_s^+ e^+ e^-)/B(D_s^{*+} \rightarrow D_s^+ \gamma)$, we need to measure the efficiencies of our selection criteria for accepting $D_s^{*+} \rightarrow D_s^+ e^+ e^-$ events for each hadronic decay mode of the D_s^+. This is determined by applying our selection criteria on the Monte Carlo simulation samples of our signal in each of the modes. The efficiency is calculated by dividing the number of events remaining within the signal region of the m_{BC} distribution, having applied all other criteria, by the number of produced sample events. Such distributions of the m_{BC} for each mode with marked signal regions are presented in Fig. 4.16 - 4.24. Measurements of these selection efficiencies are presented in Table 4.22.

Table 4.22: Selection efficiencies for reconstructing the $D_s^{*+} \to D_s^+ e^+ e^-$ signal in each of the hadronic decay modes of the D_s^+ that this analysis deals with.

Mode	Signal Selection Efficiency
$K^+K^-\pi^+$	0.0729 ± 0.0019
$K_S K^+$	0.0597 ± 0.0017
$\eta\pi^+$	0.0855 ± 0.0021
$\eta'\pi^+; \eta' \to \pi^+\pi^-\eta, \eta \to \gamma\gamma$	0.0530 ± 0.0016
$K^+K^-\pi^+\pi^0$	0.0255 ± 0.0011
$\pi^+\pi^-\pi^+$	0.0992 ± 0.0022
$K^{*+}K^{*0}$	0.0356 ± 0.0013
$\eta\rho^+$	0.0316 ± 0.0013
$\eta'\pi^+; \eta' \to \rho^0\gamma$	0.0638 ± 0.0018

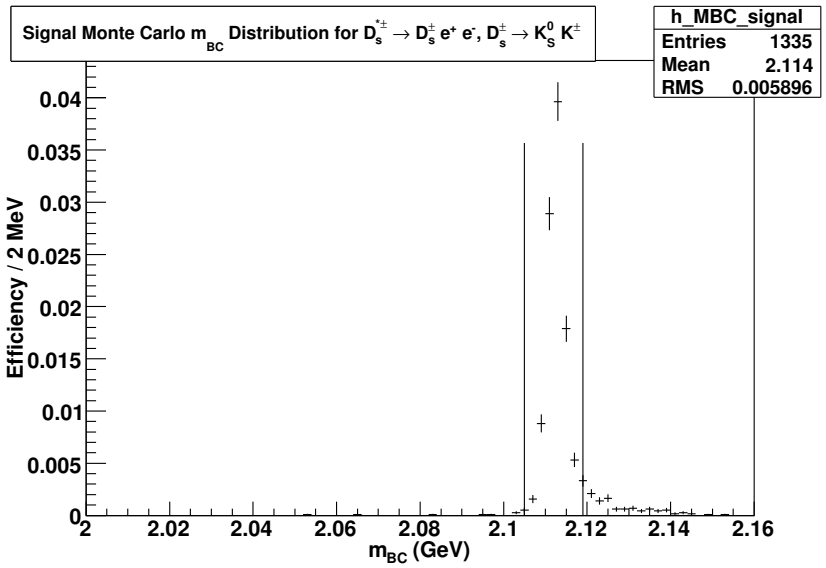

Figure 4.17: Signal efficiency for reconstructing $D_s^{*+} \to D_s^+ e^+ e^-$ in $D_s^+ \to K_S K^+$ as represented in the m_{BC} distribution.

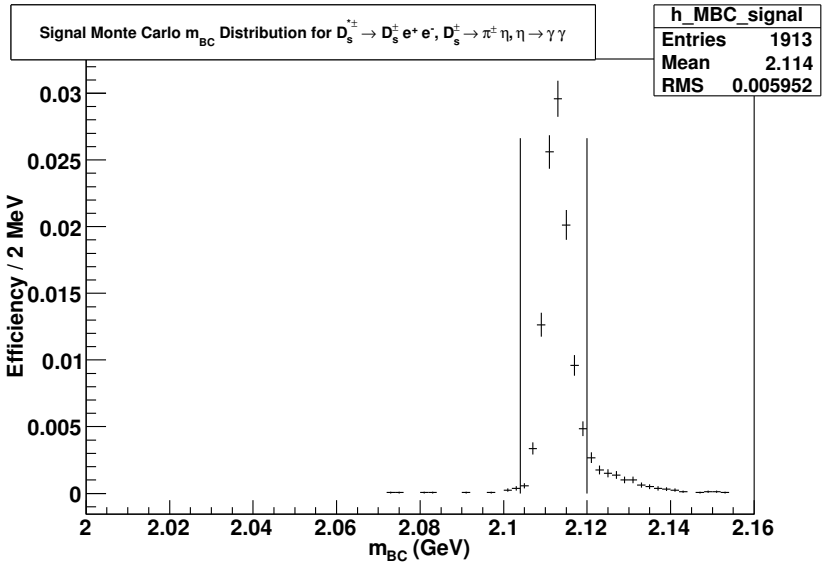

Figure 4.18: Signal efficiency for reconstructing $D_s^{*+} \to D_s^+ e^+ e^-$ in $D_s^+ \to \eta\pi^+$ as represented in the m_{BC} distribution.

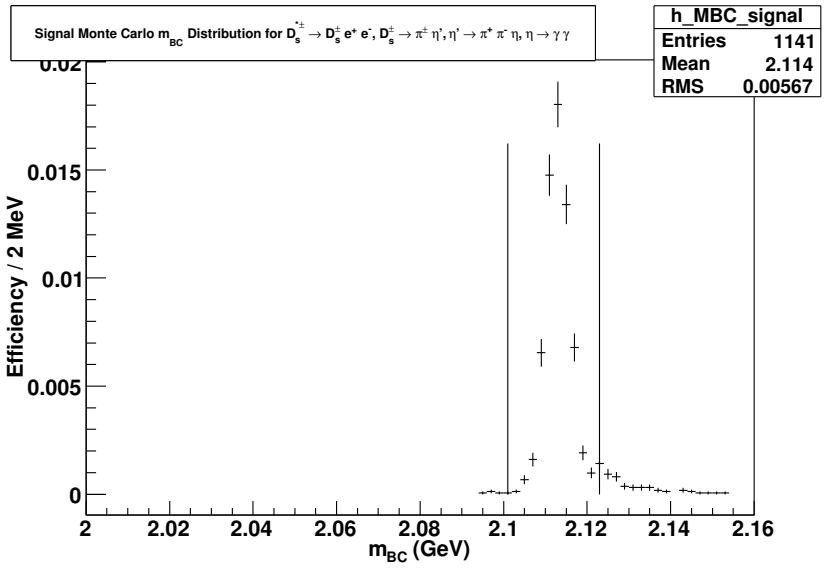

Figure 4.19: Signal efficiency for reconstructing $D_s^{*+} \to D_s^+ e^+ e^-$ in $D_s^+ \to \eta'\pi^+; \eta' \to \pi^+\pi^-\eta; \eta \to \gamma\gamma$ as represented in the m_{BC} distribution.

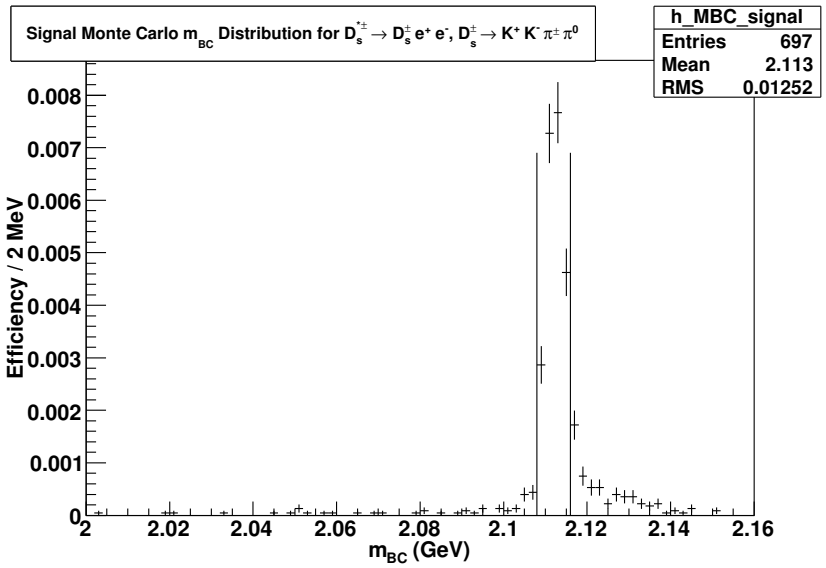

Figure 4.20: Signal efficiency for reconstructing $D_s^{*+} \rightarrow D_s^+ e^+ e^-$ in $D_s^+ \rightarrow K^+K^-\pi^+\pi^0$ as represented in the m_{BC} distribution.

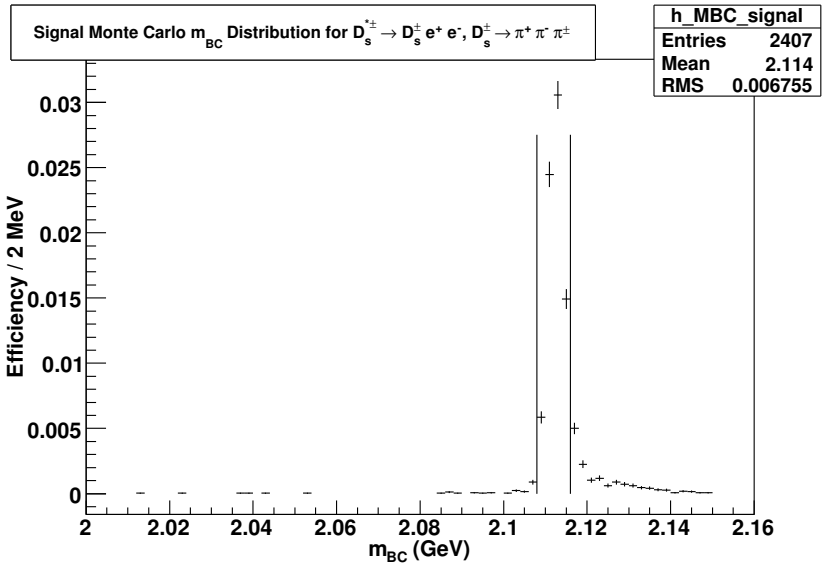

Figure 4.21: Signal efficiency for reconstructing $D_s^{*+} \rightarrow D_s^+ e^+ e^-$ in $D_s^+ \rightarrow \pi^+\pi^-\pi^+$ as represented in the m_{BC} distribution.

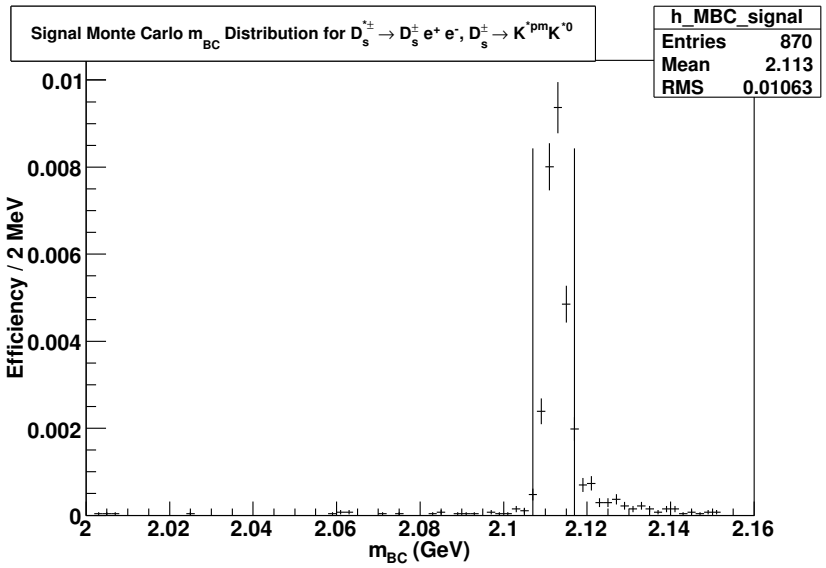

Figure 4.22: Signal efficiency for reconstructing $D_s^{*+} \rightarrow D_s^+ e^+ e^-$ in $D_s^+ \rightarrow K^{*+} K^{*0}$ as represented in the m_{BC} distribution.

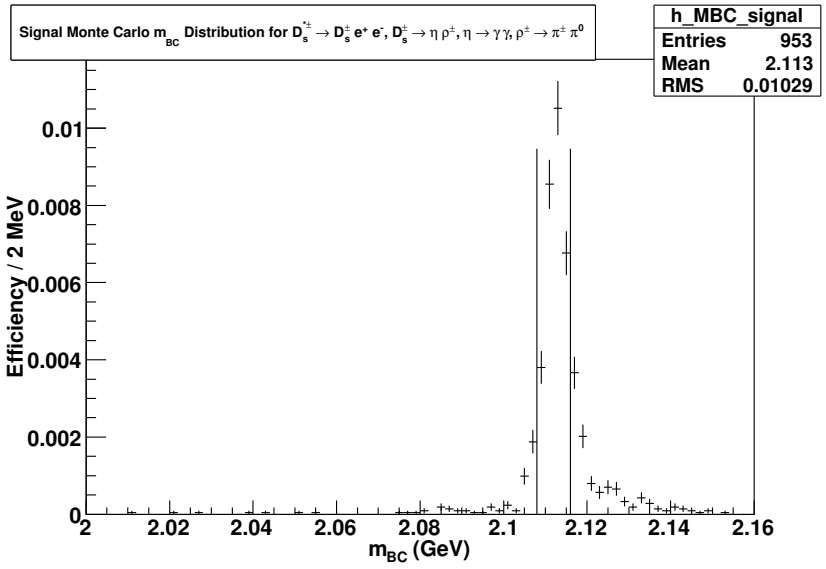

Figure 4.23: Signal efficiency for reconstructing $D_s^{*+} \rightarrow D_s^+ e^+ e^-$ in $D_s^+ \rightarrow \eta\rho^+; \eta \rightarrow \gamma\gamma; \rho^+ \rightarrow \pi^+\pi^0$ as represented in the m_{BC} distribution.

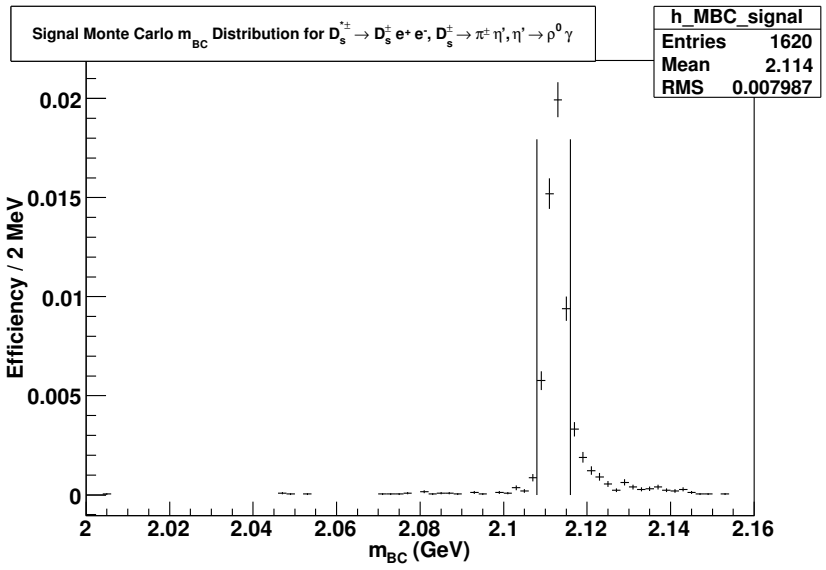

Figure 4.24: Signal efficiency for reconstructing $D_s^{*+} \rightarrow D_s^+ e^+ e^-$ in $D_s^+ \rightarrow \eta' \pi^+; \eta' \rightarrow \rho^0 \gamma$ as represented in the m_{BC} distribution.

4.9 Estimation of Background in the Signal Region of $D_s^{*+} \rightarrow D_s^+ e^+ e^-$

In this section we estimate the number of background events expected in the signal region for each of the hadronic decay modes of the D_s^+. To do this, we study the sidebands of the signal regions in the m_{BC} and δm distributions of Monte Carlo simulated backgrounds and data. When we refer to either of the kinematic distributions, we imply that all other selection criteria have been applied before plotting the distribution.

The signal regions in the m_{BC} and δm distributions are kept blinded in data for this procedure. The regions in the distributions corresponding to values of the m_{BC} and δm greater than or less than the signal region are called the sideband regions. The distributions of the m_{BC} and δm in the sideband regions of data are extrapolated into the signal region using two pre-determined shapes to estimate the number of background events we expect there. The first shape is obtained by fitting the distributions of m_{BC} and δm in the simulated background Monte Carlo. We refer to this as the "MC shape" in the rest of this section. The second shape is determined by fitting the distributions of m_{BC} and δm in the sideband regions of data. This is referred to as the "data shape" in the rest of this section.

The backgrounds are estimated for each of the hadronic decay modes of the D_s^+. However, there are not enough data and Monte Carlo simulation points at the end our selection criteria in the distributions for each of the modes to make a meaningful fit that may be normalized to extract a shape. Therefore, we add the contributions from each mode to produce a summed distribution of m_{BC} and a summed distribution of δm. These distributions are used to determine the data

and MC shapes for the m_{BC} and δm distributions as described in Sections 4.9.1 and 4.9.2 respectively.

The data and MC shapes are then scaled to fit the sideband regions of data in each of the individual modes, for both the m_{BC} and δm distributions. This is described, mode by mode, in the following sub-sections between 4.9.3 and 4.9.11. For each mode, we obtain four numbers for the estimated background from our fits extrapolating into the signal region – one for the data shape in the m_{BC} distribution, one for the MC shape in the m_{BC} distribution, one for the data shape in the δm distribution and one for the MC shape in the δm distribution. The average of the values and statistical uncertainties obtained from the the data and MC shapes in the m_{BC} distribution is used as the primary estimate for the background in each mode. The difference between this value and the average of the data and MC shape numbers for the δm distribution is quoted as the systematic uncertainty of our method for each mode. These numbers are summarized in Section 4.9.12.

Having thus obtained a summary of the background numbers expected for each of the modes, we are in a position to quantify the signal significance that can be achieved for a predicted number of signal events found in a given mode. This is described in Section 4.9.13.

Table 4.23: Maximum likelihood fit parameters for the MC shape in m_{BC} distribution.

Fit Parameters	Value
p_0	-3.91135e+02
p_1	1.91233e+02

Table 4.24: Maximum likelihood fit parameters for the data shape in m_{BC} distribution.

Fit Parameters	Value
p_0	-2.79836e+02
p_1	1.38607e+02

4.9.1 Determining the Shape of the m_{BC} Distribution

The distributions of m_{BC} in data and the Monte Carlo simulations are added up for all modes and presented in Fig. 4.25. The Monte Carlo distribution is fitted to the function given in Eq. 4.18 between 2.060 GeV and 2.155 GeV. It is depicted in the figure as a black curve and shall be called the MC shape. The data is also fitted to the same function, but between the disconnected domains of 2.060 to 2.100 GeV and 2.124 to 2.155 GeV. It is depicted in the figure as a magenta curve and shall be referred to as the data shape. Each sideband region, it may be noted, is separated from the signal region by half the width of the signal region. This is done in order to avoid contaminating the sideband region with signal.

$$y = (p_0 + p_1 x)\sqrt{2.155 - x}/GeV \tag{4.18}$$

The maximum likelihood fit parameters of the MC shape and data shape are tabulated in Tables 4.23 4.24, respectively.

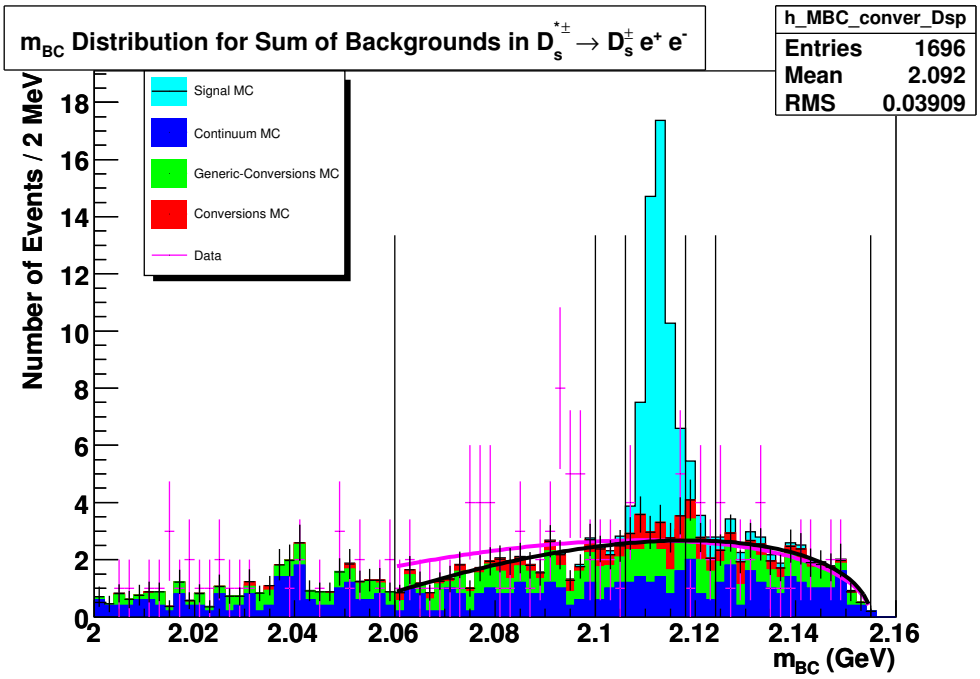

Figure 4.25: Distributions of m_{BC} in Monte Carlo and data. The blue region is distribution of m_{BC} in Continuum MC. On top of that, in green, is stacked the Generic MC with Conversion type events excluded. The Conversion MC is stacked on top of that in red. The black curve is fitted to the sum of the aforementioned background distributions. The Signal MC is stacked on top of the background MC to show roughly what expect to see when we unblind data. Data points, blinded in the signal region, are overlaid in magenta. The magenta curve is fitted to the data in the sideband regions, as described in the text.

Table 4.25: Maximum likelihood fit parameters for the MC shape in δm distribution.

Fit Parameters	Value
p_0	-2.45787e+03
p_1	6.02306e+03
p_2	-2.39666e+03
p_3	1.65951e+03

4.9.2 Determining the Shape of the δm Distribution

As we have done in the case of the m_{BC} distribution, the distributions of δm in data and the Monte Carlo simulations are added up for all modes and presented in Fig. 4.26. However, to further increase the sample sizes, the width of the m_{BC} criterion for each of the modes has been doubled. The Monte Carlo distribution is fitted to the third order Chebyshev polynomial given in Eq. 4.19 between 0.100 GeV and 0.250 GeV. It is depicted in the figure as a black curve and shall be called the MC shape. The data is also fitted to the same function, but between the disconnected domains of 0.1000 to 0.1298 GeV and 0.1578 to 0.2500 GeV. It is depicted in the figure as a magenta curve and shall be referred to as the data shape. Each sideband region, it may be noted, is separated from the signal region by half the width of the signal region.

$$y = p_0 + p_1 T_1 + p_2 T_2 + p_3 T_3 \tag{4.19}$$

The maximum likelihood fit parameters of the MC shape and data shape are tabulated in Tables 4.25 4.26, respectively.

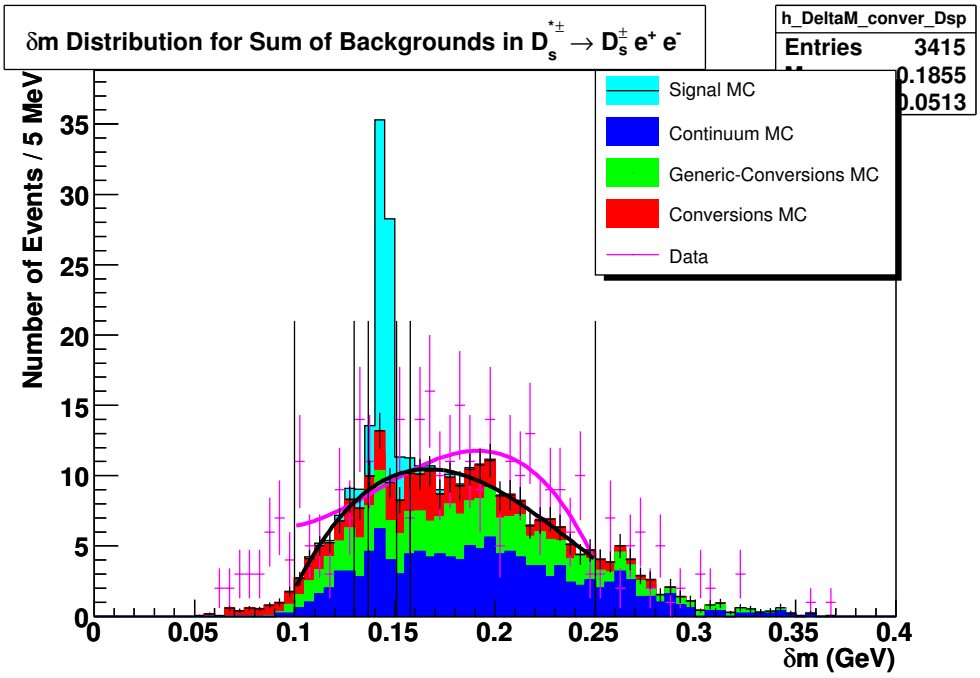

Figure 4.26: Distributions of δm in Monte Carlo and data. The blue region is distribution of δm in Continuum MC. On top of that, in green, is stacked the Generic MC with Conversion type events excluded. The Conversion MC is stacked on top of that in red. The black curve is fitted to the sum of the aforementioned background distributions. The Signal MC is stacked on top of the background MC to show roughly what expect to see when we unblind data. Data points, blinded in the signal region, are overlaid in magenta. The magenta curve is fitted to the data in the sideband regions, as described in the text.

Table 4.26: Maximum likelihood fit parameters for the *Data shape* in δm distribution.

Fit Parameters	Value
p_0	2.38215e+03
p_1	-8.89072e+03
p_2	2.35325e+03
p_3	-2.76871e+03

4.9.3 Estimating the Background in the $D_s^+ \to K^+K^-\pi^+$ Mode

Having found the generic MC shape and data shape in the m_{BC} distribution in Section 4.9.1, we now proceed to scale these shapes to fit data in the sideband regions of the $D_s^+ \to K^+K^-\pi^+$ mode. The signal region is centered at 2.112 GeV with a width of 0.008 GeV. The sideband regions are separated from the signal region by half the width of the signal region. The sideband regions extend from 2.060 to 2.104 GeV and 2.120 to 2.155 GeV. The maximum likelihood fits are displayed in Fig. 4.27 and the values for the scale parameters are presented in Table 4.27.

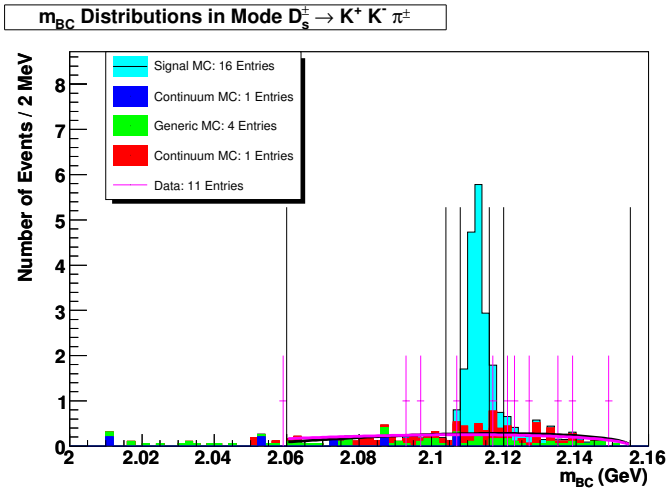

Figure 4.27: The various backgrounds and signal MC expected in the vicinity of the signal region in m_{BC} distribution of the $D_s^+ \to K^+K^-\pi^+$ mode. The data, blinded in the signal region, is overlaid in magenta points. The black and magenta curves are *MC* and *data shapes* scaled by maximum likelihood to the points of data in the sideband regions.

Also, having found the generic *MC* and *data shapes* in the δm distribution in Section 4.9.2, we can now scale those to fit data in the sideband regions of δm in the $D_s^+ \to K^+K^-\pi^+$ mode. The signal region is centered at 0.1438 GeV with a width of 0.012 GeV. The sideband regions are separated from the signal

Table 4.27: Maximum likelihood fit parameters to estimate background in the $D_s^+ \to K^+K^-\pi^+$ mode

Scale for Shape	Value
m_{BC} MC shape	1.03798e-01
δm MC shape	9.35684e-02
m_{BC} data shape	7.75452e-02
δm data shape	6.54773e-02

region by half the width of the signal region. The sideband regions extend from 0.1000 to 0.1318 GeV and 0.1558 to 0.2500 GeV. The maximum likelihood fits are displayed in Fig. 4.28 and the values for the scale parameters are presented in Table 4.27.

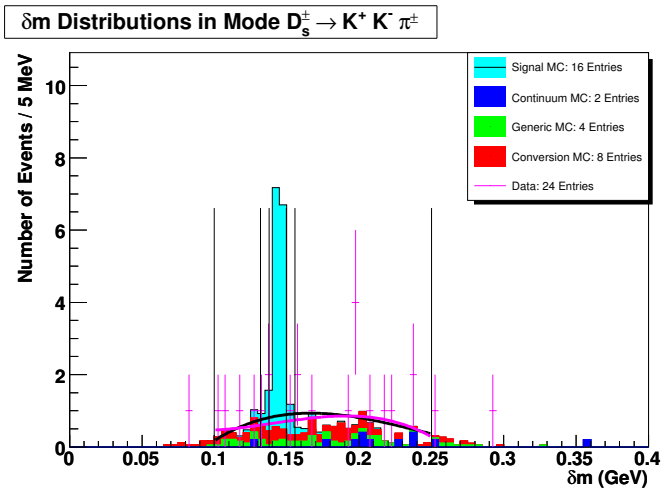

Figure 4.28: The various backgrounds and signal MC expected in the vicinity of the signal region in δm distribution of the $D_s^+ \to K^+K^-\pi^+$ mode. The data, blinded in the signal region, is overlaid in magenta points. The black and magenta curves are *MC* and *data shapes* scaled by maximum likelihood to the points of data in the sideband regions.

The four different fits give us four estimates of the background in the signal

Table 4.28: Estimates of the background in the signal region of the $D_s^+ \to K^+K^-\pi^+$ mode using four fits outlined above.

Mode	m_{BC}		δm	
	MC shape	data shape	MC shape	data shape
$K^+K^-\pi^+$	1.10 ± 0.39	1.00 ± 0.35	2.06 ± 0.49	1.61 ± 0.38

region. These are tabulated in Table 4.28. The uncertainties noted in the table are statistical and are estimated by assuming Poisson statistics on the number of data points in the sidebands. It is calculated as given in Eq. 4.20 where b is the estimated number of background events and $N_{\texttt{side}}$ is the number of events observed in the data sidebands.

$$\Delta b = \frac{b}{\sqrt{N_{\texttt{side}}}} \tag{4.20}$$

4.9.4 Estimating the Background in the $D_s^+ \to K_S K^+$ Mode

The signal region in the m_{BC} distribution of this mode is centered at 2.112 GeV with a width of 0.014 GeV. The sideband regions extend from 2.060 to 2.098 GeV and 2.126 to 2.155 GeV. The maximum likelihood fits are displayed in Fig. 4.29 and the values for the scale parameters are presented in Table 4.29.

The signal region in the δm distribution is centered at 0.1438 GeV with a width of 0.012 GeV. The sideband regions extend from 0.1000 to 0.1318 GeV and 0.1558 to 0.2500 GeV. The maximum likelihood fits are displayed in Fig. 4.30 and the values for the scale parameters are presented in Table 4.29.

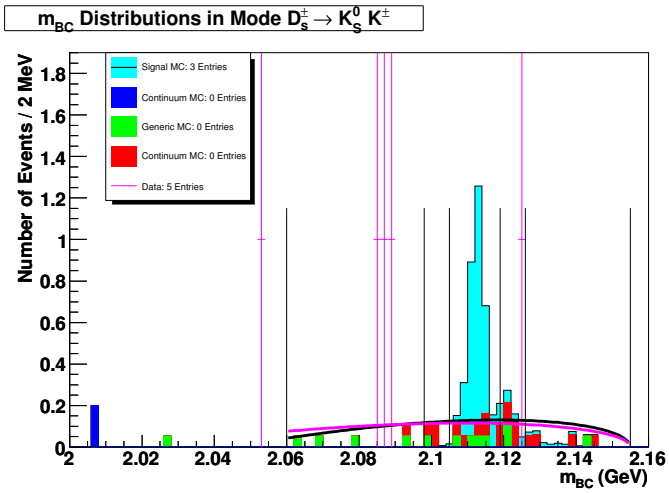

Figure 4.29: The various backgrounds and signal MC expected in the vicinity of the signal region in m_{BC} distribution of the $D_s^+ \to K_S K^+$ mode. The data, blinded in the signal region, is overlaid in magenta points. The black and magenta curves are *MC* and *data shapes* scaled by maximum likelihood to the points of data in the sideband regions.

The four different fits give us four estimates of the background in the signal region. These are tabulated in Table 4.30.

Table 4.29: Maximum likelihood fit parameters to estimate background in the $D_s^+ \to K_S K^+$ mode

Scale for Shape	Value
m_{BC} MC shape	4.86292e-02
δm MC shape	4.29587e-02
m_{BC} data shape	5.25423e-03
δm data shape	4.28206e-03

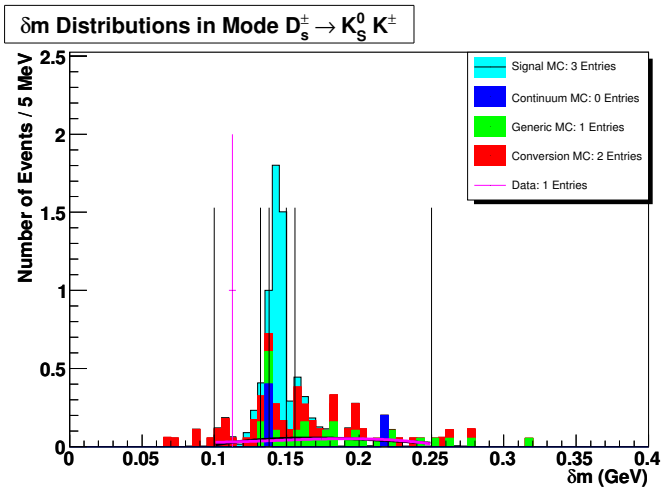

Figure 4.30: The various backgrounds and signal MC expected in the vicinity of the signal region in δm distribution of the $D_s^+ \to K_S K^+$ mode. The data, blinded in the signal region, is overlaid in magenta points. The black and magenta curves are *MC* and *data shapes* scaled by maximum likelihood to the points of data in the sideband regions.

Table 4.30: Estimates of the background in the signal region of the $D_s^+ \to K_S K^+$ mode using four fits outlined above.

Mode	m_{BC}		δm	
	MC shape	data shape	MC shape	data shape
$K_S K^+$	0.90 ± 0.45	0.80 ± 0.40	0.12 ± 0.12	0.10 ± 0.10

4.9.5 Estimating the Background in the $D_s^+ \to \eta\pi^+; \eta \to \gamma\gamma$ Mode

The signal region in the m_{BC} distribution of this mode is centered at 2.112 GeV with a width of 0.016 GeV. The sideband regions extend from 2.060 to 2.096 GeV and 2.128 to 2.155 GeV. The maximum likelihood fits are displayed in Fig. 4.31 and the values for the scale parameters are presented in Table 4.31.

The signal region in the δm distribution of this mode is centered at 0.1438 GeV with a width of 0.016 GeV. The sideband regions extend from 0.1000 to 0.1278 GeV and 0.1598 to 0.2500 GeV. The maximum likelihood fits are displayed in Fig. 4.32 and the values for the scale parameters are presented in Table 4.31.

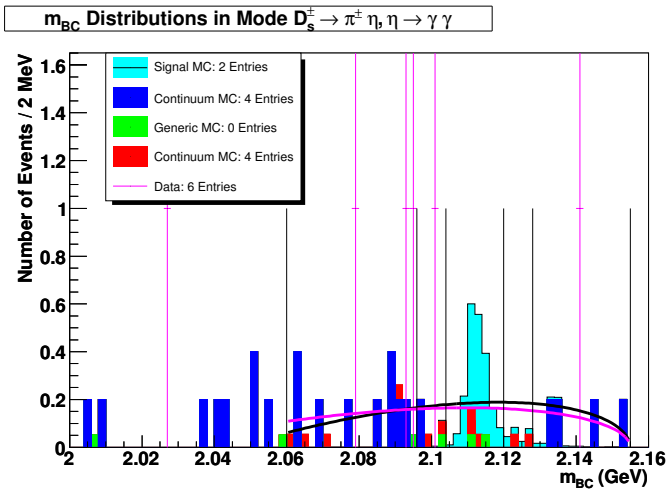

Figure 4.31: The various backgrounds and signal MC expected in the vicinity of the signal region in m_{BC} distribution of the $D_s^+ \to \eta\pi^+; \eta \to \gamma\gamma$ mode. The data, blinded in the signal region, is overlaid in magenta points. The black and magenta curves are *MC* and *data shapes* scaled by maximum likelihood to the points of data in the sideband regions.

The four different fits give us four estimates of the background in the signal region. These are tabulated in Table 4.32.

Table 4.31: Maximum likelihood fit parameters to estimate background in the $D_s^+ \to \eta\pi^+; \eta \to \gamma\gamma$ mode

Scale for Shape	Value
m_{BC} MC shape	7.05486e-02
δm MC shape	6.18039e-02
m_{BC} data shape	3.33356e-02
δm data shape	2.68789e-02

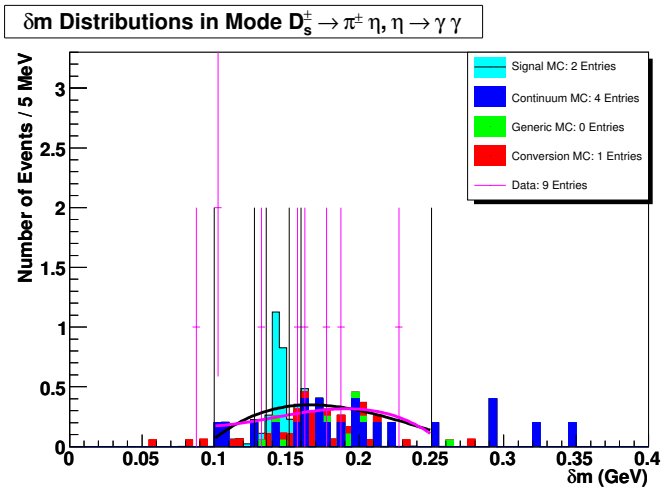

Figure 4.32: The various backgrounds and signal MC expected in the vicinity of the signal region in δm distribution of the $D_s^+ \to \eta\pi^+; \eta \to \gamma\gamma$ mode. The data, blinded in the signal region, is overlaid in magenta points. The black and magenta curves are *MC* and *data shapes* scaled by maximum likelihood to the points of data in the sideband regions.

Table 4.32: Estimates of the background in the signal region of the $D_s^+ \to \eta\pi^+; \eta \to \gamma\gamma$ mode using four fits outlined above.

Mode	m_{BC}		δm	
	MC shape	data shape	MC shape	data shape
$\eta\pi^+$	1.48 ± 0.74	1.32 ± 0.66	1.02 ± 0.39	0.79 ± 0.30

4.9.6 Estimating the Background in the $D_s^+ \to \eta'\pi^+; \eta' \to \pi^+\pi^-\eta; \eta \to \gamma\gamma$ Mode

The signal region in the m_{BC} distribution of this mode is centered at 2.112 GeV with a width of 0.022 GeV. The sideband regions extend from 2.060 to 2.090 GeV and 2.134 to 2.155 GeV. The maximum likelihood fits are displayed in Fig. 4.33 and since no data point fell within our sideband region, no fit could be made.

The signal region in the δm distribution of this mode is centered at 0.1438 GeV with a width of 0.026 GeV. The sideband regions extend from 0.1000 to 0.1178 GeV and 0.1698 to 0.2500 GeV. The maximum likelihood fits are displayed in Fig. 4.34.

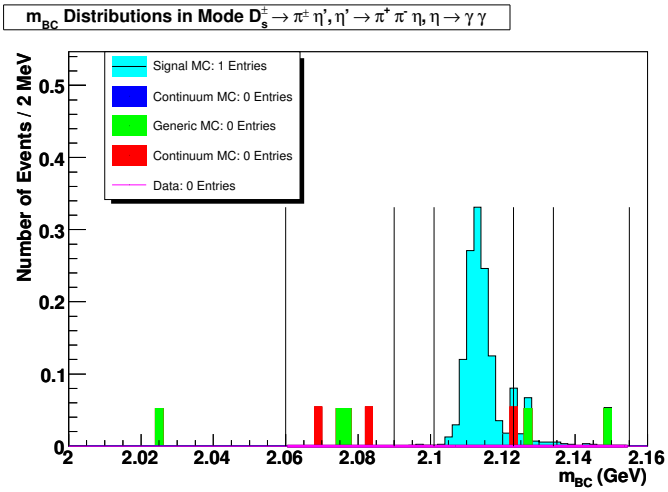

Figure 4.33: The various backgrounds and signal MC expected in the vicinity of the signal region in m_{BC} distribution of the $D_s^+ \to \eta'\pi^+; \eta' \to \pi^+\pi^-\eta; \eta \to \gamma\gamma$ mode. The data, blinded in the signal region, is overlaid in magenta points. The black and magenta curves are *MC* and *data shapes* scaled by maximum likelihood to the points of data in the sideband regions.

Not much could be estimated of the background expected in the signal region. This is tabulated in Table 4.33.

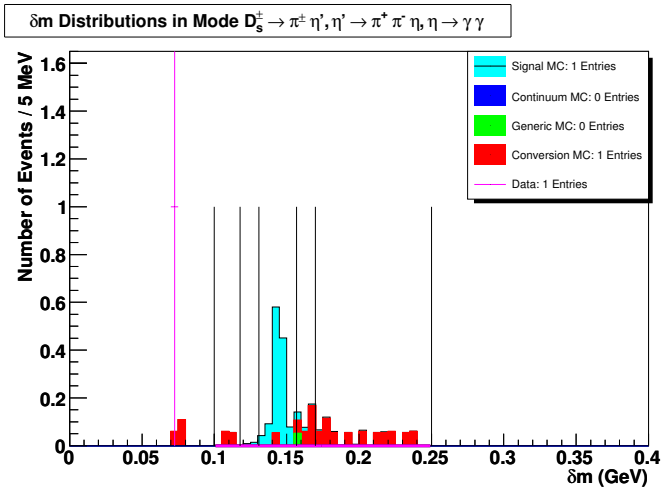

Figure 4.34: The various backgrounds and signal MC expected in the vicinity of the signal region in δm distribution of the $D_s^+ \to \eta'\pi^+; \eta' \to \pi^+\pi^-\eta; \eta \to \gamma\gamma$ mode. The data, blinded in the signal region, is overlaid in magenta points. The black and magenta curves are *MC* and *data shapes* scaled by maximum likelihood to the points of data in the sideband regions.

Table 4.33: Estimates of the background in the signal region of the $D_s^+ \to \eta'\pi^+; \eta' \to \pi^+\pi^-\eta; \eta \to \gamma\gamma$ mode using four fits outlined above.

Mode	m_{BC}		δm	
	MC shape	data shape	MC shape	data shape
$\eta'\pi^+$	0.00 + 0.68	0.00 + 0.59	0.00 + 0.34	0.00 + 0.26

Table 4.34: Maximum likelihood fit parameters to estimate background in the $D_s^+ \to K^+K^-\pi^+\pi^0$ mode

Scale for Shape	Value
m_{BC} MC shape	1.68672e-01
δm MC shape	1.52049e-01
m_{BC} data shape	1.10339e-01
δm data shape	8.99227e-02

4.9.7 Estimating the Background in the $D_s^+ \to K^+K^-\pi^+\pi^0$ Mode

The signal region in the m_{BC} distribution of this mode is centered at 2.112 GeV with a width of 0.008 GeV. The sideband regions extend from 2.060 to 2.104 GeV and 2.120 to 2.155 GeV. The maximum likelihood fits are displayed in Fig. 4.35 and the values for the scale parameters are presented in Table 4.34.

The signal region in the δm distribution of this mode is centered at 0.1438 GeV with a width of 0.012 GeV. The sideband regions extend from 0.1000 to 0.1318 GeV and 0.1558 to 0.2500 GeV. The maximum likelihood fits are displayed in Fig. 4.36 and the values for the scale parameters are presented in Table 4.34.

The four different fits give us four estimates of the background in the signal region. These are tabulated in Table 4.35.

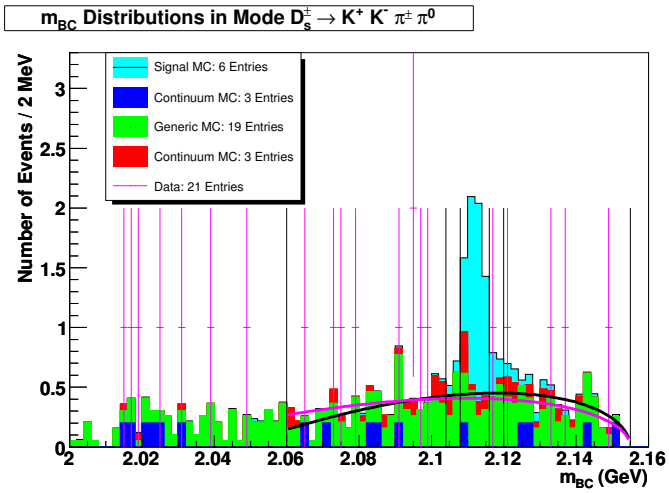

Figure 4.35: The various backgrounds and signal MC expected in the vicinity of the signal region in m_{BC} distribution of the $D_s^+ \to K^+K^-\pi^+\pi^0$ mode. The data, blinded in the signal region, is overlaid in magenta points. The black and magenta curves are *MC* and *data shapes* scaled by maximum likelihood to the points of data in the sideband regions.

Table 4.35: Estimates of the background in the signal region of the $D_s^+ \to K^+K^-\pi^+\pi^0$ mode using four fits outlined above.

Mode	m_{BC}		δm	
	MC shape	data shape	MC shape	data shape
$K^+K^-\pi^+\pi^0$	1.78 ± 0.49	1.63 ± 0.45	2.54 ± 0.54	1.99 ± 0.43

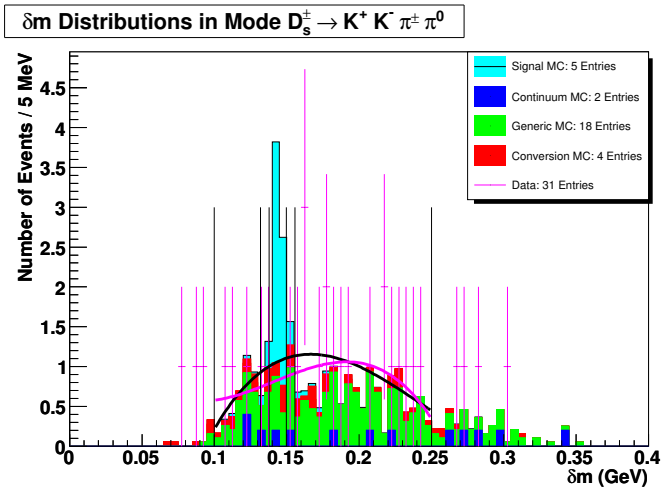

Figure 4.36: The various backgrounds and signal MC expected in the vicinity of the signal region in δm distribution of the $D_s^+ \to K^+K^-\pi^+\pi^0$ mode. The data, blinded in the signal region, is overlaid in magenta points. The black and magenta curves are *MC* and *data shapes* scaled by maximum likelihood to the points of data in the sideband regions.

4.9.8 Estimating the Background in the $D_s^+ \to \pi^+\pi^-\pi^+$ Mode

The signal region in the m_{BC} distribution of this mode is centered at 2.112 GeV with a width of 0.008 GeV. The sideband regions extend from 2.060 to 2.104 GeV and 2.120 to 2.155 GeV. The maximum likelihood fits are displayed in Fig. 4.37 and the values for the scale parameters are presented in Table 4.36.

The signal region in the δm distribution of this mode is centered at 0.1438 GeV with a width of 0.012 GeV. The sideband regions extend from 0.1000 to 0.1318 GeV and 0.1558 to 0.2500 GeV. The maximum likelihood fits are displayed in Fig. 4.38 and the values for the scale parameters are presented in Table 4.36.

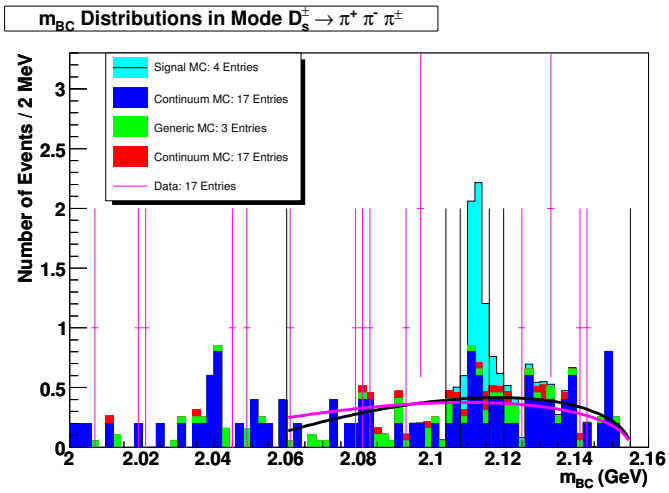

Figure 4.37: The various backgrounds and signal MC expected in the vicinity of the signal region in m_{BC} distribution of the $D_s^+ \to \pi^+\pi^-\pi^+$ mode. The data, blinded in the signal region, is overlaid in magenta points. The black and magenta curves are *MC* and *data shapes* scaled by maximum likelihood to the points of data in the sideband regions.

The four different fits give us four estimates of the background in the signal region. These are tabulated in Table 4.37.

Table 4.36: Maximum likelihood fit parameters to estimate background in the $D_s^+ \to \pi^+\pi^-\pi^+$ mode

Scale for Shape	Value
m_{BC} MC shape	1.55698e-01
δm MC shape	1.40353e-01
m_{BC} data shape	1.05085e-01
δm data shape	8.56409e-02

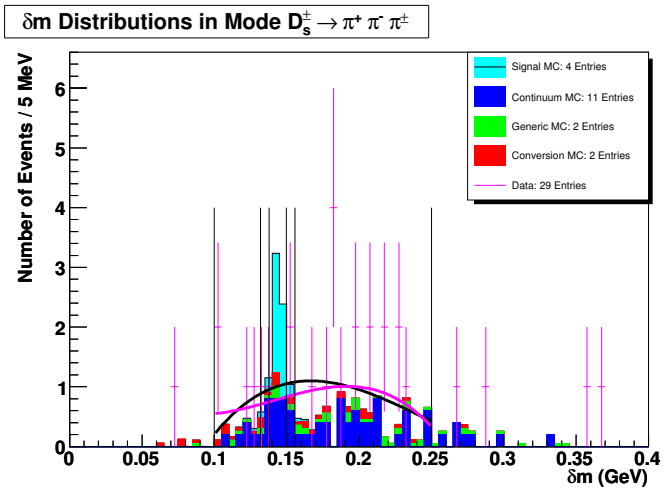

Figure 4.38: The various backgrounds and signal MC expected in the vicinity of the signal region in δm distribution of the $D_s^+ \to \pi^+\pi^-\pi^+$ mode. The data, blinded in the signal region, is overlaid in magenta points. The black and magenta curves are *MC* and *data shapes* scaled by maximum likelihood to the points of data in the sideband regions.

Table 4.37: Estimates of the background in the signal region of the $D_s^+ \to \pi^+\pi^-\pi^+$ mode using four fits outlined above.

Mode	m_{BC}		δm	
	MC shape	data shape	MC shape	data shape
$\pi^+\pi^-\pi^+$	1.64 ± 0.48	1.50 ± 0.43	2.42 ± 0.53	1.90 ± 0.41

4.9.9 Estimating the Background in the $D_s^+ \to K^{*+}K^{*0}; K^{*+} \to K_S^0\pi^+; K^{*0} \to K^-\pi^+$ Mode

The signal region in the m_{BC} distribution of this mode is centered at 2.112 GeV with a width of 0.010 GeV. The sideband regions extend from 2.060 to 2.102 GeV and 2.122 to 2.155 GeV. The maximum likelihood fits are displayed in Fig. 4.39 and the values for the scale parameters are presented in Table 4.38.

The signal region in the δm distribution of this mode is centered at 0.1438 GeV with a width of 0.016 GeV. The sideband regions extend from 0.1000 to 0.1278 GeV and 0.1598 to 0.2500 GeV. The maximum likelihood fits are displayed in Fig. 4.40 and the values for the scale parameters are presented in Table 4.38.

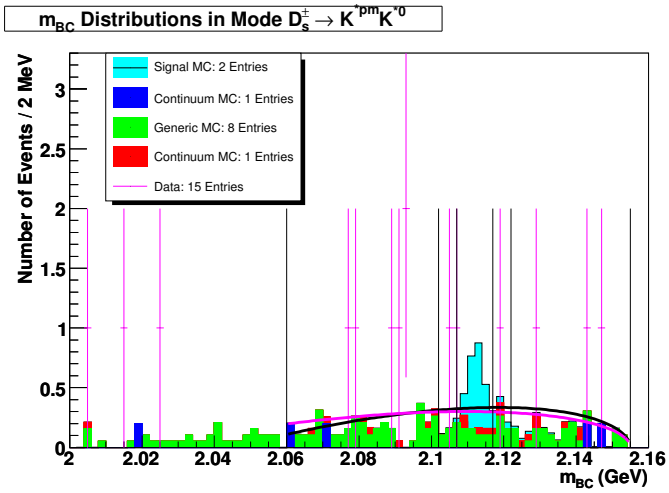

Figure 4.39: The various backgrounds and signal MC expected in the vicinity of the signal region in m_{BC} distribution of the $D_s^+ \to K^{*+}K^{*0}$ mode. The data, blinded in the signal region, is overlaid in magenta points. The black and magenta curves are *MC* and *data shapes* scaled by maximum likelihood to the points of data in the sideband regions.

The four different fits give us four estimates of the background in the signal

Table 4.38: Maximum likelihood fit parameters to estimate background in the $D_s^+ \to K^{*+}K^{*0}$ mode

Scale for Shape	Value
m_{BC} MC shape	1.25192e-01
δm MC shape	1.12174e-01
m_{BC} data shape	7.22271e-02
δm data shape	5.82375e-02

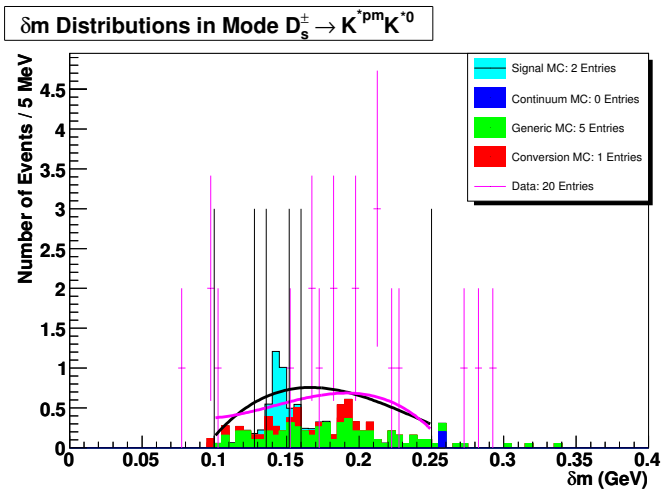

Figure 4.40: The various backgrounds and signal MC expected in the vicinity of the signal region in δm distribution of the $D_s^+ \to K^{*+}K^{*0}$ mode. The data, blinded in the signal region, is overlaid in magenta points. The black and magenta curves are *MC* and *data shapes* scaled by maximum likelihood to the points of data in the sideband regions.

region. These are tabulated in Table 4.39.

Table 4.39: Estimates of the background in the signal region of the $D_s^+ \to K^{*+}K^{*0}$ mode using four fits outlined above.

Mode	m_{BC}		δm	
	MC shape	data shape	MC shape	data shape
$K^{*+}K^{*0}$	1.65 ± 0.55	1.50 ± 0.50	2.21 ± 0.61	1.72 ± 0.48

4.9.10 Estimating the Background in the $D_s^+ \to \eta\rho^+; \eta \to \gamma\gamma; \rho^+ \to \pi^+\pi^0$ Mode

The signal region in the m_{BC} distribution of this mode is centered at 2.112 GeV with a width of 0.008 GeV. The sideband regions extend from 2.060 to 2.104 GeV and 2.120 to 2.155 GeV. The maximum likelihood fits are displayed in Fig. 4.41 and the values for the scale parameters are presented in Table 4.40.

The signal region in the δm distribution of this mode is centered at 0.1438 GeV with a width of 0.010 GeV. The sideband regions extend from 0.1000 to 0.1338 GeV and 0.1538 to 0.2500 GeV. The maximum likelihood fits are displayed in Fig. 4.42 and the values for the scale parameters are presented in Table 4.40.

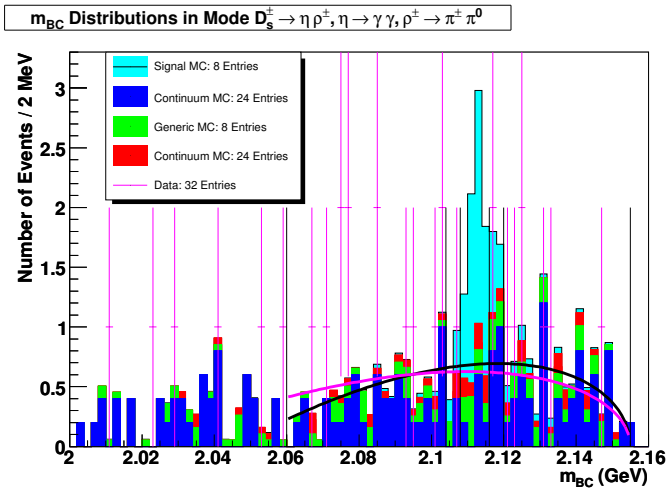

Figure 4.41: The various backgrounds and signal MC expected in the vicinity of the signal region in m_{BC} distribution of the $D_s^+ \to \eta\rho^+; \eta \to \gamma\gamma; \rho^+ \to \pi^+\pi^0$ mode. The data, blinded in the signal region, is overlaid in magenta points. The black and magenta curves are *MC* and *data shapes* scaled by maximum likelihood to the points of data in the sideband regions.

The four different fits give us four estimates of the background in the signal

Table 4.40: Maximum likelihood fit parameters to estimate background in the $D_s^+ \to \eta\rho^+; \eta \to \gamma\gamma; \rho^+ \to \pi^+\pi^0$ mode

Scale for Shape	Value
m_{BC} MC shape	2.59496e-01
δm MC shape	2.33921e-01
m_{BC} data shape	1.65995e-01
δm data shape	1.36454e-01

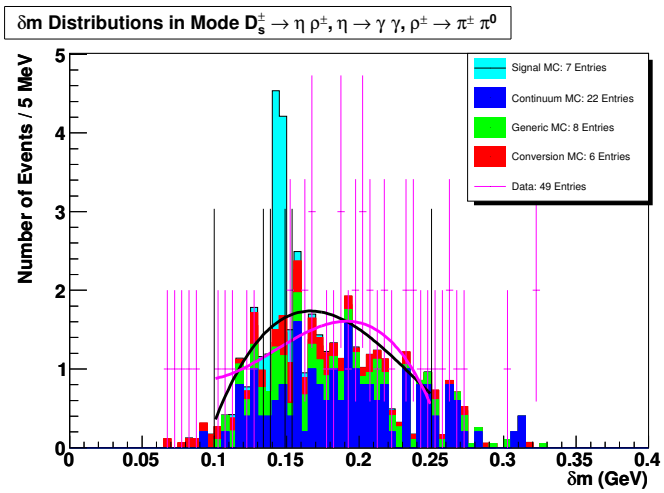

Figure 4.42: The various backgrounds and signal MC expected in the vicinity of the signal region in δm distribution of the $D_s^+ \to \eta\rho^+; \eta \to \gamma\gamma; \rho^+ \to \pi^+\pi^0$ mode. The data, blinded in the signal region, is overlaid in magenta points. The black and magenta curves are *MC* and *data shapes* scaled by maximum likelihood to the points of data in the sideband regions.

region. These are tabulated in Table 4.41.

Table 4.41: Estimates of the background in the signal region of the $D_s^+ \to \eta\rho^+; \eta \to \gamma\gamma; \rho^+ \to \pi^+\pi^0$ mode using four fits outlined above.

Mode	m_{BC}		δm	
	MC shape	data shape	MC shape	data shape
$\eta\rho^+$	2.74 ± 0.61	2.50 ± 0.56	3.19 ± 0.54	2.52 ± 0.43

4.9.11 Estimating the Background in the $D_s^+ \to \eta'\pi^+; \eta' \to \rho^0\gamma$ Mode

The signal region in the m_{BC} distribution of this mode is centered at 2.112 GeV with a width of 0.008 GeV. The sideband regions extend from 2.060 to 2.104 GeV and 2.12 to 2.155 GeV. The maximum likelihood fits are displayed in Fig. 4.43 and the values for the scale parameters are presented in Table 4.42.

The signal region in the δm distribution of this mode is centered at 0.1438 GeV with a width of 0.014 GeV. The sideband regions extend from 0.1000 to 0.1298 GeV and 0.1578 to 0.2500 GeV. The maximum likelihood fits are displayed in Fig. 4.44 and the values for the scale parameters are presented in Table 4.42.

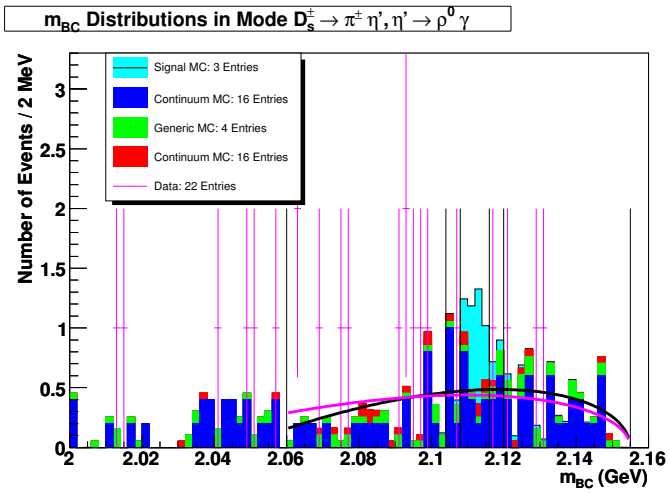

Figure 4.43: The various backgrounds and signal MC expected in the vicinity of the signal region in m_{BC} distribution of the $D_s^+ \to \eta'\pi^+; \eta' \to \rho^0\gamma$ mode. The data, blinded in the signal region, is overlaid in magenta points. The black and magenta curves are *MC* and *data shapes* scaled by maximum likelihood to the points of data in the sideband regions.

The four different fits give us four estimates of the background in the signal

Table 4.42: Maximum likelihood fit parameters to estimate background in the $D_s^+ \to \eta'\pi^+; \eta' \to \rho^0\gamma$ mode

Scale for Shape	Value
m_{BC} MC shape	1.81647e-01
δm MC shape	1.63745e-01
m_{BC} data shape	6.66708e-02
δm data shape	5.37577e-02

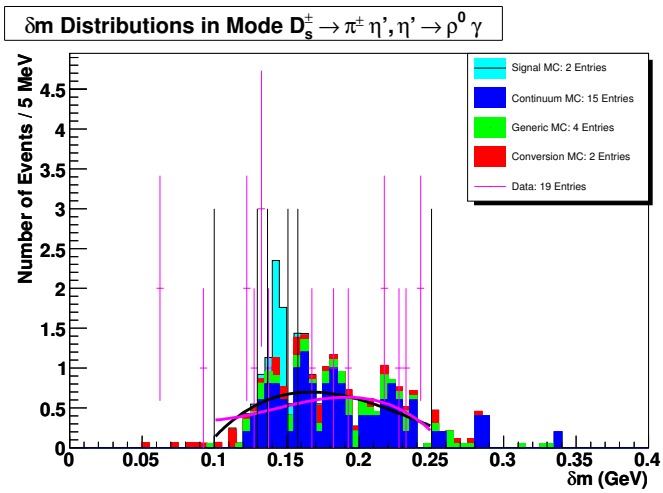

Figure 4.44: The various backgrounds and signal MC expected in the vicinity of the signal region in δm distribution of the $D_s^+ \to \eta'\pi^+; \eta' \to \rho^0\gamma$ mode. The data, blinded in the signal region, is overlaid in magenta points. The black and magenta curves are *MC* and *data shapes* scaled by maximum likelihood to the points of data in the sideband regions.

region. These are tabulated in Table 4.43.

Table 4.43: Estimates of the background in the signal region of the $D_s^+ \to \eta'\pi^+; \eta' \to \rho^0\gamma$ mode using four fits outlined above.

Mode	m_{BC}		δm	
	MC shape	data shape	MC shape	data shape
$\eta'\pi^+$	1.92 ± 0.51	1.75 ± 0.47	1.79 ± 0.52	1.39 ± 0.40

4.9.12 Summary of Estimated Background in the Various Modes

Given that we determined the shape of the m_{BC} distribution in Section 4.9.1 without loosening other cuts, that the distribution itself is less peaked, and that the difference between the predictions of the MC shape and data shape is lower than in the δm distribution, we choose to use the predictions of this distribution as the primary estimate of the backgrounds in each mode.

For each mode, we quote the mean of the MC shape and data shape predictions in the m_{BC} distribution as the estimate of the background we expect in the signal region for that mode. The statistical errors from these two predictions are averaged to obtain the statistical error for this estimate. The absolute value of the difference between this estimate and the mean of the predictions from the two shapes in the δm distribution is quoted as the systematic error. This is tabulated for each mode in Table 4.44

4.9.13 Predicted Signal Significances

It is clear from our optimization and background estimation studies that we do not expect equally significant results from each of the hadronic decay modes we are studying. For instance, it is clear that the $D_s^+ \to K^+K^-\pi^+$ decay mode will contribute more significantly than any other mode due to the marked excess of expected signal yield over the estimated background in its signal region. It therefore behooves us to establish a clear measure of signal significance over estimated background, calculate what signal significance we expect in each mode

Table 4.44: Summary of the estimates for the background in the signal region for all the modes we have studied.

Mode	m_{BC}		δm		Background ± (Stat) ± (Syst)
	MC Shape	*Data Shape*	*MC Shape*	*Data Shape*	
$K^+K^-\pi^+$	1.10 ± 0.39	1.00 ± 0.35	2.06 ± 0.49	1.61 ± 0.38	1.05 ± 0.37 ± 0.79
$K_S K^+$	0.90 ± 0.45	0.80 ± 0.40	0.12 ± 0.12	0.10 ± 0.10	0.85 ± 0.43 ± 0.74
$\eta\pi^+$	1.48 ± 0.74	1.32 ± 0.66	1.02 ± 0.39	0.79 ± 0.30	1.40 ± 0.70 ± 0.49
$\eta'\pi^+; \eta' \to \pi^+\pi^-\eta$	0.00 + 0.68	0.00 + 0.59	0.00 + 0.34	0.00 + 0.26	0.00 + 0.63 + 0.00
$K^+K^-\pi^+\pi^0$	1.78 ± 0.49	1.63 ± 0.45	2.54 ± 0.54	1.99 ± 0.43	1.70 ± 0.47 ± 0.56
$\pi^+\pi^-\pi^+$	1.64 ± 0.48	1.50 ± 0.43	2.42 ± 0.53	1.90 ± 0.41	1.57 ± 0.45 ± 0.59
$K^{*+}K^{*0}$	1.65 ± 0.55	1.50 ± 0.50	2.21 ± 0.61	1.72 ± 0.48	1.58 ± 0.53 ± 0.40
$\eta\rho^+$	2.74 ± 0.61	2.50 ± 0.56	3.19 ± 0.54	2.52 ± 0.43	2.62 ± 0.59 ± 0.23
$\eta'\pi^+; \eta' \to \rho^0\gamma$	1.92 ± 0.51	1.75 ± 0.47	1.79 ± 0.52	1.39 ± 0.40	1.84 ± 0.49 ± 0.25

based on a Monte Carlo estimate of the signal and the background we've estimated from data in section 4.9.12, and converge on a group of modes to unblind together in order to achieve the most significant result.

In order to establish a measure of our signal significance, we assume that the uncertainty in our estimated background is shaped as a Gaussian with a standard deviation equal to the quadrature sum of the statistical and systematic uncertainties in the estimated background. Then we calculate the Poisson probability of such a background fluctuating to higher than the number of events we find in the signal region on unblinding. In effect, we convolute a Gaussian smeared background with a Poisson distribution to model the probability of it fluctuating to the yield we see in data. So, if we call the background estimate b with a standard deviation of σ, and unblind our data to discover n events in the signal region, we may estimate the probability for it to be a fluctuation of the background as P given in Eq. 4.21. We may express this probability, P, in terms

of the number of standard deviations in a Gaussian that one must go out to in order to exclude a region of such probability, and we will use this number as a measure of signal significance.

$$P(b,\sigma,n) = \frac{\sum_{i=n}^{i=\infty} \int_{x=0}^{x=\infty} \frac{x^i}{i!} e^{-[x+\frac{1}{2}(\frac{x-b}{\sigma})^2]} dx}{\int_{x=0}^{x=\infty} e^{-\frac{1}{2}(\frac{x-b}{\sigma})^2} dx} \tag{4.21}$$

The signal significance projected for each individual hadronic decay mode of the D_s^+ is tabulated in Table 4.45. The uncertainty on the estimated background is the quadrature sum of the statistical and systematic uncertainties. The projected signal is estimated by Monte Carlo simulation. As expected, the $D_s^+ \to K^+K^-\pi^+$ mode is projected to give us the highest signal significance among individual modes of 5.40. However, we notice that summing all modes can give us a significance of 6.39, which is higher than any of the individual mode. Therefore, we choose to unblind data in all the modes in order to attain the highest signal significance if we make an observation.

Table 4.45: The projected signal significance expected for each individual hadronic decay mode of the D_s^+, as well as modes combined.

Hadronic Decay Mode	Estimated Background	Projected Signal	Signal Significance
$K^+K^-\pi^+$	1.05 ± 0.37 ± 0.79	13.65	5.40
$K_S K^+$	0.85 ± 0.43 ± 0.74	3.02	1.95
$\eta\pi^+$	1.40 ± 0.70 ± 0.49	1.81	1.25
$\eta'\pi^+; \eta' \to \pi^+\pi^-\eta$	0.00 + 0.63 + 0.00	1.20	0.98
$K^+K^-\pi^+\pi^0$	1.70 ± 0.47 ± 0.56	4.85	2.71
$\pi^+\pi^-\pi^+$	1.57 ± 0.45 ± 0.59	3.75	2.03
$K^{*+}K^{*0}$	1.58 ± 0.53 ± 0.40	1.99	1.65
$\eta\rho^+; \eta \to \gamma\gamma$	2.62 ± 0.59 ± 0.23	5.49	2.59
$\eta'\pi^+; \eta' \to \rho^0\gamma$	1.84 ± 0.49 ± 0.25	2.42	1.52
Combination of All Modes	12.60 ± 2.50 ± 1.08	38.18	6.39

4.10 Signal Yields and Selection Efficiencies for $D_s^{*+} \to D_s^+\gamma$

In this section, we measure the selection efficiencies and yields for $D_s^{*+} \to D_s^+\gamma$ where the D_s^+ decays through the 9 hadronic decays modes we have focused on for this analysis. For all modes, we begin by generating a Monte Carlo sample of $D_s^{*+} \to D_s^+\gamma$ where the D_s^+ is forced to decay through the mode we are investigating while the D_s^- is allowed to decay generically. Selection criteria very similar to those used for the corresponding $D_s^{*+} \to D_s^+e^+e^-$ analysis are used, though with a wider δm selection criterion. The reason for this can be seen from the δm distribution of the $K^+K^-\pi^+$ channel as shown in Fig. 4.45. The low-end tail implies that a loss in the reconstructed energy of photons is expected. This may not be well modeled in Monte Carlo simulations, and to avoid possible discrepancies between simulations and data in that region, a larger region containing the peak is selected. Next, we study the m_{BC} distribution of various backgrounds where the D_s^{*+} is incorrectly reconstructed using the D_s^-. These backgrounds are accounted for in data before calculating the signal yield for each mode, as summarized in Table 4.46 along with the signal selection efficiencies. A similar summary for the generic MC is presented in Table 4.47. Discrepancies between the recovered branching fractions and the value for it programmed into the Generic Monte Carlo simulation result from inconsistencies between the decay models of the D_s^+ in the Generic Monte Carlo and our signal Monte Carlo simulations. The manner in which we measure our signal selection efficiency and evaluate the various backgrounds before we estimate the signal yield is described in detail for the $K^+K^-\pi^+$ mode.

Table 4.46: Signal yields and efficiencies for $D_s^{*+} \to D_s^+\gamma$ from all the modes of decay of the D_s^+ relevant for our measurement of the ratio $B(D_s^{*+} \to D_s^+e^+e^-)/B(D_s^{*+} \to D_s^+\gamma)$. $B(D_s^+ \to i)$ is the known branching fraction for D_s^+ to decay via the i^{th} hadronic mode we are studying. $\epsilon^i_{D_s\gamma}$ is the efficiency of our selection criteria for the mode. $N^i_{D_s\gamma}$ is the signal yield observed for this mode.

i (Decay Mode of D_s^+)	$B(D_s^+ \to i)$	$\epsilon^i_{D_s\gamma}$	$N^i_{D_s\gamma} \pm (stat) \pm (syst)$
$K^+K^-\pi^+$	0.055 ± 0.0028	0.339 ± 0.002	9114 ± 110 ± 201
K_SK^+	0.0149 ± 0.0009	0.2573 ± 0.0004	1902 ± 57 ± 45
$D_s^+ \to \eta\pi^+; \eta \to \gamma\gamma$	0.00621 ± 0.00083	0.3310 ± 0.0015	1037 ± 46 ± 37
$D_s^+ \to \eta'\pi^+; \eta' \to \pi^+\pi^-\eta; \eta \to \gamma\gamma$	0.00666 ± 0.00070	0.2101 ± 0.0013	691 ± 34 ± 40
$D_s^+ \to K^+K^-\pi^+\pi^0$	0.056 ± 0.005	0.1225 ± 0.0010	3592 ± 118 ± 72
$D_s^+ \to \pi^+\pi^-\pi^+$	0.0111 ± 0.0008	0.4583 ± 0.0018	2745 ± 93 ± 52
$D_s^+ \to K^{*+}K^{*0}$	0.0164 ± 0.0012	0.1913 ± 0.0012	1570 ± 74 ± 13
$D_s^+ \to \eta\rho^+; \eta \to \gamma\gamma; \rho^+ \to \pi^+\pi^0$	0.0348 ± 0.0031	0.1839 ± 0.0013	3170 ± 161 ± 313
$D_s^+ \to \eta'\pi^+; \eta' \to \rho^0\gamma$	0.0112 ± 0.0012	0.3171 ± 0.0015	1531 ± 80 ± 122

Table 4.47: Signal yields and efficiencies for $D_s^{*+} \to D_s^+\gamma$ from all the modes of decay of the D_s^+ relevant for our measurement of the ratio $B(D_s^{*+} \to D_s^+e^+e^-)/B(D_s^{*+} \to D_s^+\gamma)$ in Generic Monte Carlo. $B(D_s^+ \to i)$ is the known branching fraction for D_s^+ to decay via the i^{th} hadronic mode we are studying. $\epsilon^i_{D_s\gamma}$ is the efficiency of our selection criteria for the mode. $N^i_{D_s\gamma}$ is the signal yield observed for this mode. $B(D_s^{*+} \to D_s^+\gamma)$ is the branching fraction for $D_s^{*+} \to D_s^+e^+e^-$ inferred from this mode. Error [1] on the inferred branching fraction is the statistical error from the final fit. Error [2] encapsulates the systematic uncertainties from the signal efficiency and the uncertainty in the number of produced generic MC events as described in Section 4.4.1.

i (Mode)	$B(D_s^+ \to i)$	$\epsilon^i_{D_s\gamma}$	$N^i_{D_s\gamma}$	$B(D_s^{*+} \to D_s^+\gamma)$
$K^+K^-\pi^+$	0.0537	0.339 ± 0.002	9364 ± 40	$0.9259 \pm 0.0040^{[1]} \pm 0.0043^{[2]}$
$K_S K^+$	0.01465	0.25727 ± 0.00043	2006 ± 17	$0.9581 \pm 0.0083^{[1]} \pm 0.0018^{[2]}$
$D_s^+ \to \eta\pi^+; \eta \to \gamma\gamma$	0.0061	0.3310 ± 0.0015	998 ± 27	$0.8933 \pm 0.0240^{[1]} \pm 0.0043^{[2]}$
$D_s^+ \to \eta'\pi^+; \eta' \to \pi^+\pi^-\eta; \eta \to \gamma\gamma$	0.00633	0.2101 ± 0.0013	690 ± 11	$0.9341 \pm 0.0149^{[1]} \pm 0.0058^{[2]}$
$D_s^+ \to K^+K^-\pi^+\pi^0$	0.0525	0.1225 ± 0.0010	3178 ± 49	$0.8894 \pm 0.0138^{[1]} \pm 0.0073^{[2]}$
$D_s^+ \to \pi^+\pi^-\pi^+$	0.0103	0.4583 ± 0.0018	2706 ± 43	$1.0327 \pm 0.0162^{[1]} \pm 0.0041^{[2]}$
$D_s^+ \to K^{*+}K^{*0}$	0.01628	0.1913 ± 0.0012	1644 ± 22	$0.9502 \pm 0.0129^{[1]} \pm 0.0058^{[2]}$
$D_s^+ \to \eta\rho^+; \eta \to \gamma\gamma; \rho^+ \to \pi^+\pi^0$	0.0298	0.1839 ± 0.0013	2993 ± 87	$0.9829 \pm 0.0284^{[1]} \pm 0.0070^{[2]}$
$D_s^+ \to \eta'\pi^+; \eta' \to \rho^0\gamma$	0.0111	0.3171 ± 0.0015	1930 ± 45	$0.9886 \pm 0.0231^{[1]} \pm 0.0049^{[2]}$

Table 4.48: Selection criteria for $D_s^{*+} \to D_s^+\gamma$ events where $D_s^+ \to K^+K^-\pi^+$. The δm cut has been widened to accommodate the wider peak for the signal in this distribution.

Selection Criterion	Cut Center ± Width
$m_{D_s^+}$	1.969 ± 0.011 GeV
δm	0.140 ± 0.02 GeV
γ Shower Energy	10 MeV to 2.0 GeV
γ Hot Crystals	None
Tracks Matched to γ	None
γ E9/E25 Unfolded	99 percentile

4.10.1 $D_s^+ \to K^+K^-\pi^+$

We begin with a Monte Carlo signal sample of $D_s^{*+} \to D_s^+\gamma$ events where D_s^+ decays to $K^+K^-\pi^+$ and the D_s^- is allowed to decay generically. The selection criteria applied are tabulated in Table 4.48. Instead of the cuts on Δd_0 and $\Delta\phi_0$, which are applicable to the soft e^+e^- pair, we have some selection criteria on the γ that is kept common across all modes of decay of the D_s^+ and shall not be repeated in subsequent tables of this section. A plot of the δm distribution is presented in Fig. 4.45.

To obtain the selection efficiency using the condition on m_{BC} as our last selection criterion, we produce a plot of the m_{BC} distribution of the signal sample, having applied all other criteria, as shown in Fig. 4.46. For a handle on the shape of the peak in this plot, we produce one more plot – that of m_{BC} where the D_s^+ and the photon are matched to their generated counterparts in the Monte Carlo simulation. This plot, shown in Fig. 4.47, is fitted to a Crystal Ball function of the form given in Eq. 4.22 that has the power law shoulder on the higher

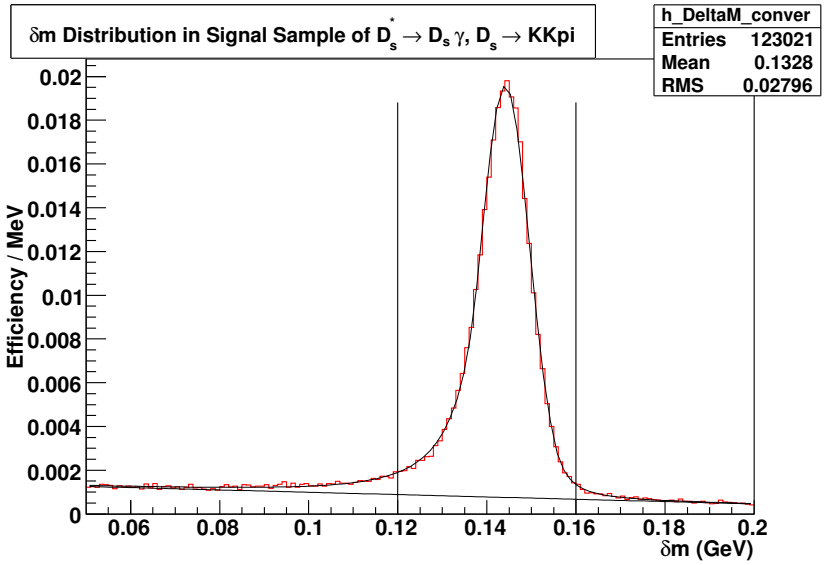

Figure 4.45: Distribution of δm in the signal Monte Carlo sample of $D_s^{*+} \to D_s^+\gamma$ events where $D_s^+ \to K^+K^-\pi^+$. The plot is normalized so as to directly read out the efficiency of the δm selection criterion.

side of the central peak and also contains a wide Gaussian on this shoulder. The shape of this peak is attenuated by a scaling factor and added to a background shape modeled by Eq. 4.23 to fit the m_{BC} distribution of the signal Monte Carlo between 2.08 and 2.15 GeV as shown in 4.46. The signal efficiency of our selection criteria is read off from this plot as the integral of the fit to the data within the marked region minus the background curve within that region.

$$\begin{aligned} f(x;\bar{x_0},\sigma_0,\alpha,n,N_0,\bar{x_1},\sigma_1,N_1) &= N_1 \exp\left(-\frac{(x-\bar{x_1})^2}{2\sigma_1^2}\right) \\ &+ N_0 \cdot \begin{cases} A\cdot\left(B+\frac{x-\bar{x_0}}{\sigma_0}\right)^{-n}, & \text{for} \quad \alpha < \frac{x-\bar{x_0}}{\sigma_0} \\ \exp\left(-\frac{(x-\bar{x_0})^2}{2\sigma_0^2}\right), & \text{for} \quad \frac{x-\bar{x_0}}{\sigma_0} \leq \alpha \end{cases} \end{aligned} \tag{4.22}$$

where

$$A = \left(\frac{n}{\alpha}\right)^n \exp\left(-\frac{\alpha^2}{2}\right),$$

$$B = \frac{n}{\alpha} - \alpha$$

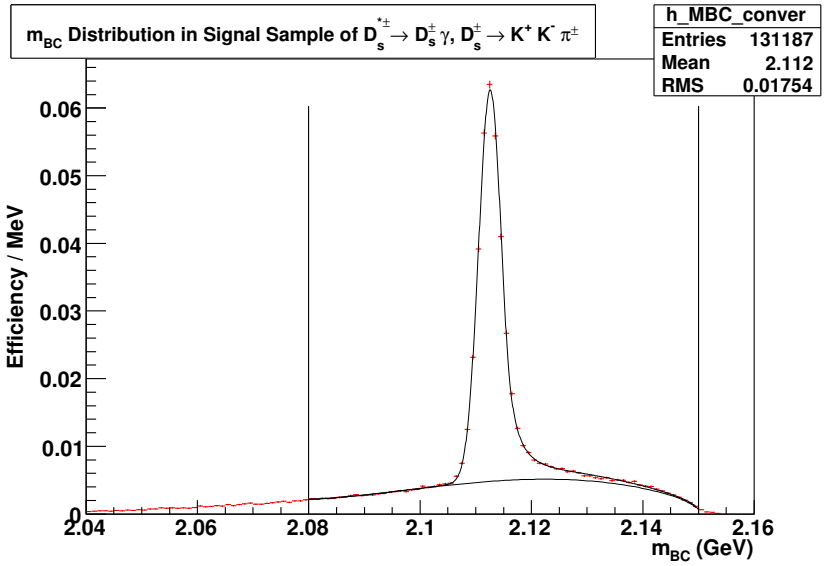

Figure 4.46: Distribution of m_{BC} in the signal Monte Carlo sample of $D_s^{*+} \to D_s^+\gamma$ events where $D_s^+ \to K^+K^-\pi^+$. The plot is normalized so as to directly read out the efficiency of the m_{BC} selection criterion.

$$f(x; x_0, p, C_0, C_1, C_2, C_3) = (C_0 + C_1 x + C_2 x^2 + C_3 x^3)(x - x_0)^p, \quad 0 < p < 1 \qquad (4.23)$$

The m_{BC} distribution in data contains more features than just a signal peak. A structured background emerges from events where our selection criteria reconstructs the D_s^{*+} incorrectly using the D_s^- and the γ. The D_s^- would then have been reconstructed from its decay to $K^+K^-\pi^-$. A Monte Carlo sample where the D_s^{*+} decays to $D_s^+\gamma$ but only the D_s^- is forced to decay to $K^+K^-\pi^-$ is generated to help us model this background in data. For reasons that will soon become clear, this background is decomposed into two components. The first includes cases where the D_s^- and the photon are matched to their generated counterparts in Monte Carlo. The m_{BC} distribution of these events is shown in Fig. 4.48. The second component includes cases where the D_s^- has been matched but the photon failed to match the photon from the D_s^{*+} decay at the generator level of the

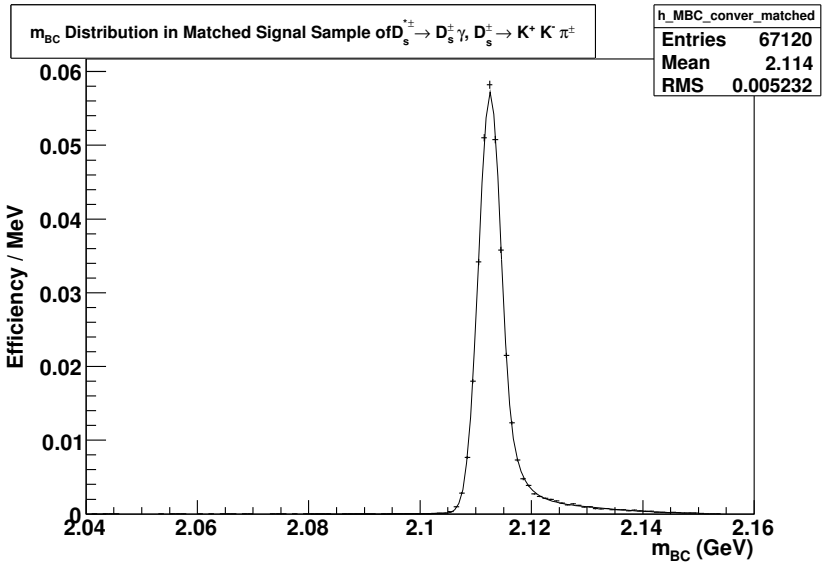

Figure 4.47: Distribution of m_{BC} in the signal Monte Carlo sample of $D_s^{*+} \to D_s^+\gamma$ events where $D_s^+ \to K^+K^-\pi^+$.

Monte Carlo simulation. These events have m_{BC} distributed as shown in Fig. 4.49. These two components are cleft apart and fitted separately in data because there is no reason for such combinatorial backgrounds to maintain the same ratio to one another as modeled in our privately produced Monte Carlo.

Fig. 4.48 is fitted to a function that contains a Crystal Ball shape with the power law on the high side, a wide Gaussian on the high side, and another Gaussian on the lower side of the center of the Crystal Ball as described by Eq. 4.24. The fit is restricted to 2.08 GeV $< m_{BC} <$ 2.15 GeV.

$$
\begin{aligned}
f(x;\bar{x_0},\sigma_0,\alpha,n,N_0,\bar{x_1},\sigma_1,N_1,\bar{x_2},\sigma_2,N_2) &= N_1 \exp\left(-\frac{(x-\bar{x_1})^2}{2\sigma_1^2}\right) \\
&+ N_0 \cdot \left\{ \begin{array}{ll} A\cdot\left(B+\frac{x-\bar{x_0}}{\sigma_0}\right)^{-n}, & \text{for} \quad \alpha < \frac{x-\bar{x_0}}{\sigma_0} \\ \exp\left(-\frac{(x-\bar{x_0})^2}{2\sigma_0^2}\right), & \text{for} \quad \frac{x-\bar{x_0}}{\sigma_0} \leq \alpha \end{array} \right\}
\end{aligned}
$$

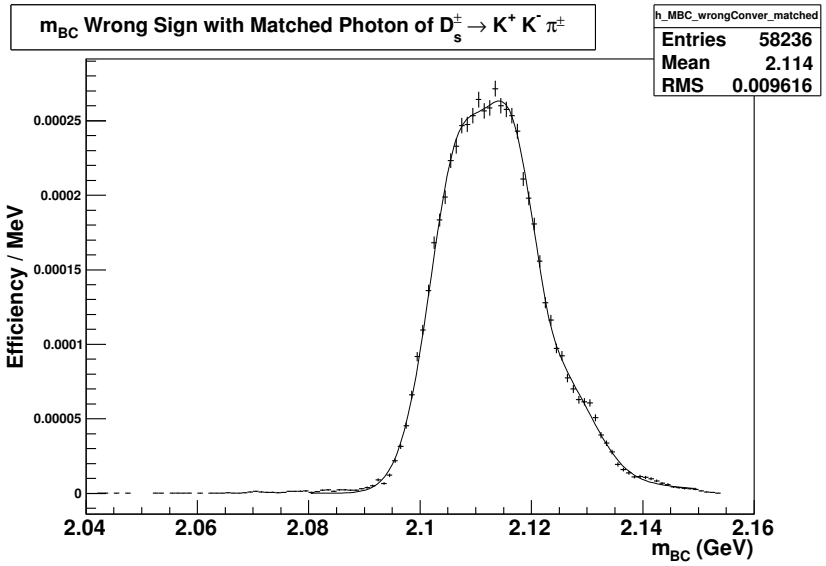

Figure 4.48: Combinatorial background structured in the m_{BC} distribution consisting of events where the D_s^{*+} has been reconstructed out of the D_s^- and the γ, and where both the D_s^- and the γ have been matched to their generated counterparts in the Monte Carlo simulation. This distribution has been fitted to a shape described by Eq. 4.24.

$$+ \quad N_2 \exp\left(-\frac{(x-\bar{x_2})^2}{2\sigma_2^2}\right) \tag{4.24}$$

where

$$A = \left(\frac{n}{\alpha}\right)^n \exp\left(-\frac{\alpha^2}{2}\right),$$

$$B = \frac{n}{\alpha} - \alpha$$

Fig. 4.49 is fitted to a function that contains a Crystal Ball centered around the higher edge of the trapezoidal shape with the power law on the higher side of the Gaussian, and continued analytically on the lower side with a straight line as described by Eq. 4.25. The fit is restricted to 2.08GeV $< m_{BC} <$ 2.15GeV

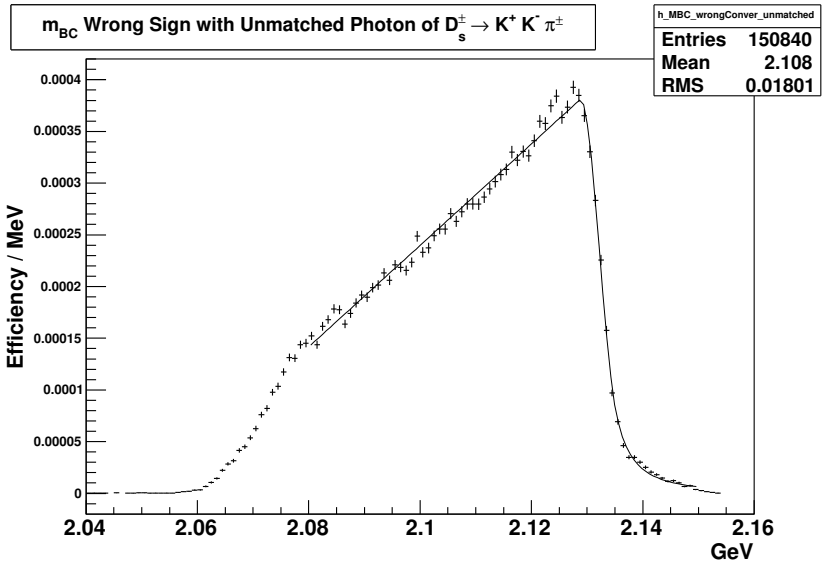

Figure 4.49: Combinatorial background structured in the m_{BC} distribution consisting of events where the D_s^{*+} has been reconstructed out of the D_s^- and the γ, and the D_s^- has been matched to its generated counterpart but the γ has failed to match the photon from the D_s^{*+} decay at the generator level of the Monte Carlo simulation. This distribution has been fitted to a shape described by Eq. 4.25.

$$f(x;\bar{x},\sigma,\alpha,n,\beta,N) = N_0 \cdot \left\{ \begin{array}{c} A\cdot\left(B+\frac{x-\bar{x}}{\sigma}\right)^{-n}, \quad \text{for} \quad \alpha < \frac{x-\bar{x}}{\sigma} \\ \exp\left(-\frac{(x-\bar{x})^2}{2\sigma^2}\right), \quad \text{for} \quad \beta \geq \frac{x-\bar{x}}{\sigma} \leq \alpha \\ C + D\frac{x-\bar{x}}{\sigma}, \quad \text{for} \quad \frac{x-\bar{x}}{\sigma} < \beta \end{array} \right\} \tag{4.25}$$

where

$$A = \left(\frac{n}{\alpha}\right)^n \exp\left(-\frac{\alpha^2}{2}\right),$$

$$B = \frac{n}{\alpha} - \alpha,$$

$$C = \left(1+\frac{\beta^2}{\sigma^2}\right)\exp\left(-\frac{\beta^2}{2\sigma^2}\right),$$

$$D = \frac{-\beta}{\sigma^2}\exp\left(-\frac{\beta^2}{2\sigma^2}\right)$$

Having established the shapes of the signal and various backgrounds, we first study the m_{BC} distribution of the Generic Monte Carlo sample to see how well our fits fare in reproducing the branching fraction for $B(D_s^{*+} \to D_s^+\gamma)$ that had been programmed into the simulation. The plot of m_{BC} and the fits of the signal and various backgrounds to it are presented in Fig. 4.50. The lowest curve is a function of the form given in Eq. 4.23 that models the continuum and featureless combinatorial backgrounds. The curve above that is a scaled version of the shape fitted to the plot in Fig. 4.48. Above that is a scaled version of the shape fitted to the plot in Fig. 4.49. On top of these backgrounds lies the signal peak, which is a scaled version of the shape fitted to Fig. 4.47. The fit is restricted to the range 2.08 GeV $< m_{BC} <$ 2.15 GeV. The signal yield is measured by the integral of the highest curve that includes the signal peak minus the integral of all the backgrounds between 2.08 and 2.15 GeV. This may be combined with the efficiency of our selection criteria $\epsilon^i_{D_s\gamma}$, the integrated luminosity of data being used L, the cross section for producing $D_s^{*\pm}D_s^{\mp}$ (values given in Section 4.4) and the value for $B(D_s^+ \to K^+K^-\pi^+)$ programmed into the simulation to give us an estimate for $B(D_s^{*+} \to D_s^+\gamma)$ as tabulated in Table 4.49. We find the thus estimated value for $B(D_s^{*+} \to D_s^+\gamma)$ equal to 0.9259 ± 0.0058 to be 2.8σ away from the programmed value of 0.942 in the Monte Carlo simulation.

We present the distribution of m_{BC} in data in Fig. 4.51. It is fitted to the signal and background shapes as described in the previous paragraph. The ratio of amplitudes for the signal peak shape to the shape for the incorrectly reconstructed D_s^{*+} with the photon strictly unmatched (second curve from the top) is carried over as a constant from the fit to the generic MC. A systematic uncertainty is evaluated by repeating this fit without such constraints on the ratio. The signal yield is measured by subtracting the integral of all the backgrounds

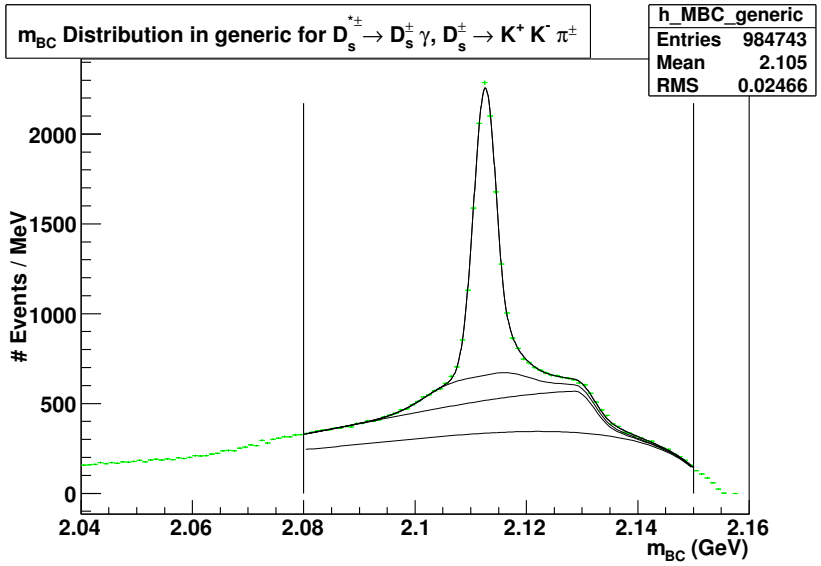

Figure 4.50: Distribution of m_{BC} of $D_s^{*+} \to D_s^+\gamma$ events where $D_s^+ \to K^+K^-\pi^+$ in 586 pb^{-1} of Generic Monte Carlo.

Table 4.49: $\epsilon^i_{D_s\gamma}$ is the efficiency of our selection criteria for the mode. $N^i_{D_s\gamma}$ is the signal yield observed in generic Monte Carlo for this mode. $B(D_s^{*+} \to D_s^+\gamma)$ is the branching fraction for $D_s^{*+} \to D_s^+e^+e^-$ inferred from this mode. Error [1] on the inferred branching fraction is the statistical error from the final fit. Error [2] encapsulates the systematic uncertainties from the signal efficiency and the uncertainty in the number of produced generic MC events.

i (Decay Mode of D_s^+)	$B(D_s^+ \to i)$	$\epsilon^i_{D_s\gamma}$	$N^i_{D_s\gamma}$	$B(D_s^{*+} \to D_s^+\gamma)$ Inferred
$K^+K^-\pi^+$	0.0537	0.339 ± 0.002	9364 ± 40	0.9259 ± 0.0040[1] ± 0.0043[2]

from the integral of the total fit between 2.08 and 2.15 GeV, as described earlier. We do not present any calculation of the branching fraction $B(D_s^{*+} \to D_s^+\gamma)$ as we have no measure of the systematic uncertainty arising from the reconstruction of the D_s^+. We expect this systematic uncertainty to cancel in our final calculation of the ratio of branching fractions $B(D_s^{*+} \to D_s^+e^+e^-)/B(D_s^{*+} \to D_s^+\gamma)$. Arriving at a result for this ratio will only require us to report the signal yields and efficiencies for $D_s^{*+} \to D_s^+\gamma$ for each of the decay modes of the D_s^+.

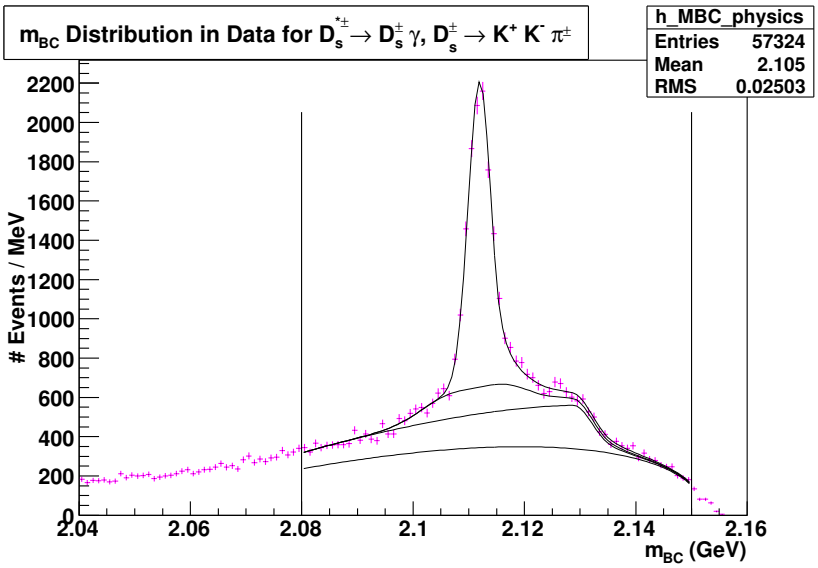

Figure 4.51: Distribution of m_{BC} of $D_s^{*+} \to D_s^+\gamma$ events where $D_s^+ \to K^+K^-\pi^+$ in 586 pb^{-1} of data.

Table 4.50: $\epsilon^i_{D_s\gamma}$ is the efficiency of our selection criteria for the mode. $N^i_{D_s\gamma}$ is the signal yield in data observed for this mode.

i (Decay Mode of D_s^+)	$B(D_s^+ \to i)$	$\epsilon^i_{D_s\gamma}$	$N^i_{D_s\gamma} \pm (stat) \pm (syst)$
$K^+K^-\pi^+$	0.055 ± 0.0028	0.339 ± 0.002	9114 ± 110 ± 201

Table 4.51: Selection criteria for $D_s^{*+} \to D_s^+\gamma$ events where $D_s^+ \to K_S K^+$. The δm cut has been widened to accomodate the wider peak for the signal in this distribution.

Selection Criterion	Cut Center ± Width
$m_{D_s^+}$	1.969 ± 0.008 GeV
δm	0.140 ± 0.02 GeV

4.10.2 $D_s^+ \to K_S K^+$

We begin with a Monte Carlo signal sample of $D_s^{*+} \to D_s^+\gamma$ events where $D_s^+ \to K_S K^+$ and the D_s^- is allowed to decay generically. The selection criteria applied are tabulated in Table 4.51. Fig. 4.52 depicts the δm distribution of this signal sample and the region selected by our criterion.

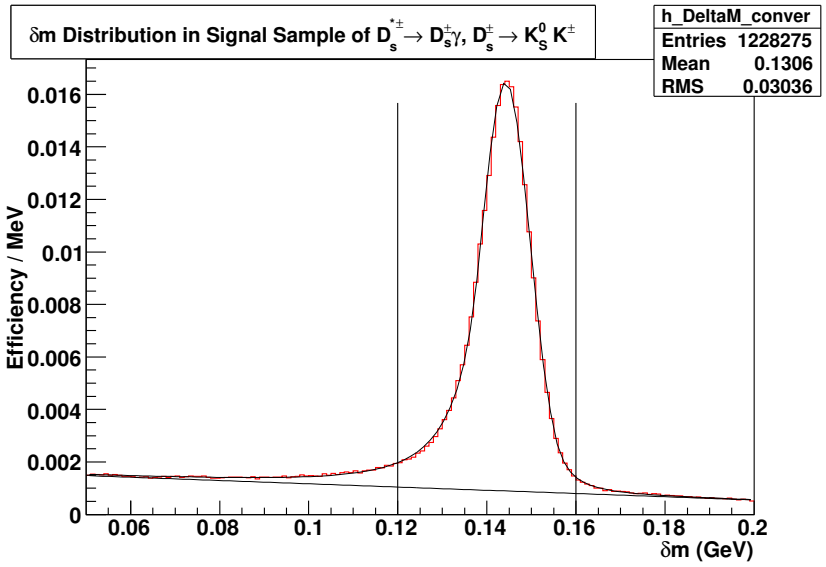

Figure 4.52: Distribution of δm in the signal Monte Carlo sample of $D_s^{*+} \to D_s^+\gamma$ events where $D_s^+ \to K_S K^+$. The plot is normalized so as to directly read out the efficiency of the δm selection criterion.

To obtain the selection efficiency using the condition on m_{BC} as our last selection criterion, we produce a plot of the m_{BC} distribution of the signal sample,

having applied all other criteria, as shown in Fig. 4.53. We extract the shape of the peak from the plot of m_{BC} where the D_s^+ and the photon are matched to their generated counterparts in the Monte Carlo simulation as shown in Fig. 4.54. The equations that parameterize all fits and the range they are fitted in are identical to those used in the $K^+K^-\pi^+$ mode.

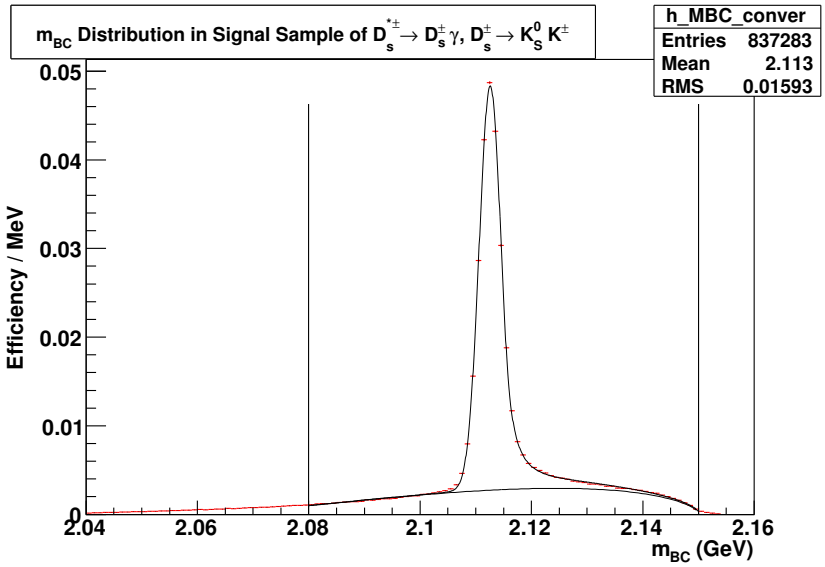

Figure 4.53: Distribution of m_{BC} in the signal Monte Carlo sample of $D_s^{*+} \to D_s^+\gamma$ events where $D_s^+ \to K_S K^+$. The plot is normalized so as to directly read out the efficiency of the m_{BC} selection criterion.

Structured backgrounds arising from incorrectly reconstructed D_s^{*+} are simulated as done previously for the $K^+K^-\pi^+$ mode. Fig. 4.55 shows the structure of the D_s^- matched and photon matched background, and our fit to parameterize this shape. The background with the D_s^- matched and a photon that failed matching is shown in Fig. 4.56 along with our fit to parameterize the shape.

As a check on how well our background and signal estimation performs, we present the overall fit to generic MC, as described for the $K^+K^-\pi^+$ mode, in Fig. 4.57. Our measurement of the signal selection efficiency and the signal yield

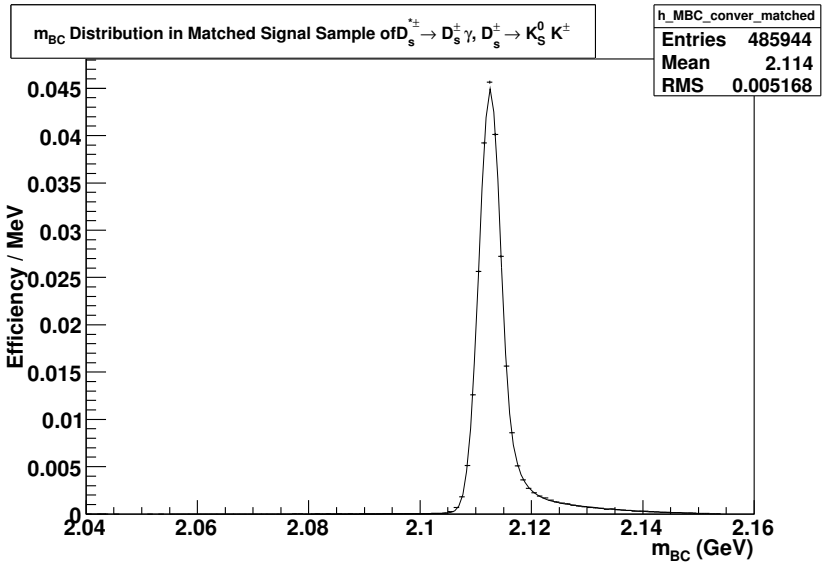

Figure 4.54: Distribution of m_{BC} in the signal Monte Carlo sample of $D_s^{*+} \to D_s^+\gamma$ events where $D_s^+ \to K_S K^+$.

Table 4.52: $\epsilon^i_{D_s\gamma}$ is the efficiency of our selection criteria for the mode. $N^i_{D_s\gamma}$ is the signal yield in generic Monte Carlo observed for this mode. $B(D_s^{*+} \to D_s^+\gamma)$ is the branching fraction for $D_s^{*+} \to D_s^+ e^+ e^-$ inferred from this mode. Error [1] on the inferred branching fraction is the statistical error from the final fit. Error [2] encapsulates the systematic uncertainties from the signal efficiency and the uncertainty in the number of produced generic MC events.

i (Decay Mode of D_s^+)	$B(D_s^+ \to i)$	$\epsilon^i_{D_s\gamma}$	$N^i_{D_s\gamma}$	$B(D_s^{*+} \to D_s^+\gamma)$ Inferred
$K_S K^+$	0.01465	0.25727 ± 0.00043	2006 ± 17	$0.9581 \pm 0.0083^{[1]} \pm 0.0018^{[2]}$

is presented in Table 4.52. We find the thus estimated value for $B(D_s^{*+} \to D_s^+\gamma)$ equal to 0.9616 ± 0.0085 to be 2.3σ away from the programmed value of 0.942 in the Monte Carlo simulation.

We present the distribution of m_{BC} in data and our fits to estimate the signal yield over the backgrounds, as described for the $K^+K^-\pi^+$ mode, in Fig. 4.51. Our measurements of the signal efficiency and signal yield are presented in Table

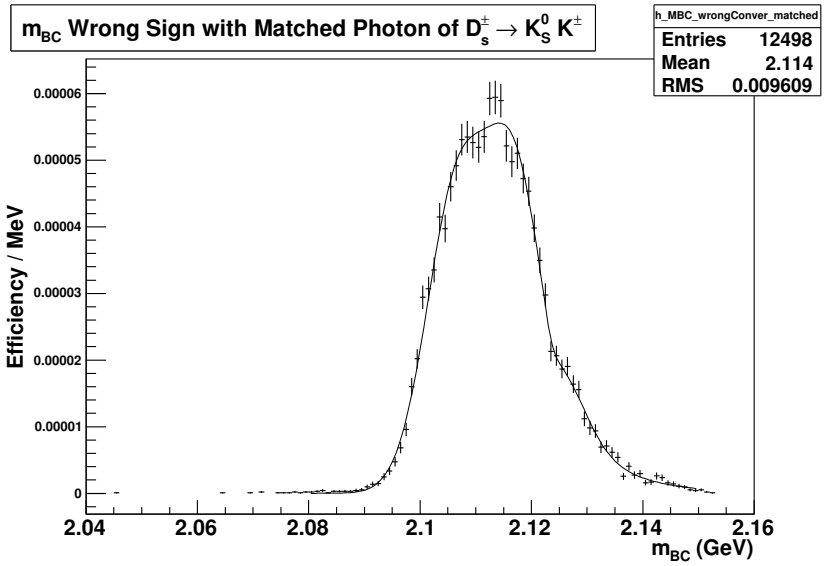

Figure 4.55: Combinatorial background in the m_{BC} distribution consisting of events where the D_s^{*+} has been reconstructed out of the D_s^- and the γ, and where both the D_s^- and the γ have been matched to their generated counterparts in the Monte Carlo simulation. This distribution has been fitted to a shape described by Eq. 4.24.

Table 4.53: $\epsilon^i_{D_s\gamma}$ is the efficiency of our selection criteria for the mode. $N^i_{D_s\gamma}$ is the signal yield in data observed for this mode.

i (Decay Mode of D_s^+)	$B(D_s^+ \to i)$	$\epsilon^i_{D_s\gamma}$	$N^i_{D_s\gamma}$
$K_S K^+$	0.0149 ± 0.0009	0.2573 ± 0.0004	1902 ± 57 ± 45

4.53.

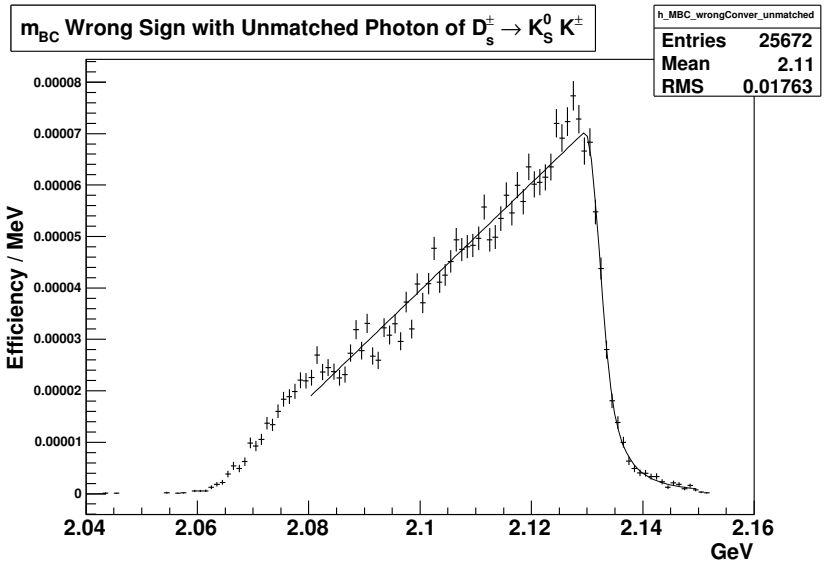

Figure 4.56: Combinatorial background structured in the m_{BC} distribution consisting of events where the D_s^{*+} has been reconstructed out of the D_s^- and the γ, and the D_s^- has been matched to its generated counterpart but the γ has failed to match the photon from the D_s^{*+} decay at the generator level of the Monte Carlo simulation. This distribution has been fitted to a shape described by Eq. 4.25.

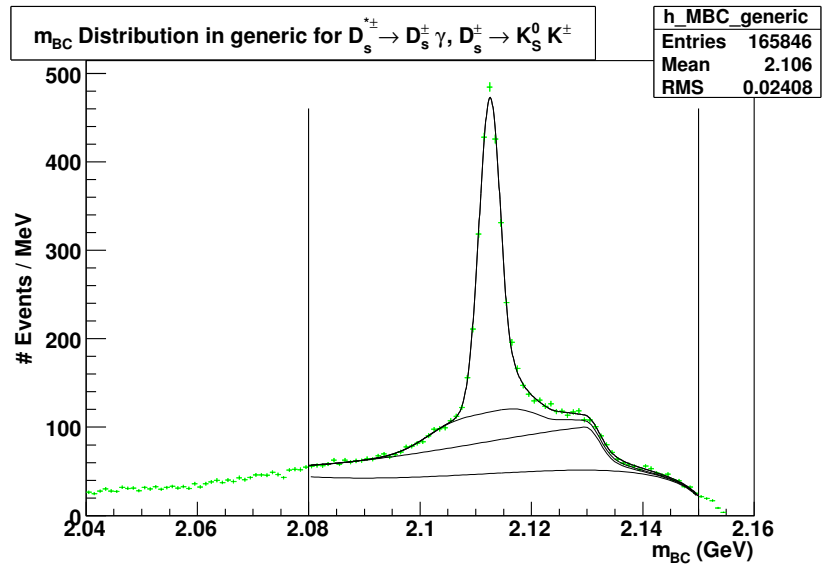

Figure 4.57: Distribution of m_{BC} of $D_s^{*+} \to D_s^+\gamma$ events where $D_s^+ \to K_S K^+$ in 586 pb^{-1} of Generic Monte Carlo.

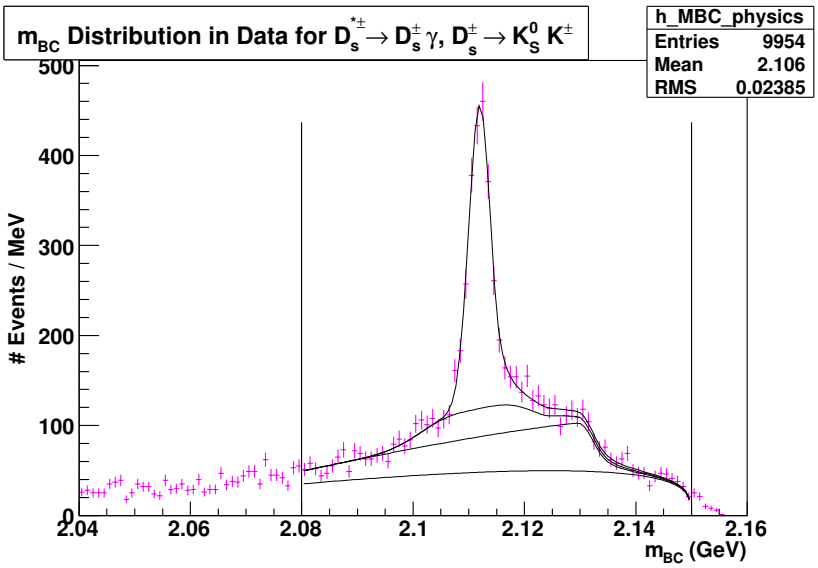

Figure 4.58: Distribution of m_{BC} of $D_s^{*+} \to D_s^+\gamma$ events where $D_s^+ \to K_S K^+$ in 586 pb^{-1} of data.

Table 4.54: Selection criteria for $D_s^{*+} \to D_s^+\gamma$ events where $D_s^+ \to \eta\pi^+; \eta \to \gamma\gamma$. The δm cut has been widened to accomodate the wider peak for the signal in this distribution.

Selection Criterion	Cut Center ± Width
$m_{D_s^+}$	1.969 ± 0.016 GeV
δm	0.140 ± 0.02 GeV

4.10.3 $D_s^+ \to \eta\pi^+; \eta \to \gamma\gamma$

We begin with a Monte Carlo signal sample of $D_s^{*+} \to D_s^+\gamma$ events where $D_s^+ \to \eta\pi^+; \eta \to \gamma\gamma$ and the D_s^- is allowed to decay generically. The selection criteria applied are tabulated in Table 4.54. Fig. 4.59 depicts the δm distribution of this signal sample and the region selected by our criterion.

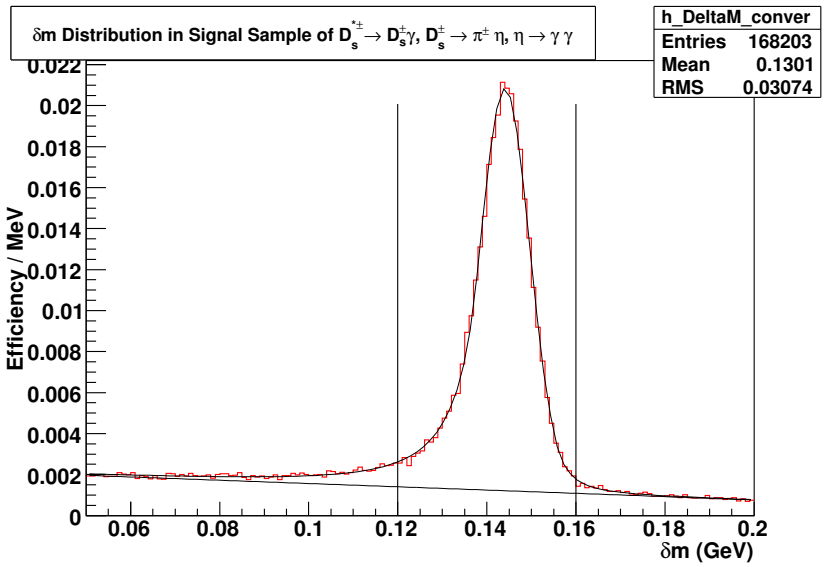

Figure 4.59: Distribution of δm in the signal Monte Carlo sample of $D_s^{*+} \to D_s^+\gamma$ events where $D_s^+ \to \eta\pi^+; \eta \to \gamma\gamma$. The plot is normalized so as to directly read out the efficiency of the δm selection criterion.

To obtain the selection efficiency using the condition on m_{BC} as our last se-

lection criterion, we produce a plot of the m_{BC} distribution of the signal sample, having applied all other criteria, as shown in Fig. 4.60. We extract the shape of the peak from the plot of m_{BC} where the D_s^+ and the photon are matched to their generated counterparts in the Monte Carlo simulation as shown in Fig. 4.61. The equations that parameterize all fits and the range they are fitted in are identical to those used in the $K^+K^-\pi^+$ mode.

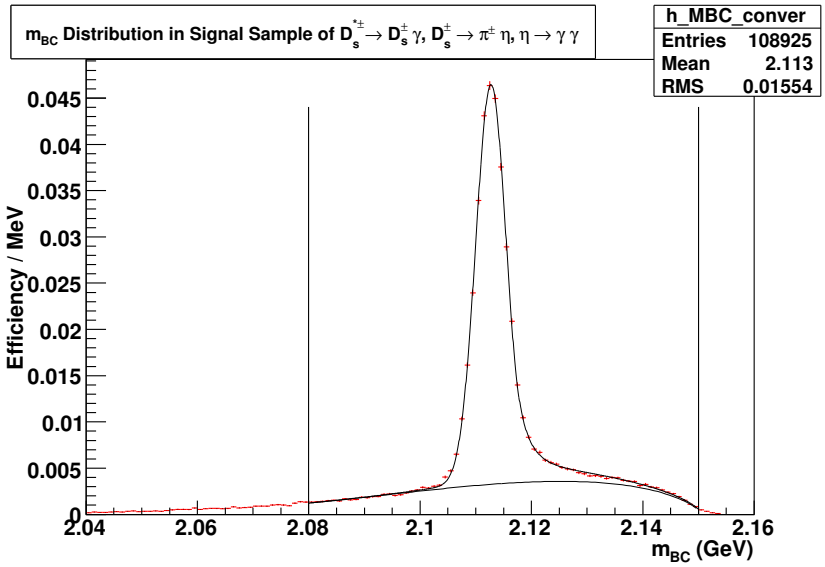

Figure 4.60: Distribution of m_{BC} in the signal Monte Carlo sample of $D_s^{*+} \to D_s^+\gamma$ events where $D_s^+ \to \eta\pi^+; \eta \to \gamma\gamma$. The plot is normalized so as to directly read out the efficiency of the m_{BC} selection criterion from the area under the fit within the signal region.

Structured backgrounds arising from incorrectly reconstructed D_s^{*+} are simulated as done previously for the $K^+K^-\pi^+$ mode. Fig. 4.62 shows the structure of the D_s^- matched and photon matched background, and our fit to parameterize this shape. The background with the D_s^- matched and a photon that failed matching is shown in Fig. 4.63 along with our fit to parameterize the shape.

As a check on how well our background and signal estimation performs, we present the overall fit to generic MC, as described for the $K^+K^-\pi^+$ mode, in Fig.

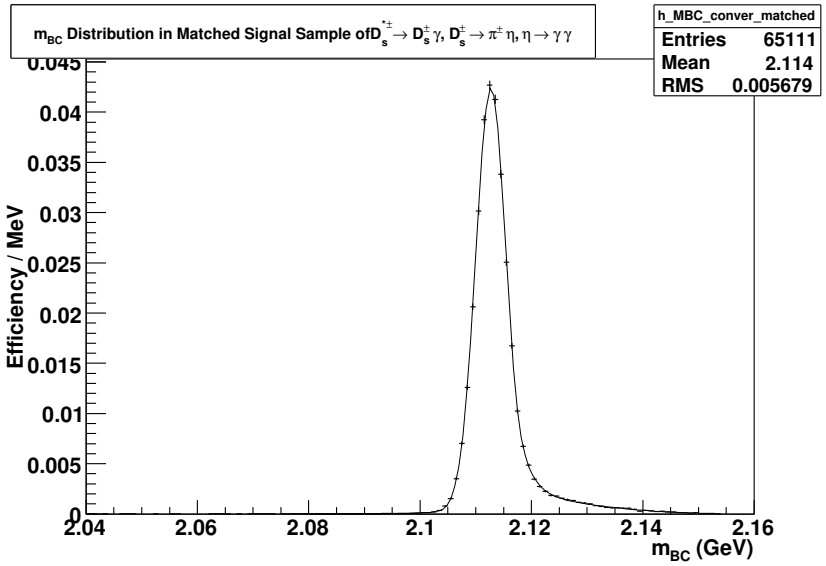

Figure 4.61: Distribution of m_{BC} in the signal Monte Carlo sample of $D_s^{*+} \to D_s^+\gamma$ events where $D_s^+ \to \eta\pi^+; \eta \to \gamma\gamma$.

Table 4.55: $\epsilon^i_{D_s\gamma}$ is the efficiency of our selection criteria for the mode. $N^i_{D_s\gamma}$ is the signal yield in generic Monte Carlo observed for this mode. $B(D_s^{*+} \to D_s^+\gamma)$ is the branching fraction for $D_s^{*+} \to D_s^+e^+e^-$ inferred from this mode. Error [1] on the inferred branching fraction is the statistical error from the final fit. Error [2] encapsulates the systematic uncertainties from the signal efficiency, the integrated luminosity and the production cross section for $D_s^{*\pm}D_s^{\mp}$.

i (Decay Mode of D_s^+)	$B(D_s^+ \to i)$	$\epsilon^i_{D_s\gamma}$	$N^i_{D_s\gamma}$	$B(D_s^{*+} \to D_s^+\gamma)$ Inferred
$D_s^+ \to \eta\pi^+; \eta \to \gamma\gamma$	0.0061	0.3310 ± 0.0015	998 ± 27	$0.8933 \pm 0.0240^{[1]} \pm 0.0043^{[2]}$

4.64. Our measurement of the signal selection efficiency and the signal yield is presented in Table 4.55. We find the thus estimated value for $B(D_s^{*+} \to D_s^+\gamma)$ equal to 0.893 ± 0.024 to be 2σ away from the programmed value of 0.942 in the Monte Carlo simulation.

We present the distribution of m_{BC} in data and our fits to estimate the signal yield over the backgrounds, as described for the $K^+K^-\pi^+$ mode, in Fig. 4.65. Our

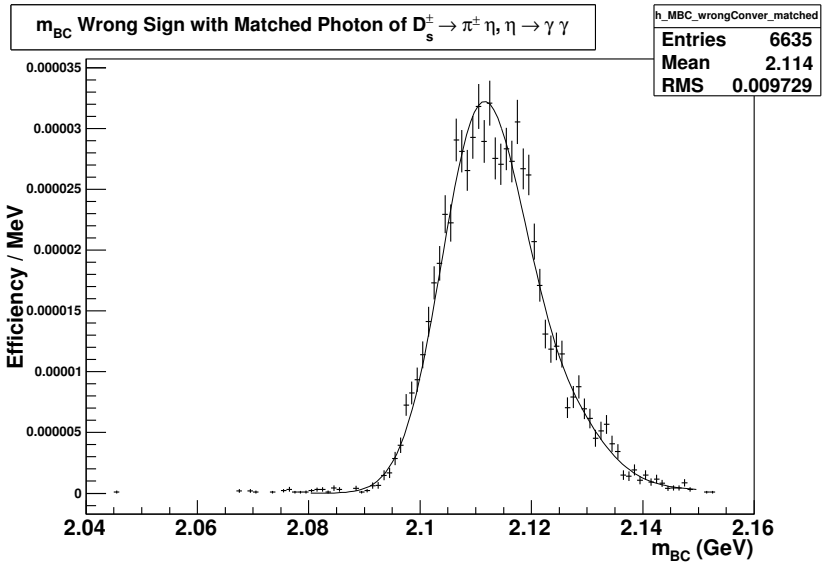

Figure 4.62: Combinatorial background in the m_{BC} distribution consisting of events where the D_s^{*+} has been reconstructed out of the D_s^- and the γ, and where both the D_s^- and the γ have been matched to their generated counterparts in the Monte Carlo simulation. This distribution has been fitted to a shape described by Eq. 4.24.

measurements of the signal efficiency and signal yield are presented in Table 4.56.

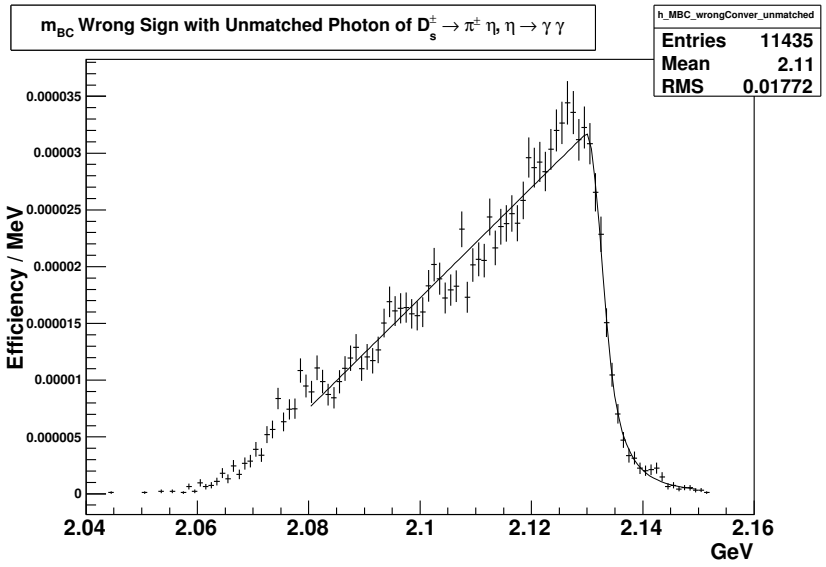

Figure 4.63: Combinatorial background structured in the m_{BC} distribution consisting of events where the D_s^{*+} has been reconstructed out of the D_s^- and the γ, and the D_s^- has been matched to its generated counterpart but the γ has failed to match the photon from the D_s^{*+} decay at the generator level of the Monte Carlo simulation. This distribution has been fitted to a shape described by Eq. 4.25.

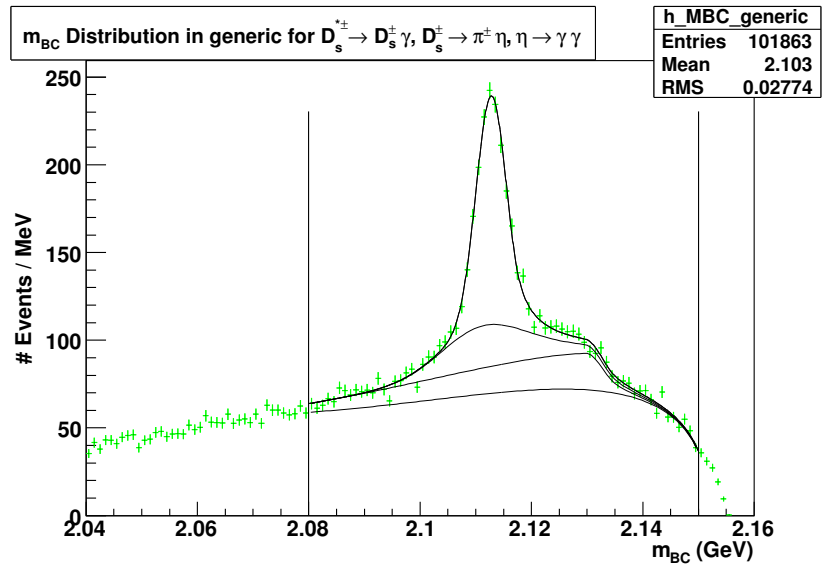

Figure 4.64: Distribution of m_{BC} of $D_s^{*+} \to D_s^+\gamma$ events where $D_s^+ \to \eta\pi^+; \eta \to \gamma\gamma$ in 586 pb^{-1} of Generic Monte Carlo.

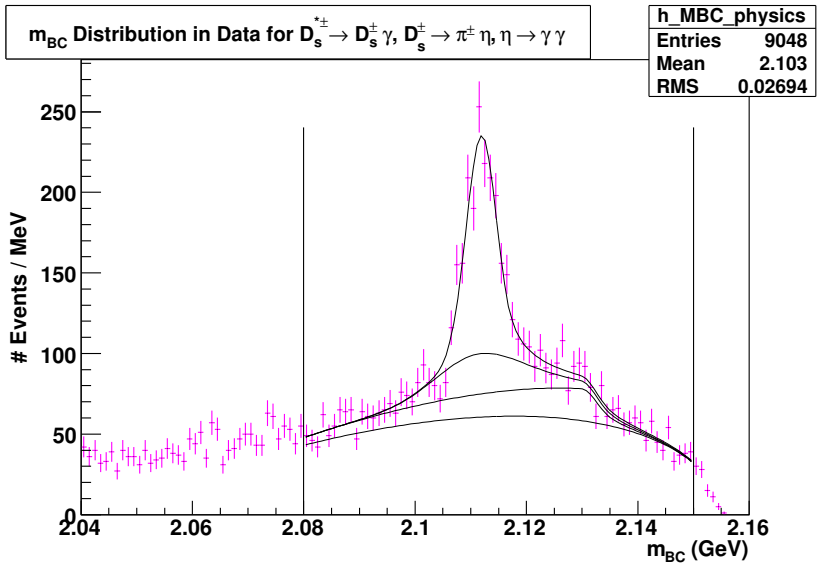

Figure 4.65: Distribution of m_{BC} of $D_s^{*+} \to D_s^+\gamma$ events where $D_s^+ \to \eta\pi^+; \eta \to \gamma\gamma$ in 586 pb^{-1} of data.

Table 4.56: $\epsilon^i_{D_s\gamma}$ is the efficiency of our selection criteria for the mode. $N^i_{D_s\gamma}$ is the signal yield observed in data for this mode. $B(D_s^{*+} \to D_s^+\gamma)$ is the branching fraction for $D_s^{*+} \to D_s^+e^+e^-$ inferred from this mode. Error [1] on the inferred branching fraction is the statistical error from the final fit. Error [2] arises from the uncertainty in the branching fraction for $D_s^+ \to i$. Error [3] encapsulates the systematic uncertainties from the signal efficiency, the integrated luminosity and the production cross section for $D_s^{*\pm}D_s^{\mp}$. Error [4] encapsulates the systematic error arising from the fit.

i (Decay Mode of D_s^+)	$B(D_s^+ \to i)$	$\epsilon^i_{D_s\gamma}$	$N^i_{D_s\gamma}$
$D_s^+ \to \eta\pi^+; \eta \to \gamma\gamma$	0.00621 ± 0.00083	0.3310 ± 0.0015	1037 ± 46 ± 37

Table 4.57: Selection criteria for $D_s^{*+} \to D_s^+\gamma$ events where $D_s^+ \to \eta'\pi^+; \eta' \to \pi^+\pi^-\eta; \eta \to \gamma\gamma$. The δm cut has been widened to accomodate the wider peak for the signal in this distribution.

Selection Criterion	Cut Center ± Width
$m_{D_s^+}$	1.969 ± 0.011 GeV
δm	0.140 ± 0.020 GeV

4.10.4 $D_s^+ \to \eta'\pi^+; \eta' \to \pi^+\pi^-\eta; \eta \to \gamma\gamma$

We begin with a Monte Carlo signal sample of $D_s^{*+} \to D_s^+\gamma$ events where $D_s^+ \to \eta'\pi^+; \eta' \to \pi^+\pi^-\eta; \eta \to \gamma\gamma$ and the D_s^- is allowed to decay generically. The selection criteria applied are tabulated in Table 4.57. Fig. 4.66 depicts the δm distribution of this signal sample and the region selected by our criterion.

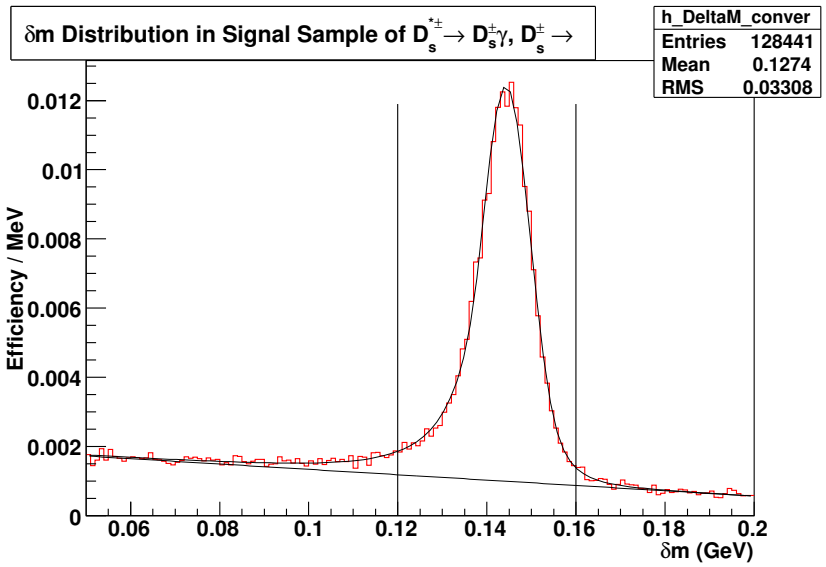

Figure 4.66: Distribution of δm in the signal Monte Carlo sample of $D_s^{*+} \to D_s^+\gamma$ events where $D_s^+ \to \eta'\pi^+; \eta' \to \pi^+\pi^-\eta; \eta \to \gamma\gamma$. The plot is normalized so as to directly read out the efficiency of the δm selection criterion.

To obtain the selection efficiency using the condition on m_{BC} as our last se-

lection criterion, we produce a plot of the m_{BC} distribution of the signal sample, having applied all other criteria, as shown in Fig. 4.67. We extract the shape of the peak from the plot of m_{BC} where the D_s^+ and the photon are matched to their generated counterparts in the Monte Carlo simulation as shown in Fig. 4.68. The equations that parameterize all fits and the range they are fitted in are identical to those used in the $K^+K^-\pi^+$ mode.

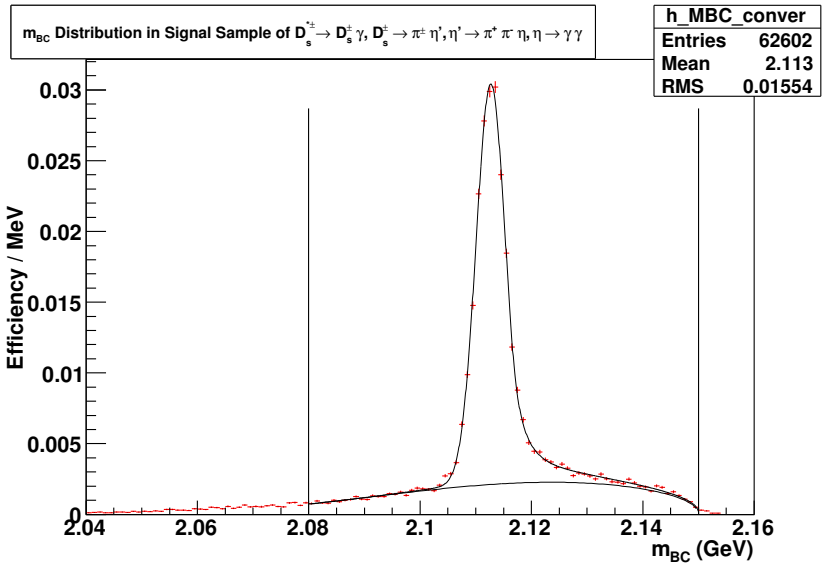

Figure 4.67: Distribution of m_{BC} in the signal Monte Carlo sample of $D_s^{*+} \to D_s^+\gamma$ events where $D_s^+ \to \eta'\pi^+; \eta' \to \pi^+\pi^-\eta; \eta \to \gamma\gamma$. The plot is normalized so as to directly read out the efficiency of the m_{BC} selection criterion from the area under the fit within the signal region.

Structured backgrounds arising from incorrectly reconstructed D_s^{*+} are simulated as done previously for the $K^+K^-\pi^+$ mode. Fig. 4.69 shows the structure of the D_s^- matched and photon matched background, and our fit to parameterize this shape. The background with the D_s^- matched and a photon that failed matching is shown in Fig. 4.70 along with our fit to parameterize the shape.

As a check on how well our background and signal estimation performs, we

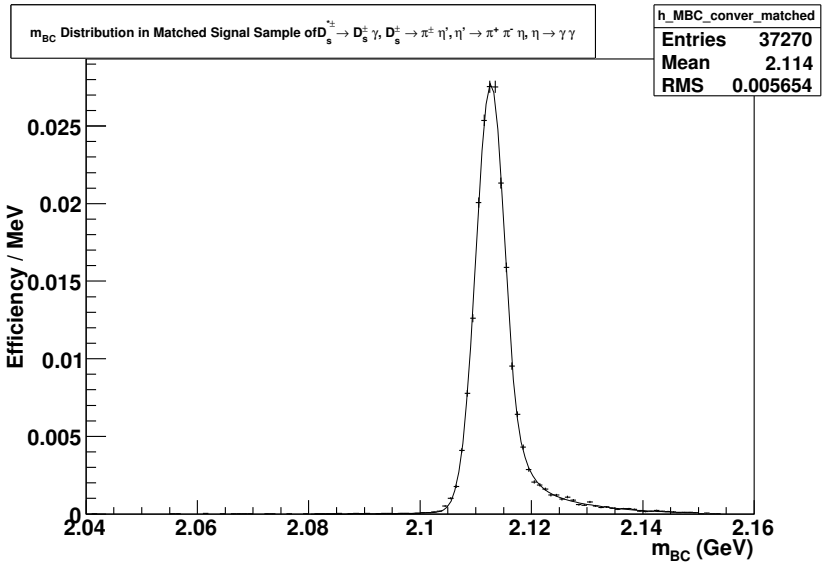

Figure 4.68: Distribution of m_{BC} in the signal Monte Carlo sample of $D_s^{*+} \to D_s^+\gamma$ events where $D_s^+ \to \eta'\pi^+; \eta' \to \pi^+\pi^-\eta; \eta \to \gamma\gamma$.

Table 4.58: $\epsilon^i_{D_s\gamma}$ is the efficiency of our selection criteria for the mode. $N^i_{D_s\gamma}$ is the signal yield observed in generic Monte Carlo for this mode. $B(D_s^{*+} \to D_s^+\gamma)$ is the branching fraction for $D_s^{*+} \to D_s^+e^+e^-$ inferred from this mode. Error [1] on the inferred branching fraction is the statistical error from the final fit. Error [2] encapsulates the systematic uncertainties from the signal efficiency, the integrated luminosity and the production cross section for $D_s^{*\pm}D_s^{\mp}$.

i (Decay Mode of D_s^+)	$B(D_s^+ \to i)$	$\epsilon^i_{D_s\gamma}$	$N^i_{D_s\gamma}$	$B(D_s^{*+} \to D_s^+\gamma)$ Inferred
$D_s^+ \to \eta'\pi^+; \eta' \to \pi^+\pi^-\eta; \eta \to \gamma\gamma$	0.00633	0.2101 ± 0.0013	690 ± 11	$0.9341 \pm 0.0149^{[1]} \pm 0.0058^{[2]}$

present the overall fit to generic MC, as described for the $K^+K^-\pi^+$ mode, in Fig. 4.71. Our measurement of the signal selection efficiency and the signal yield is presented in Table 4.58. We find the thus estimated value for $B(D_s^{*+} \to D_s^+\gamma)$ equal to 0.934 ± 0.016 to be 0.5σ away from the programmed value of 0.942 in the Monte Carlo simulation.

We present the distribution of m_{BC} in data and our fits to estimate the signal

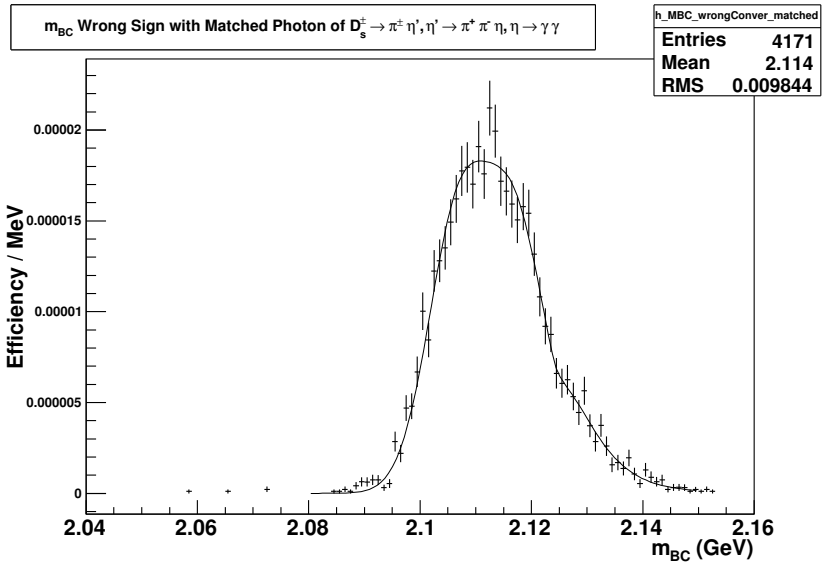

Figure 4.69: Combinatorial background in the m_{BC} distribution consisting of events where the D_s^{*+} has been reconstructed out of the D_s^- and the γ, and where both the D_s^- and the γ have been matched to their generated counterparts in the Monte Carlo simulation. This distribution has been fitted to a shape described by Eq. 4.24.

yield over the backgrounds, as described for the $K^+K^-\pi^+$ mode, in Fig. 4.72. Our measurements of the signal efficiency and signal yield are presented in Table 4.59.

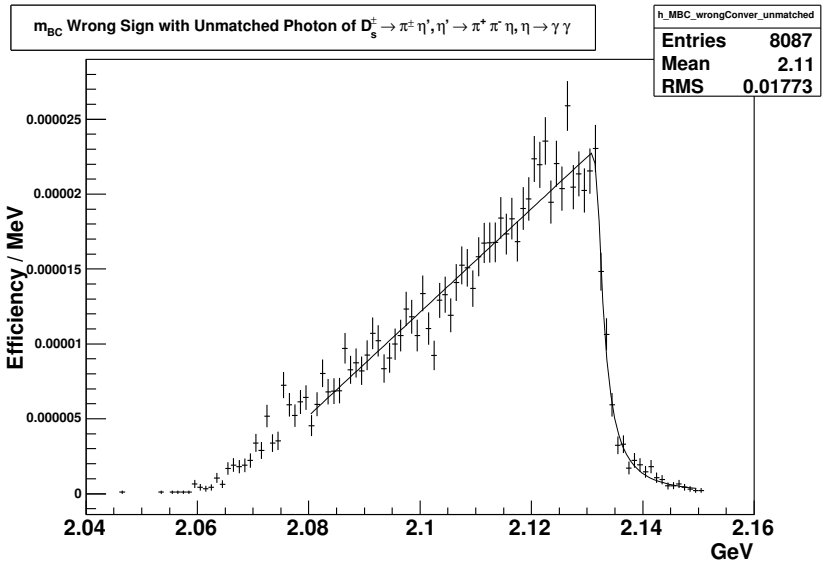

Figure 4.70: Combinatorial background structured in the m_{BC} distribution consisting of events where the D_s^{*+} has been reconstructed out of the D_s^- and the γ, and the D_s^- has been matched to its generated counterpart but the γ has failed to match the photon from the D_s^{*+} decay at the generator level of the Monte Carlo simulation. This distribution has been fitted to a shape described by Eq. 4.25.

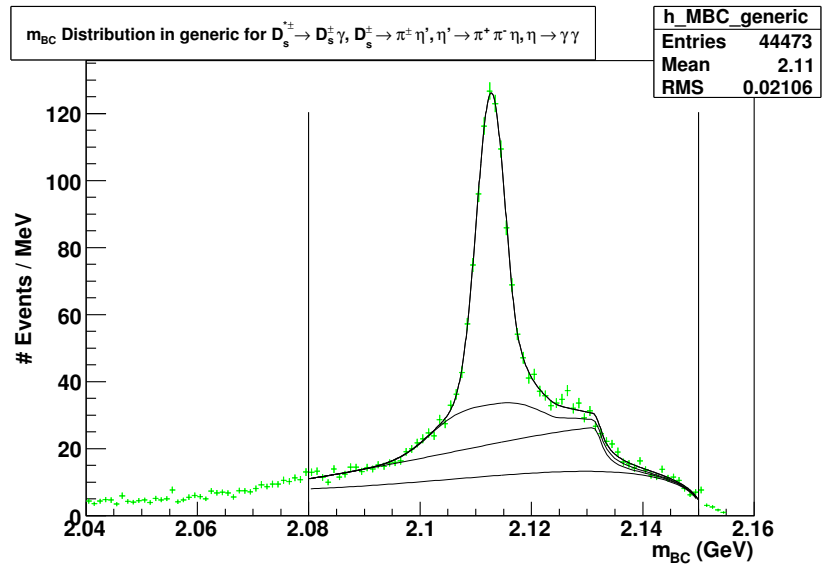

Figure 4.71: Distribution of m_{BC} of $D_s^{*+} \to D_s^+\gamma$ events where $D_s^+ \to \eta'\pi^+; \eta' \to \pi^+\pi^-\eta; \eta \to \gamma\gamma$ in 586 pb^{-1} of Generic Monte Carlo.

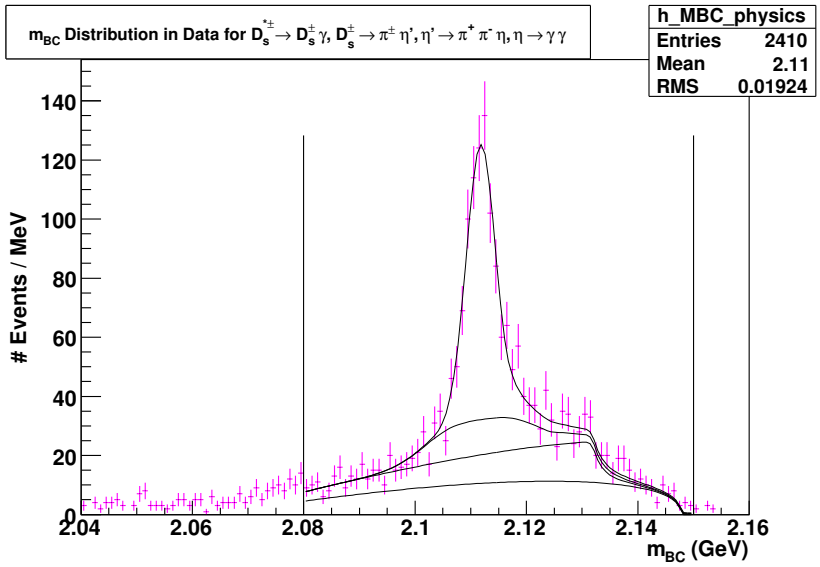

Figure 4.72: Distribution of m_{BC} of $D_s^{*+} \to D_s^+\gamma$ events where $D_s^+ \to \eta'\pi^+; \eta' \to \pi^+\pi^-\eta; \eta \to \gamma\gamma$ in 586 pb^{-1} of data.

Table 4.59: $\epsilon^i_{D_s\gamma}$ is the efficiency of our selection criteria for the mode. $N^i_{D_s\gamma}$ is the signal yield in data observed for this mode. $B(D_s^{*+} \to D_s^+\gamma)$ is the branching fraction for $D_s^{*+} \to D_s^+e^+e^-$ inferred from this mode. Error [1] on the inferred branching fraction is the statistical error from the final fit. Error [2] arises from the uncertainty in the branching fraction for $D_s^+ \to i$. Error [3] encapsulates the systematic uncertainties from the signal efficiency, the integrated luminosity and the production cross section for $D_s^{*\pm}D_s^{\mp}$. Error [4] encapsulates the systematic error arising from the fit.

i (Decay Mode of D_s^+)	$B(D_s^+ \to i)$	$\epsilon^i_{D_s\gamma}$	$N^i_{D_s\gamma}$
$D_s^+ \to \eta'\pi^+; \eta' \to \pi^+\pi^-\eta; \eta \to \gamma\gamma$	0.00666 ± 0.00070	0.2101 ± 0.0013	691 ± 34 ± 40

Table 4.60: Selection criteria for $D_s^{*+} \to D_s^+\gamma$ events where $D_s^+ \to K^+K^-\pi^+\pi^0$. The δm cut has been widened to accomodate the wider peak for the signal in this distribution.

Selection Criterion	Cut Center ± Width
$m_{D_s^+}$	1.969 ± 0.010 GeV
δm	0.140 ± 0.020 GeV

4.10.5 $D_s^+ \to K^+K^-\pi^+\pi^0$

We begin with a Monte Carlo signal sample of $D_s^{*+} \to D_s^+\gamma$ events where $D_s^+ \to K^+K^-\pi^+\pi^0$ and the D_s^- is allowed to decay generically. The selection criteria applied are tabulated in Table 4.60. Fig. 4.73 depicts the δm distribution of this signal sample and the region selected by our criterion.

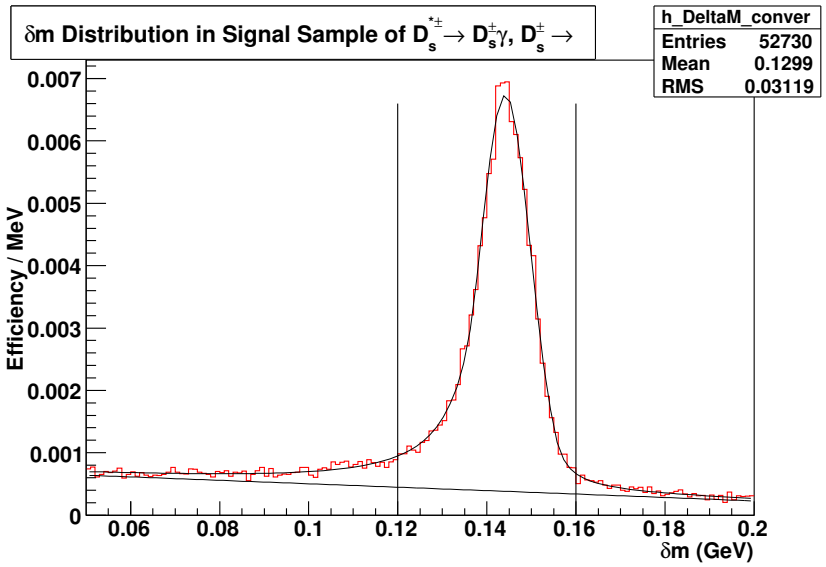

Figure 4.73: Distribution of δm in the signal Monte Carlo sample of $D_s^{*+} \to D_s^+\gamma$ events where $D_s^+ \to K^+K^-\pi^+\pi^0$. The plot is normalized so as to directly read out the efficiency of the δm selection criterion.

To obtain the selection efficiency using the condition on m_{BC} as our last se-

lection criterion, we produce a plot of the m_{BC} distribution of the signal sample, having applied all other criteria, as shown in Fig. 4.74. We extract the shape of the peak from the plot of m_{BC} where the D_s^+ and the photon are matched to their generated counterparts in the Monte Carlo simulation as shown in Fig. 4.75. The equations that parameterize all fits and the range they are fitted in are identical to those used in the $K^+K^-\pi^+$ mode.

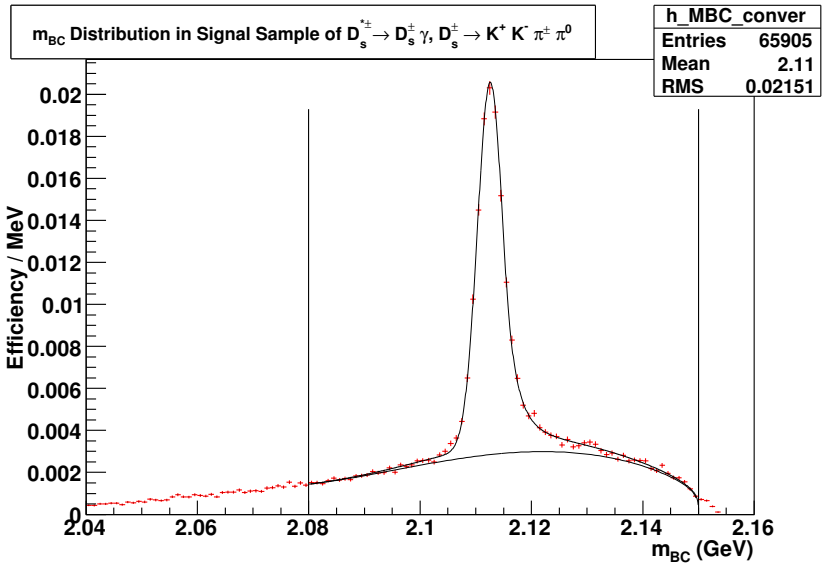

Figure 4.74: Distribution of m_{BC} in the signal Monte Carlo sample of $D_s^{*+} \to D_s^+\gamma$ events where $D_s^+ \to K^+K^-\pi^+\pi^0$. The plot is normalized so as to directly read out the efficiency of the m_{BC} selection criterion from the area under the fit within the signal region.

Structured backgrounds arising from incorrectly reconstructed D_s^{*+} are simulated as done previously for the $K^+K^-\pi^+$ mode. Fig. 4.76 shows the structure of the D_s^- matched and photon matched background, and our fit to parameterize this shape. The background with the D_s^- matched and a photon that failed matching is shown in Fig. 4.77 along with our fit to parameterize the shape.

As a check on how well our background and signal estimation performs, we present the overall fit to generic MC, as described for the $K^+K^-\pi^+$ mode, in Fig.

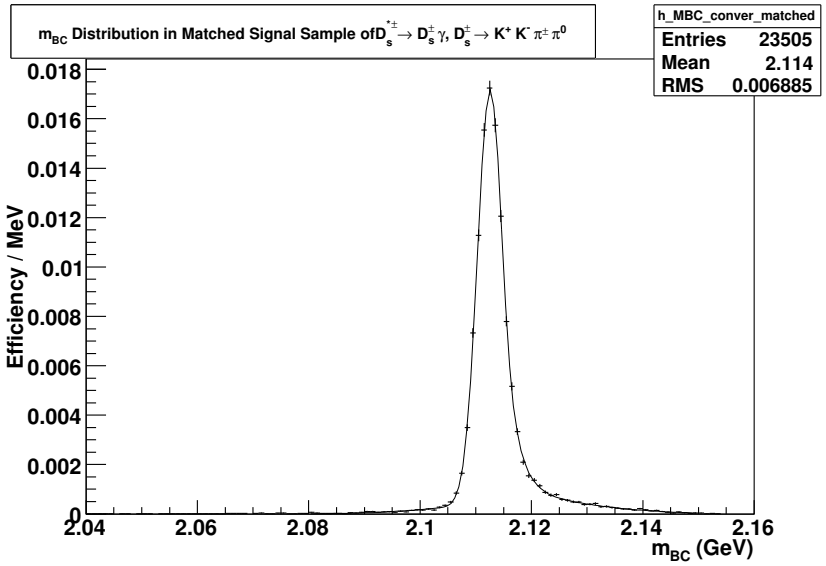

Figure 4.75: Distribution of m_{BC} in the signal Monte Carlo sample of $D_s^{*+} \to D_s^+\gamma$ events where $D_s^+ \to K^+K^-\pi^+\pi^0$.

Table 4.61: $\epsilon^i_{D_s\gamma}$ is the efficiency of our selection criteria for the mode. $N^i_{D_s\gamma}$ is the signal yield observed in generic Monte Carlo for this mode. $B(D_s^{*+} \to D_s^+\gamma)$ is the branching fraction for $D_s^{*+} \to D_s^+e^+e^-$ inferred from this mode. Error [1] on the inferred branching fraction is the statistical error from the final fit. Error [2] encapsulates the systematic uncertainties from the signal efficiency, the integrated luminosity and the production cross section for $D_s^{*\pm}D_s^{\mp}$.

i (Decay Mode of D_s^+)	$B(D_s^+ \to i)$	$\epsilon^i_{D_s\gamma}$	$N^i_{D_s\gamma}$	$B(D_s^{*+} \to D_s^+\gamma)$ Inferred
$D_s^+ \to K^+K^-\pi^+\pi^0$	0.0525	0.1225 ± 0.0010	3178 ± 49	$0.8894 \pm 0.0138^{[1]} \pm 0.0073^{[2]}$

4.78. Our measurement of the signal selection efficiency and the signal yield is presented in Table 4.61. We find the thus estimated value for $B(D_s^{*+} \to D_s^+\gamma)$ equal to 0.889 ± 0.016 to be 3.3σ away from the programmed value of 0.942 in the Monte Carlo simulation.

We present the distribution of m_{BC} in data and our fits to estimate the signal yield over the backgrounds, as described for the $K^+K^-\pi^+$ mode, in Fig. 4.79. Our

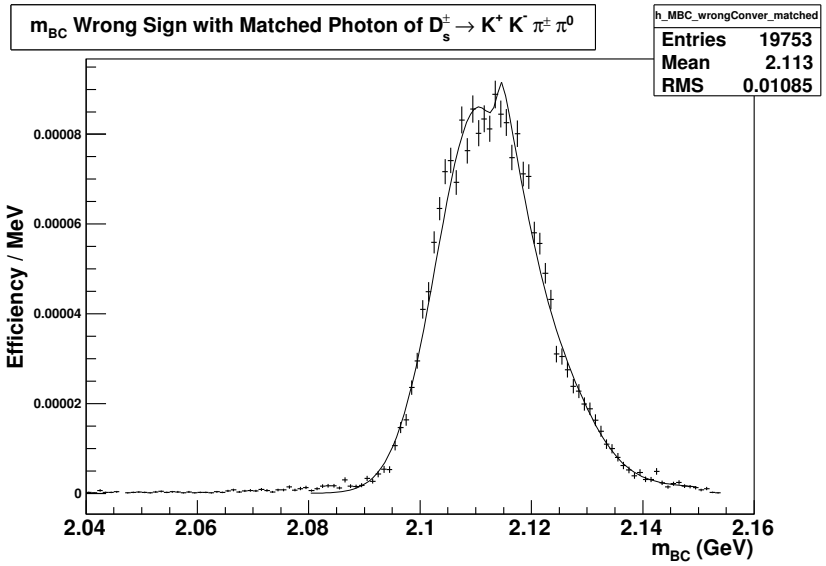

Figure 4.76: Combinatorial background in the m_{BC} distribution consisting of events where the D_s^{*+} has been reconstructed out of the D_s^- and the γ, and where both the D_s^- and the γ have been matched to their generated counterparts in the Monte Carlo simulation. This distribution has been fitted to a shape described by Eq. 4.24.

measurements of the signal efficiency and signal yield are presented in Table 4.62.

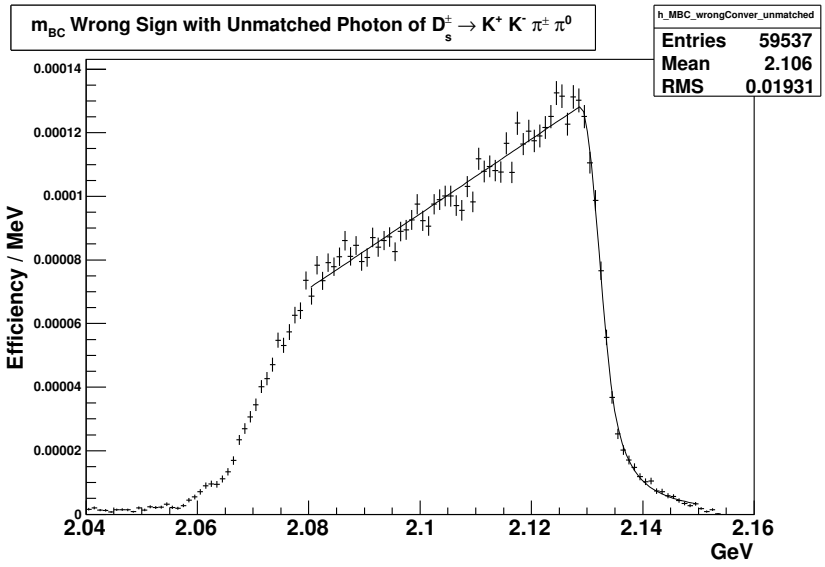

Figure 4.77: Combinatorial background structured in the m_{BC} distribution consisting of events where the D_s^{*+} has been reconstructed out of the D_s^- and the γ, and the D_s^- has been matched to its generated counterpart but the γ has failed to match the photon from the D_s^{*+} decay at the generator level of the Monte Carlo simulation. This distribution has been fitted to a shape described by Eq. 4.25.

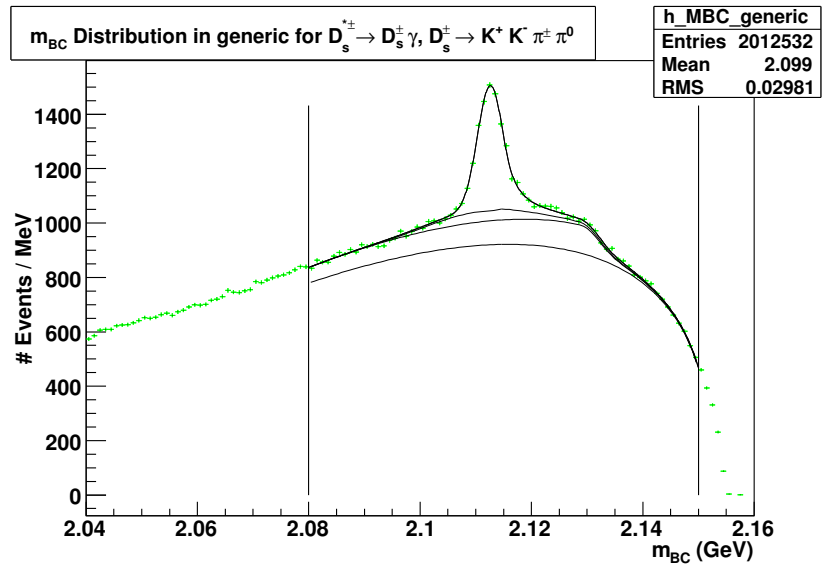

Figure 4.78: Distribution of m_{BC} of $D_s^{*+} \to D_s^+\gamma$ events where $D_s^+ \to K^+K^-\pi^+\pi^0$ in 586 pb^{-1} of Generic Monte Carlo.

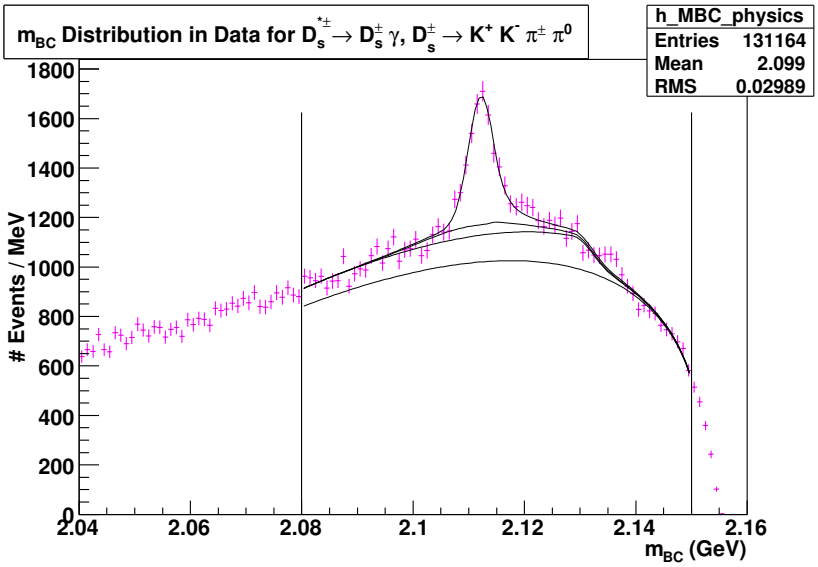

Figure 4.79: Distribution of m_{BC} of $D_s^{*+} \to D_s^+\gamma$ events where $D_s^+ \to K^+K^-\pi^+\pi^0$ in 586 pb^{-1} of data.

Table 4.62: $\epsilon^i_{D_s\gamma}$ is the efficiency of our selection criteria for the mode. $N^i_{D_s\gamma}$ is the signal yield observed in data for this mode. $B(D_s^{*+} \to D_s^+\gamma)$ is the branching fraction for $D_s^{*+} \to D_s^+e^+e^-$ inferred from this mode. Error [1] on the inferred branching fraction is the statistical error from the final fit. Error [2] arises from the uncertainty in the branching fraction for $D_s^+ \to i$. Error [3] encapsulates the systematic uncertainties from the signal efficiency, the integrated luminosity and the production cross section for $D_s^{*\pm}D_s^{\mp}$. Error [4] encapsulates the systematic error arising from the fit.

i (Decay Mode of D_s^+)	$B(D_s^+ \to i)$	$\epsilon^i_{D_s\gamma}$	$N^i_{D_s\gamma}$
$D_s^+ \to K^+K^-\pi^+\pi^0$	0.056 ± 0.005	0.1225 ± 0.0010	3592 ± 118 ± 72

Table 4.63: Selection criteria for $D_s^{*+} \to D_s^+\gamma$ events where $D_s^+ \to \pi^+\pi^-\pi^+$. The δm cut has been widened to accomodate the wider peak for the signal in this distribution.

Selection Criterion	Cut Center ± Width
$m_{D_s^+}$	1.969 ± 0.012 GeV
δm	0.140 ± 0.020 GeV

4.10.6 $D_s^+ \to \pi^+\pi^-\pi^+$

We begin with a Monte Carlo signal sample of $D_s^{*+} \to D_s^+\gamma$ events where $D_s^+ \to \pi^+\pi^-\pi^+$ and the D_s^- is allowed to decay generically. The selection criteria applied are tabulated in Table 4.63. Fig. 4.80 depicts the δm distribution of this signal sample and shows why the corresponding selection criterion had to be widened relative to the $D_s^{*+} \to D_s^+e^+e^-$ signal selection.

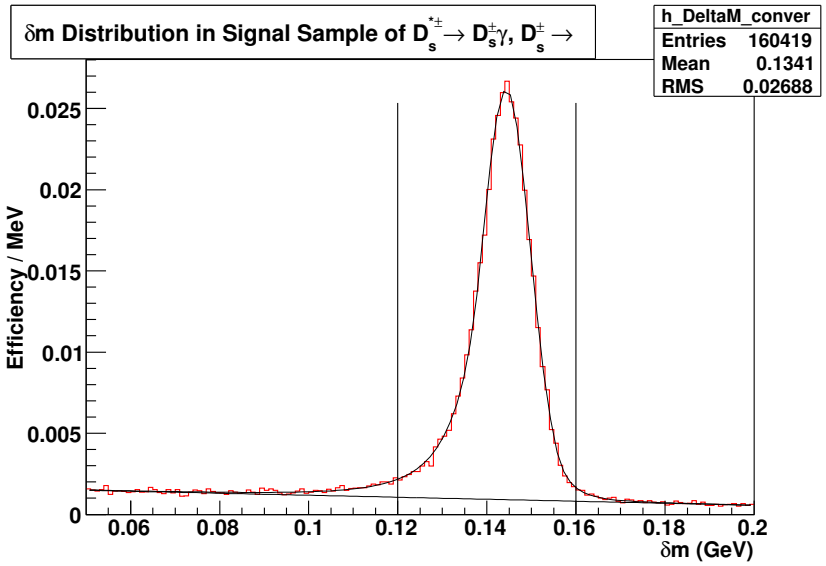

Figure 4.80: Distribution of δm in the signal Monte Carlo sample of $D_s^{*+} \to D_s^+\gamma$ events where $D_s^+ \to \pi^+\pi^-\pi^+$. The plot is normalized so as to directly read out the efficiency of the δm selection criterion.

To obtain the selection efficiency using the condition on m_{BC} as our last se-

lection criterion, we produce a plot of the m_{BC} distribution of the signal sample, having applied all other criteria, as shown in Fig. 4.81. We extract the shape of the peak from the plot of m_{BC} where the D_s^+ and the photon are matched to their generated counterparts in the Monte Carlo simulation as shown in Fig. 4.82. The equations that parameterize all fits and the range they are fitted in are identical to those used in the $K^+K^-\pi^+$ mode.

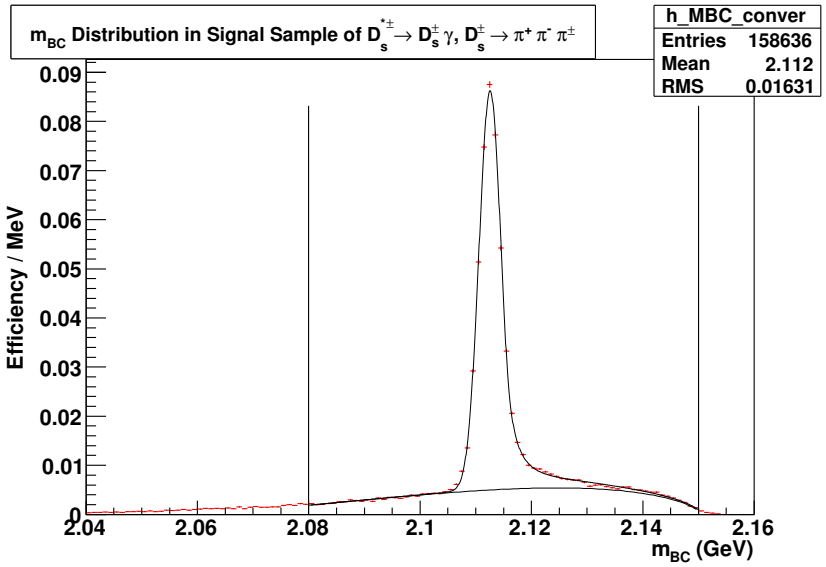

Figure 4.81: Distribution of m_{BC} in the signal Monte Carlo sample of $D_s^{*+} \to D_s^+\gamma$ events where $D_s^+ \to \pi^+\pi^-\pi^+$. The plot is normalized so as to directly read out the efficiency of the m_{BC} selection criterion from the area under the fit within the signal region.

Structured backgrounds arising from incorrectly reconstructed D_s^{*+} are simulated as done previously for the $K^+K^-\pi^+$ mode. Fig. 4.83 shows the structure of the D_s^- matched and photon matched background, and our fit to parameterize this shape. The background with the D_s^- matched and a photon that failed matching is shown in Fig. 4.84 along with our fit to parameterize the shape.

As a check on how well our background and signal estimation performs, we present the overall fit to generic MC, as described for the $K^+K^-\pi^+$ mode, in Fig.

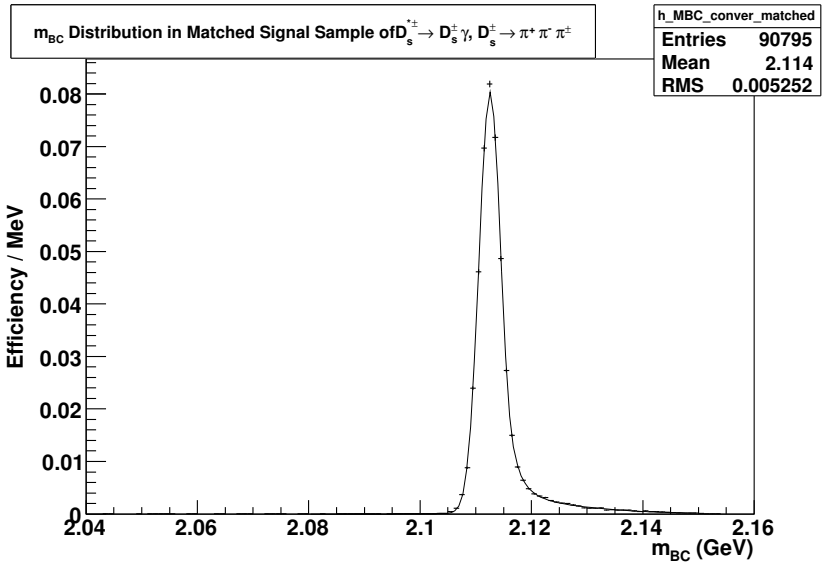

Figure 4.82: Distribution of m_{BC} in the signal Monte Carlo sample of $D_s^{*+} \to D_s^+\gamma$ events where $D_s^+ \to \pi^+\pi^-\pi^+$.

Table 4.64: $\epsilon^i_{D_s\gamma}$ is the efficiency of our selection criteria for the mode. $N^i_{D_s\gamma}$ is the signal yield observed in generic Monte Carlo for this mode. $B(D_s^{*+} \to D_s^+\gamma)$ is the branching fraction for $D_s^{*+} \to D_s^+e^+e^-$ inferred from this mode. Error [1] on the inferred branching fraction is the statistical error from the final fit. Error [2] encapsulates the systematic uncertainties from the signal efficiency, the integrated luminosity and the production cross section for $D_s^{*\pm}D_s^{\mp}$.

i (Decay Mode of D_s^+)	$B(D_s^+ \to i)$	$\epsilon^i_{D_s\gamma}$	$N^i_{D_s\gamma}$	$B(D_s^{*+} \to D_s^+\gamma)$ Inferred
$D_s^+ \to \pi^+\pi^-\pi^+$	0.0103	0.4583 ± 0.0018	2706 ± 43	$1.0327 \pm 0.0162^{[1]} \pm 0.0041^{[2]}$

4.85. Our measurement of the signal selection efficiency and the signal yield is presented in Table 4.64. We find the thus estimated value for $B(D_s^{*+} \to D_s^+\gamma)$ equal to 1.0327 ± 0.0167 to be 5.4σ away from the programmed value of 0.942 in the Monte Carlo simulation.

We present the distribution of m_{BC} in data and our fits to estimate the signal yield over the backgrounds, as described for the $K^+K^-\pi^+$ mode, in Fig. 4.86. Our

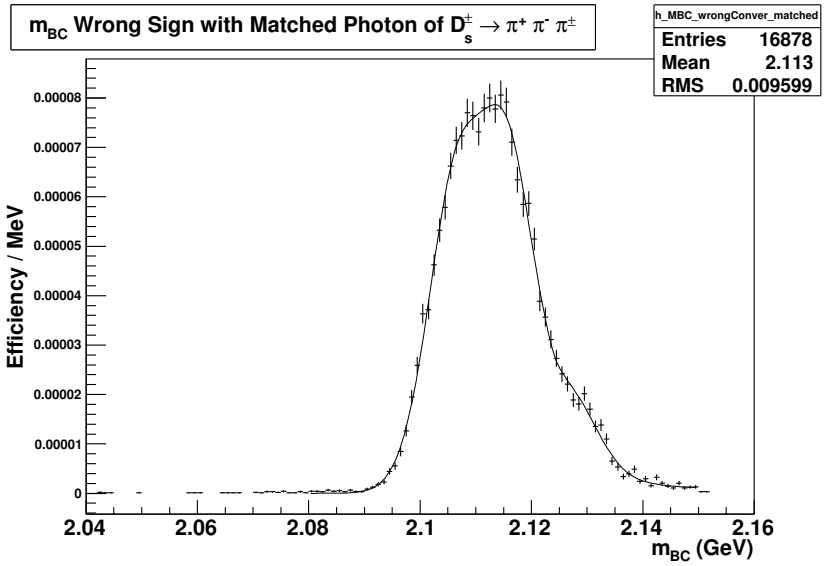

Figure 4.83: Combinatorial background in the m_{BC} distribution consisting of events where the D_s^{*+} has been reconstructed out of the D_s^- and the γ, and where both the D_s^- and the γ have been matched to their generated counterparts in the Monte Carlo simulation. This distribution has been fitted to a shape described by Eq. 4.24.

measurements of the signal efficiency and signal yield are presented in Table 4.65.

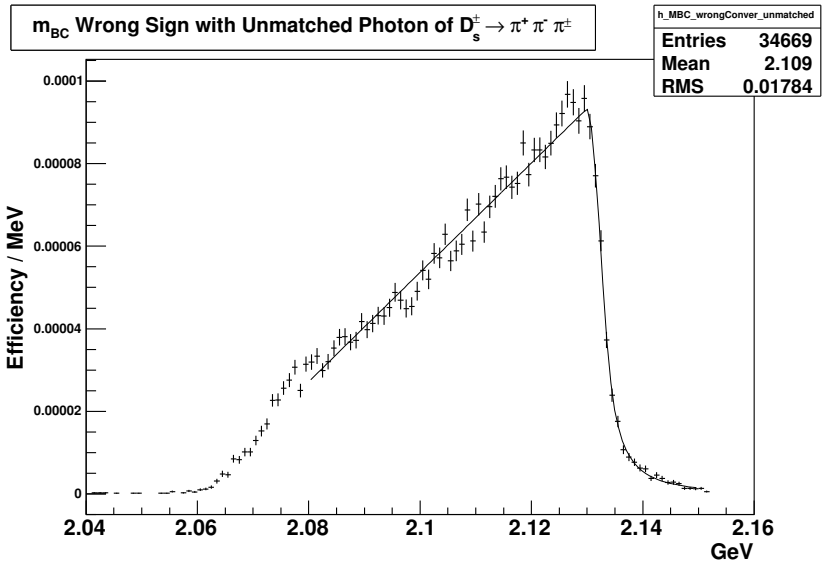

Figure 4.84: Combinatorial background structured in the m_{BC} distribution consisting of events where the D_s^{*+} has been reconstructed out of the D_s^- and the γ, and the D_s^- has been matched to its generated counterpart but the γ has failed to match the photon from the D_s^{*+} decay at the generator level of the Monte Carlo simulation. This distribution has been fitted to a shape described by Eq. 4.25.

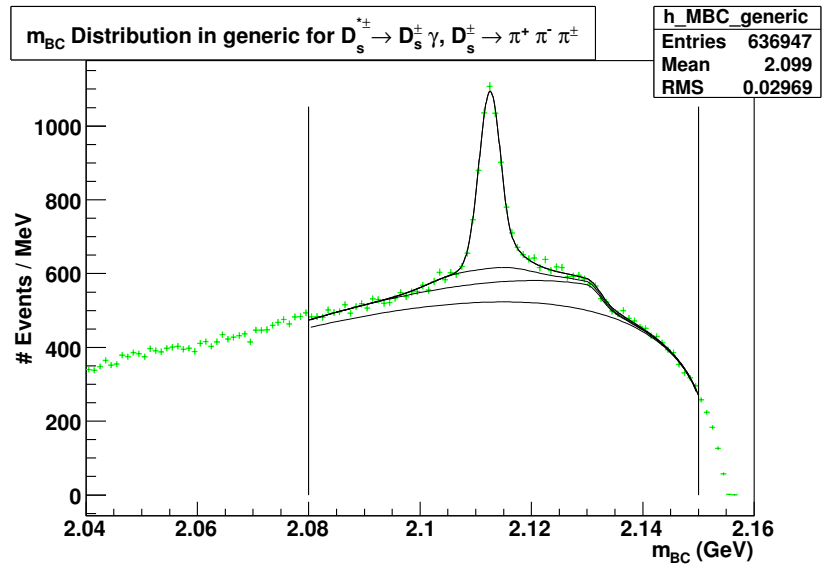

Figure 4.85: Distribution of m_{BC} of $D_s^{*+} \to D_s^+\gamma$ events where $D_s^+ \to \pi^+\pi^-\pi^+$ in 586 pb^{-1} of Generic Monte Carlo.

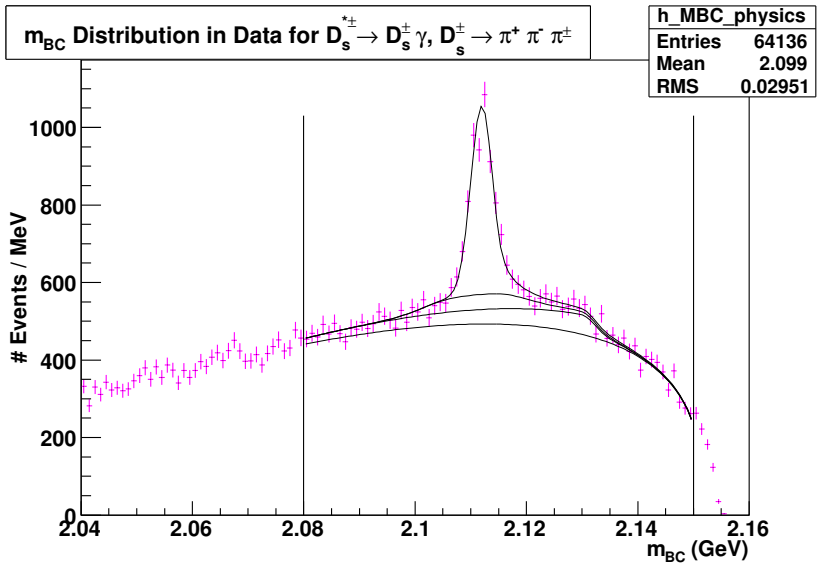

Figure 4.86: Distribution of m_{BC} of $D_s^{*+} \to D_s^+\gamma$ events where $D_s^+ \to \pi^+\pi^-\pi^+$ in 586 pb^{-1} of data.

Table 4.65: $\epsilon^i_{D_s\gamma}$ is the efficiency of our selection criteria for the mode. $N^i_{D_s\gamma}$ is the signal yield observed in data for this mode. $B(D_s^{*+} \to D_s^+\gamma)$ is the branching fraction for $D_s^{*+} \to D_s^+e^+e^-$ inferred from this mode. Error [1] on the inferred branching fraction is the statistical error from the final fit. Error [2] arises from the uncertainty in the branching fraction for $D_s^+ \to i$. Error [3] encapsulates the systematic uncertainties from the signal efficiency, the integrated luminosity and the production cross section for $D_s^{*\pm}D_s^{\mp}$. Error [4] encapsulates the systematic error arising from the fit.

i (Decay Mode of D_s^+)	$B(D_s^+ \to i)$	$\epsilon^i_{D_s\gamma}$	$N^i_{D_s\gamma}$
$D_s^+ \to \pi^+\pi^-\pi^+$	0.0111 ± 0.0008	0.4583 ± 0.0018	2745 ± 93 ± 52

Table 4.66: Selection criteria for $D_s^{*+} \to D_s^+\gamma$ events where $D_s^+ \to K^{*+}K^{*0}$. The δm cut has been widened to accomodate the wider peak for the signal in this distribution.

Selection Criterion	Cut Center ± Width
$m_{D_s^+}$	1.969 ± 0.006 GeV
m_{BC}	2.112 ± 0.005 GeV
δm	0.140 ± 0.020 GeV

4.10.7 $D_s^+ \to K^{*+}K^{*0}; K^{*+} \to K_S^0\pi^+; K^{*0} \to K^-\pi^+$

We begin with a Monte Carlo signal sample of $D_s^{*+} \to D_s^+\gamma$ events where $D_s^+ \to K^{*+}K^{*0}$ and the D_s^- is allowed to decay generically. The selection criteria applied are tabulated in Table 4.66. Fig. 4.87 depicts the δm distribution of this signal sample and shows why the corresponding selection criterion had to be widened relative to the $D_s^{*+} \to D_s^+e^+e^-$ signal selection.

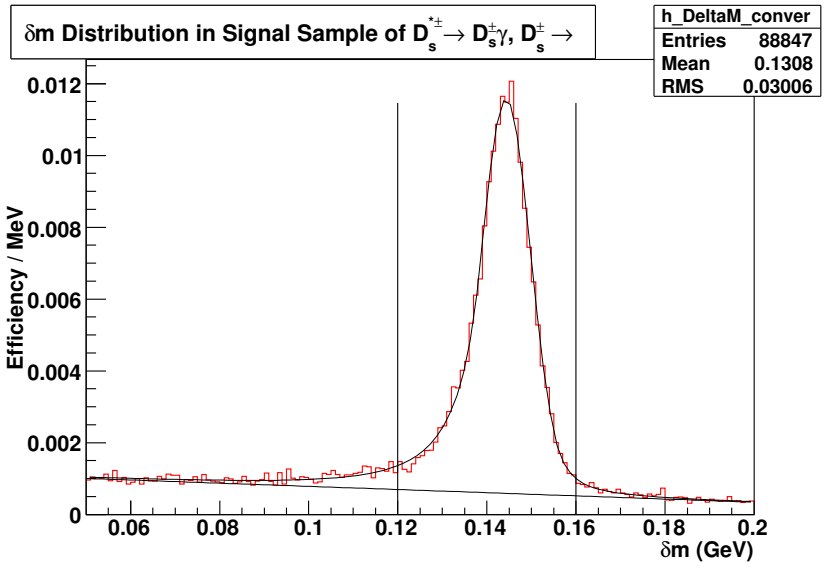

Figure 4.87: Distribution of δm in the signal Monte Carlo sample of $D_s^{*+} \to D_s^+\gamma$ events where $D_s^+ \to K^{*+}K^{*0}$. The plot is normalized so as to directly read out the efficiency of the δm selection criterion.

To obtain the selection efficiency using the condition on m_{BC} as our last selection criterion, we produce a plot of the m_{BC} distribution of the signal sample, having applied all other criteria, as shown in Fig. 4.88. We extract the shape of the peak from the plot of m_{BC} where the D_s^+ and the photon are matched to their generated counterparts in the Monte Carlo simulation as shown in Fig. 4.89. The equations that parameterize all fits and the range they are fitted in are identical to those used in the $K^+K^-\pi^+$ mode.

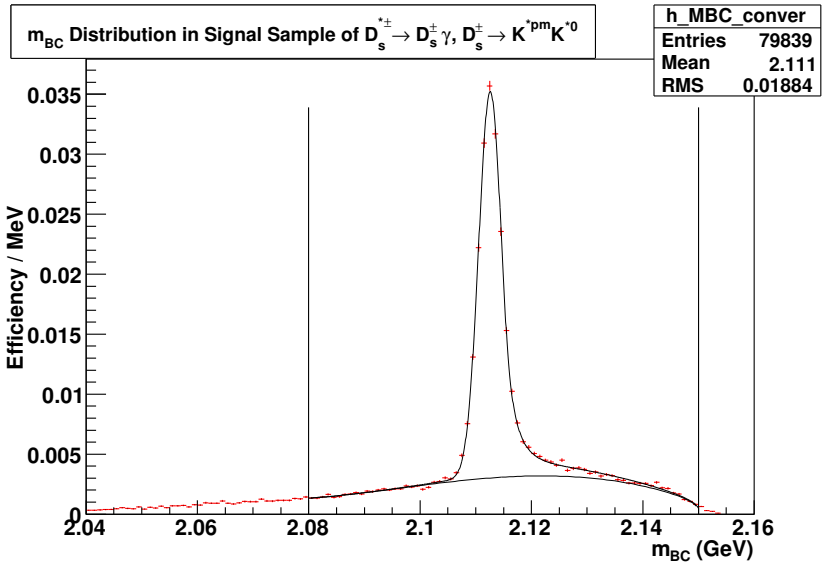

Figure 4.88: Distribution of m_{BC} in the signal Monte Carlo sample of $D_s^{*+} \to D_s^+\gamma$ events where $D_s^+ \to K^{*+}K^{*0}$. The plot is normalized so as to directly read out the efficiency of the m_{BC} selection criterion from the area under the fit within the signal region.

Structured backgrounds arising from incorrectly reconstructed D_s^{*+} are simulated as done previously for the $K^+K^-\pi^+$ mode. Fig. 4.90 shows the structure of the D_s^- matched and photon matched background, and our fit to parameterize this shape. The background with the D_s^- matched and a photon that failed matching is shown in Fig. 4.91 along with our fit to parameterize the shape.

As a check on how well our background and signal estimation performs, we

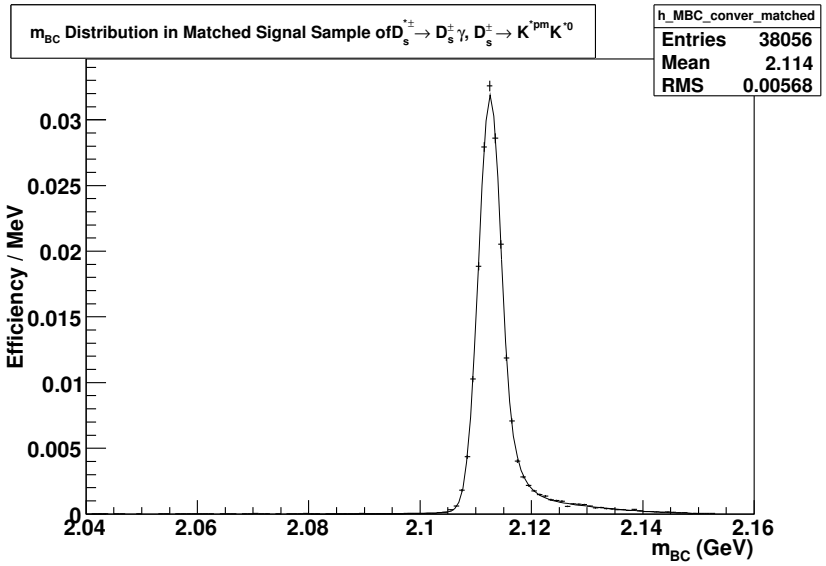

Figure 4.89: Distribution of m_{BC} in the signal Monte Carlo sample of $D_s^{*+} \to D_s^+\gamma$ events where $D_s^+ \to K^{*+}K^{*0}$.

Table 4.67: $\epsilon^i_{D_s\gamma}$ is the efficiency of our selection criteria for the mode. $N^i_{D_s\gamma}$ is the signal yield observed in generic Monte Carlo for this mode. $B(D_s^{*+} \to D_s^+\gamma)$ is the branching fraction for $D_s^{*+} \to D_s^+e^+e^-$ inferred from this mode. Error [1] on the inferred branching fraction is the statistical error from the final fit. Error [2] encapsulates the systematic uncertainties from the signal efficiency, the integrated luminosity and the production cross section for $D_s^{*\pm}D_s^{\mp}$.

i (Decay Mode of D_s^+)	$B(D_s^+ \to i)$	$\epsilon^i_{D_s\gamma}$	$N^i_{D_s\gamma}$	$B(D_s^{*+} \to D_s^+\gamma)$ Inferred
$D_s^+ \to K^{*+}K^{*0}$	0.01628	0.1913 ± 0.0012	1644 ± 22	$0.9502 \pm 0.0129^{[1]} \pm 0.0058^{[2]}$

present the overall fit to generic MC, as described for the $K^+K^-\pi^+$ mode, in Fig. 4.92. Our measurement of the signal selection efficiency and the signal yield is presented in Table 4.67. We find the thus estimated value for $B(D_s^{*+} \to D_s^+\gamma)$ equal to 0.950 ± 0.014 to be 0.6σ away from the programmed value of 0.942 in the Monte Carlo simulation.

We present the distribution of m_{BC} in data and our fits to estimate the signal

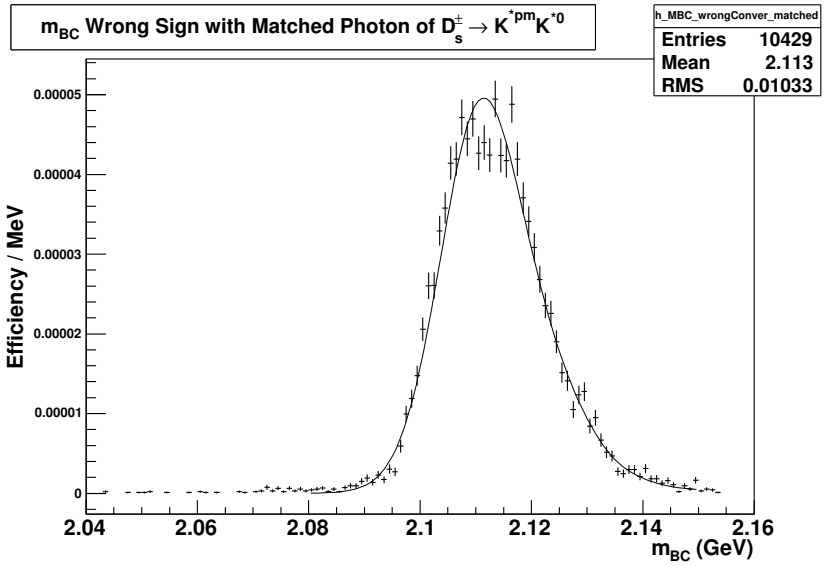

Figure 4.90: Combinatorial background in the m_{BC} distribution consisting of events where the D_s^{*+} has been reconstructed out of the D_s^- and the γ, and where both the D_s^- and the γ have been matched to their generated counterparts in the Monte Carlo simulation. This distribution has been fitted to a shape described by Eq. 4.24.

yield over the backgrounds, as described for the $K^+K^-\pi^+$ mode, in Fig. 4.93. Our measurements of the signal efficiency and signal yield are presented in Table 4.68.

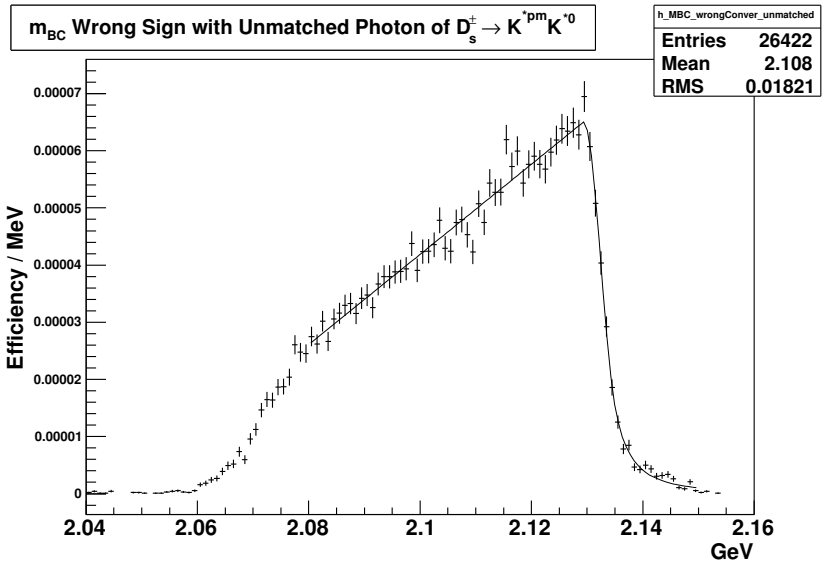

Figure 4.91: Combinatorial background structured in the m_{BC} distribution consisting of events where the D_s^{*+} has been reconstructed out of the D_s^- and the γ, and the D_s^- has been matched to its generated counterpart but the γ has failed to match the photon from the D_s^{*+} decay at the generator level of the Monte Carlo simulation. This distribution has been fitted to a shape described by Eq. 4.25.

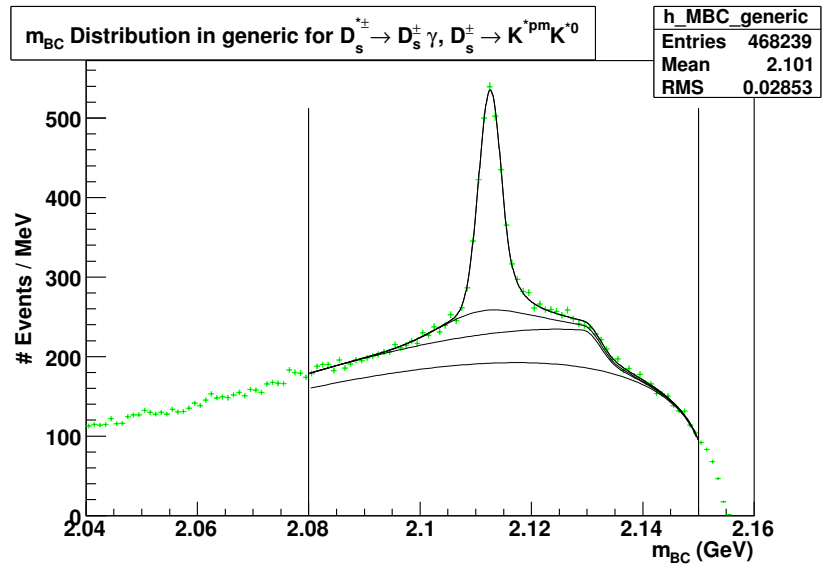

Figure 4.92: Distribution of m_{BC} of $D_s^{*+} \to D_s^+\gamma$ events where $D_s^+ \to K^{*+}K^{*0}$ in 586 pb^{-1} of Generic Monte Carlo.

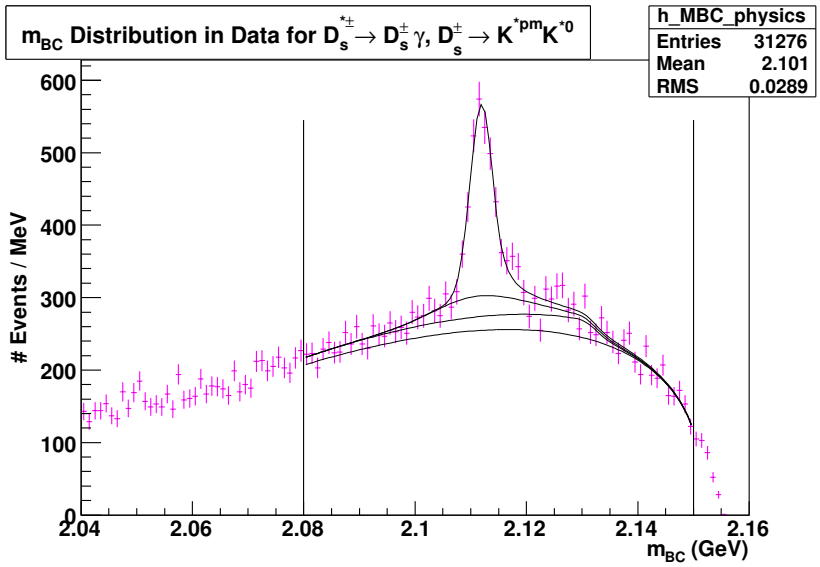

Figure 4.93: Distribution of m_{BC} of $D_s^{*+} \to D_s^+\gamma$ events where $D_s^+ \to K^{*+}K^{*0}$ in 586 pb^{-1} of data.

Table 4.68: $\epsilon^i_{D_s\gamma}$ is the efficiency of our selection criteria for the mode. $N^i_{D_s\gamma}$ is the signal yield observed in data for this mode. $B(D_s^{*+} \to D_s^+\gamma)$ is the branching fraction for $D_s^{*+} \to D_s^+e^+e^-$ inferred from this mode. Error [1] on the inferred branching fraction is the statistical error from the final fit. Error [2] arises from the uncertainty in the branching fraction for $D_s^+ \to i$. Error [3] encapsulates the systematic uncertainties from the signal efficiency, the integrated luminosity and the production cross section for $D_s^{*\pm}D_s^{\mp}$. Error [4] encapsulates the systematic error arising from the fit.

i (Decay Mode of D_s^+)	$B(D_s^+ \to i)$	$\epsilon^i_{D_s\gamma}$	$N^i_{D_s\gamma}$
$D_s^+ \to K^{*+}K^{*0}$	0.0164 ± 0.0012	0.1913 ± 0.0012	1570 ± 74 ± 13

Table 4.69: Selection criteria for $D_s^{*+} \to D_s^+\gamma$ events where $D_s^+ \to \eta\rho^+$. The δm cut has been widened to accomodate the wider peak for the signal in this distribution.

Selection Criterion	Cut Center ± Width
$m_{D_s^+}$	1.969 ± 0.015 GeV
δm	0.140 ± 0.020 GeV

4.10.8 $D_s^+ \to \eta\rho^+; \eta \to \gamma\gamma; \rho^+ \to \pi^+\pi^0$

We begin with a Monte Carlo signal sample of $D_s^{*+} \to D_s^+\gamma$ events where $D_s^+ \to \eta\rho^+; \eta \to \gamma\gamma; \rho^+ \to \pi^+\pi^0$ and the D_s^- is allowed to decay generically. The selection criteria applied are tabulated in Table 4.69. Fig. 4.94 depicts the δm distribution of this signal sample and shows why the corresponding selection criterion had to be widened relative to the $D_s^{*+} \to D_s^+e^+e^-$ signal selection.

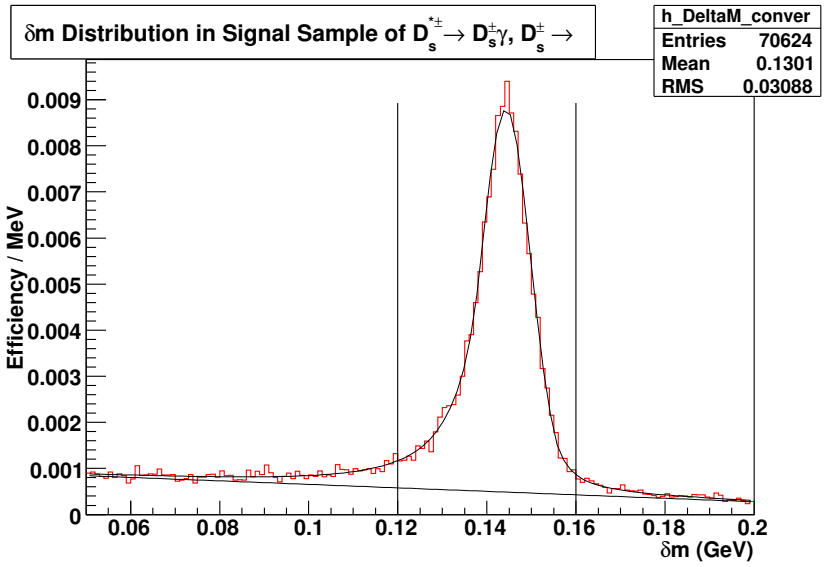

Figure 4.94: Distribution of δm in the signal Monte Carlo sample of $D_s^{*+} \to D_s^+\gamma$ events where $D_s^+ \to \eta\rho^+$. The plot is normalized so as to directly read out the efficiency of the δm selection criterion.

To obtain the selection efficiency using the condition on m_{BC} as our last se-

lection criterion, we produce a plot of the m_{BC} distribution of the signal sample, having applied all other criteria, as shown in Fig. 4.95. We extract the shape of the peak from the plot of m_{BC} where the D_s^+ and the photon are matched to their generated counterparts in the Monte Carlo simulation as shown in Fig. 4.96. The equations that parameterize all fits and the range they are fitted in are identical to those used in the $K^+K^-\pi^+$ mode.

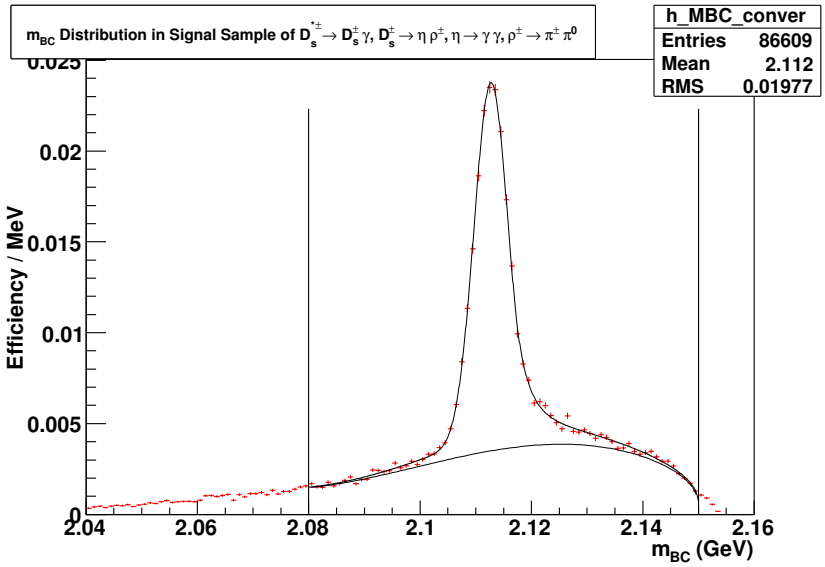

Figure 4.95: Distribution of m_{BC} in the signal Monte Carlo sample of $D_s^{*+} \to D_s^+\gamma$ events where $D_s^+ \to \eta\rho^+; \eta \to \gamma\gamma; \rho^+ \to \pi^+\pi^0$. The plot is normalized so as to directly read out the efficiency of the m_{BC} selection criterion from the area under the fit within the signal region.

Structured backgrounds arising from incorrectly reconstructed D_s^{*+} are simulated as done previously for the $K^+K^-\pi^+$ mode. Fig. 4.97 shows the structure of the D_s^- matched and photon matched background, and our fit to parameterize this shape. The background with the D_s^- matched and a photon that failed matching is shown in Fig. 4.98 along with our fit to parameterize the shape.

As a check on how well our background and signal estimation performs, we

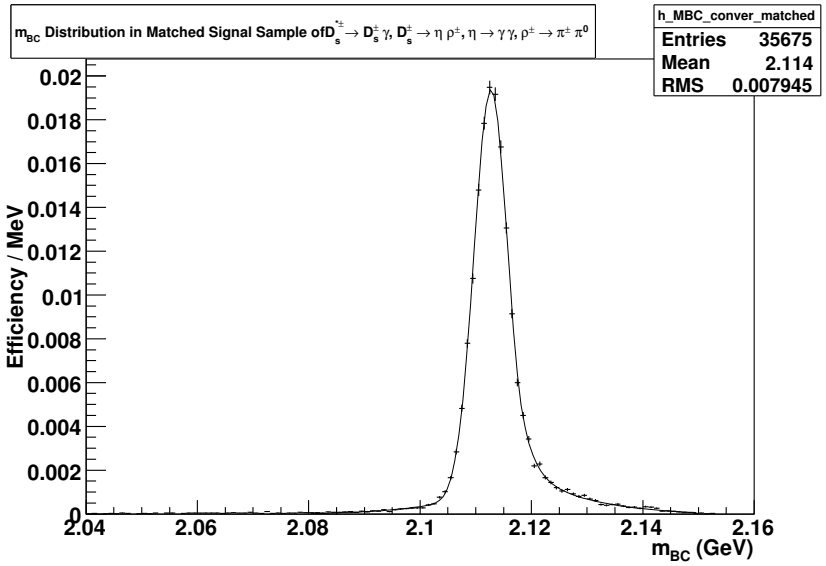

Figure 4.96: Distribution of m_{BC} in the signal Monte Carlo sample of $D_s^{*+} \to D_s^+\gamma$ events where $D_s^{*+} \to D_s^+\gamma$ events where $D_s^+ \to \eta\rho^+; \eta \to \gamma\gamma; \rho^+ \to \pi^+\pi^0$.

Table 4.70: $\epsilon^i_{D_s\gamma}$ is the efficiency of our selection criteria for the mode. $N^i_{D_s\gamma}$ is the signal yield observed in generic Monte Carlo for this mode. $B(D_s^{*+} \to D_s^+\gamma)$ is the branching fraction for $D_s^{*+} \to D_s^+e^+e^-$ inferred from this mode. Error [1] on the inferred branching fraction is the statistical error from the final fit. Error [2] encapsulates the systematic uncertainties from the signal efficiency, the integrated luminosity and the production cross section for $D_s^{*\pm}D_s^{\mp}$.

i (Decay Mode of D_s^+)	$B(D_s^+ \to i)$	$\epsilon^i_{D_s\gamma}$	$N^i_{D_s\gamma}$	$B(D_s^{*+} \to D_s^+\gamma)$ Inferred
$D_s^+ \to \eta\rho^+; \eta \to \gamma\gamma; \rho^+ \to \pi^+\pi^0$	0.0298	0.1839 ± 0.0013	2993 ± 87	$0.9829 \pm 0.0284^{[1]} \pm 0.0070^{[2]}$

present the overall fit to generic MC, as described for the $K^+K^-\pi^+$ mode, in Fig. 4.99. Our measurement of the signal selection efficiency and the signal yield is presented in Table 4.70. We find the thus estimated value for $B(D_s^{*+} \to D_s^+\gamma)$ equal to 0.983 ± 0.029to be 1.4σ away from the programmed value of 0.942 in the Monte Carlo simulation.

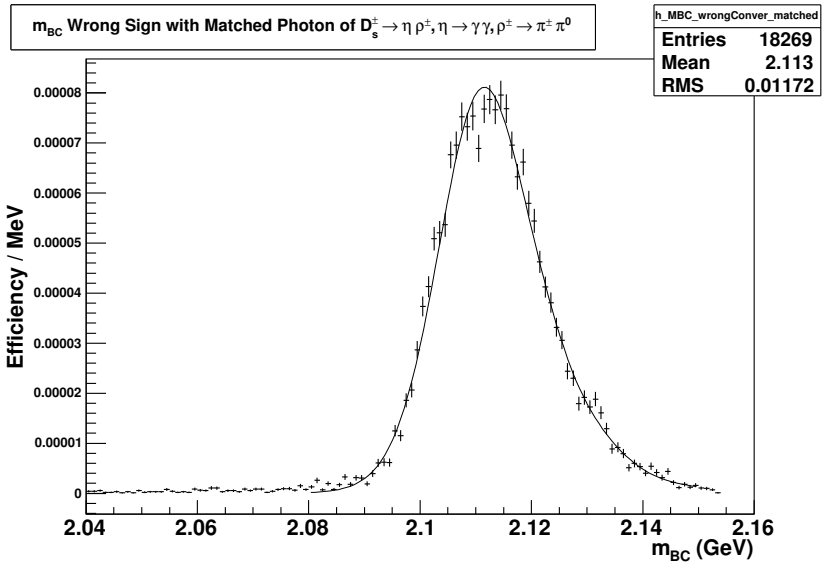

Figure 4.97: Combinatorial background in the m_{BC} distribution consisting of events where the D_s^{*+} has been reconstructed out of the D_s^- and the γ, and where both the D_s^- and the γ have been matched to their generated counterparts in the Monte Carlo simulation. This distribution has been fitted to a shape described by Eq. 4.24.

We present the distribution of m_{BC} in data and our fits to estimate the signal yield over the backgrounds, as described for the $K^+K^-\pi^+$ mode, in Fig. 4.100. Our measurements of the signal efficiency and signal yield are presented in Table 4.71.

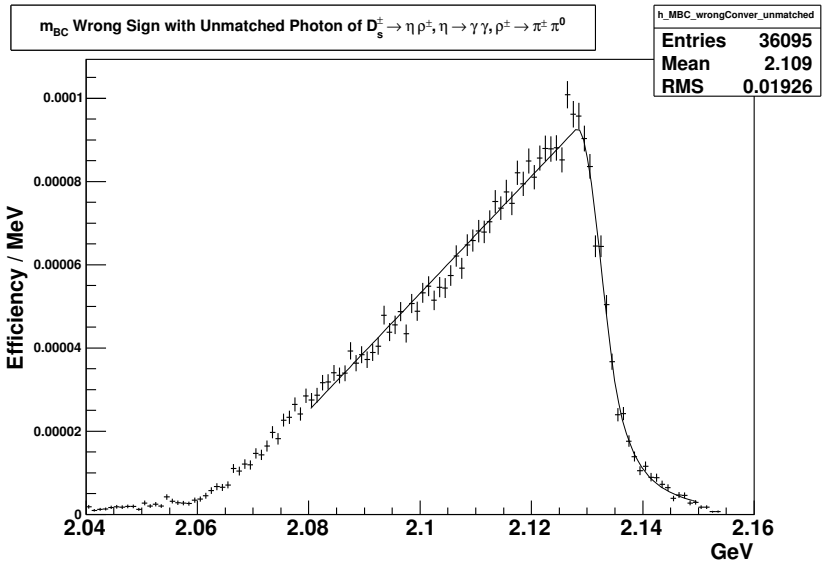

Figure 4.98: Combinatorial background structured in the m_{BC} distribution consisting of events where the D_s^{*+} has been reconstructed out of the D_s^- and the γ, and the D_s^- has been matched to its generated counterpart but the γ has failed to match the photon from the D_s^{*+} decay at the generator level of the Monte Carlo simulation. This distribution has been fitted to a shape described by Eq. 4.25.

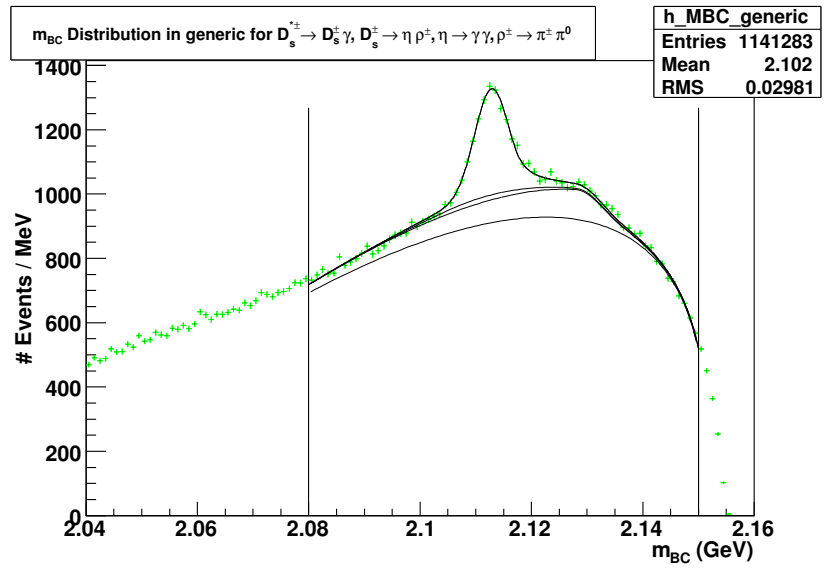

Figure 4.99: Distribution of m_{BC} of $D_s^{*+} \to D_s^+\gamma$ events where $D_s^+ \to \eta\rho^+; \eta \to \gamma\gamma; \rho^+ \to \pi^+\pi^0$ in 586 pb^{-1} of Generic Monte Carlo.

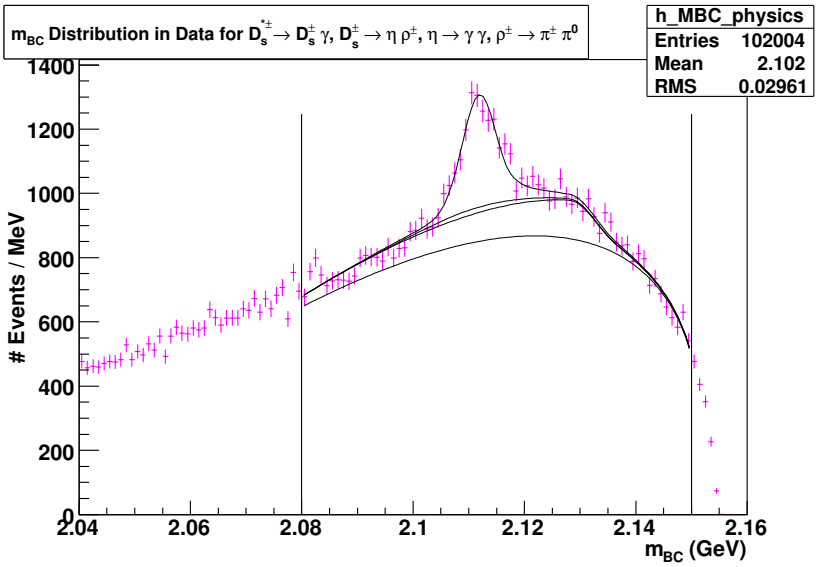

Figure 4.100: Distribution of m_{BC} of $D_s^{*+} \to D_s^+\gamma$ events where $D_s^+ \to \eta\rho^+; \eta \to \gamma\gamma; \rho^+ \to \pi^+\pi^0$ in 586 pb^{-1} of data.

Table 4.71: $\epsilon^i_{D_s\gamma}$ is the efficiency of our selection criteria for the mode. $N^i_{D_s\gamma}$ is the signal yield observed in data for this mode. $B(D_s^{*+} \to D_s^+\gamma)$ is the branching fraction for $D_s^{*+} \to D_s^+e^+e^-$ inferred from this mode. Error [1] on the inferred branching fraction is the statistical error from the final fit. Error [2] arises from the uncertainty in the branching fraction for $D_s^+ \to i$. Error [3] encapsulates the systematic uncertainties from the signal efficiency, the integrated luminosity and the production cross section for $D_s^{*\pm}D_s^{\mp}$. Error [4] encapsulates the systematic error arising from the fit.

i (Decay Mode of D_s^+)	$B(D_s^+ \to i)$	$\epsilon^i_{D_s\gamma}$	$N^i_{D_s\gamma}$
$D_s^+ \to \eta\rho^+; \eta \to \gamma\gamma; \rho^+ \to \pi^+\pi^0$	0.0348 ± 0.0031	0.1839 ± 0.0013	3170 ± 161 ± 313

Table 4.72: Selection criteria for $D_s^{*+} \to D_s^+\gamma$ events where $D_s^+ \to \eta'\pi^+; \eta' \to \rho^0\gamma$. The δm cut has been widened to accomodate the wider peak for the signal in this distribution.

Selection Criterion	Cut Center ± Width
$m_{D_s^+}$	1.969 ± 0.012 GeV
δm	0.140 ± 0.020 GeV

4.10.9 $D_s^+ \to \eta'\pi^+; \eta' \to \rho^0\gamma$

We begin with a Monte Carlo signal sample of $D_s^+ \to \eta'\pi^+; \eta' \to \rho^0\gamma$ and the D_s^- is allowed to decay generically. The selection criteria applied are tabulated in Table 4.72. Fig. 4.101 depicts the δm distribution of this signal sample and shows why the corresponding selection criterion had to be widened relative to the $D_s^{*+} \to D_s^+e^+e^-$ signal selection.

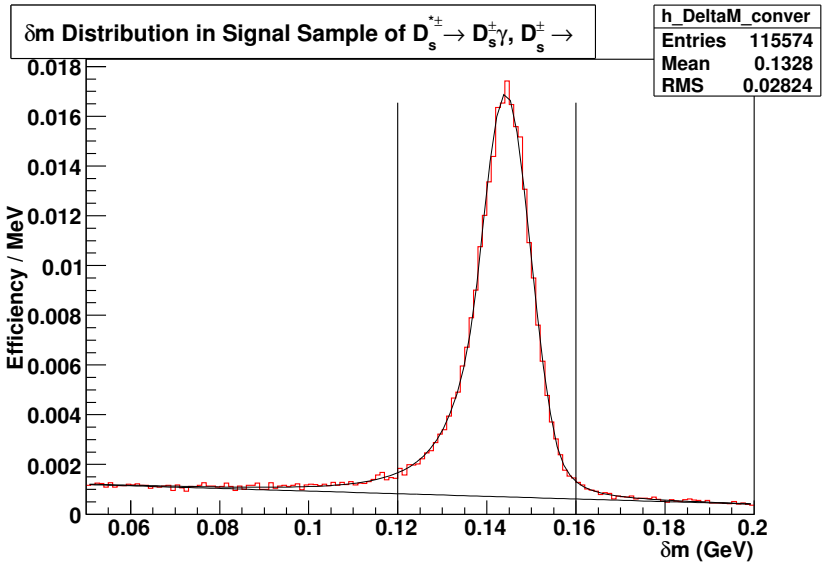

Figure 4.101: Distribution of δm in the signal Monte Carlo sample of $D_s^{*+} \to D_s^+\gamma$ events where $D_s^+ \to \eta'\pi^+; \eta' \to \rho^0\gamma$. The plot is normalized so as to directly read out the efficiency of the δm selection criterion.

To obtain the selection efficiency using the condition on m_{BC} as our last selection criterion, we produce a plot of the m_{BC} distribution of the signal sample, having applied all other criteria, as shown in Fig. 4.102. We extract the shape of the peak from the plot of m_{BC} where the D_s^+ and the photon are matched to their generated counterparts in the Monte Carlo simulation as shown in Fig. 4.103. The equations that parameterize all fits and the range they are fitted in are identical to those used in the $K^+K^-\pi^+$ mode.

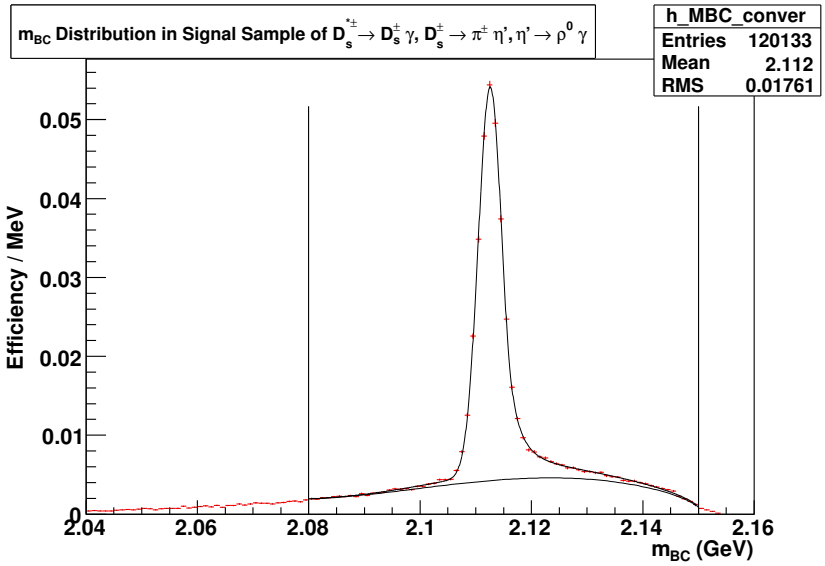

Figure 4.102: Distribution of m_{BC} in the signal Monte Carlo sample of $D_s^{*+} \to D_s^+\gamma$ events where $D_s^+ \to \eta'\pi^+; \eta' \to \rho^0\gamma$. The plot is normalized so as to directly read out the efficiency of the m_{BC} selection criterion from the area under the fit within the signal region.

Structured backgrounds arising from incorrectly reconstructed D_s^{*+} are simulated as done previously for the $K^+K^-\pi^+$ mode. Fig. 4.104 shows the structure of the D_s^- matched and photon matched background, and our fit to parameterize this shape. The background with the D_s^- matched and a photon that failed matching is shown in Fig. 4.105 along with our fit to parameterize the shape.

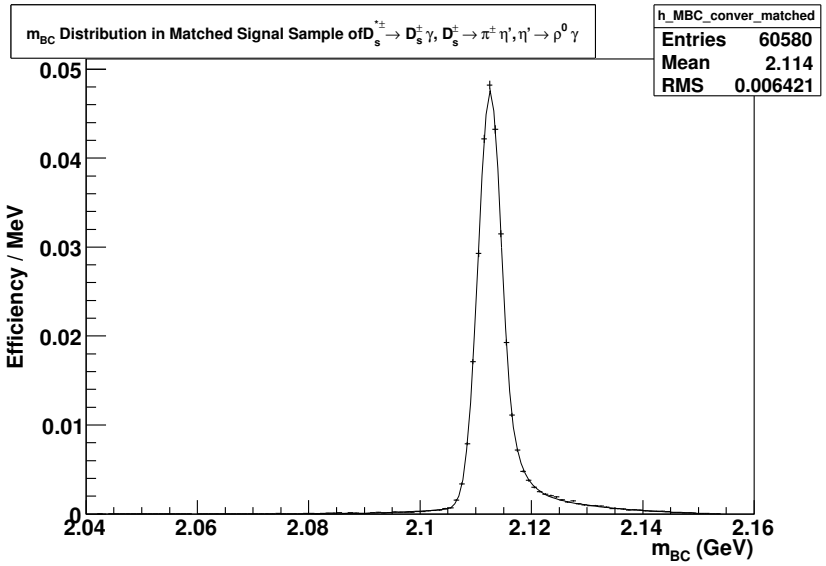

Figure 4.103: Distribution of m_{BC} in the signal Monte Carlo sample of $D_s^{*+} \to D_s^+\gamma$ events where $D_s^{*+} \to D_s^+\gamma$ events where $D_s^+ \to \eta'\pi^+; \eta' \to \rho^0\gamma$.

Table 4.73: $\epsilon^i_{D_s\gamma}$ is the efficiency of our selection criteria for the mode. $N^i_{D_s\gamma}$ is the signal yield observed in generic Monte Carlo for this mode. $B(D_s^{*+} \to D_s^+\gamma)$ is the branching fraction for $D_s^{*+} \to D_s^+e^+e^-$ inferred from this mode. Error [1] on the inferred branching fraction is the statistical error from the final fit. Error [2] encapsulates the systematic uncertainties from the signal efficiency, the integrated luminosity and the production cross section for $D_s^{*\pm}D_s^{\mp}$.

i (Decay Mode of D_s^+)	$B(D_s^+ \to i)$	$\epsilon^i_{D_s\gamma}$	$N^i_{D_s\gamma}$	$B(D_s^{*+} \to D_s^+\gamma)$ Inferred
$D_s^+ \to \eta'\pi^+; \eta' \to \rho^0\gamma$	0.0111	0.3171 ± 0.0015	1930 ± 45	$0.9886 \pm 0.0231^{[1]} \pm 0.0049^{[2]}$

As a check on how well our background and signal estimation performs, we present the overall fit to generic MC, as described for the $K^+K^-\pi^+$ mode, in Fig. 4.106. Our measurement of the signal selection efficiency and the signal yield is presented in Table 4.73. We find the thus estimated value for $B(D_s^{*+} \to D_s^+\gamma)$ equal to 0.989 ± 0.024 to be about 2σ away from the programmed value of 0.942 in the Monte Carlo simulation.

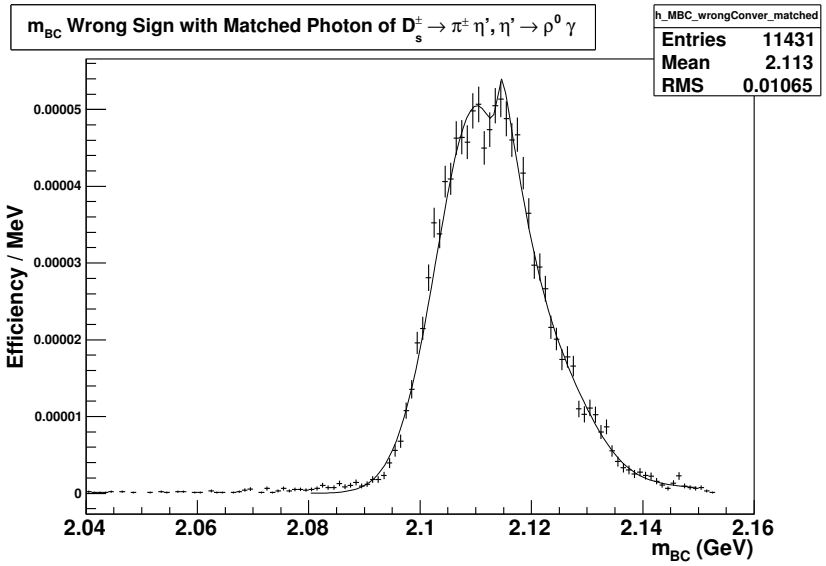

Figure 4.104: Combinatorial background in the m_{BC} distribution consisting of events where the D_s^{*+} has been reconstructed out of the D_s^- and the γ, and where both the D_s^- and the γ have been matched to their generated counterparts in the Monte Carlo simulation. This distribution has been fitted to a shape described by Eq. 4.24.

We present the distribution of m_{BC} in data and our fits to estimate the signal yield over the backgrounds, as described for the $K^+K^-\pi^+$ mode, in Fig. 4.107. Our measurements of the signal efficiency and signal yield are presented in Table 4.74.

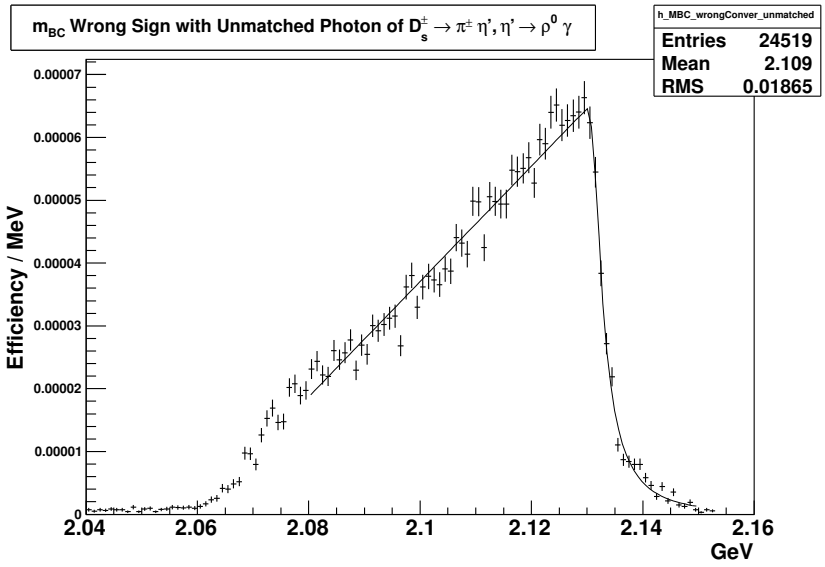

Figure 4.105: Combinatorial background structured in the m_{BC} distribution consisting of events where the D_s^{*+} has been reconstructed out of the D_s^- and the γ, and the D_s^- has been matched to its generated counterpart but the γ has failed to match the photon from the D_s^{*+} decay at the generator level of the Monte Carlo simulation. This distribution has been fitted to a shape described by Eq. 4.25.

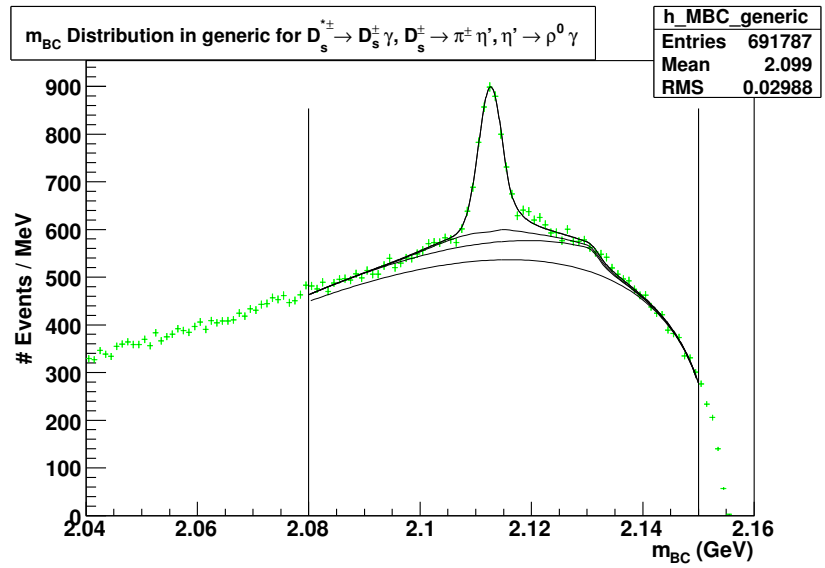

Figure 4.106: Distribution of m_{BC} of $D_s^{*+} \to D_s^+\gamma$ events where $D_s^+ \to \eta'\pi^+; \eta' \to \rho^0\gamma$ in 586 pb^{-1} of Generic Monte Carlo.

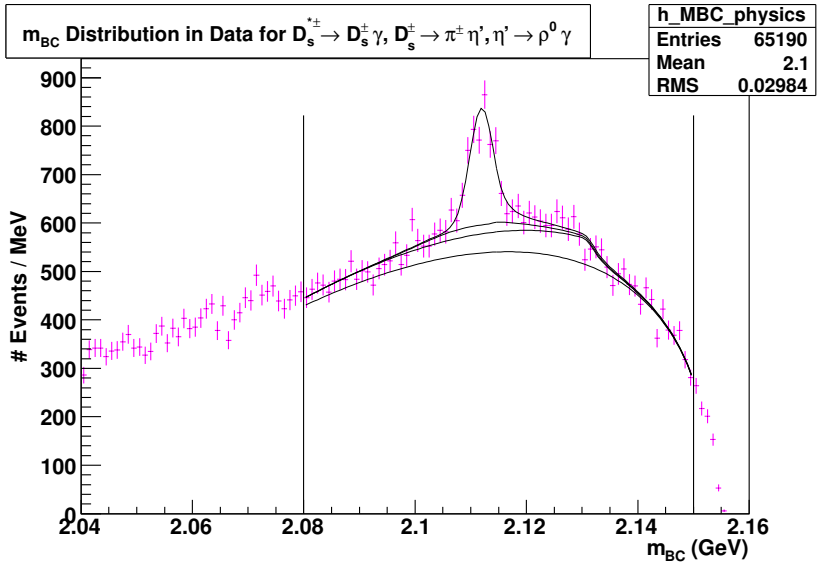

Figure 4.107: Distribution of m_{BC} of $D_s^{*+} \to D_s^+\gamma$ events where $D_s^+ \to \eta'\pi^+; \eta' \to \rho^0\gamma$ in 586 pb^{-1} of data.

Table 4.74: $\epsilon^i_{D_s\gamma}$ is the efficiency of our selection criteria for the mode. $N^i_{D_s\gamma}$ is the signal yield observed in data for this mode. $B(D_s^{*+} \to D_s^+\gamma)$ is the branching fraction for $D_s^{*+} \to D_s^+e^+e^-$ inferred from this mode. Error [1] on the inferred branching fraction is the statistical error from the final fit. Error [2] arises from the uncertainty in the branching fraction for $D_s^+ \to i$. Error [3] encapsulates the systematic uncertainties from the signal efficiency, the integrated luminosity and the production cross section for $D_s^{*\pm}D_s^{\mp}$. Error [4] encapsulates the systematic error arising from the fit.

i (Decay Mode of D_s^+)	$B(D_s^+ \to i)$	$\epsilon^i_{D_s\gamma}$	$N^i_{D_s\gamma}$
$D_s^+ \to \eta'\pi^+; \eta' \to \rho^0\gamma$	0.0112 ± 0.0012	0.3171 ± 0.0015	1531 ± 80 ± 122

4.11 Un-blinding Data and Results

Having estimated, for each decay mode of the D_s^+, the background levels in the signal region for the reconstruction of $D_s^{*+} \to D_s^+ e^+ e^-$ (Section 4.9), the efficiency of our selection criteria in reconstructing the $D_s^{*+} \to D_s^+ e^+ e^-$ (Section 4.8), and the yields and efficiencies of our selection criteria in reconstructing the $D_s^{*+} \to D_s^+ \gamma$ (Section 4.10), we are now in a position to unblind our data and observe the yield in the signal region of $D_s^{*+} \to D_s^+ e^+ e^-$. We unblind our data in the m_{BC} kinematic variable, as that is the variable we obtained our primary estimate of the background from. We count the yield in the signal region and subtract off the estimated background to determine the background subtracted yield. This is tabulated in Table 4.75, along with the significance of observing such a signal over the background and the number of signal events expected from Monte Carlo simulations. The unblinded distributions of m_{BC} for the individual modes are presented in the following sub-sections.

The statistical and systematic uncertainties in the estimated backgrounds have been derived in Section 4.9. The systematic uncertainties from the estimated backgrounds simply carry over as the systematic uncertainties in the estimated number of signal events. The statistical uncertainties in the estimated number of signal events is the quadrature sum, denoted by the symbol $\oplus$, of the statistical uncertainties in the estimated background and one standard deviation of the Poisson distribution with mean equal to the yields. That is,

$$\Delta N^i_{e^+e^-}(\text{stat}) = \Delta B^i_{e^+e^-}(\text{stat}) \oplus \Delta Y^i_{e^+e^-}$$

where i refers to a hadronic decay mode of the D_s^+, $\Delta Y^i_{e^+e^-} = \sqrt{Y^i_{e^+e^-}}$ is the statistical uncertainty in the signal yield of data found in the signal region for the i^{th} mode, $\Delta B^i_{e^+e^-}(\text{stat})$ is the statistical uncertainty in the number of background

Table 4.75: Data and estimated backgrounds in the signal region used to estimate the numbers of signal events found in each mode and the corresponding significance of the signal. Expected numbers of signal events from Monte Carlo simulations also listed.

Mode	Yield Found in the Signal Region	Estimated Background	Background Subtracted Yield in Signal Region	Expected Signal Yield from Monte Carlo	Signal Significance
i	$Y^i_{e^+e^-}$	$B^i_{e^+e^-}$ ± stat ± syst	$N^i_{e^+e^-}$ ± stat ± syst	± stat	
$K^+K^-\pi^+$	14	1.05 ± 0.37 ± 0.79	12.95 ± 3.76 ± 0.79	13.65 ± 0.65	5.13
$K_S K^+$	1	0.85 ± 0.43 ± 0.74	0.15 ± 1.09 ± 0.74	3.02 ± 0.15	0.73
$\eta\pi^+$	4	1.40 ± 0.70 ± 0.49	2.60 ± 2.12 ± 0.49	1.81 ± 0.08	1.66
$\eta'\pi^+;\eta' \to \pi^+\pi^-\eta$	4	0.00 + 0.63 + 0.00	4.00 ± 2.10 ± 0.00	1.20 ± 0.06	2.68
$K^+K^-\pi^+\pi^0$	6	1.70 ± 0.47 ± 0.56	4.30 ± 2.49 ± 0.56	4.85 ± 0.29	2.34
$\pi^+\pi^-\pi^+$	7	1.57 ± 0.45 ± 0.59	5.43 ± 2.68 ± 0.59	3.75 ± 0.17	2.79
$K^{*+}K^{*0}$	4	1.58 ± 0.53 ± 0.40	2.42 ± 2.07 ± 0.40	1.99 ± 0.11	1.65
$\eta\rho^+$	7	2.62 ± 0.59 ± 0.23	4.38 ± 2.71 ± 0.23	5.49 ± 0.31	2.23
$\eta'\pi^+;\eta' \to \rho^0\gamma$	4	1.84 ± 0.49 ± 0.25	2.16 ± 2.06 ± 0.25	2.42 ± 0.12	1.52
Sum of all modes	51	12.61 ± 2.50 ± 1.08	38.39 ± 7.32 ± 1.53	38.18 ± 0.83	6.39

events to $D_s^{*+} \to D_s^+ e^+ e^-$ we expected in the signal region for the i^{th} mode, and $\Delta N^i_{e^+e^-}$(stat) is the statistical uncertainty in the background subtracted yield in our signal region for the i^{th} mode.

We tabulate the signal yields and efficiencies for $D_s^{*+} \to D_s^+ e^+ e^-$ and $D_s^{*+} \to D_s^+ \gamma$ in Table 4.76. In it we compute and tabulate the ratio of branching fractions

$$K = \frac{B(D_s^{*+} \to D_s^+ e^+ e^-)}{B(D_s^{*+} \to D_s^+ \gamma)}$$

for each mode using Eq. 4.26 and with all modes using Eq. 4.27.

$$K = \left(\frac{N^i_{e^+e^-}}{N^i_\gamma}\right)\left(\frac{\epsilon^i_{D_s^+\gamma}}{\epsilon^i_{D_s^+e^+e^-}}\right) \tag{4.26}$$

$$K = \left(\frac{\sum_i N^i_{e^+e^-}}{\sum_i N^i_\gamma}\right)\left(\frac{\sum_i \epsilon^i_{D_s^+\gamma} B(D_s^+ \to i)}{\sum_i \epsilon^i_{D_s^+e^+e^-} B(D_s^+ \to i)}\right) \tag{4.27}$$

where K is the aforementioned ratio of branching fractions we're trying to measure, N^i_γ is the background subtracted yield of $D^{*+}_s \to D^+_s\gamma$ events we find in our signal region for the i^{th} mode of D^+_s decay, and $\epsilon^i_{D^+_s\gamma}$ encodes the detection and selection efficiency for the $D^{*+}_s \to D^+_s\gamma$ selection criteria, for the i^{th} mode of D^+_s decay.

Uncertainties in the ratio of branching fractions, K, are calculated for each mode using Eq. 4.28 and Eq. 4.29.

$$\left(\frac{\Delta K(\text{stat})}{K}\right)^2 = \left(\frac{\Delta N^i_{e^+e^-}(\text{stat})}{N^i_{e^+e^-}}\right)^2 + \left(\frac{\Delta N^i_\gamma(\text{stat})}{N_\gamma}\right)^2 \tag{4.28}$$

$$\left(\frac{\Delta K(\text{syst})}{K}\right)^2 = \left(\frac{\Delta N^i_{e^+e^-}(\text{syst})}{N^i_{e^+e^-}}\right)^2 + \left(\frac{\Delta N^i_\gamma(\text{syst})}{N^i_\gamma}\right)^2 + \left(\frac{\Delta \epsilon^i_{D^+_s e^+e^-}}{\epsilon^i_{D^+_s e^+e^-}}\right)^2 + \left(\frac{\Delta \epsilon^i_{D^+_s\gamma}}{\epsilon^i_{D^+_s\gamma}}\right)^2 \tag{4.29}$$

Uncertainties in the ratio of branching fractions, K, are calculated using the sum of all modes as follows. The statistical uncertainty depends solely on the statistical uncertainties associated with the signal yields, $N^i_{e^+e^-}$ and N^i_γ. These statistical uncertainties for each mode are tabulated in Table 4.76. Therefore, the statistical uncertainty in K is calculated using Eq. 4.30.

$$\left(\frac{\Delta K(\text{stat})}{K}\right)^2 = \frac{\sum_i (\Delta N^i_{e^+e^-}(\text{stat}))^2}{(\sum_i N^i_{e^+e^-})^2} + \frac{\sum_i (\Delta N^i_\gamma)^2}{(\sum_i N_\gamma)^2} \tag{4.30}$$

For an estimate of the systematic error, we decompose Eq. 4.27 as

$$K = \left(\frac{\sum_i N^i_{e^+e^-}}{\sum_i N^i_\gamma}\right)\left(\frac{\epsilon_\gamma}{\epsilon_{e^+e^-}}\right)\left(\frac{\sum_i \epsilon^i_{D^+_s} B(D^+_s \to i)}{\sum_i \epsilon^i_{D^+_s} B(D^+_s \to i)}\right) \tag{4.31}$$

where ϵ_γ and $\epsilon_{e^+e^-}$ are the reconstruction efficiencies for the photon and the e^+e^- which are common to all modes of the D^+_s decay, and $\epsilon^i_{D^+_s}$ is the reconstruction

Table 4.76: The ratio of branching fractions $B(D_s^{*+} \to D_s^+ e^+ e^-)/B(D_s^{*+} \to D_s^+ \gamma)$ inferred from the signal yields and efficiencies of each and all modes.

D_s^+ Decay	$B(D_s^+ \to i)$	$D_s^{*+} \to D_s^+ e^+ e^-$		$D_s^{*+} \to D_s^+ \gamma$		
Mode		Signal Events	Selection Efficiency	Signal Events	Selection Efficiency	$K = \frac{B(D_s^{*+} \to D_s^+ e^+ e^-)}{B(D_s^{*+} \to D_s^+ \gamma)}$
i		$N^i_{e^+e^-}$	$\epsilon^i_{D_s^+ e^+ e^-}$	N^i_γ	$\epsilon^i_{D_s^+ \gamma}$	
		± stat ± syst		± stat ± syst		± stat ± syst
$K^+K^-\pi^+$	0.0550 ± 0.0028	12.95 ± 3.76 ± 0.79	0.0730 ± 0.0019	9114 ± 110 ± 201	0.339 ± 0.002	0.0066 ± 0.0019 ± 0.0005
$K_S K^+$	0.0149 ± 0.0009	0.15 ± 1.09 ± 0.74	0.0597 ± 0.0017	1902 ± 57 ± 45	0.2573 ± 0.0004	0.0003 ± 0.0025 ± 0.0017
$\eta\pi^+; \eta \to \gamma\gamma$	0.0062 ± 0.0008	2.60 ± 2.12 ± 0.49	0.0855 ± 0.0021	1037 ± 46 ± 37	0.3310 ± 0.0015	0.0097 ± 0.0079 ± 0.0019
$\eta'\pi^+; \eta' \to \pi^+\pi^-\eta; \eta \to \gamma\gamma$	0.0067 ± 0.0007	4.00 ± 2.10 ± 0.00	0.0530 ± 0.0016	691 ± 34 ± 40	0.2101 ± 0.0013	0.023 ± 0.0123 ± 0.0015
$K^+K^-\pi^+\pi^0$	0.056 ± 0.005	4.30 ± 2.49 ± 0.56	0.0255 ± 0.0011	3592 ± 118 ± 72	0.1225 ± 0.0010	0.0058 ± 0.0033 ± 0.0008
$\pi^+\pi^-\pi^+$	0.0111 ± 0.0008	5.43 ± 2.68 ± 0.59	0.0992 ± 0.0022	2745 ± 93 ± 52	0.4583 ± 0.0018	0.0091 ± 0.0045 ± 0.0010
$K^{*+}K^{*0}$	0.0164 ± 0.0012	2.42 ± 2.07 ± 0.40	0.0356 ± 0.0013	1570 ± 74 ± 13	0.1913 ± 0.0012	0.0083 ± 0.0071 ± 0.0014
$\eta\rho^+; \eta \to \gamma\gamma; \rho^+ \to \pi^+\pi^0$	0.0298 ± 0.0051	4.38 ± 2.71 ± 0.23	0.0316 ± 0.0013	3170 ± 161 ± 313	0.1839 ± 0.0013	0.0080 ± 0.0050 ± 0.0010
$\eta'\pi^+; \eta' \to \rho^0\gamma$	0.0112 ± 0.0012	2.16 ± 2.06 ± 0.25	0.064 ± 0.0018	1531 ± 80 ± 122	0.3171 ± 0.0015	0.0070 ± 0.0067 ± 0.0010
Sum of all modes		38.39 ± 7.32 ± 1.53		25351.03 ± 280.93		0.0072 ± 0.0014 ± 0.0003

efficiency for the D_s^+ as it decays into the i^{th} hadronic decay mode. This can be simplified to

$$K = \left(\frac{\sum_i N^i_{e^+e^-}}{\sum_i N^i_\gamma}\right)\left(\frac{\epsilon_\gamma}{\epsilon_{e^+e^-}}\right) \tag{4.32}$$

Therefore, we may estimate the systematic uncertainty in K as given in Eq. 4.33.

$$\left(\frac{\Delta K(\text{syst})}{K}\right)^2 = \frac{\sum_i(\Delta N^i_{e^+e^-}(\text{syst}))^2}{(\sum_i N^i_{e^+e^-})^2} \oplus \frac{\sum_i(\Delta N^i_\gamma(\text{syst}))^2}{(\sum_i N^i_\gamma)^2} \oplus \left(\frac{\Delta(\epsilon_\gamma/\epsilon_{e^+e^-})}{\epsilon_\gamma/\epsilon_{e^+e^-}}\right)^2 \tag{4.33}$$

A plot of the m_{BC} and δm distributions in unblinded data summed over all modes are presented in Fig. 4.108 and Fig. 4.109. The data points are marked by magenta points with error bars. The data-driven estimated backgrounds are marked by the black and magenta curves. The cyan histograms mark the expected signal yield. The agreement with data is remarkable. Histograms of unblinded data in each of the individual modes are presented in the following subsections.

Table 4.75 summarizes the signal yield observed in all modes and their significances. The total signal yield of 51 events carries a significance of 6.39 σ. The signal yields and efficiencies for $D_s^{*+} \to D_s^+ e^+ e^-$ that we just unblinded and $D_s^{*+} \to D_s^+ \gamma$ discussed in Section 4.10 are tabulated together in Table 4.75. The ratio of branching fractions $B(D_s^{*+} \to D_s^+ e^+ e^-)/B(D_s^{*+} \to D_s^+ \gamma)$ are calculated from each mode and with all modes combined. The measurement of this ratio using the combination of all modes is given in Eq. 4.34. However, the systematic uncertainty in K has been estimated only using the systematic uncertainties in the signal yields for $D_s^{*+} \to D_s^+ e^+ e^-$ and $D_s^{*+} \to D_s^+ \gamma$. We must also include the systematic uncertainty arising from the reconstruction of soft e^+e^- pairs and the γ as indicated in Eq. 4.33 for a complete result.

$$K = \frac{B(D_s^{*+} \to D_s^+ e^+ e^-)}{B(D_s^{*+} \to D_s^+ \gamma)} = (0.72 \pm 0.14(\text{stat}) \pm 0.03(\text{syst}))\% \tag{4.34}$$

This last source of systematic uncertainty is estimated in Section 4.12. There we measure this fractional uncertainty to be 6.51%. 6.51% of 0.72% is 0.047% and therefore, our final result stands to be:

$$K = \frac{B(D_s^{*+} \to D_s^+ e^+ e^-)}{B(D_s^{*+} \to D_s^+ \gamma)} = (0.72 \pm 0.14(\text{stat}) \pm 0.06(\text{syst}))\% \tag{4.35}$$

where

- (stat) is the statistical uncertainty arising from the limited signal yields of $D_s^{*+} \to D_s^+ e^+ e^-$ and $D_s^{*+} \to D_s^+ \gamma$. Larger datasets will decrease this error.
- (syst) is the systematic uncertainty arising from systematic uncertainties in the estimated background for the $D_s^{*+} \to D_s^+ e^+ e^-$ signal, systematic uncertainties in the signal yield for $D_s^{*+} \to D_s^+ \gamma$, and the systematic uncertainty arising from the $e^+ e^-$ and γ reconstruction efficiencies in the energy range relevant for this analysis.

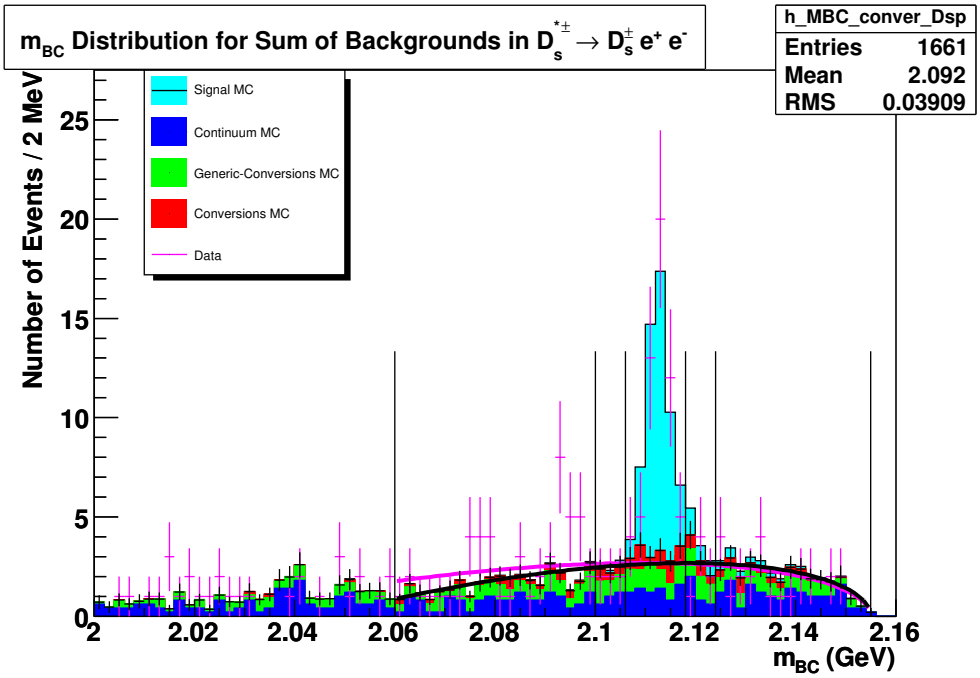

Figure 4.108: Distribution of m_{BC} in data after unblinding.

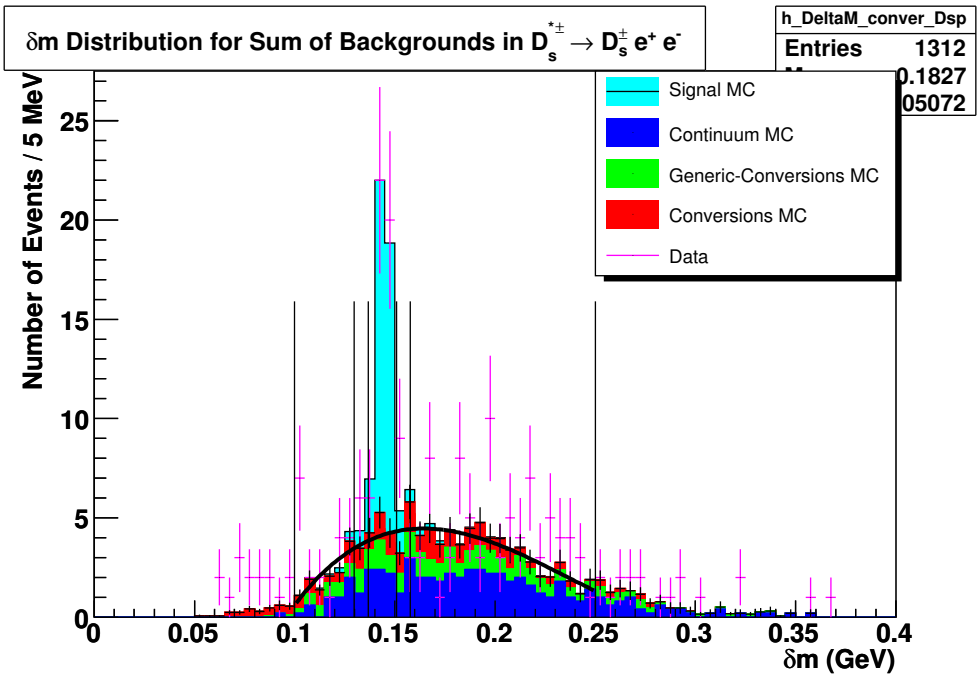

Figure 4.109: Distribution of δm in data after unblinding.

4.11.1 $D_s^+ \to K^+K^-\pi^+$

The distributions of m_{BC} and δm in data after unblinding are presented overlaid with Monte Carlo in Fig. 4.110 and 4.111. A mean of 14.7 events were expected from Monte Carlo simulations and 14 events were observed. The significance for this observation is 5.13 σ.

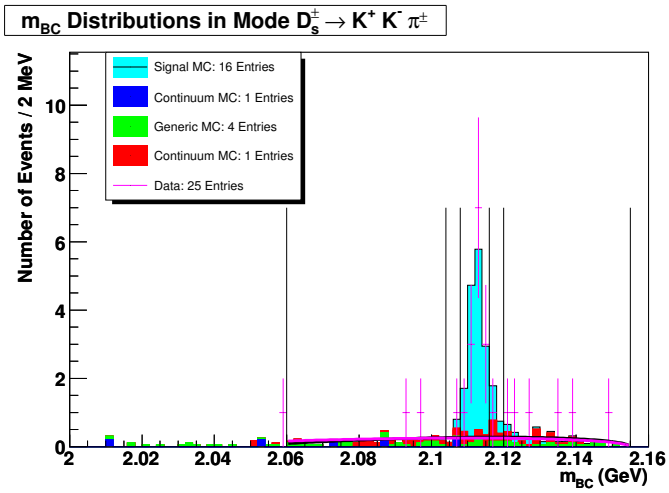

Figure 4.110: Distribution of m_{BC} in data after unblinding overlaid with prediction from Monte Carlo.

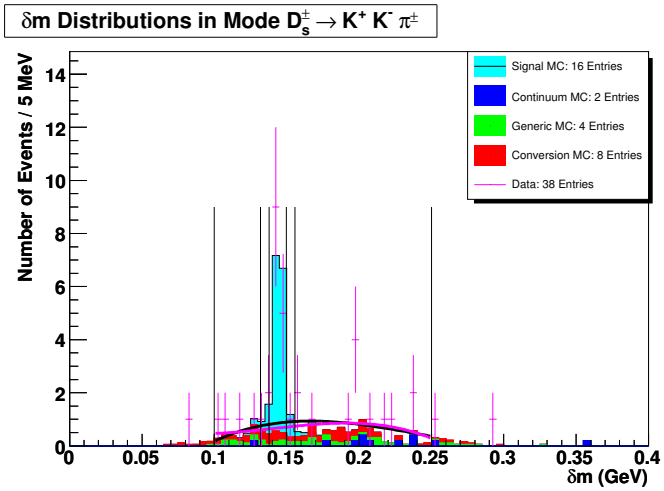

Figure 4.111: Distribution of δm in data after unblinding overlaid with prediction from Monte Carlo.

4.11.2 $D_s^+ \to K_S K^+$

The distributions of m_{BC} and δm in data after unblinding are presented overlaid with Monte Carlo in Fig. 4.112 and 4.113. A mean of 3.87 events were expected from Monte Carlo simulations and 1 events was observed. The significance for this observation is 0.73 σ.

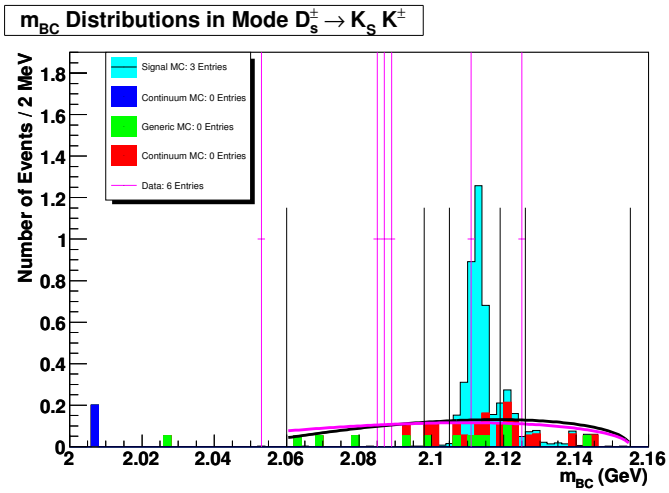

Figure 4.112: Distribution of m_{BC} in data after unblinding overlaid with prediction from Monte Carlo.

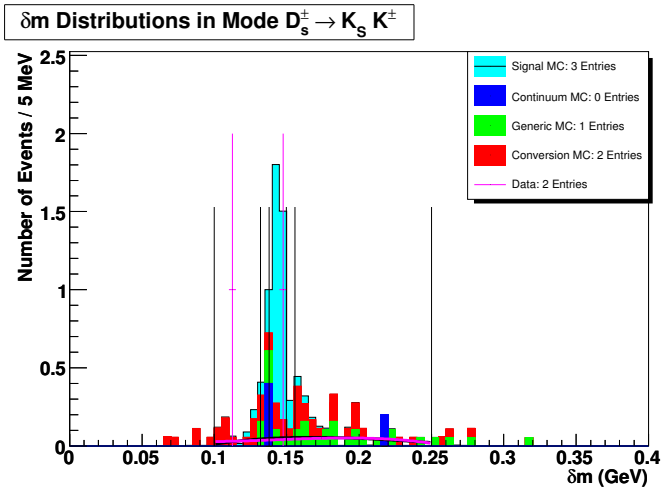

Figure 4.113: Distribution of δm in data after unblinding overlaid with prediction from Monte Carlo.

4.11.3 $D_s^+ \to \eta\pi^+; \eta \to \gamma\gamma$

The distributions of m_{BC} and δm in data after unblinding are presented overlaid with Monte Carlo in Fig. 4.114 and 4.115. A mean of 3.21 events were expected from Monte Carlo simulations and 4 events were observed. The significance for this observation is 1.66 σ.

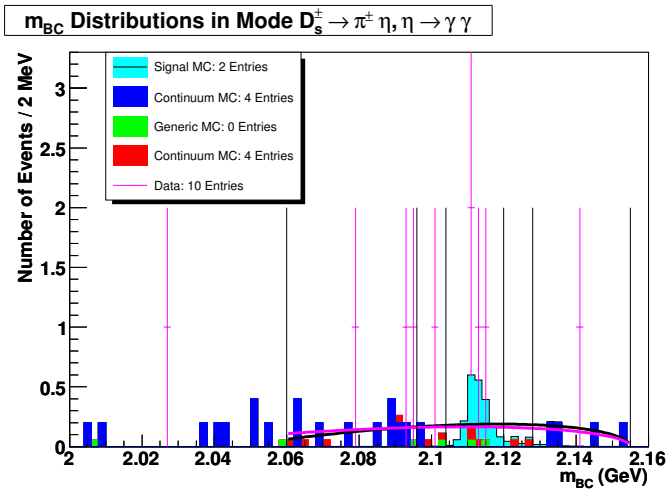

Figure 4.114: Distribution of m_{BC} in data after unblinding overlaid with prediction from Monte Carlo.

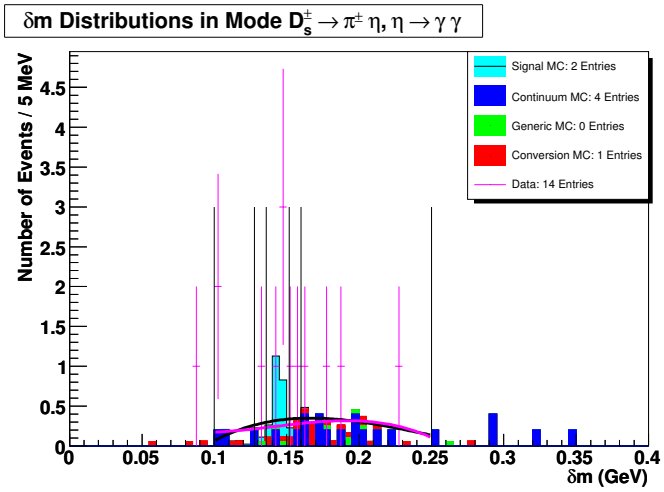

Figure 4.115: Distribution of δm in data after unblinding overlaid with prediction from Monte Carlo.

4.11.4 $D_s^+ \to \eta'\pi^+; \eta' \to \pi^+\pi^-\eta; \eta \to \gamma\gamma$

The distributions of m_{BC} and δm in data after unblinding are presented overlaid with Monte Carlo in Fig. 4.116 and 4.117. 1.20 events were expected from Monte Carlo simulations and 4 events were observed. The significance for this observation is 2.68 σ.

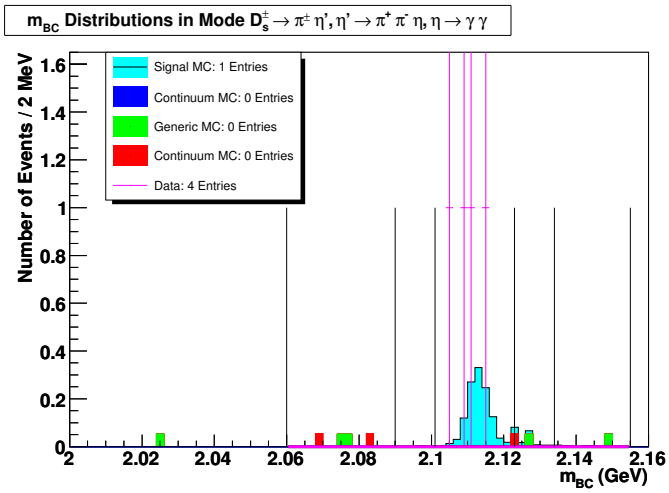

Figure 4.116: Distribution of m_{BC} in data after unblinding overlaid with prediction from Monte Carlo.

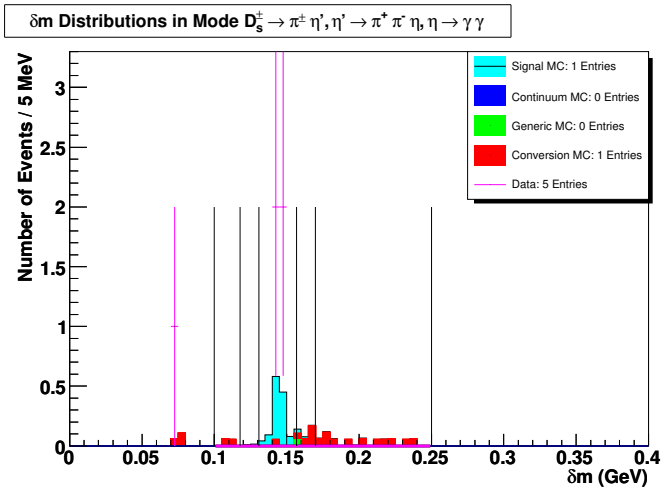

Figure 4.117: Distribution of δm in data after unblinding overlaid with prediction from Monte Carlo.

4.11.5 $D_s^+ \to K^+K^-\pi^+\pi^0$

The distributions of m_{BC} and δm in data after unblinding are presented overlaid with Monte Carlo in Fig. 4.118 and 4.119. 6.55 events were expected from Monte Carlo simulations and 6 events were observed. The significance for this observation is 2.34 σ.

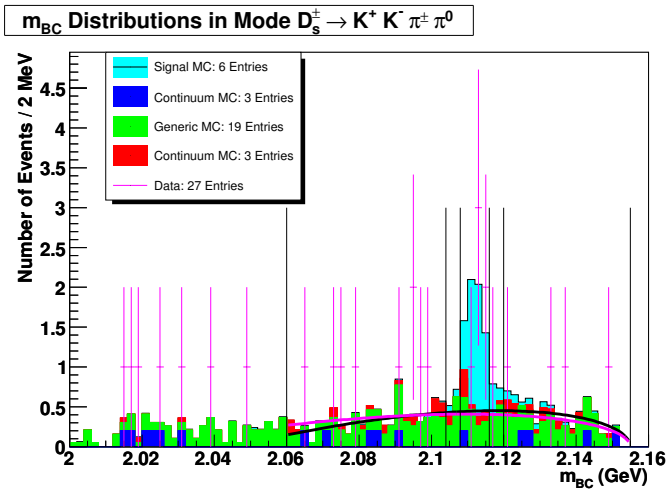

Figure 4.118: Distribution of m_{BC} in data after unblinding overlaid with prediction from Monte Carlo.

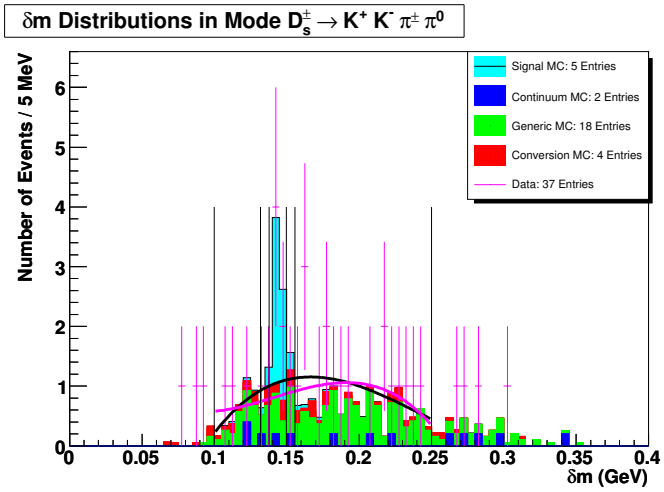

Figure 4.119: Distribution of δm in data after unblinding overlaid with prediction from Monte Carlo.

4.11.6 $D_s^+ \to \pi^+\pi^-\pi^+$

The distributions of m_{BC} and δm in data after unblinding are presented overlaid with Monte Carlo in Fig. 4.120 and 4.121. 5.32 events were expected from Monte Carlo simulations and 7 events were observed. The significance for this observation is 2.79 σ.

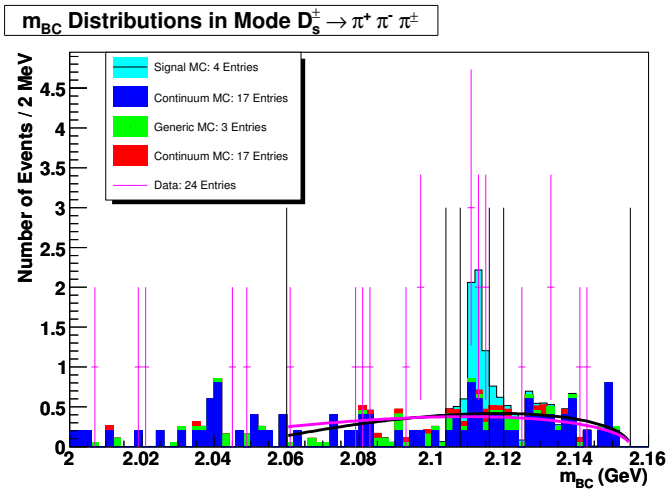

Figure 4.120: Distribution of m_{BC} in data after unblinding overlaid with prediction from Monte Carlo.

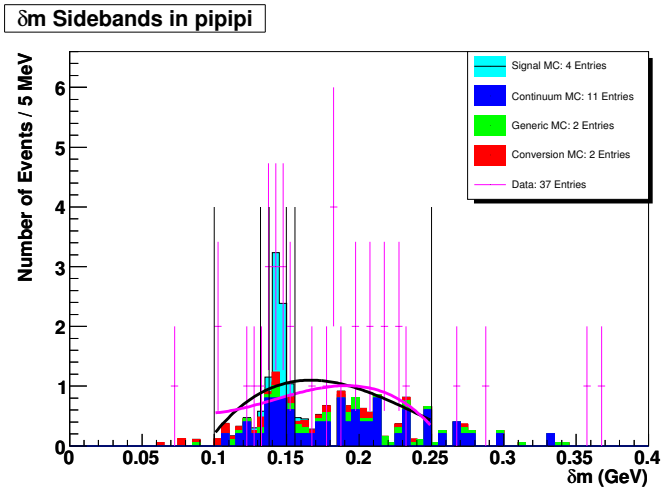

Figure 4.121: Distribution of δm in data after unblinding overlaid with prediction from Monte Carlo.

4.11.7 $D_s^+ \to K^{*+}K^{*0}; K^{*+} \to K_S^0\pi^+; K^{*0} \to K^-\pi^+$

The distributions of m_{BC} and δm in data after unblinding are presented overlaid with Monte Carlo in Fig. 4.122 and 4.123. 3.57 events were expected from Monte Carlo simulations and 4 events were observed. The significance for this observation is 1.65 σ.

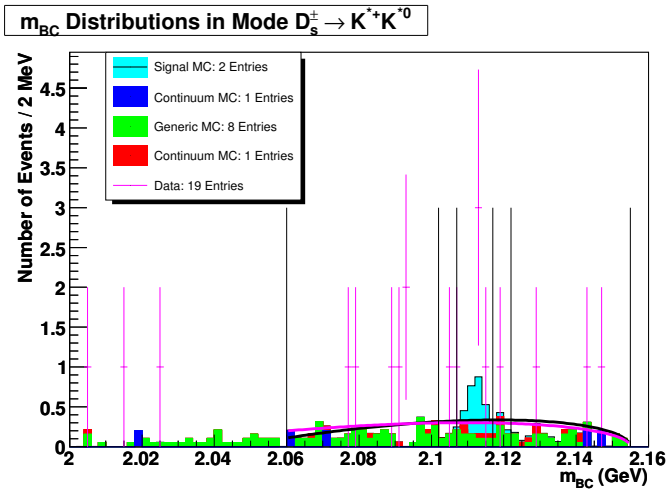

Figure 4.122: Distribution of m_{BC} in data after unblinding overlaid with prediction from Monte Carlo.

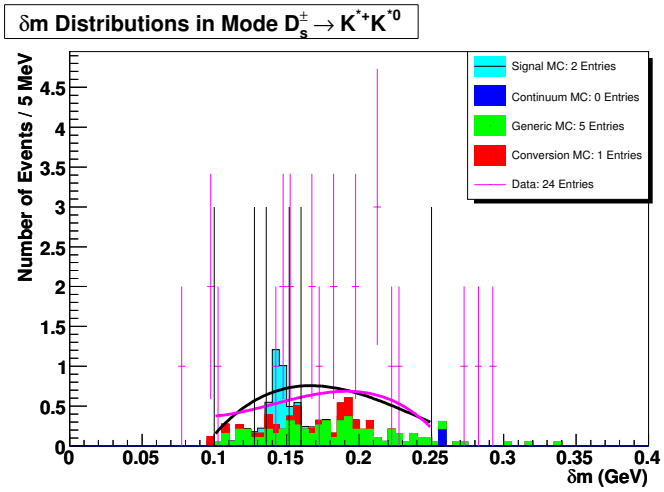

Figure 4.123: Distribution of δm in data after unblinding overlaid with prediction from Monte Carlo.

4.11.8 $D_s^+ \to \eta\rho^+; \eta \to \gamma\gamma; \rho^+ \to \pi^+\pi^0$

The distributions of m_{BC} and δm in data after unblinding are presented overlaid with Monte Carlo in Fig. 4.124 and 4.125. 8.11 events were expected from Monte Carlo simulations and 7 events were observed. The significance for this observation is 2.23 σ.

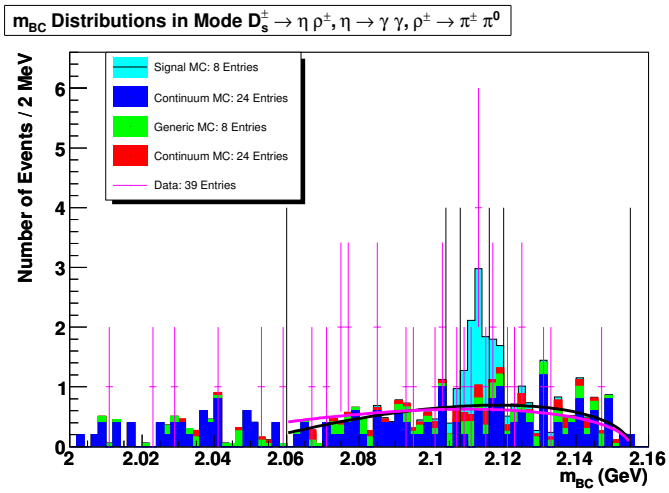

Figure 4.124: Distribution of m_{BC} in data after unblinding overlaid with prediction from Monte Carlo.

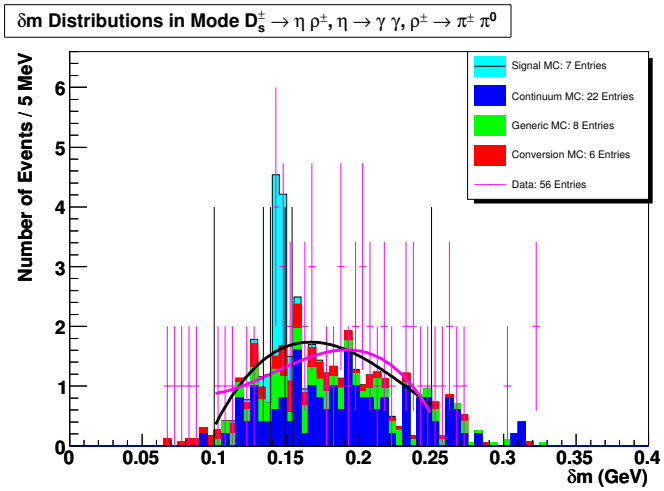

Figure 4.125: Distribution of δm in data after unblinding overlaid with prediction from Monte Carlo.

4.11.9 $D_s^+ \to \eta'\pi^+; \eta' \to \rho^0\gamma$

The distributions of m_{BC} and δm in data after unblinding are presented overlaid with Monte Carlo in Fig. 4.126 and 4.127. 4.26 events were expected from Monte Carlo simulations and 4 events were observed. The significance for this observation is 1.52 σ.

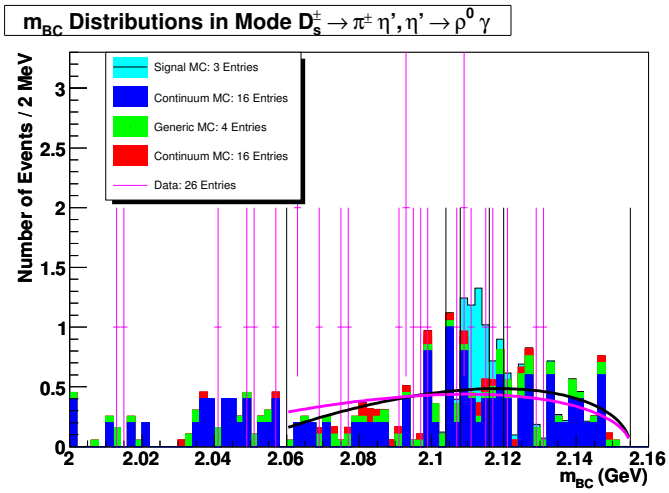

Figure 4.126: Distribution of m_{BC} in data after unblinding overlaid with prediction from Monte Carlo.

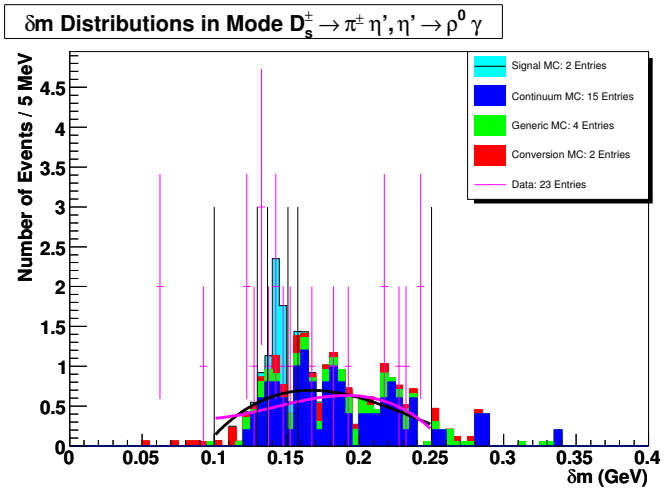

Figure 4.127: Distribution of δm in data after unblinding overlaid with prediction from Monte Carlo.

4.11.10 Comparison of $m_{e^+e^-}$ between Data and Monte Carlo Simulation

Fig. 4.128 shows the distribution of the invariant mass of the e^+e^- in the 51 data points uncovered when compared to the general shape predicted by our Monte Carlo simulations. It must be noted that we did not depend on the numbers from Monte Carlo for our estimation of the backgrounds. This plot is presented as a rough check. The Kolmogorov probability for the data and Monte Carlo points to have come from the same distribution is found to be 0.86.

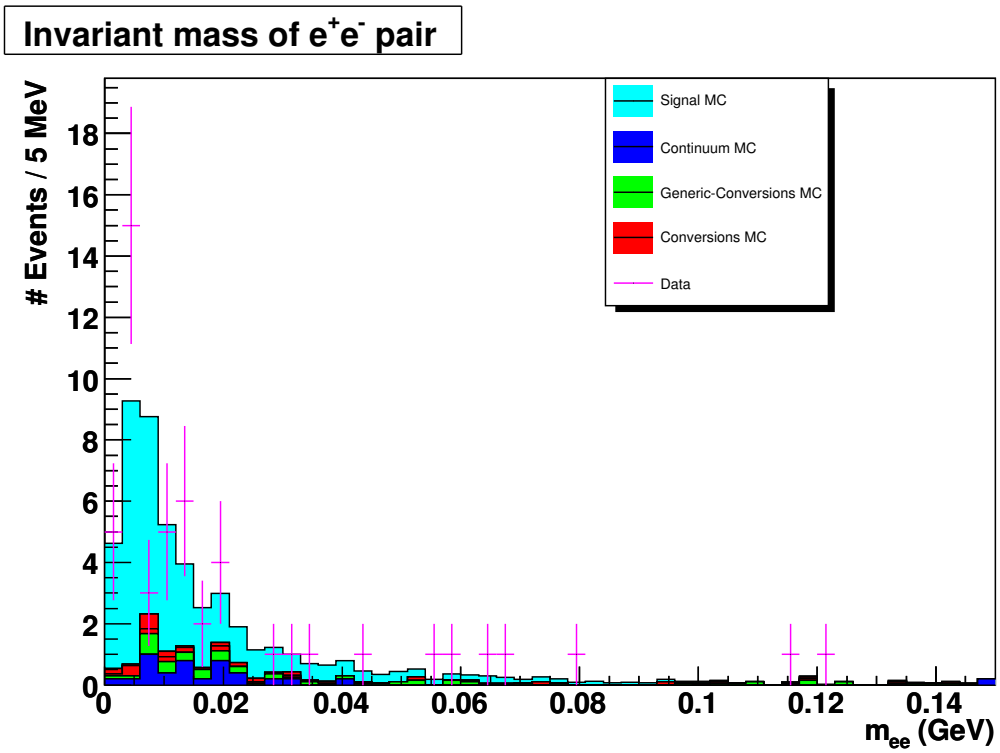

Figure 4.128: Distribution of $m_{e^+e^-}$ in data after unblinding overlaid with prediction from Monte Carlo.

4.11.11 A Re-evaluation of All D_s^{*+} Branching Fractions

Now that we have a measurement of the ratio of branching fractions $B(D_s^{*+} \to D_s^+ e^+ e^-)/B(D_s^{*+} \to D_s^+ \gamma)$, we may combine it with the measurement of $B(D_s^{*+} \to D_s^+ \pi^0)/B(D_s^{*+} \to D_s^+ \gamma)$ as measured by the BABAR collaboration [5] to re-evaluate the absolute branching fractions $B(D_s^{*+} \to D_s^+ \gamma)$, $B(D_s^{*+} \to D_s^+ \pi^0)$ and $B(D_s^{*+} \to D_s^+ e^+ e^-)$. For notational convenience, we shall denote $B(D_s^{*+} \to D_s^+ \gamma)$ by b_γ, $B(D_s^{*+} \to D_s^+ \pi^0)$ by b_{π^0} and $B(D_s^{*+} \to D_s^+ e^+ e^-)$ by $b_{e^+e^-}$. If we call our measurements of the ratios m_1 and m_2 as indicated in Eq. 4.36 & 4.37,

$$m_1 = \frac{b_{\pi^0}}{b_\gamma} = 0.062 \pm 0.005 \pm 0.006 \tag{4.36}$$

$$m_2 = \frac{b_{e^+e^-}}{b_\gamma} = 0.0072 \pm 0.0014 \pm 0.0006 \tag{4.37}$$

and have the absolute branching fractions add up to unity, we may write

$$b_\gamma = \frac{1}{1 + m_1 + m_2} \tag{4.38}$$

$$\Delta b_\gamma = \frac{\partial b_\gamma}{\partial m_1}\Delta m_1 \oplus \frac{\partial b_\gamma}{\partial m_2}\Delta m_2 \tag{4.39}$$

where

$$\frac{\partial b_\gamma}{\partial m_1} = \frac{\partial b_\gamma}{\partial m_2} = \frac{-1}{(1 + m_1 + m_2)^2}$$

In a similar vein, one may write the solutions for b_{π^0} and $b_{e^+e^-}$ as follows.

$$b_{\pi^0} = \frac{m_1}{1 + m_1 + m_2} \tag{4.40}$$

$$\Delta b_{\pi^0} = \frac{\partial b_{\pi^0}}{\partial m_1}\Delta m_1 \oplus \frac{\partial b_{\pi^0}}{\partial m_2}\Delta m_2 \tag{4.41}$$

where

$$\frac{\partial b_{\pi^0}}{\partial m_1} = \frac{1 + m_2}{(1 + m_1 + m_2)^2}$$

$$\frac{\partial b_{\pi^0}}{\partial m_2} = \frac{-m_1}{(1+m_1+m_2)^2}$$

and

$$b_{e^+e^-} = \frac{m_2}{1+m_1+m_2} \tag{4.42}$$

$$\Delta b_{e^+e^-} = \frac{\partial b_{e^+e^-}}{\partial m_1}\Delta m_1 \oplus \frac{\partial b_{e^+e^-}}{\partial m_2}\Delta m_2 \tag{4.43}$$

where

$$\frac{\partial b_{e^+e^-}}{\partial m_1} = \frac{-m_2}{(1+m_1+m_2)^2}$$
$$\frac{\partial b_{e^+e^-}}{\partial m_2} = \frac{1+m_1}{(1+m_1+m_2)^2}$$

We evaluate these derivatives using the central values of the measurements m_1 and m_2 and propagate the statistical and systematic errors independently to give us absolute measures for the branching fractions of the D_s^{*+} thus far discovered.

$$B(D_s^{*+} \to D_s^+\gamma) = (93.5 \pm 0.5 \pm 0.5)\% \tag{4.44}$$

$$B(D_s^{*+} \to D_s^+\pi^0) = (5.8 \pm 0.4 \pm 0.5)\% \tag{4.45}$$

$$B(D_s^{*+} \to D_s^+e^+e^-) = (0.67 \pm 0.13 \pm 0.05)\% \tag{4.46}$$

4.12 Systematic Uncertainties from the Tracking of Soft Electrons and Photons

As reported in Section 4.11, systematic errors in the measurement of $\epsilon_{e^+e^-}/\epsilon_\gamma$ will contribute to the systematic uncertainty in our measurement of the ratio of branching fractions $B(D_s^{*+} \to D_s^+ e^+ e^-)/B(D_s^{*+} \to D_s^+ \gamma)$. In this section, we seek to estimate the systematic uncertainty in the measurement of $\epsilon_{e^+e^-}/\epsilon_\gamma$ in the energy range relevant for our analysis by studying the decay of $\psi(2S)$ mesons to $J/\psi\pi^0\pi^0$. We estimate this systematic error by measuring the ratio of the numbers of events where one of the π^0 Dalitz decays to $\gamma e^+ e^-$ to the number of events where both π^0 decay to $\gamma\gamma$ and comparing this to the ratio expected from the currently accepted branching fractions for $\pi^0 \to \gamma e^+ e^-$ and $\pi^0 \to \gamma\gamma$.

Dataset 42, which contains 53 pb^{-1} of data taken at the $\psi(2S)$ resonance, was used for this study. Since soft electrons from the Dalitz decay of the π^0 would also suffer from the systematic deviation in their energy and other track parameters if their tracks are fitted to the pion mass hypothesis, we reprocessed this dataset to include track fits to the electron mass hypothesis. This has been described in Section 4.5.

In the following paragraphs, we describe a method that completely reconstructs the $\psi(2S)$ from its decay into $J/\psi\pi^0\pi^0$ in order to estimate our systematic error in the measurement of $\epsilon_{e^+e^-}/\epsilon_\gamma$.

For our convenience, events where one of the π^0 Dalitz decays to $e^+e^-\gamma$ will be called events of Type I. Events where both π^0 decay to $\gamma\gamma$ will be called events of Type II. The latest fit in the Review of Particle Physics 2010 establishes the

ratio $B(\pi^0 \to \gamma e^+ e^-)/B(\pi^0 \to \gamma\gamma)$ to be $(1.188 \pm 0.034) \times 10^{-2}$ [11, 3]. From this, we can establish that the ratio of numbers of these two types of events produced in our dataset should be $(2.376 \pm 0.068) \times 10^{-2}$ from Eq. 4.47.

$$r = \frac{n_I}{n_{II}} = 2 \times \frac{B(\pi^0 \to \gamma e^+ e^-)}{B(\pi^0 \to \gamma\gamma} = 0.02376 \pm 0.00068 \tag{4.47}$$

In our method, we obtain a measurement of this ratio from data and compute the branching fraction $B(\pi^0 \to \gamma e^+ e^-)$. The deviation of this measurement from the currently accepted value of the branching fraction translates to the systematic uncertainty in our measurement of $\epsilon_{e^+e^-}/\epsilon_\gamma$:

$$\frac{\Delta\epsilon_{e^+e^-}/\epsilon_\gamma}{\epsilon_{e^+e^-}/\epsilon_\gamma} = \frac{\Delta B(\pi^0 \to \gamma e^+ e^-)}{B(\pi^0 \to \gamma e^+ e^-)} \tag{4.48}$$

Our method reconstructs the $\psi(2S)$ through events of Type I ($\psi(2S) \to J/\psi\pi^0\pi^0; \pi^0 \to \gamma\gamma; \pi^0 \to e^+e^-\gamma$) and events of Type II ($\psi(2S) \to J/\psi\pi^0\pi^0; \pi^0 \to \gamma\gamma; \pi^0 \to \gamma\gamma$). We estimate the reconstruction efficiencies for both types of events using Monte Carlo samples. First, we establish a set of criteria to reconstruct Type I events in our data. To illustrate our method, we shall call the efficiency of selecting Type I events from an MC sample of Type I events ϵ_s. The efficiency of keeping Type II events in the signal region of these criteria from an MC sample of Type II events shall be called ϵ_c. For n_I produced Type I and n_{II} produced Type II events, we can expect an yield of y events after applying this set of selection criteria to our data as expressed in Eq. 4.49.

$$n_I\epsilon_s + n_{_I I}\epsilon_c = y \tag{4.49}$$

Using the currently accepted ratio of n_I/n_{II} from Eq. 4.47, we may calculate n_I, the number of Type I events in our data, from this.

Hereafter, we construct a set of selection criteria to reconstruct Type II events in our data. Using Type II Monte Carlo event samples, we find the reconstruction efficiency ϵ_γ for this set of criteria. Then we estimate the number of produced Type II events in our data with this method as n_{II} using

$$n_{II}\epsilon_\gamma = y_\gamma \tag{4.50}$$

where y_γ is the yield of our set of criteria on data to isolate Type II events.

Having estimated the numbers of Type I and II events in our data, we may estimate the branching fraction $B(\pi^0 \to e^+e^-\gamma)$ using

$$B(\pi^0 \to e^+e^-\gamma) = \frac{B(\pi^0 \to \gamma\gamma)}{2}\frac{n_I}{n_{II}}. \tag{4.51}$$

.

In order to establish a systematic uncertainty in our measurement of $B(\pi^0 \to e^+e^-\gamma)$, we implement a second method for measuring this branching fraction. In this method, we use Type I and Type II events in our data that are most likely conversion events, events where one of the photons from the π^0 converts to a e^+e^- in material, in combination with Eq. 4.49 to estimate the total number of Type I and Type II events in the data. In order to select events that are most likely to be conversion events, we select events that are rejected by the Δd_0 and $\Delta\phi_0$ criteria on the tracks of the e^+e^- pair. These selection criteria have been described in Sections 4.2.5 and 4.2.6. The efficiency of selecting such conversion-type events from a Monte Carlo sample of Type I events shall be called ϵ'_s. The efficiency of selecting such events from a Monte Carlo sample of Type II events shall be called ϵ'_c. Thus, upon the application of our selection criteria (that in-

verts the standard Δd_0 and $\delta\phi_0$ requirements), the yield in data may be denoted by y' as expressed in Eq. 4.52.

$$n_I\epsilon'_s + n_{II}\epsilon'_c = y' \tag{4.52}$$

Solving Equations 4.49 and 4.50 simultaneously gives us the number of Type I events in the data. The number of Type II events is used as deduced earlier from the selection of Type II events. This ratio, n_I/n_{II}, is plugged into Equation 4.51 to give us a second estimate for the π^0 Dalitz decay branching fraction.

Now we shall discuss the details of implementation of the two methods.

4.12.1 Method 1

First, we shall describe the selection criteria used to select events from data in our first method.

The J/ψ is reconstructed from its decays to e^+e^- and $\mu^-\mu^+$. The tracks of these leptons are fitted with the Kalman fitter using electron and muon mass hypotheses respectively. 50% of the expected number of hits on a track are required to be present. The momentum of each track is required to be between 500 MeV and 10 GeV. They may be reconstructed upto a $\cos\theta$ of 0.93. The track parameter d_0 must be less than 5 mm and z_0 must be less than 5 cm. The dE/dx of electron and muon tracks are required to be within 3 σ of their expected values. The J/ψ has a mass of 3096.92 ± 0.001 MeV and a full natural width of 93.2 ± 2.1 keV. In our study, we require the invariant mass of the e^+e^- pair to be within 30 MeV of 3.09200 GeV, and the invariant mass of the $\mu^-\mu^+$ pair to be within 30 MeV of

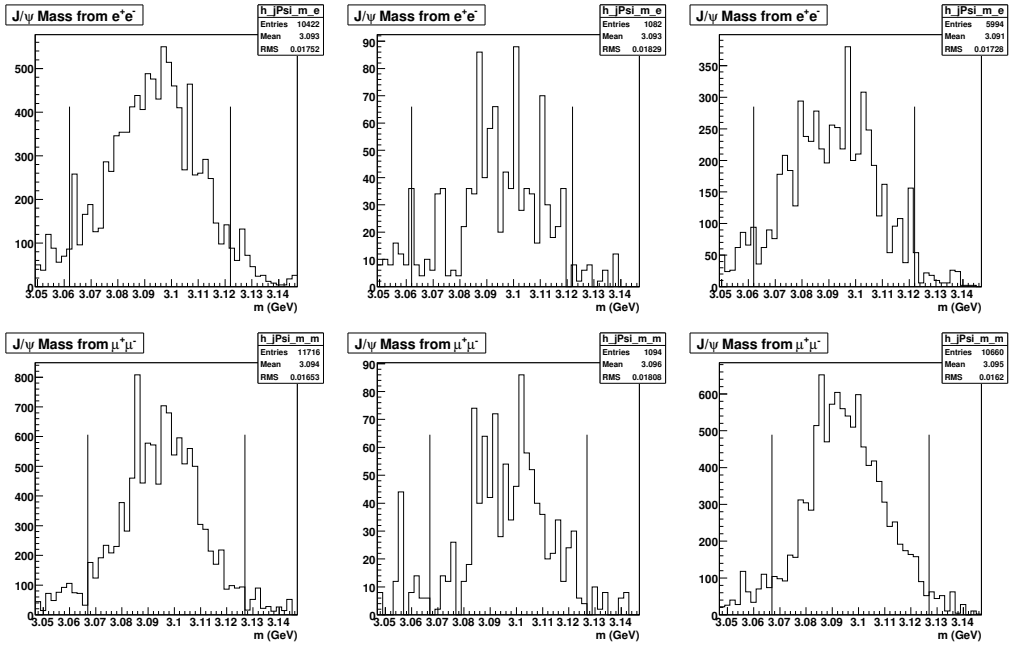

Figure 4.129: Invariant mass of the J/ψ reconstructed from its decay to e^+e^- (top plots) and $\mu^+\mu^-$ (bottom plots). The column on the left is from signal MC of Type I events. The column at the center is from signal MC of Type II events. The column on the right is from data.

3.09692 GeV as depicted in Fig 4.129.

The first π^0 in Type I events is reconstructed from its decay to two photons. The photons must not have showered in known noisy crystals and must not have tracks matched to them. Each of their shower energies are required to be between 10 Mev and 2 Gev. The pull mass of the π^0 is required to be within ± 2.5 σ. This is shown in Fig. 4.130.

The second π^0 in Type II events is reconstructed from its decay to a photon and a soft e^+e^- pair. Requirements on the photon are identical to those of the photons from the first π^0. The electron is Kalman fitted using the electron mass hypothesis and is required to have a momentum between 10 Mev and 2 GeV. It must be reconstructed within an angle of $\cos\theta = 0.93$. The track parameter d_0

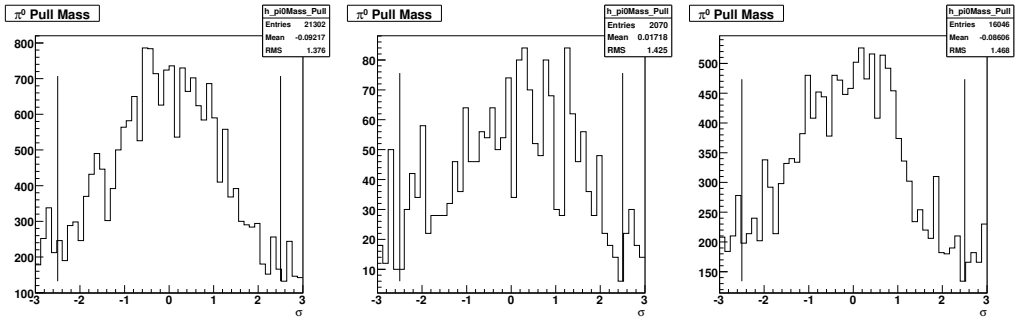

Figure 4.130: The invariant mass of the first π^0. The column on the left is from signal MC of Type I events. The column at the center is from MC of Type II events. The column on the right is from data.

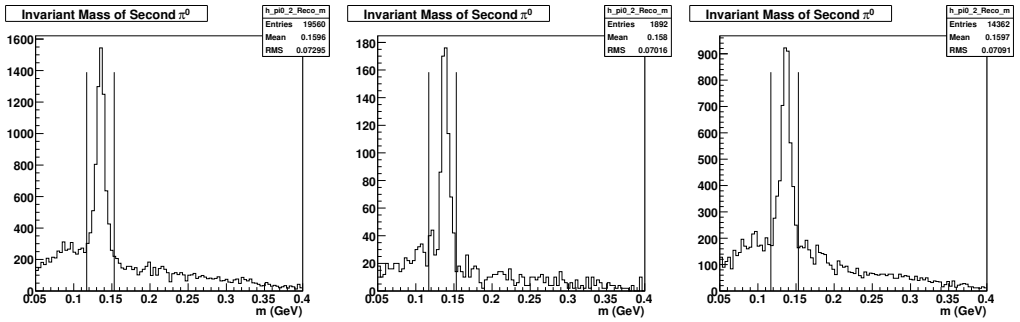

Figure 4.131: The invariant mass of the second π^0. The column on the left is from signal MC of Type I events. The column at the center is from MC of Type II events. The column on the right is from data.

must be less than 5 mm and z_0 must be less than 5 cm. The dE/dx of the track is required to be within 3 σ of the value expected of an electron. The invariant mass of the $\gamma e^+ e^-$ is required to be within 18 MeV of the nominal mass of the π^0 which is 134.9766 MeV. The distribution of this invariant mass and the selection range is shown in Fig. 4.131.

The electron and the positron are each required to have an energy less than 144 MeV as indicated in Fig. 4.132. This is the range of energies of the positron and the electron from the decay $D_s^{*+} \to D_s^+ e^+ e^-$.

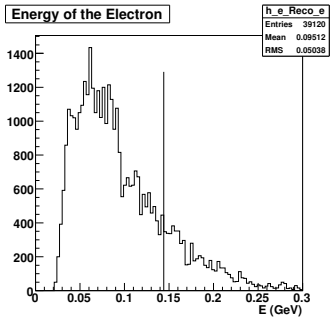

Figure 4.132: The distribution of energy of the positron and the electron from the Dalitz decay of the π^0 in the MC. Events containing positron and electrons with energy less than 144 MeV, as indicated, are accepted.

Next, we combine the four-momenta of the J/ψ and two π^0 to get the four-momentum of the $\psi(2S)$ meson. This must be close to the four-momentum of the colliding e^+e^- pair at the center of the CLEO-c detector. Hence, we apply selection criteria constraining each component of the momentum of the $\psi(2S)$ to be within 40 MeV of that of the collision momentum. This is shown in Fig. 4.133.

We select events where the difference between the invariant masses of the reconstructed $\psi(2S)$ candidate and the J/ψ candidate is within 30 MeV of the nominal difference in masses. This is depicted in Fig. 4.134.

A background to the selection of Type I events are Type II events where one of the photons from a π^0 converts in material to produce an e^+e^- pair. We reject this background using the $\Delta d_0 > -5mm$ and $\Delta\phi_0 < 0.12$ criteria used in our $D_s^{*+} \to D_s^+ e^+ e^-$ reconstruction. This is shown in Fig. 4.135 and 4.136.

The aforementioned selection criteria are found to accept 1,069 Type I events out of a Monte Carlo sample of 299,794. Thus, we record the efficiency $\epsilon_s = 0.0357 \pm 0.0011$ as applicable in Eq. 4.49. They are also found to accept 10 Type

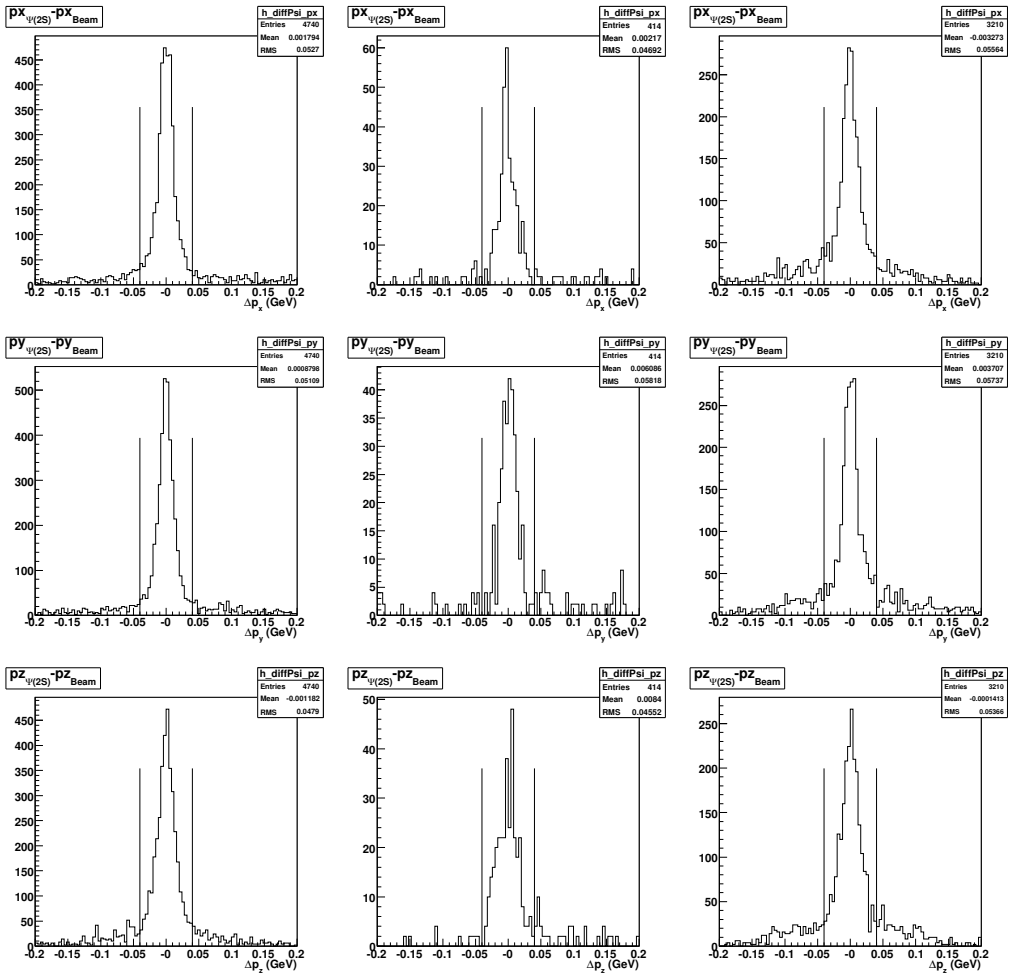

Figure 4.133: Four momenta of $\psi(2S)$ relative to the e^+e^- collision four momenta. The column on the left is from signal MC of Type I events. The column at the center is from MC of Type II events. The column on the right is from data.

II events out of a Monte Carlo sample of 149,888 and thus we may write $\epsilon_c = 2/149,888 = (1.33 \pm 0.94) \times 10^{-5}$. When these selection criteria are applied to our data, we get an yield of $y = 306$ events.

Assuming the established ratio of Type I to Type II events detailed in Eq. 4.47 to hold true, we may solve Eq. 4.49 for n_I. The solution is given in Eq. 4.53 and 4.54. The $\oplus$ symbol is used to denote addition in quadrature. This gives us

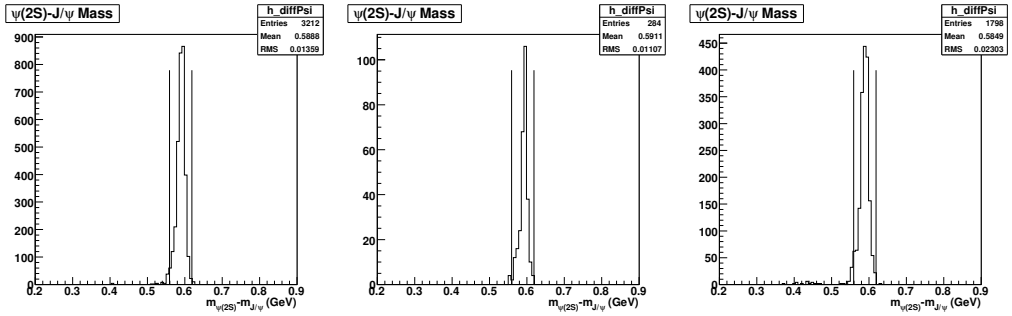

Figure 4.134: Difference between the invariant masses of the $\psi(2S)$ and the J/ψ. The column on the left is from signal MC of Type I events. The column at the center is from MC of Type II events. The column on the right is from data.

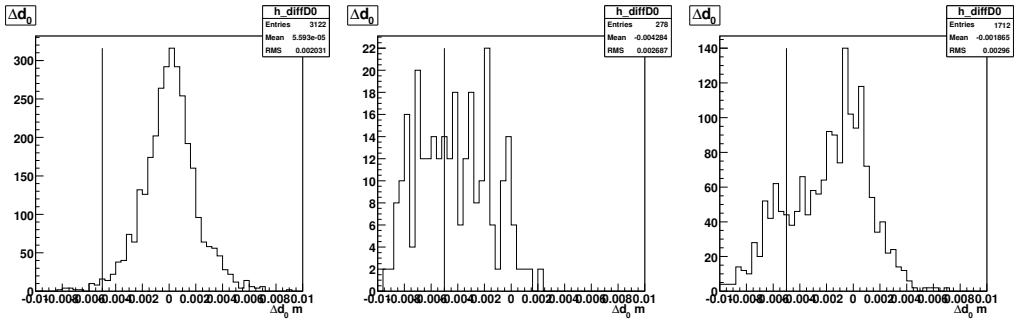

Figure 4.135: The Δd_0 between the e^+e^- pair from the second π^0. The column on the left is from signal MC of Type I events. The column at the center is from MC of Type II events. The column on the right is from data.

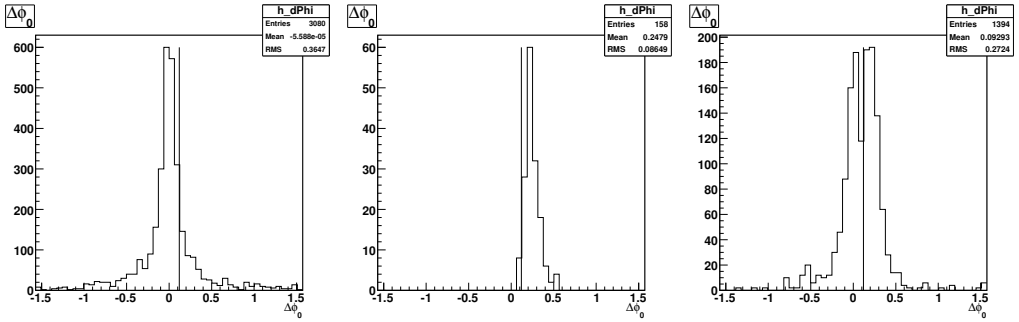

Figure 4.136: The $\Delta\phi_0$ between the e^+e^- pair from the second π^0. The column on the left is from signal MC of Type I events. The column at the center is from MC of Type II events. The column on the right is from data.

$n_I = 8447 \pm 554$.

$$n_I = \frac{y}{\epsilon_s + \epsilon_c/r} \tag{4.53}$$

$$\frac{\Delta n_I}{n_I} = \frac{\Delta y}{y} \oplus \frac{\Delta\epsilon_s \oplus (\epsilon_c/r)(\Delta\epsilon_c/\epsilon_c \oplus \Delta r/r)}{\epsilon_s + \epsilon_c/r} \tag{4.54}$$

Having calculated the number of Type I events in our data, we may now estimate the number of Type II events present in the data sample. The reconstruction of Type II events is similar to the reconstruction of Type I events. The second π^0 is reconstructed from photons with the same selection criteria as the first π^0. The Δd_0 and $\Delta\phi_0$ cuts are not used as they are clearly inapplicable. A signal MC for Type II events was generated to calculate the signal efficiency of our criteria. Distributions of the J/ψ mass, the pull masses of the two π^0, the momentum of the $\psi(2S)$ relative to the collision momentum and the mass difference between the $\psi(2S)$ and the J/ψ are presented in Fig. 4.137, 4.138, 4.139, 4.140 and 4.141.

25,713 events out of 149,888 signal MC events were seen to be accepted by our criteria. This gives a signal efficiency $\epsilon_\gamma = 0.1716 \pm 0.0011$. We find the yield in data to be $y_{II} = 58,602$ events. Using Eq. 4.50 we infer that the number of Type II events is our data is $n_{II} = 341,607 \pm 2,555$.

Now, we may calculate the ratio of Type I to Type II events in our data as n_I/n_{II} and from that estimate the branching fraction $B(\pi^0 \to \gamma e^+ e^-)$ thus:

$$\frac{n_I}{n_{II}} = \frac{8447 \pm 554}{341607 \pm 2555} = \frac{2B(\pi^0 \to e^+e^-\gamma)}{(98.823 \pm 0.034) \times 10^{-2}}. \tag{4.55}$$

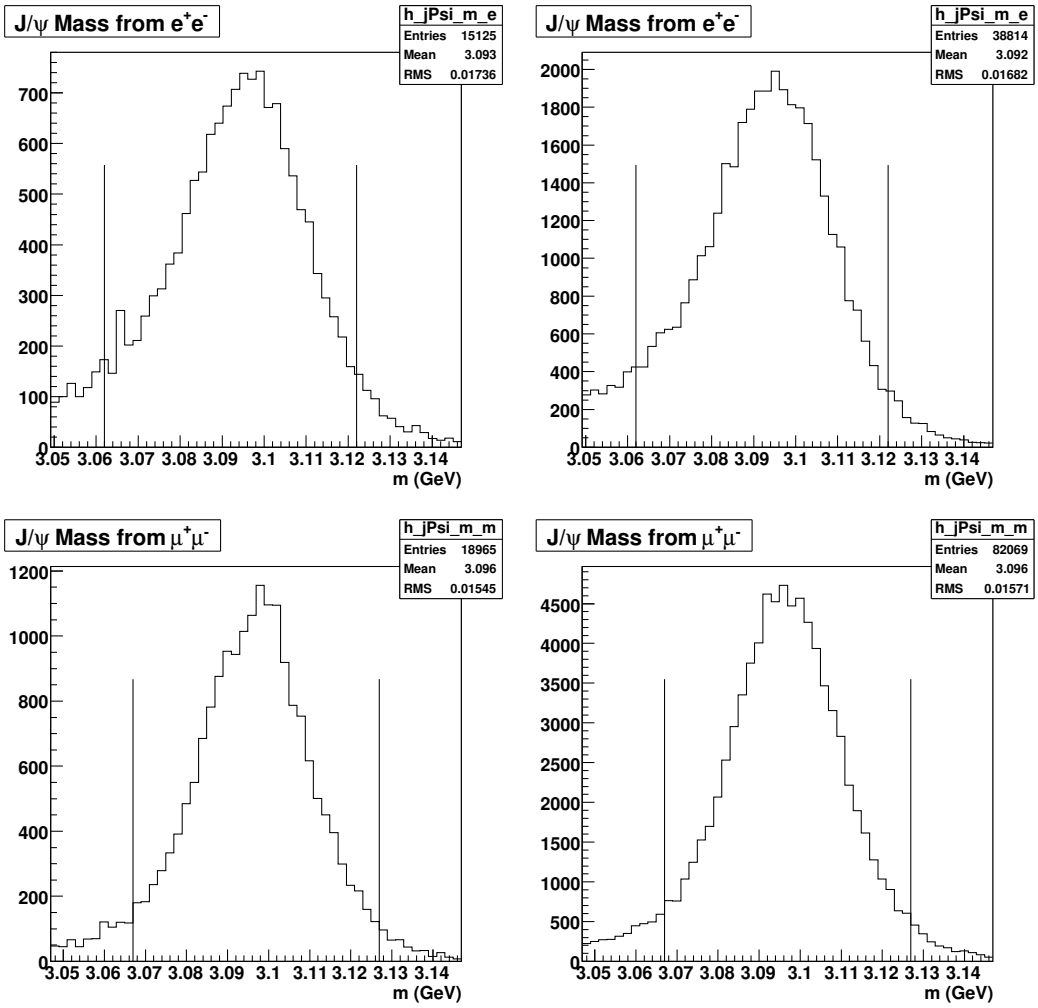

Figure 4.137: Invariant mass of the J/ψ reconstructed from its decay to e^+e^- (top plots) and $\mu^+\mu^-$ (bottom plots). The column on the left is from signal MC of Type II events. The column on the right is from data.

From this, we calculate $B(\pi^0 \to e^+e^-\gamma) = 0.01222 \pm 0.00081(\text{stat})$. In order to establish a systematic uncertainty in this measurement, we use a second method to estimate $B(\pi^0 \to e^+e^-\gamma)$.

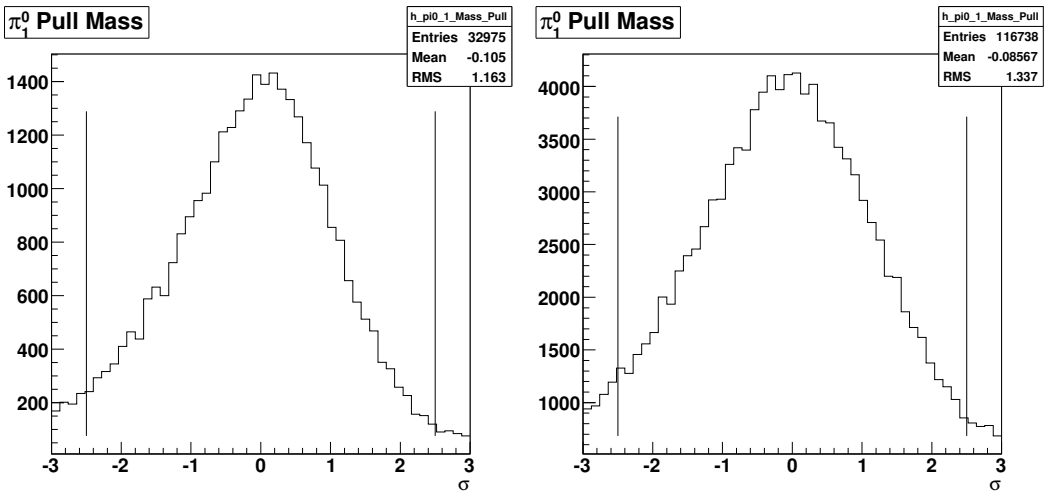

Figure 4.138: The invariant mass of the first π^0. The column on the left is from signal MC of Type II events. The column on the right is from data.

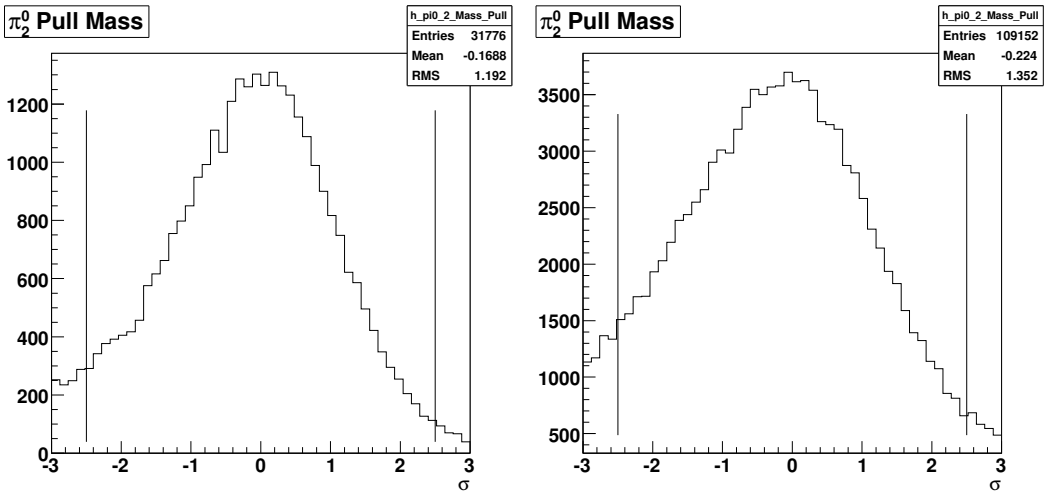

Figure 4.139: The invariant mass of the second π^0. The column on the left is from signal MC of Type II events. The column on the right is from data.

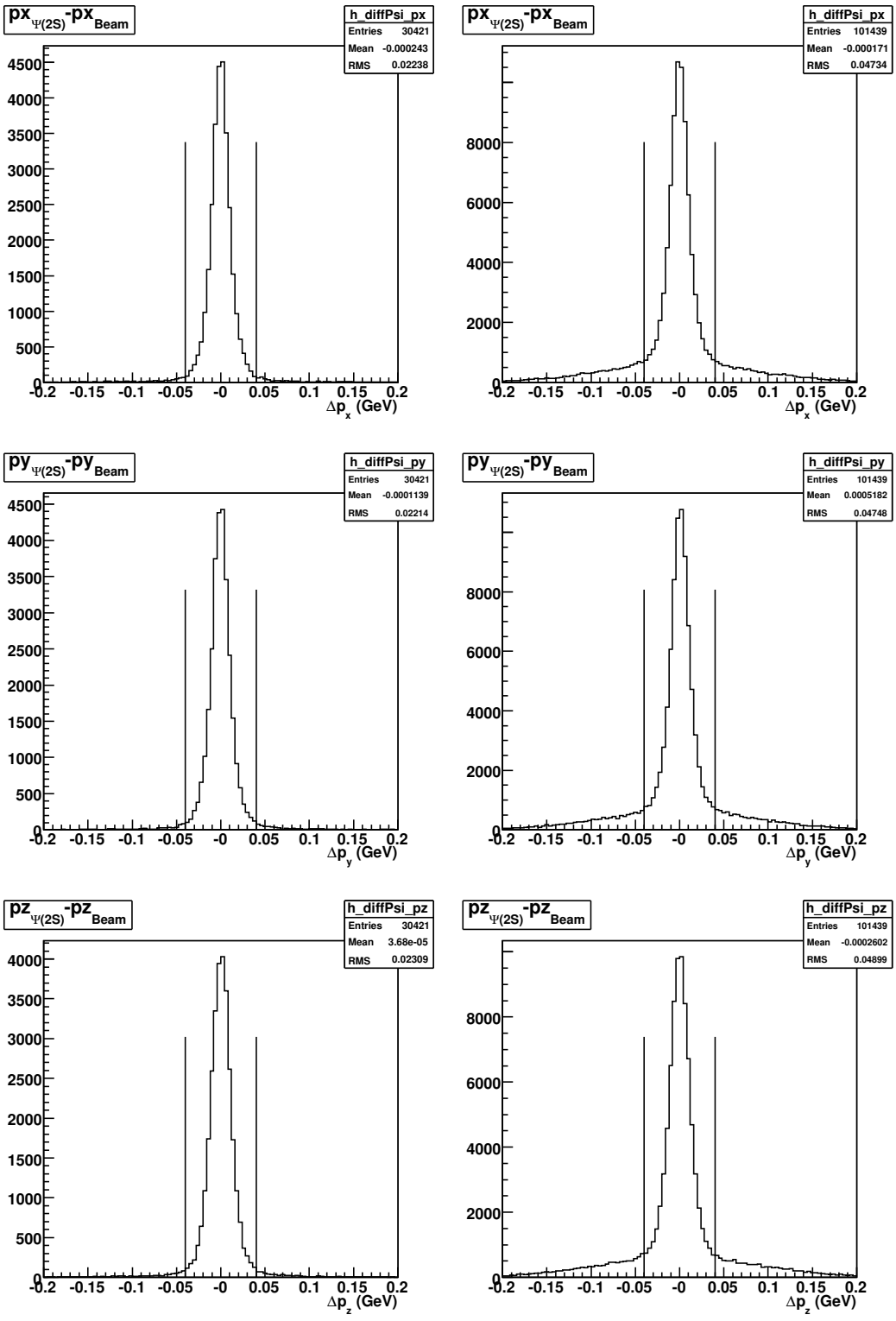

Figure 4.140: Four momenta of $\psi(2S)$ relative to the e^+e^- collision four momenta. The column on the left is from signal MC of Type II events. The column on the right is from data.

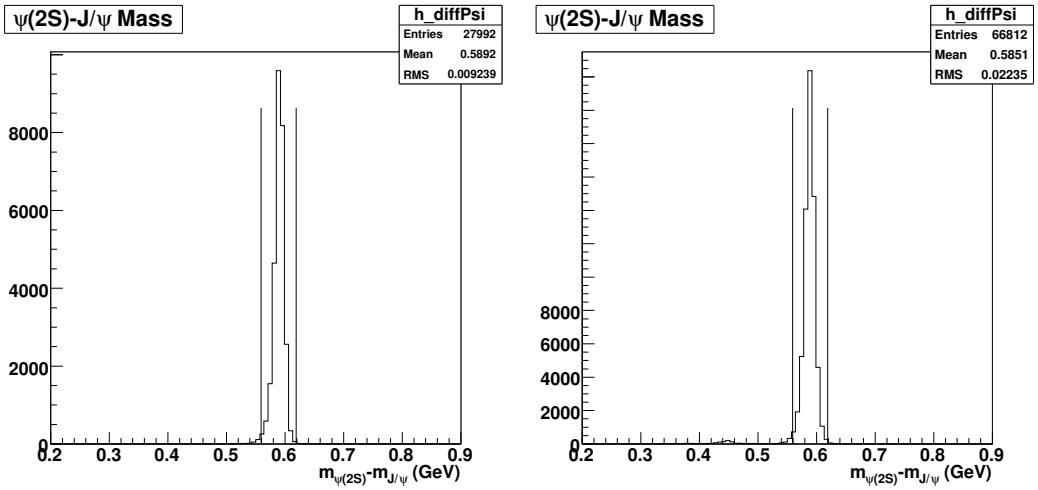

Figure 4.141: Difference between the invariant masses of the $\psi(2S)$ and the J/ψ. The column on the left is from signal MC of Type II events. The column on the right is from data.

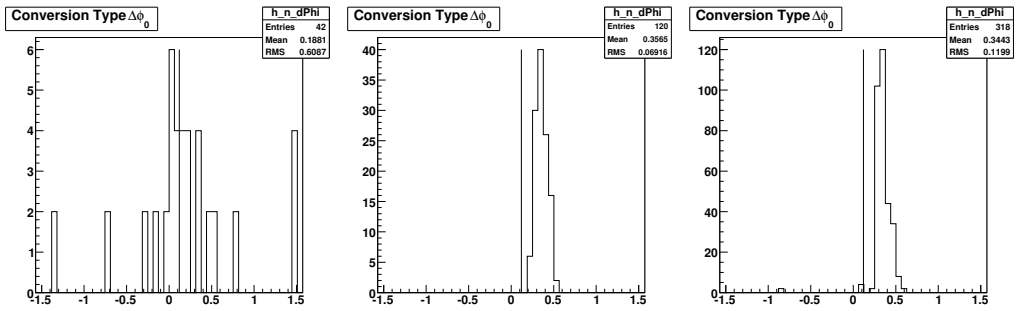

Figure 4.142: The $\Delta\phi_0$ between the e^+e^- pair. Now we accept events with $\Delta\phi_0$ greater than 0.12. These were previously rejected as likely to be conversion-type events. The column on the left is from signal MC of Type I events. The column at the center is from MC of Type II events. The column on the right is from data.

4.12.2 Method 2

Our second method for estimating $B(\pi^0 \rightarrow e^+e^-\gamma)$ uses conversion-type events found in data. Conversion-type events are those where both π^0 decay to $\gamma\gamma$ but at least one photon converts in material to form a e^+e^- pair. We select for such events by requiring all the criteria on J/ψ and the invariant masses of the π^0 used to select Type I events, except now we look at the "wrong side" of the Δd_0 and $\Delta\phi_0$ criteria. In other words, we keep events which were previously rejected by both the Δd_0 and the $\Delta\phi_0$ criteria. The distribution of Δd_0 is the same as Fig. 4.135 since all preceding criteria are identical. The distribution of $\Delta\phi_0$ after having accepted tracks on the "wrong side" of Δd_0 is presented in Fig. 4.142.

The efficiency of such a set of selection criteria for Type I events is found to be $\epsilon_s' = 10/29,974 = (3.34 \pm 1.1(\text{stat})) \times 10^{-4}$. The efficiency for Type II events is found to be $\epsilon_c' = 54/149,888 = (3.60 \pm 0.49(\text{stat})) \times 10^{-4}$. On applying these selection criteria to our data, we are left with an yield of $y' = 141$ events. These values may be plugged into Eq. 4.52 and solved simultaneously with Eq. 4.49

to get $n_I = 8437 \pm 342$. The solution for n_I is given in Eq. 4.56 and 4.57.

$$n_I = \frac{y\epsilon'_c - y'\epsilon_c}{\epsilon_s\epsilon'_c - \epsilon_c\epsilon'_s} \tag{4.56}$$

$$\Delta n_I = \frac{\delta n_I}{\delta y}\Delta y \oplus \frac{\delta n_I}{\delta y'}\Delta y' \oplus \frac{\delta n_I}{\delta \epsilon_c}\Delta\epsilon_c \oplus \frac{\delta n_I}{\delta \epsilon_s}\Delta\epsilon_s \oplus \frac{\delta n_I}{\delta \epsilon'_c}\Delta\epsilon'_c \oplus \frac{\delta n_I}{\delta \epsilon'_s}\Delta\epsilon'_s \tag{4.57}$$

where

$$\frac{\delta n_I}{\delta y} = \epsilon'_c$$

$$\frac{\delta n_I}{\delta y'} = -\epsilon_c$$

$$\frac{\delta n_I}{\delta \epsilon_c} = \frac{-y}{\epsilon_s\epsilon'_c - \epsilon_c\epsilon'_s} + \frac{y\epsilon'_c - y'\epsilon_c}{(\epsilon_s\epsilon'_c - \epsilon_c\epsilon'_s)^2}\epsilon'_s$$

$$\frac{\delta n_I}{\delta \epsilon_s} = -\frac{y\epsilon'_c - y'\epsilon_c}{(\epsilon_s\epsilon'_c - \epsilon_c\epsilon'_s)^2}\epsilon'_c$$

$$\frac{\delta n_I}{\delta \epsilon'_c} = \frac{y}{\epsilon_s\epsilon'_c - \epsilon_c\epsilon'_s} - \frac{y\epsilon'_c - y'\epsilon_c}{(\epsilon_s\epsilon'_c - \epsilon_c\epsilon'_s)^2}\epsilon_s$$

$$\frac{\delta n_I}{\delta \epsilon'_s} = \frac{y\epsilon'_c - y'\epsilon_c}{(\epsilon_s\epsilon'_c - \epsilon_c\epsilon'_s)^2}\epsilon_c$$

Now, we may calculate the ratio of Type I to Type II events in our data as n_I/n_{II} and from that estimate the branching fraction $B(\pi^0 \to \gamma e^+ e^-)$ thus:

$$\frac{n_I}{n_{II}} = \frac{8437 \pm 342}{341607 \pm 2555} = \frac{2B(\pi^0 \to e^+e^-\gamma)}{(98.823 \pm 0.034) \times 10^{-2}}. \tag{4.58}$$

From this, we calculate $B(\pi^0 \to e^+e^-\gamma) = 0.01220 \pm 0.00050(\text{stat})$.

Now, we may combine our results from the two methods to establish a systematic error. Result from method 1: $B(\pi^0 \to e^+e^-\gamma) = 0.01222 \pm 0.00081(\text{stat})$. Result from method 2: $B(\pi^0 \to e^+e^-\gamma) = 0.01220 \pm 0.00050(\text{stat})$. The result of method 2 has the smaller uncertainty and will, therefore, be quoted as the central value of our measurement. The statistical uncertainty will quoted as the quadrature sum of the uncertainties in the two results. The absolute difference between the central values of the two results will be quoted as the systematic uncertainty in our measurement. Hence, we report $B(\pi^0 \to e^+e^-\gamma) = (1.222 \pm 0.081(\text{stat}) \pm 0.002(\text{syst})) \times 10^{-2}$.

The currently accepted branching fraction for the Dalitz decay of the π^0 is $(1.174 \pm 0.035) \times 10^{-2}$ [6, 22, 21, 7, 3]. The difference between this and our result is 0.046%. Hence, we cannot motivate a correction to the tracking efficiency and must settle for an uncertainty. We add the difference between our measured branching fraction and the currently accepted measurement, and the uncertainties in our result in quadrature to get a total uncertainty of 0.077%. Thus, the fractional uncertainty that we set out to estimate is found to be 6.51% as shown in Eq. 4.59.

$$\frac{\Delta\epsilon_{e^+e^-}/\epsilon_\gamma}{\epsilon_{e^+e^-}/\epsilon_\gamma} = \frac{\Delta B(\pi^0 \to \gamma e^+e^-)}{B(\pi^0 \to \gamma e^+e^-)} = \frac{0.077\%}{1.174\%} = 6.51\% \tag{4.59}$$

CHAPTER 5

RESULTS AND CONCLUSION

We conclude this dissertation with a compilation of the results of our analysis.

We have observed the Dalitz decay $D_s^{*+} \to D_s^+ e^+ e^-$ with a signal significance of 6.4 σ using nine hadronic decays of the D_s^+ as tabulated in Table 4.75. It is the first instance of a Dalitz decay that has been observed in the electromagnetic decay of mesons containing the heavy charm or bottom quark.

We have also measured the ratio of branching fractions $B(D_s^{*+} \to D_s^+ e^+ e^-)/B(D_s^{*+} \to D_s^+ \gamma)$ to be $(0.72 \pm 0.14(\text{stat}) \pm 0.06(\text{syst}))\%$ as presented in Eq. 4.35 of Section 4.11. The statistical uncertainty arises from the limited signal yields of $D_s^{*+} \to D_s^+ e^+ e^-$ and $D_s^{*+} \to D_s^+ \gamma$. Larger datasets will decrease this error. The systematic uncertainty arises from systematic uncertainties in the estimated background for the $D_s^{*+} \to D_s^+ e^+ e^-$ yield, systematic uncertainties in the signal yield for $D_s^{*+} \to D_s^+ \gamma$, and the systematic uncertainty from the $e^+ e^-$ and γ reconstruction efficiencies in the energy range relevant for this analysis.

Finally, in Section 4.11.11 we have recomputed the absolute branching fractions of the D_s^{*+} meson in light of our discovery and measurement as follows.

$$\begin{aligned} B(D_s^{*+} \to D_s^+ \gamma) &= (93.5 \pm 0.5 \pm 0.5)\% \\ B(D_s^{*+} \to D_s^+ \pi^0) &= (5.8 \pm 0.4 \pm 0.5)\% \\ B(D_s^{*+} \to D_s^+ e^+ e^-) &= (0.67 \pm 0.13 \pm 0.05)\% \end{aligned}$$

APPENDIX A

PLOTS USED TO OPTIMIZE SELECTION CRITERIA FOR $D_s^{*+} \to D_s^+ e^+ e^-$

A.1 $D_s^+ \to K_S K^+$

Optimization plots for the $m_{D_s^+}$ selection criterion in the $D_s^+ \to K_S K^+$ mode. Plots on the left grouped as Fig. A.1 correspond to pion-fitted tracks in the simulated samples. Plots on the right grouped as Fig. A.2 correspond to electron-fitted tracks in the samples. The top left plots, for both samples, is the distribution of $m_{D_s^+}$ in the signal Monte Carlo sample. The top right plot graphs the signal MC sample accepted by the criterion as we increase the cut width plotted on the x-axis. For the pion-fitted samples on the left, the plots in the second and third rows correspond to the generic and continuum MC samples, respectively. For the electron-fitted samples on the right, the plots in the second, third and fourth rows correspond to the $D_s^{*+} \to D_s^+ \gamma$, generic and continuum MC samples, respectively. For both sets of plots, the bottom left shows the significance of the signal over background. The bottom right plot shows the precision of the signal.

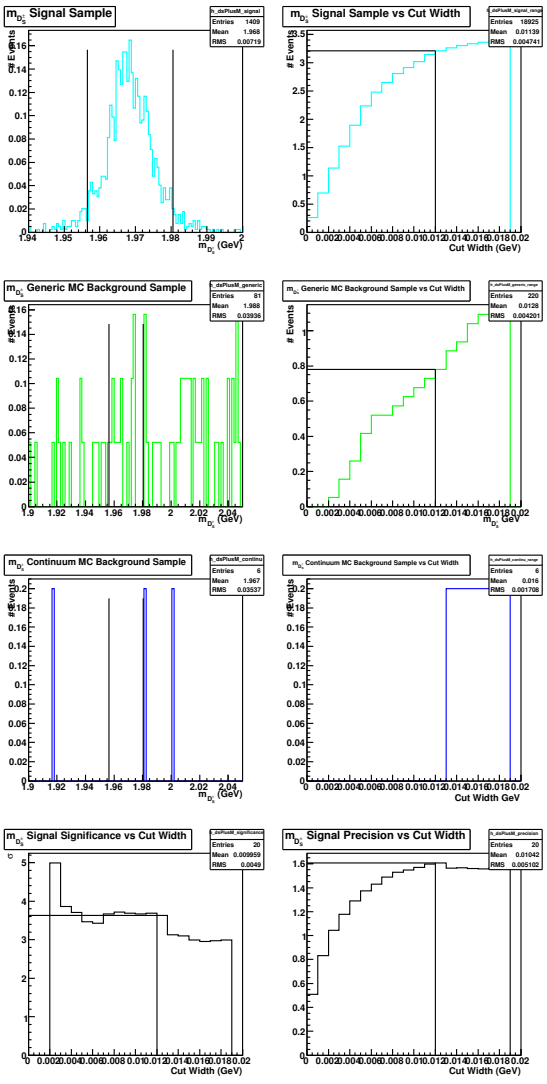

Figure A.1: $m_{D_s^+}$, $K_S K^+$, pion-fit

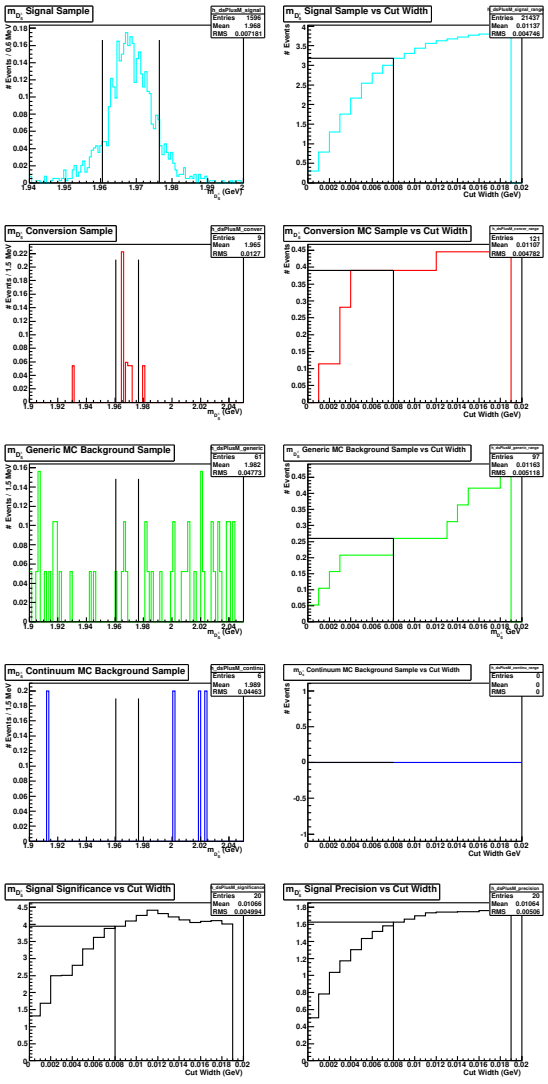

Figure A.2: $m_{D_s^+}$, $K_S K^+$, electron-fit

Optimization plots for the m_{BC} selection criterion in the $D_s^+ \to K_S K^+$ decay mode. Plots on the left grouped as Fig. A.3 correspond to pion-fitted tracks in the simulated samples. Plots on the right grouped as Fig. A.4 correspond to electron-fitted tracks in the samples. The top left plots, for both samples, is the distribution of m_{BC} in the signal Monte Carlo sample. The top right plot graphs the signal MC sample accepted by the criterion as we increase the cut width plotted on the x-axis. For the pion-fitted samples on the left, the plots in the second and third rows correspond to the generic and continuum MC samples, respectively. For the electron-fitted samples on the right, the plots in the second, third and fourth rows correspond to the $D_s^{*+} \to D_s^+ \gamma$, generic and continuum MC samples, respectively. For both sets of plots, the bottom left shows the significance of the signal over background. The bottom right plot shows the precision of the signal.

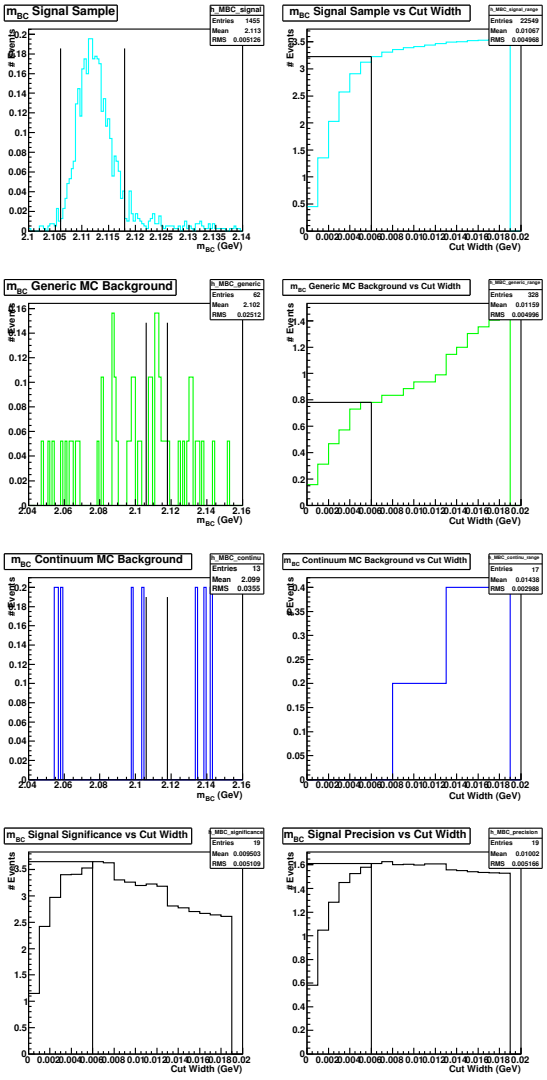

Figure A.3: m_{BC}, $K_S K^+$, pion-fit

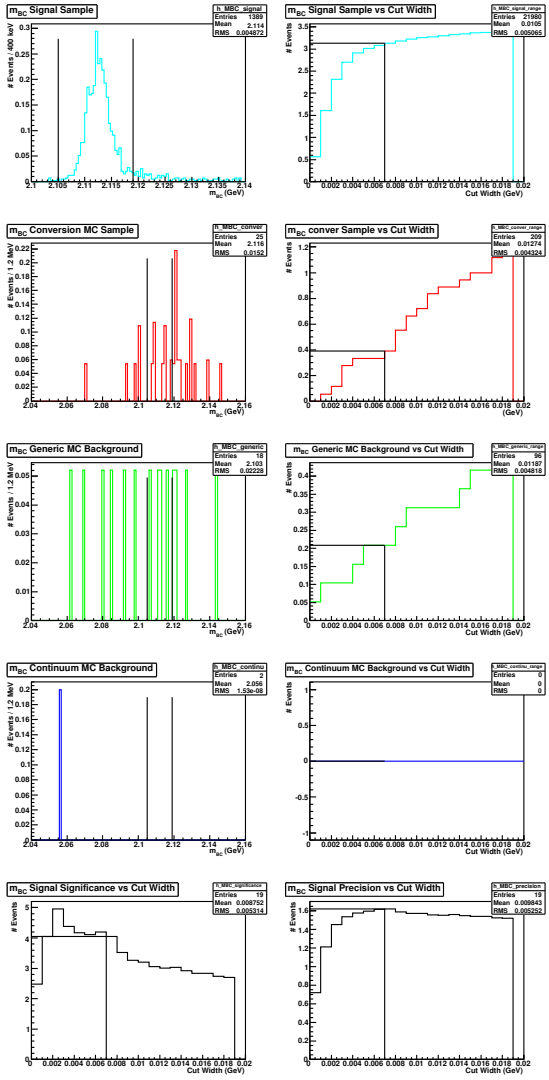

Figure A.4: m_{BC}, $K_S K^+$, electron-fit

Optimization plots for the δm selection criterion in the $D_s^+ \to K_S K^+$ decay mode. Plots on the left grouped as Fig. A.5 correspond to pion-fitted tracks in the simulated samples. Plots on the right grouped as Fig. A.6 correspond to electron-fitted tracks in the samples. The top left plots, for both samples, is the distribution of δm in the signal Monte Carlo sample. The top right plot graphs the signal MC sample accepted by the criterion as we increase the cut width plotted on the x-axis. For the pion-fitted samples on the left, the plots in the second and third rows correspond to the generic and continuum MC samples, respectively. For the electron-fitted samples on the right, the plots in the second, third and fourth rows correspond to the $D_s^{*+} \to D_s^+ \gamma$, generic and continuum MC samples, respectively. For both sets of plots, the bottom left shows the significance of the signal over background. The bottom right plot shows the precision of the signal.

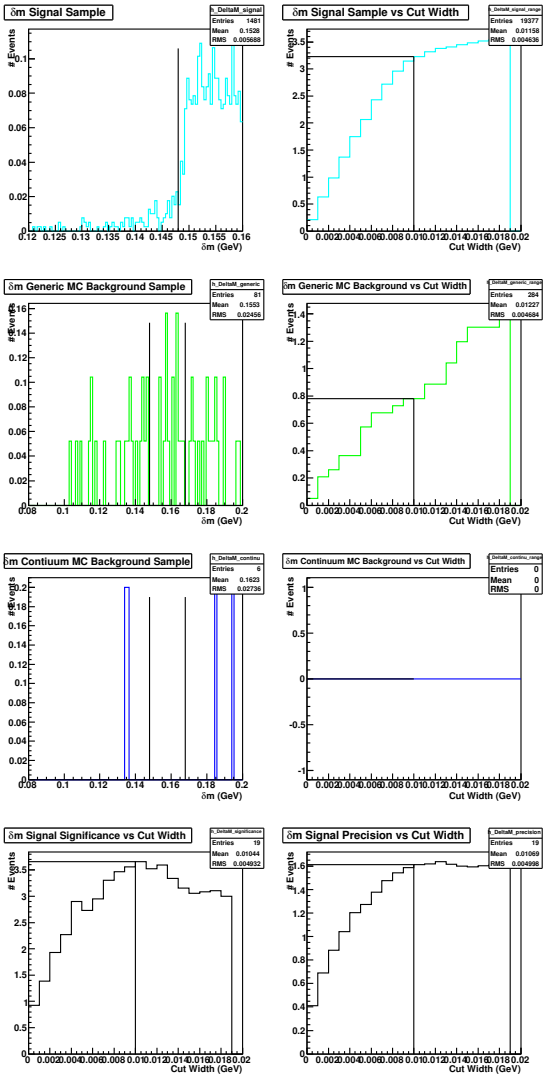

Figure A.5: δm, $K_S K^+$, pion-fit

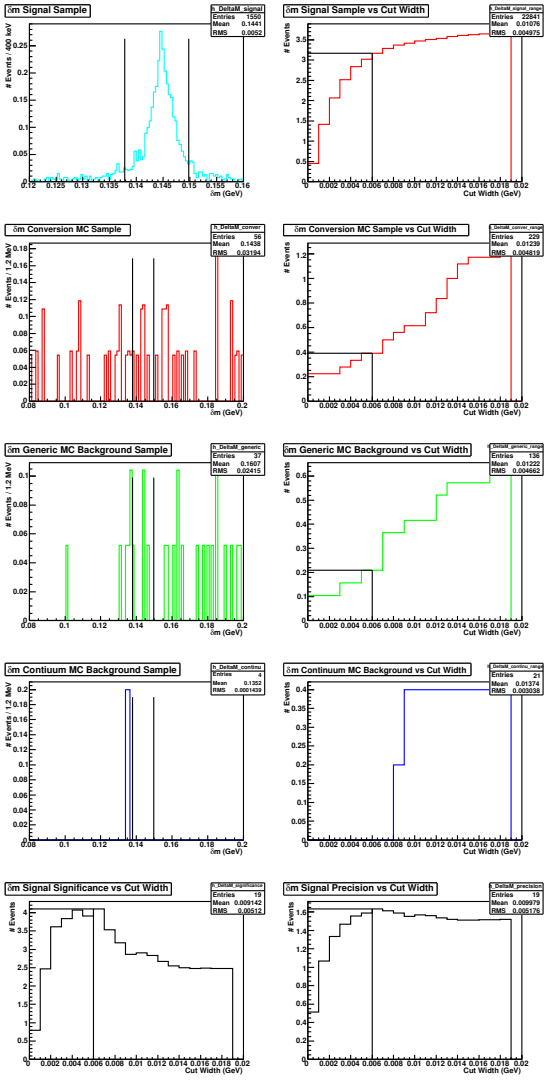

Figure A.6: δm, $K_S K^+$, electron-fit

Optimization plots for the selection criterion on the Δd_0 between the e^+e^- in the $D_s^+ \to K_S K^+$ decay mode. Plots on the left grouped as Fig. A.7 correspond to pion-fitted tracks in the simulated samples. Plots on the right grouped as Fig. A.8 correspond to electron-fitted tracks in the samples. The top left plots, for both samples, is the distribution of Δd_0 in the signal Monte Carlo sample. The top right plot graphs the signal MC sample accepted by the criterion as we vary the cut on the x-axis. For the pion-fitted samples on the left, the plots in the second and third rows correspond to the generic and continuum MC samples, respectively. For the electron-fitted samples on the right, the plots in the second, third and fourth rows correspond to the $D_s^{*+} \to D_s^+\gamma$, generic and continuum MC samples, respectively. For both sets of plots, the bottom left shows the significance of the signal over background. The bottom right plot shows the precision of the signal.

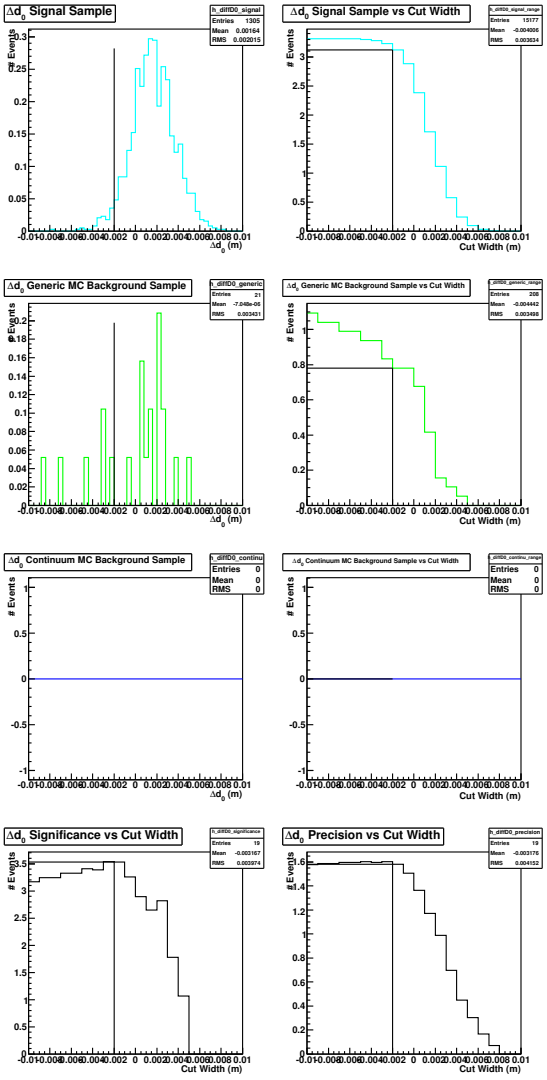

Figure A.7: Δd_0, $K_S K^+$, pion-fit

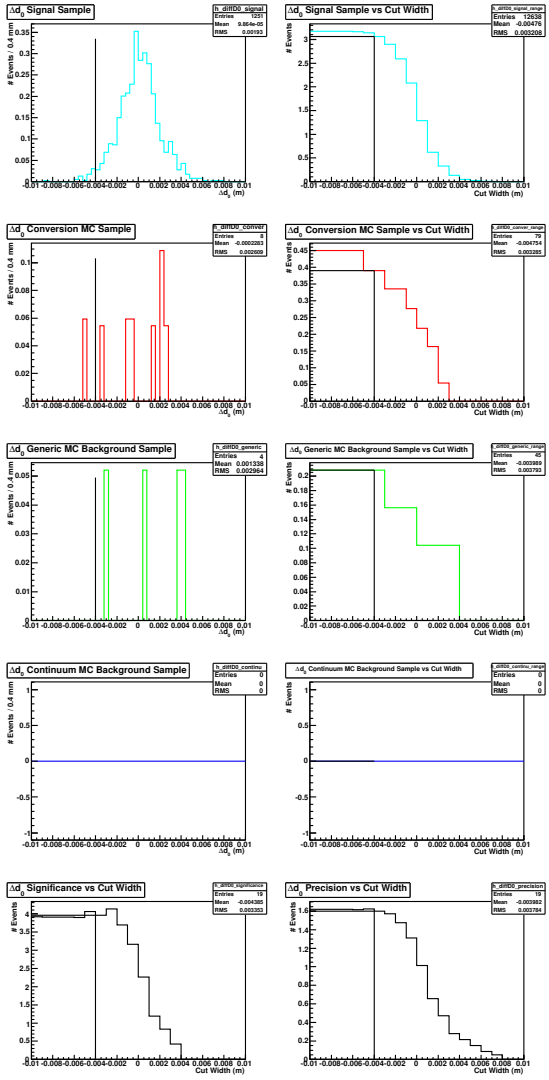

Figure A.8: Δd_0, $K_S K^+$, electron-fit

Optimization plots for the selection criterion on the $\Delta\phi_0$ between the e^+e^- in the $D_s^+ \to K_S K^+$ decay mode. Plots on the left grouped as Fig. A.9 correspond to pion-fitted tracks in the simulated samples. Plots on the right grouped as Fig. A.10 correspond to electron-fitted tracks in the samples. The top left plots, for both samples, is the distribution of $\Delta\phi_0$ in the signal Monte Carlo sample. The top right plot graphs the signal MC sample accepted by the criterion as we vary the cut on the x-axis. For the pion-fitted samples on the left, the plots in the second and third rows correspond to the generic and continuum MC samples, respectively. For the electron-fitted samples on the right, the plots in the second, third and fourth rows correspond to the $D_s^{*+} \to D_s^+\gamma$, generic and continuum MC samples, respectively. For both sets of plots, the bottom left shows the significance of the signal over background. The bottom right plot shows the precision of the signal.

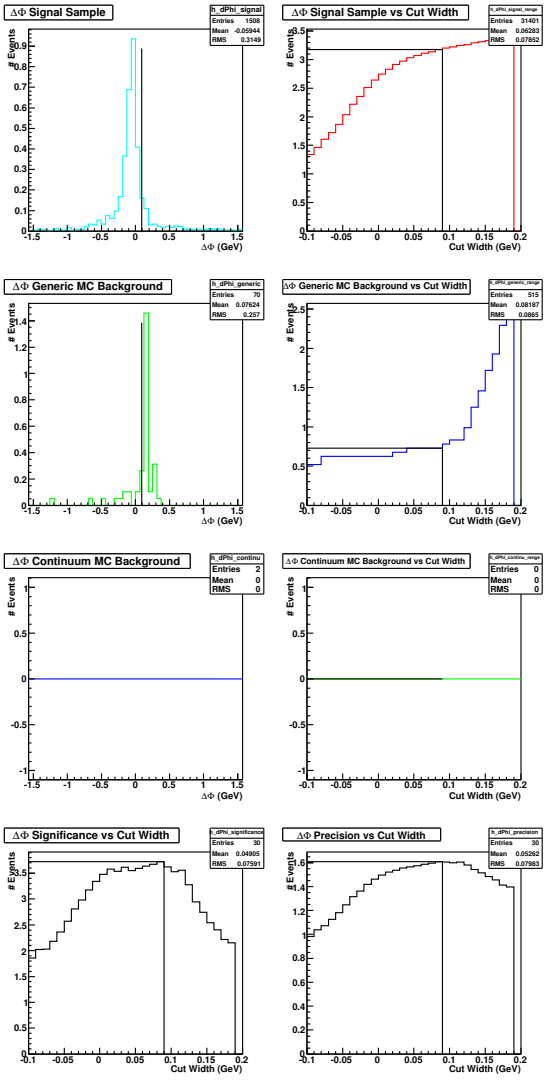

Figure A.9: $\Delta\phi_0$, $K_S K^+$, pion-fit

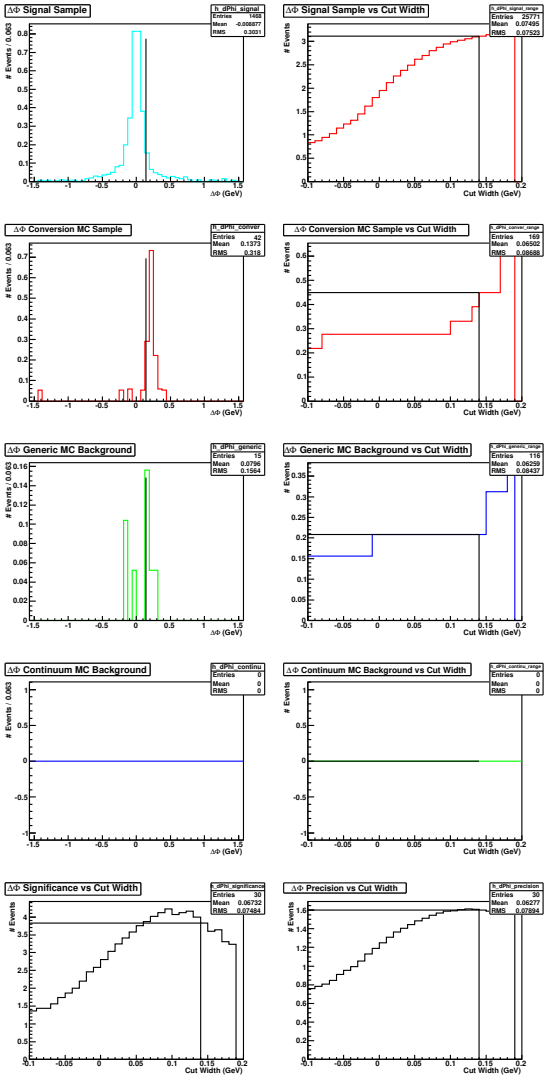

Figure A.10: $\Delta\phi_0$, $K_S K^+$, electron-fit

A.2 $D_s^+ \to \eta\pi^+; \eta \to \gamma\gamma$

Optimization plots for the $m_{D_s^+}$ selection criterion in the $D_s^+ \to \eta\pi^+$ mode. Plots on the left grouped as Fig. A.11 correspond to pion-fitted tracks in the simulated samples. Plots on the right grouped as Fig. A.12 correspond to electron-fitted tracks in the samples. The top left plots, for both samples, is the distribution of $m_{D_s^+}$ in the signal Monte Carlo sample. The top right plot graphs the signal MC sample accepted by the criterion as we increase the cut width plotted on the x-axis. For the pion-fitted samples on the left, the plots in the second and third rows correspond to the generic and continuum MC samples, respectively. For the electron-fitted samples on the right, the plots in the second, third and fourth rows correspond to the $D_s^{*+} \to D_s^+\gamma$, generic and continuum MC samples, respectively. For both sets of plots, the bottom left shows the significance of the signal over background. The bottom right plot shows the precision of the signal.

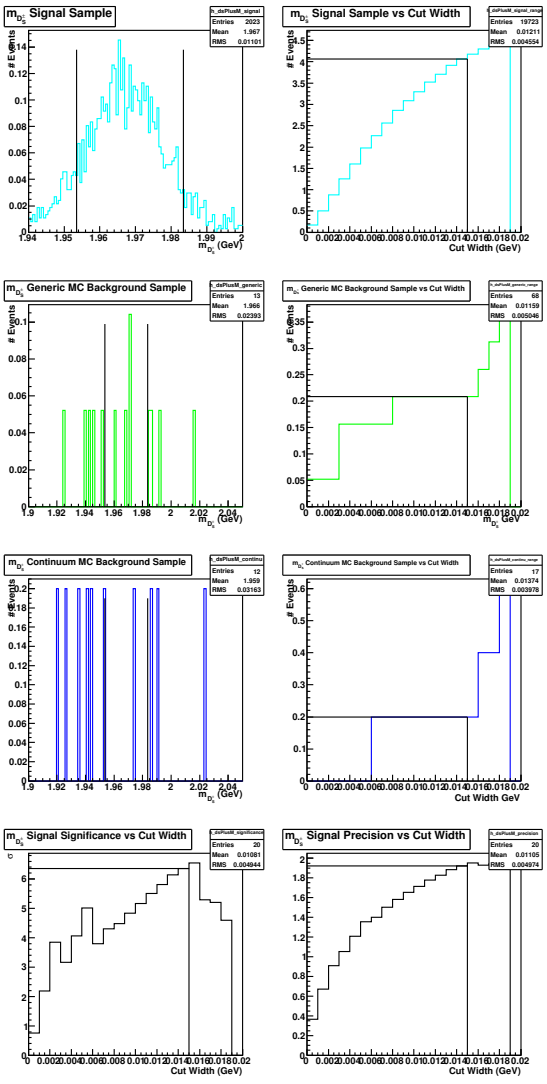

Figure A.11: $m_{D_s^+}$, $\eta\pi^+$, pion-fit

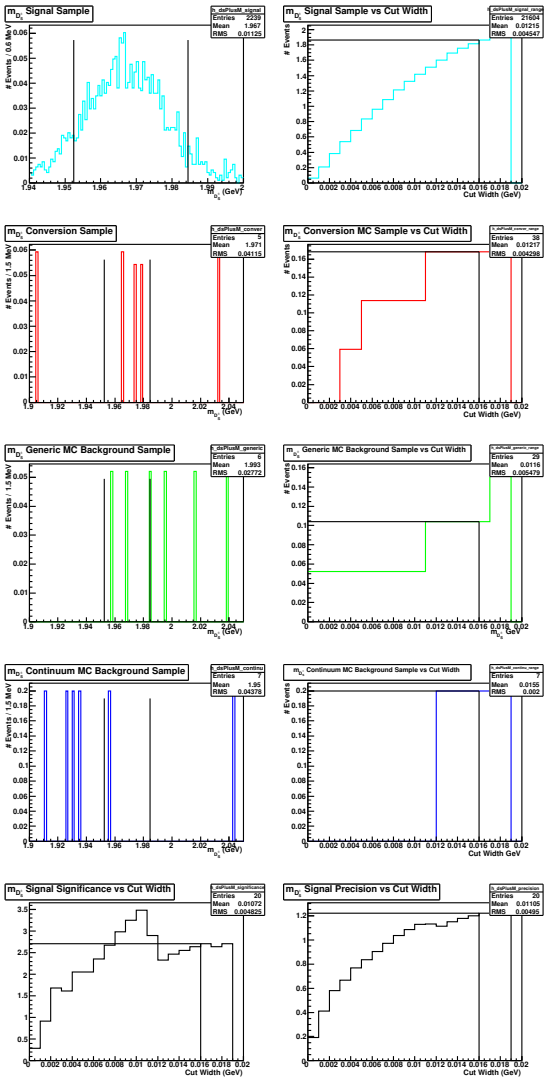

Figure A.12: $m_{D_s^+}$, $\eta\pi^+$, electron-fit

Optimization plots for the m_{BC} selection criterion in the $D_s^+ \to \eta\pi^+$ decay mode. Plots on the left grouped as Fig. A.13 correspond to pion-fitted tracks in the simulated samples. Plots on the right grouped as Fig. A.14 correspond to electron-fitted tracks in the samples. The top left plots, for both samples, is the distribution of m_{BC} in the signal Monte Carlo sample. The top right plot graphs the signal MC sample accepted by the criterion as we increase the cut width plotted on the x-axis. For the pion-fitted samples on the left, the plots in the second and third rows correspond to the generic and continuum MC samples, respectively. For the electron-fitted samples on the right, the plots in the second, third and fourth rows correspond to the $D_s^{*+} \to D_s^+\gamma$, generic and continuum MC samples, respectively. For both sets of plots, the bottom left shows the significance of the signal over background. The bottom right plot shows the precision of the signal.

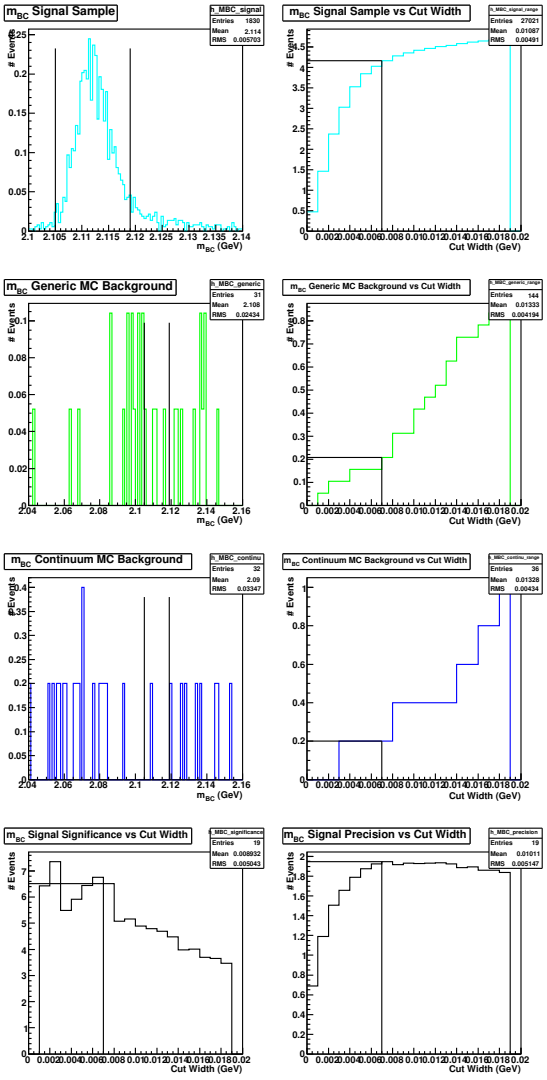

Figure A.13: m_{BC}, $\eta\pi^+$, pion-fit

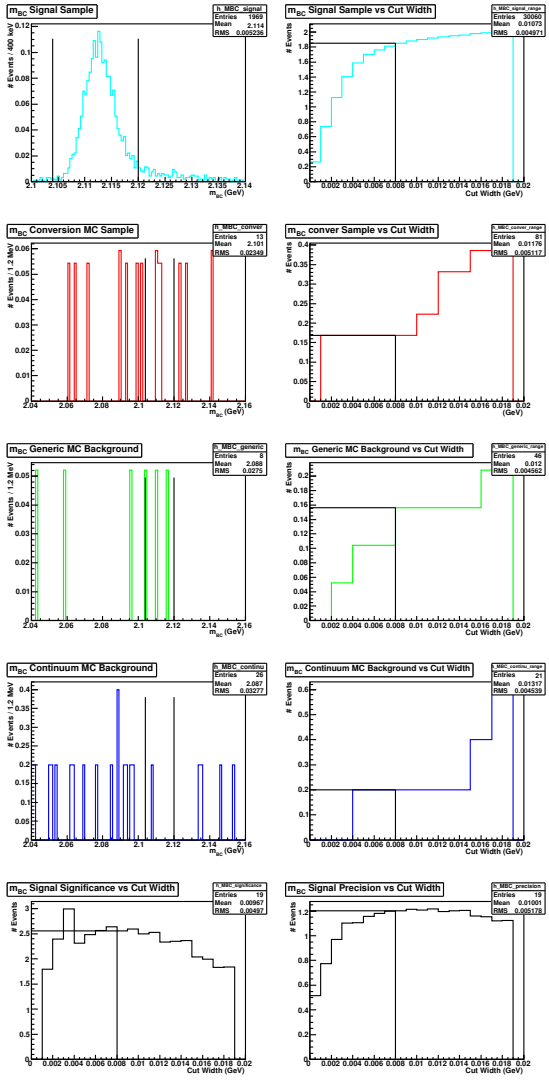

Figure A.14: m_{BC}, $\eta\pi^+$, electron-fit

Optimization plots for the δm selection criterion in the $D_s^+ \to \eta\pi^+$ decay mode. Plots on the left grouped as Fig. A.15 correspond to pion-fitted tracks in the simulated samples. Plots on the right grouped as Fig. A.16 correspond to electron-fitted tracks in the samples. The top left plots, for both samples, is the distribution of δm in the signal Monte Carlo sample. The top right plot graphs the signal MC sample accepted by the criterion as we increase the cut width plotted on the x-axis. For the pion-fitted samples on the left, the plots in the second and third rows correspond to the generic and continuum MC samples, respectively. For the electron-fitted samples on the right, the plots in the second, third and fourth rows correspond to the $D_s^{*+} \to D_s^+\gamma$, generic and continuum MC samples, respectively. For both sets of plots, the bottom left shows the significance of the signal over background. The bottom right plot shows the precision of the signal.

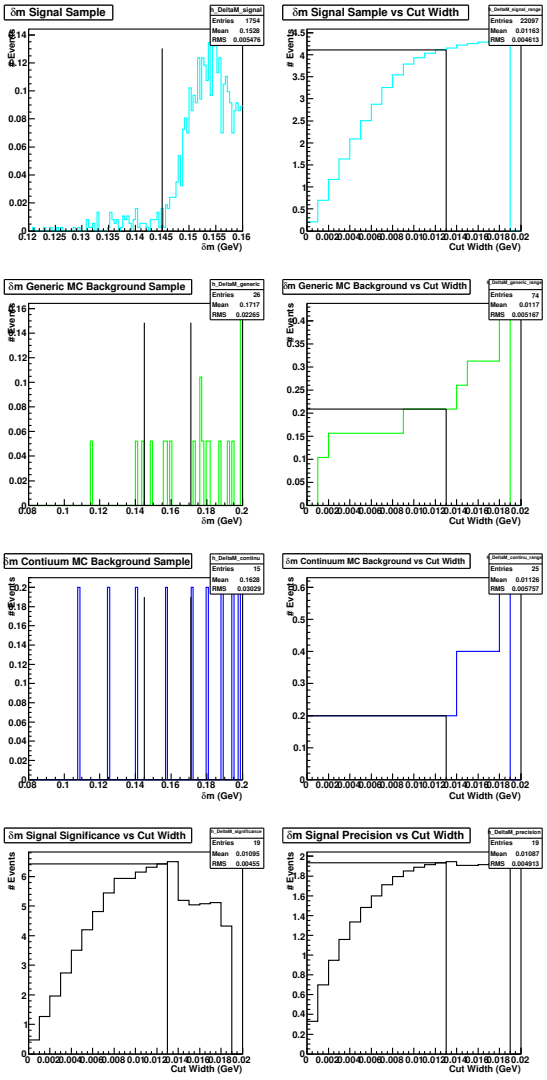

Figure A.15: δm, $\eta\pi^+$, pion-fit

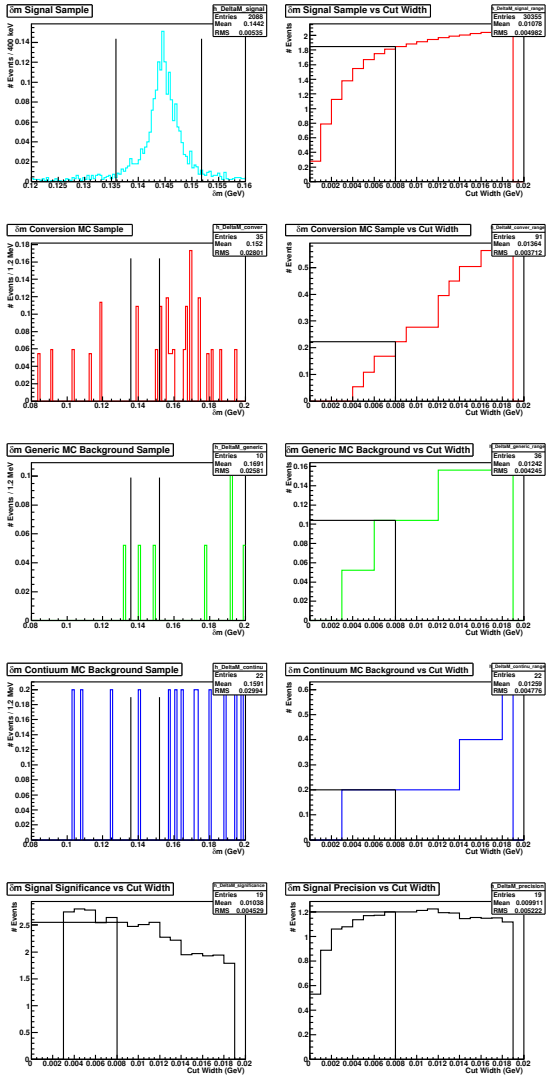

Figure A.16: δm, $\eta\pi^+$, electron-fit

Optimization plots for the selection criterion on the Δd_0 between the e^+e^- in the $D_s^+ \to \eta\pi^+$ decay mode. Plots on the left grouped as Fig. A.17 correspond to pion-fitted tracks in the simulated samples. Plots on the right grouped as Fig. A.18 correspond to electron-fitted tracks in the samples. The top left plots, for both samples, is the distribution of Δd_0 in the signal Monte Carlo sample. The top right plot graphs the signal MC sample accepted by the criterion as we vary the cut on the x-axis. For the pion-fitted samples on the left, the plots in the second and third rows correspond to the generic and continuum MC samples, respectively. For the electron-fitted samples on the right, the plots in the second, third and fourth rows correspond to the $D_s^{*+} \to D_s^+\gamma$, generic and continuum MC samples, respectively. For both sets of plots, the bottom left shows the significance of the signal over background. The bottom right plot shows the precision of the signal.

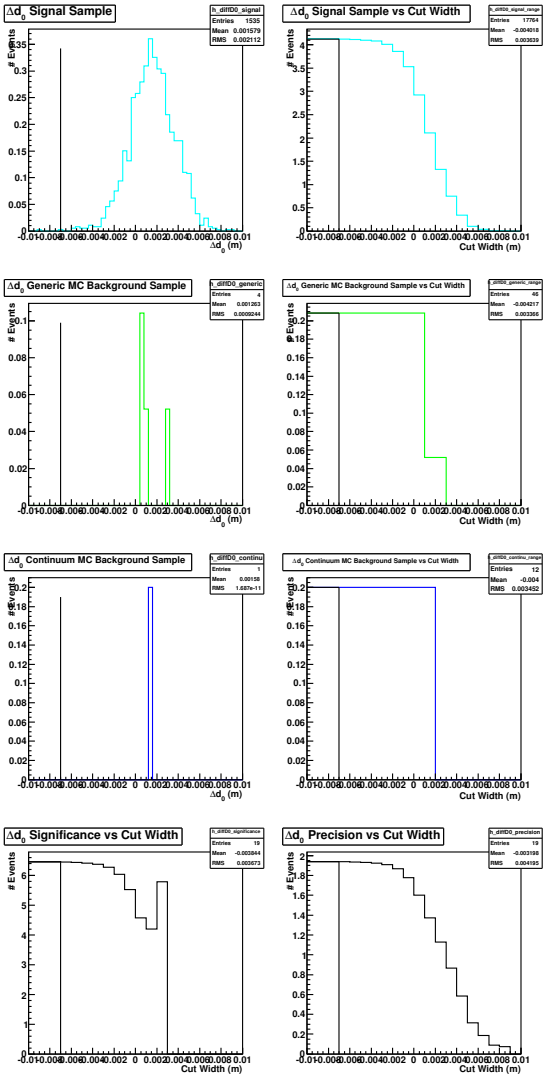

Figure A.17: Δd_0, $\eta\pi^+$, pion-fit

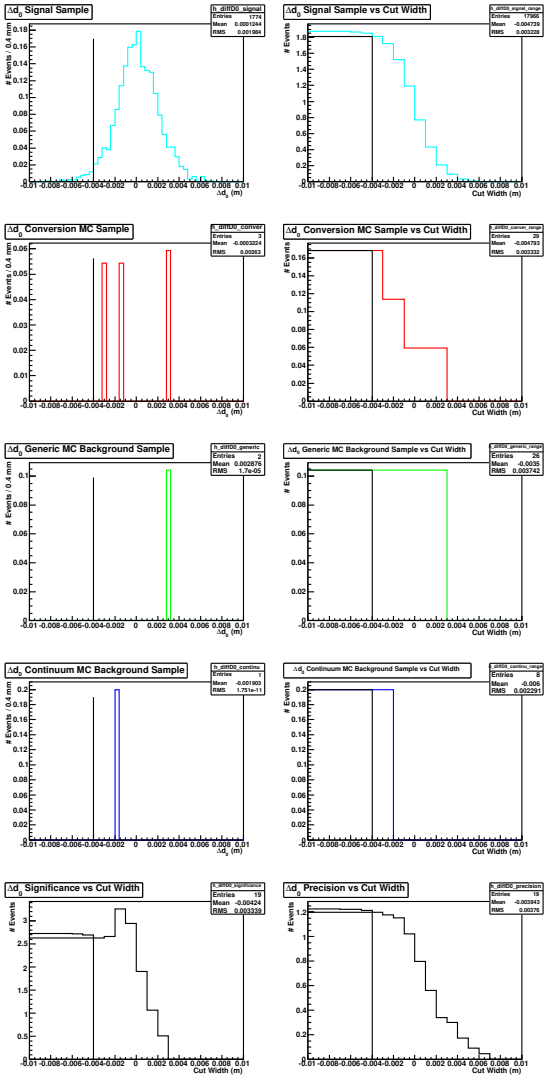

Figure A.18: Δd_0, $\eta\pi^+$, electron-fit

Optimization plots for the selection criterion on the $\Delta\phi_0$ between the e^+e^- in the $D_s^+ \to \eta\pi^+$ decay mode. Plots on the left grouped as Fig. A.19 correspond to pion-fitted tracks in the simulated samples. Plots on the right grouped as Fig. A.20 correspond to electron-fitted tracks in the samples. The top left plots, for both samples, is the distribution of $\Delta\phi_0$ in the signal Monte Carlo sample. The top right plot graphs the signal MC sample accepted by the criterion as we vary the cut on the x-axis. For the pion-fitted samples on the left, the plots in the second and third rows correspond to the generic and continuum MC samples, respectively. For the electron-fitted samples on the right, the plots in the second, third and fourth rows correspond to the $D_s^{*+} \to D_s^+\gamma$, generic and continuum MC samples, respectively. For both sets of plots, the bottom left shows the significance of the signal over background. The bottom right plot shows the precision of the signal.

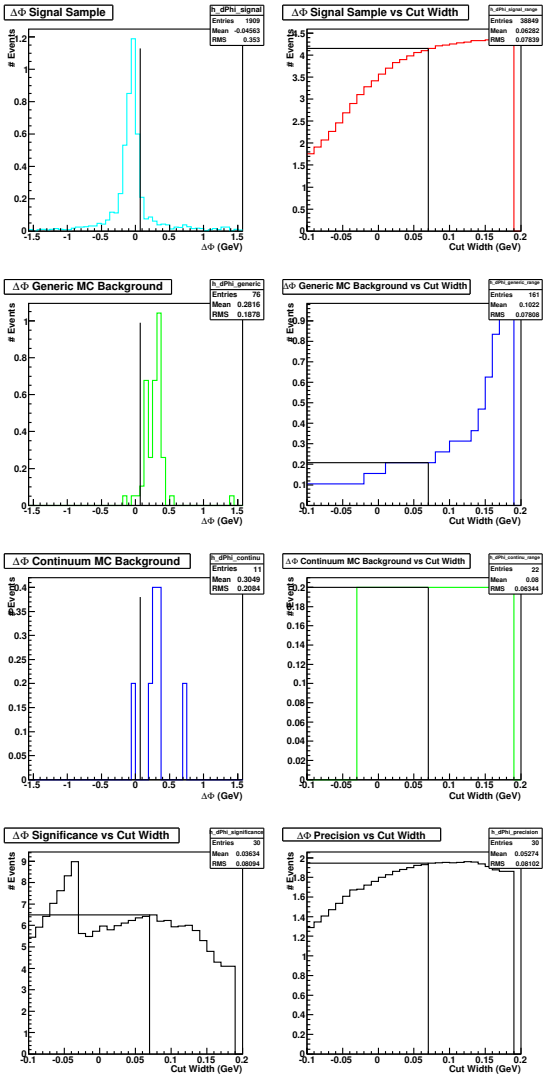

Figure A.19: $\Delta\phi_0$, $\eta\pi^+$, pion-fit

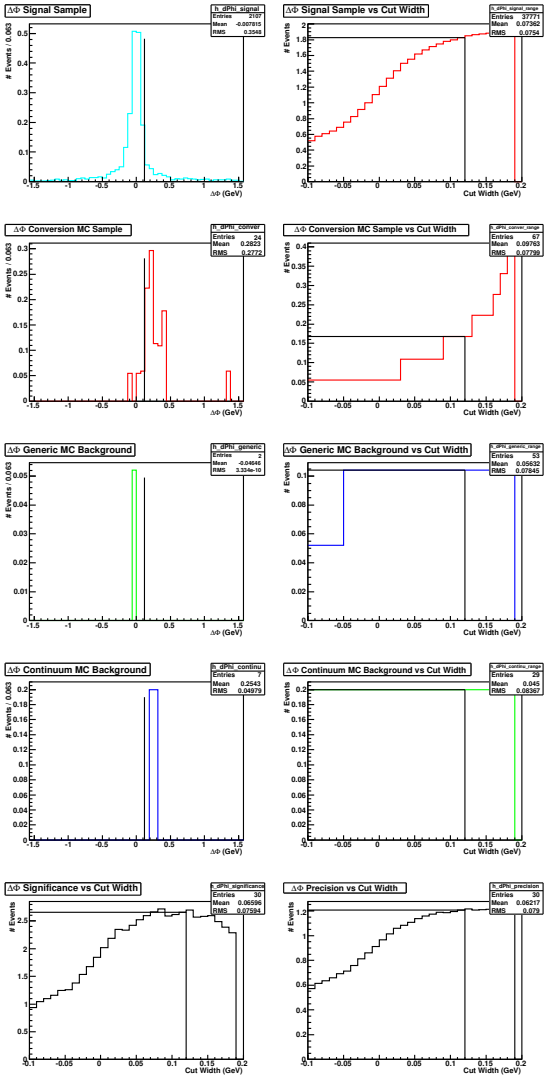

Figure A.20: $\Delta\phi_0$, $\eta\pi^+$, electron-fit

A.3 $D_s^+ \to \eta'\pi^+; \eta' \to \pi^+\pi^-\eta; \eta \to \gamma\gamma$

Optimization plots for the $m_{D_s^+}$ selection criterion in the $D_s^+ \to \eta'\pi^+; \eta' \to \pi^+\pi^-\eta; \eta \to \gamma\gamma$ mode. Plots on the left grouped as Fig. A.21 correspond to pion-fitted tracks in the simulated samples. Plots on the right grouped as Fig. A.22 correspond to electron-fitted tracks in the samples. The top left plots, for both samples, is the distribution of $m_{D_s^+}$ in the signal Monte Carlo sample. The top right plot graphs the signal MC sample accepted by the criterion as we increase the cut width plotted on the x-axis. For the pion-fitted samples on the left, the plots in the second and third rows correspond to the generic and continuum MC samples, respectively. For the electron-fitted samples on the right, the plots in the second, third and fourth rows correspond to the $D_s^{*+} \to D_s^+\gamma$, generic and continuum MC samples, respectively. For both sets of plots, the bottom left shows the significance of the signal over background. The bottom right plot shows the precision of the signal.

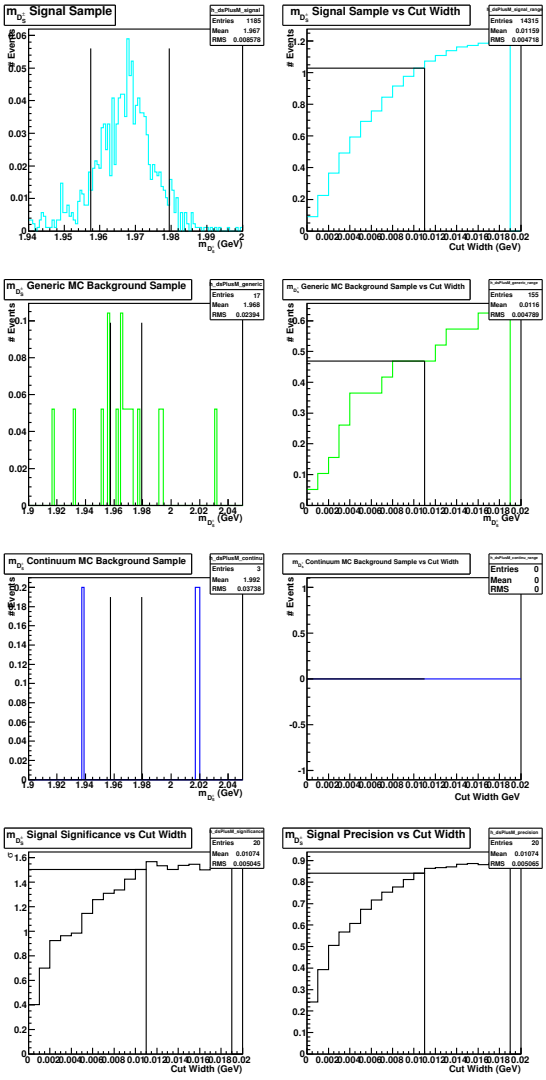

Figure A.21: $m_{D_s^+}, \eta'\pi^+; \eta' \to \pi^+\pi^-\eta$, pion-fit

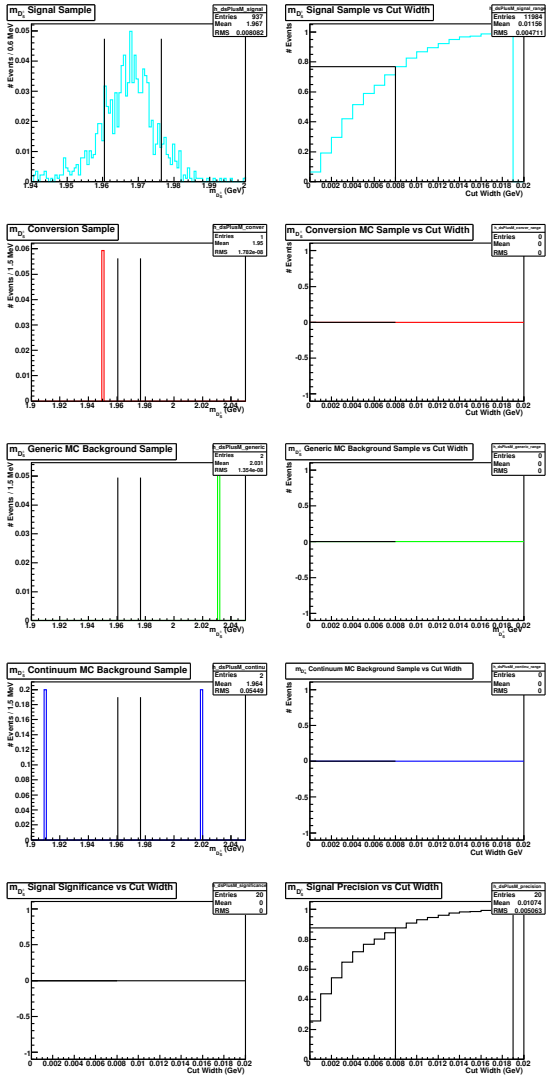

Figure A.22: $m_{D_s^+}, \eta'\pi^+; \eta' \to \pi^+\pi^-\eta$, e-fit

Optimization plots for the m_{BC} selection criterion in the $D_s^+ \to \eta'\pi^+; \eta' \to \pi^+\pi^-\eta; \eta \to \gamma\gamma$ decay mode. Plots on the left grouped as Fig. A.23 correspond to pion-fitted tracks in the simulated samples. Plots on the right grouped as Fig. A.24 correspond to electron-fitted tracks in the samples. The top left plots, for both samples, is the distribution of m_{BC} in the signal Monte Carlo sample. The top right plot graphs the signal MC sample accepted by the criterion as we increase the cut width plotted on the x-axis. For the pion-fitted samples on the left, the plots in the second and third rows correspond to the generic and continuum MC samples, respectively. For the electron-fitted samples on the right, the plots in the second, third and fourth rows correspond to the $D_s^{*+} \to D_s^+\gamma$, generic and continuum MC samples, respectively. For both sets of plots, the bottom left shows the significance of the signal over background. The bottom right plot shows the precision of the signal.

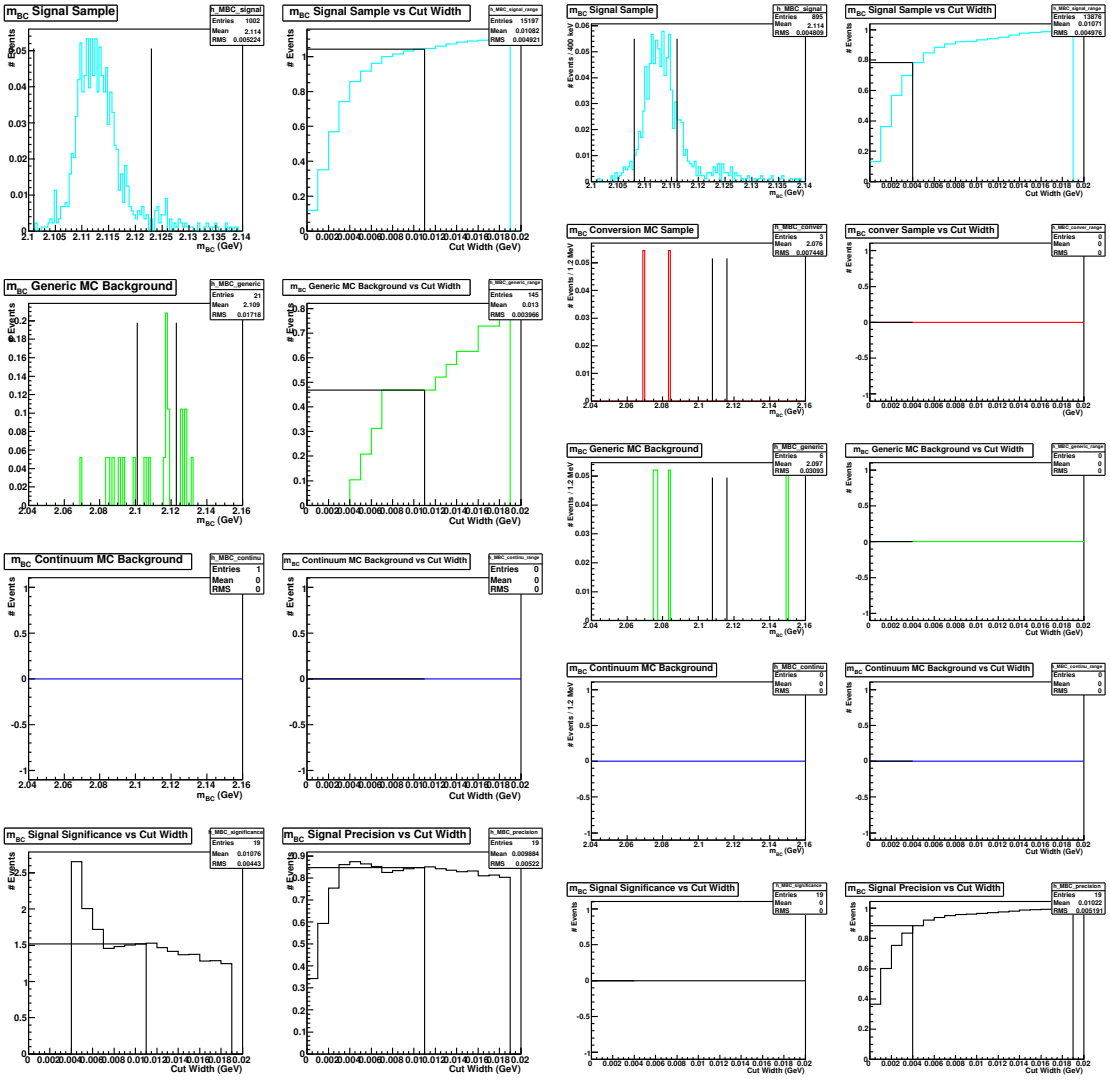

Figure A.23: m_{BC}, $\eta'\pi^+; \eta' \to \pi^+\pi^-\eta$, Figure A.24: m_{BC}, $\eta'\pi^+; \eta' \to \pi^+\pi^-\eta$, e-fit pion-fit

Optimization plots for the δm selection criterion in the $D_s^+ \to \eta'\pi^+; \eta' \to \pi^+\pi^-\eta; \eta \to \gamma\gamma$ decay mode. Plots on the left grouped as Fig. A.25 correspond to pion-fitted tracks in the simulated samples. Plots on the right grouped as Fig. A.26 correspond to electron-fitted tracks in the samples. The top left plots, for both samples, is the distribution of δm in the signal Monte Carlo sample. The top right plot graphs the signal MC sample accepted by the criterion as we increase the cut width plotted on the x-axis. For the pion-fitted samples on the left, the plots in the second and third rows correspond to the generic and continuum MC samples, respectively. For the electron-fitted samples on the right, the plots in the second, third and fourth rows correspond to the $D_s^{*+} \to D_s^+\gamma$, generic and continuum MC samples, respectively. For both sets of plots, the bottom left shows the significance of the signal over background. The bottom right plot shows the precision of the signal.

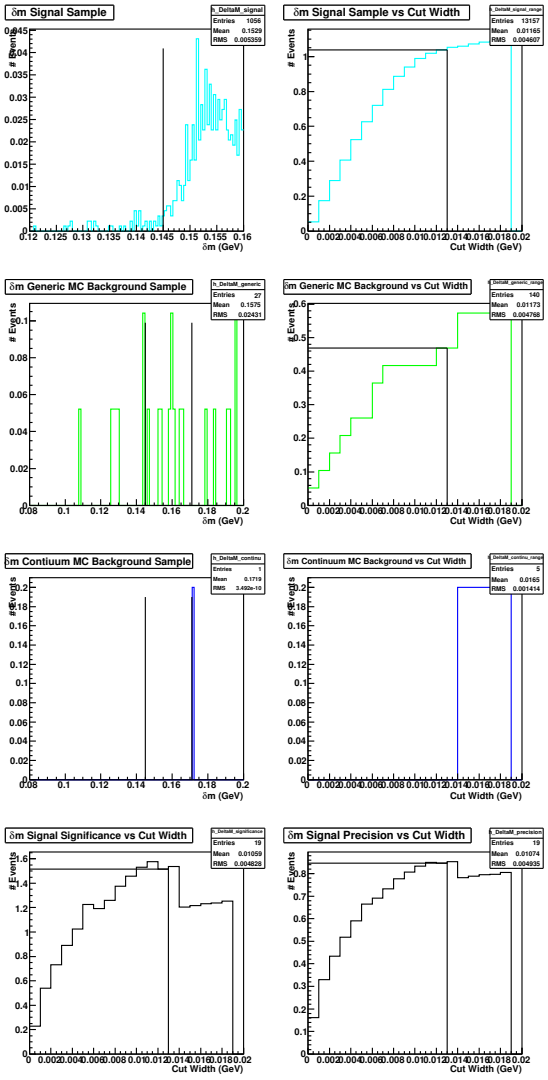

Figure A.25: δm, $\eta'\pi^+; \eta' \to \pi^+\pi^-\eta$, pion-fit

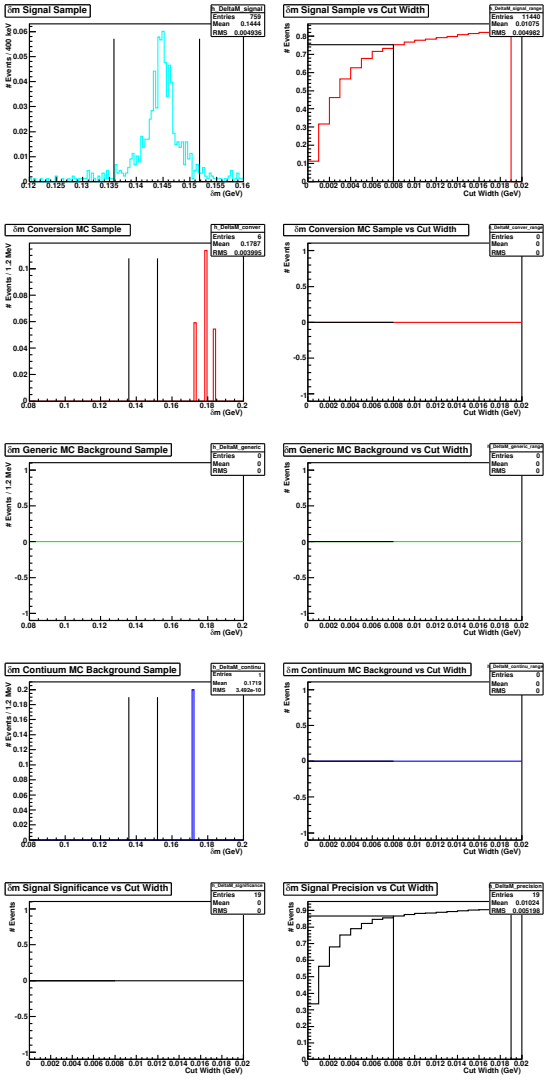

Figure A.26: δm, $\eta'\pi^+; \eta' \to \pi^+\pi^-\eta$, e-fit

Optimization plots for the selection criterion on the Δd_0 between the e^+e^- in the $D_s^+ \to \eta'\pi^+; \eta' \to \pi^+\pi^-\eta; \eta \to \gamma\gamma$ decay mode. Plots on the left grouped as Fig. A.27 correspond to pion-fitted tracks in the simulated samples. Plots on the right grouped as Fig. A.28 correspond to electron-fitted tracks in the samples. The top left plots, for both samples, is the distribution of Δd_0 in the signal Monte Carlo sample. The top right plot graphs the signal MC sample accepted by the criterion as we vary the cut on the x-axis. For the pion-fitted samples on the left, the plots in the second and third rows correspond to the generic and continuum MC samples, respectively. For the electron-fitted samples on the right, the plots in the second, third and fourth rows correspond to the $D_s^{*+} \to D_s^+\gamma$, generic and continuum MC samples, respectively. For both sets of plots, the bottom left shows the significance of the signal over background. The bottom right plot shows the precision of the signal.

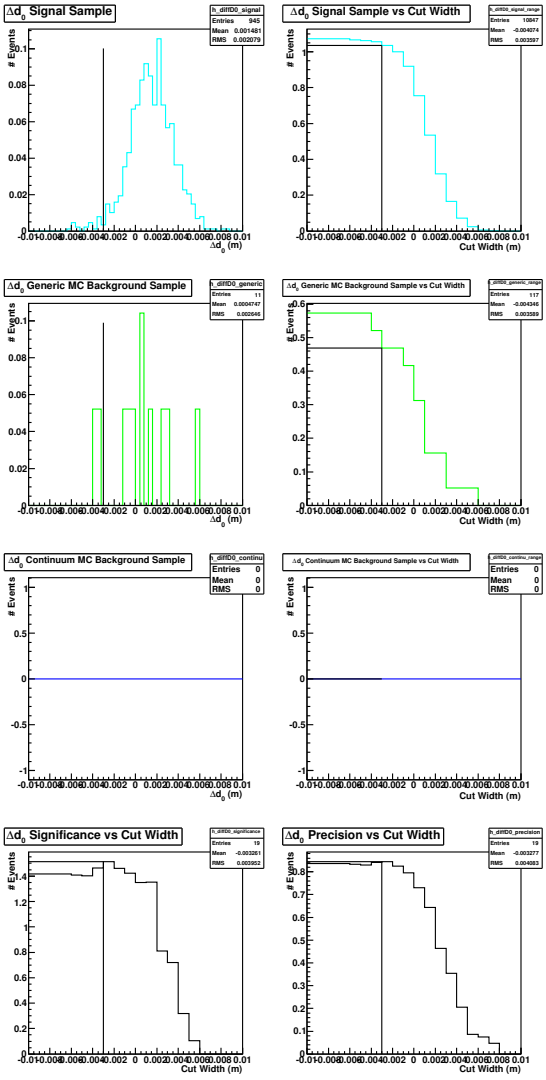

Figure A.27: Δd_0, $\eta'\pi^+; \eta' \to \pi^+\pi^-\eta$, pion-fit

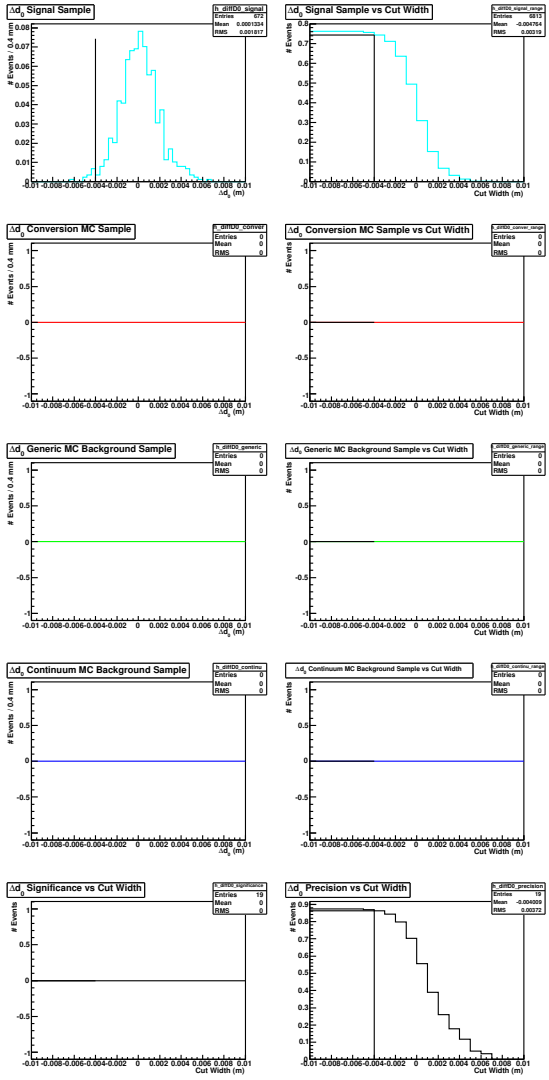

Figure A.28: Δd_0, $\eta'\pi^+; \eta' \to \pi^+\pi^-\eta$, e-fit

Optimization plots for the selection criterion on the $\Delta\phi_0$ between the e^+e^- in the $D_s^+ \to \eta'\pi^+; \eta' \to \pi^+\pi^-\eta; \eta \to \gamma\gamma$ decay mode. Plots on the left grouped as Fig. A.29 correspond to pion-fitted tracks in the simulated samples. Plots on the right grouped as Fig. A.30 correspond to electron-fitted tracks in the samples. The top left plots, for both samples, is the distribution of $\Delta\phi_0$ in the signal Monte Carlo sample. The top right plot graphs the signal MC sample accepted by the criterion as we vary the cut on the x-axis. For the pion-fitted samples on the left, the plots in the second and third rows correspond to the generic and continuum MC samples, respectively. For the electron-fitted samples on the right, the plots in the second, third and fourth rows correspond to the $D_s^{*+} \to D_s^+\gamma$, generic and continuum MC samples, respectively. For both sets of plots, the bottom left shows the significance of the signal over background. The bottom right plot shows the precision of the signal.

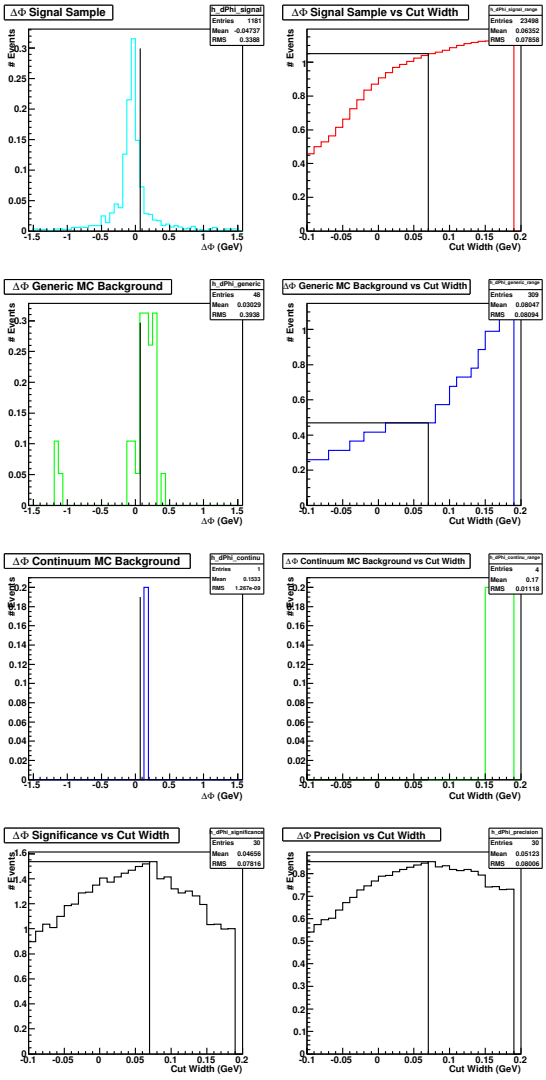

Figure A.29: $\Delta\phi_0, \eta'\pi^+; \eta' \to \pi^+\pi^-\eta$, pion-fit

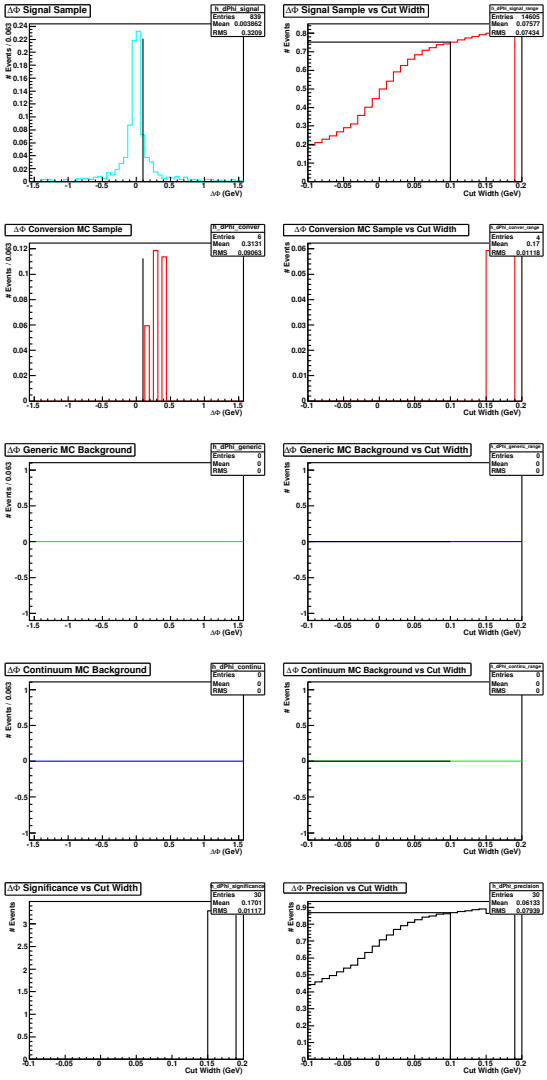

Figure A.30: $\Delta\phi_0, \eta'\pi^+; \eta' \to \pi^+\pi^-\eta$, e-fit

A.4 $D_s^+ \to K^+K^-\pi^+\pi^0$

Optimization plots for the $m_{D_s^+}$ selection criterion in the $D_s^+ \to K^+K^-\pi^+\pi^0$ mode. Plots on the left grouped as Fig. A.31 correspond to pion-fitted tracks in the simulated samples. Plots on the right grouped as Fig. A.32 correspond to electron-fitted tracks in the samples. The top left plots, for both samples, is the distribution of $m_{D_s^+}$ in the signal Monte Carlo sample. The top right plot graphs the signal MC sample accepted by the criterion as we increase the cut width plotted on the x-axis. For the pion-fitted samples on the left, the plots in the second and third rows correspond to the generic and continuum MC samples, respectively. For the electron-fitted samples on the right, the plots in the second, third and fourth rows correspond to the $D_s^{*+} \to D_s^+\gamma$, generic and continuum MC samples, respectively. For both sets of plots, the bottom left shows the significance of the signal over background. The bottom right plot shows the precision of the signal.

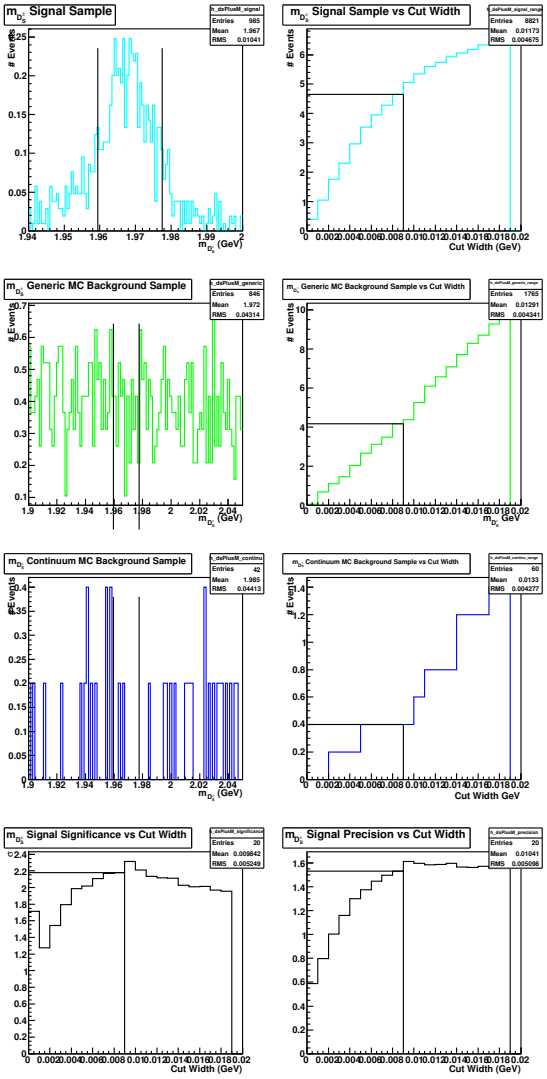

Figure A.31: $m_{D_s^+}$, $K^+K^-\pi^+\pi^0$, pion-fit

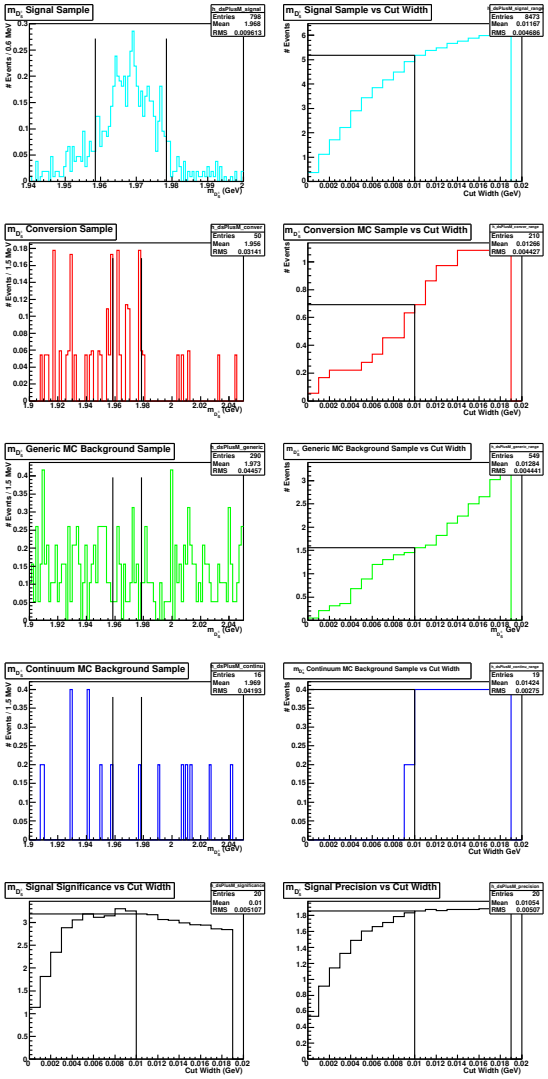

Figure A.32: $m_{D_s^+}$, $K^+K^-\pi^+\pi^0$, electron-fit

Optimization plots for the m_{BC} selection criterion in the $D_s^+ \to K^+K^-\pi^+\pi^0$ decay mode. Plots on the left grouped as Fig. A.33 correspond to pion-fitted tracks in the simulated samples. Plots on the right grouped as Fig. A.34 correspond to electron-fitted tracks in the samples. The top left plots, for both samples, is the distribution of m_{BC} in the signal Monte Carlo sample. The top right plot graphs the signal MC sample accepted by the criterion as we increase the cut width plotted on the x-axis. For the pion-fitted samples on the left, the plots in the second and third rows correspond to the generic and continuum MC samples, respectively. For the electron-fitted samples on the right, the plots in the second, third and fourth rows correspond to the $D_s^{*+} \to D_s^+\gamma$, generic and continuum MC samples, respectively. For both sets of plots, the bottom left shows the significance of the signal over background. The bottom right plot shows the precision of the signal.

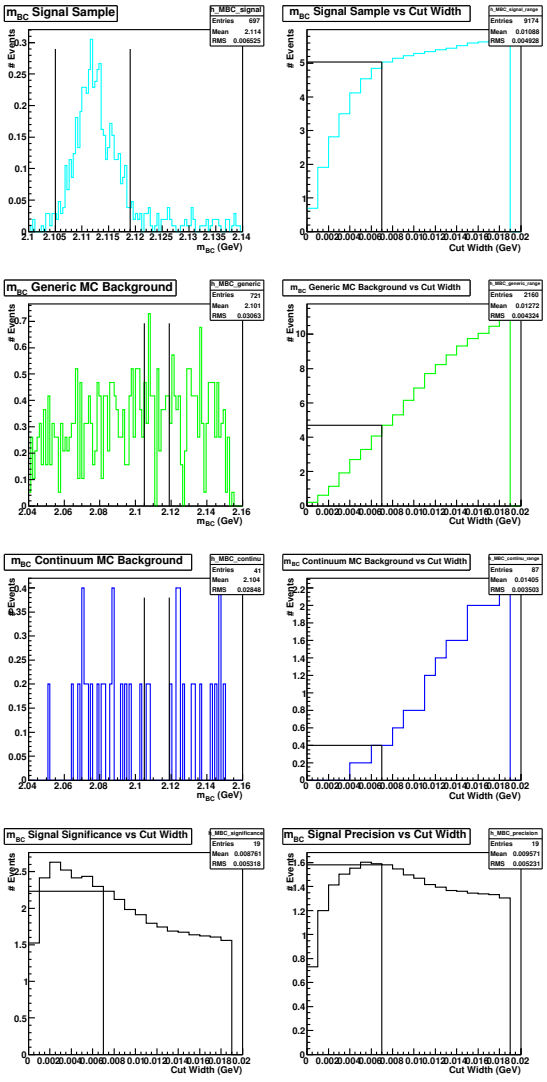

Figure A.33: m_{BC}, $K^+K^-\pi^+\pi^0$, pion-fit

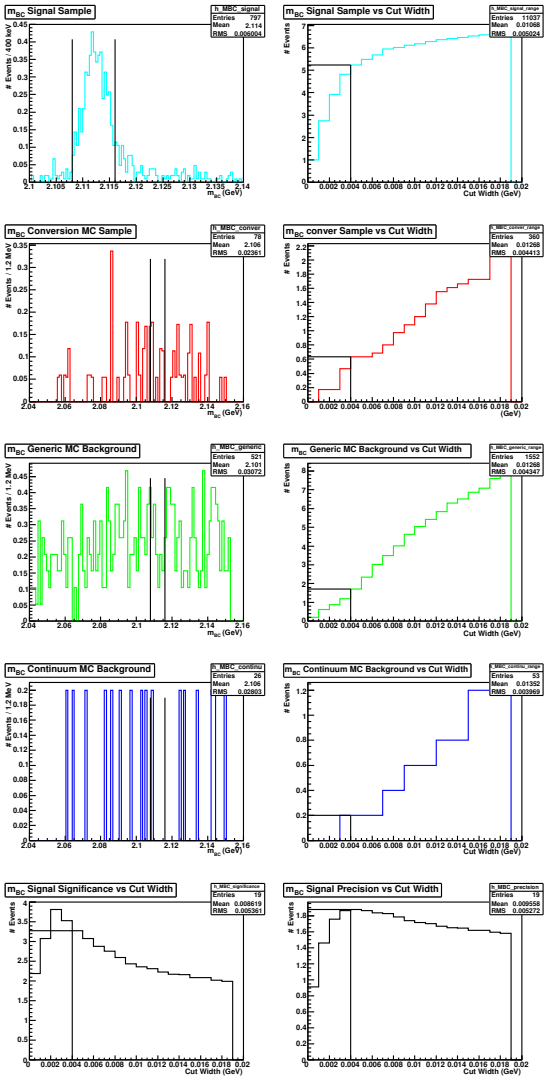

Figure A.34: m_{BC}, $K^+K^-\pi^+\pi^0$, electron-fit

Optimization plots for the δm selection criterion in the $D_s^+ \to K^+K^-\pi^+\pi^0$ decay mode. Plots on the left grouped as Fig. A.35 correspond to pion-fitted tracks in the simulated samples. Plots on the right grouped as Fig. A.36 correspond to electron-fitted tracks in the samples. The top left plots, for both samples, is the distribution of δm in the signal Monte Carlo sample. The top right plot graphs the signal MC sample accepted by the criterion as we increase the cut width plotted on the x-axis. For the pion-fitted samples on the left, the plots in the second and third rows correspond to the generic and continuum MC samples, respectively. For the electron-fitted samples on the right, the plots in the second, third and fourth rows correspond to the $D_s^{*+} \to D_s^+\gamma$, generic and continuum MC samples, respectively. For both sets of plots, the bottom left shows the significance of the signal over background. The bottom right plot shows the precision of the signal.

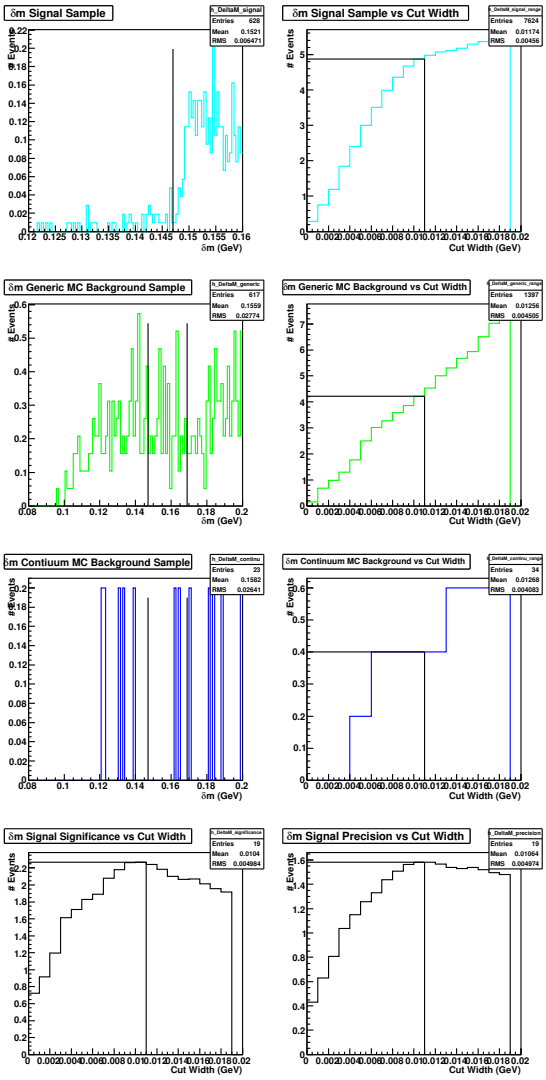

Figure A.35: δm, $K^+K^-\pi^+\pi^0$, pion-fit

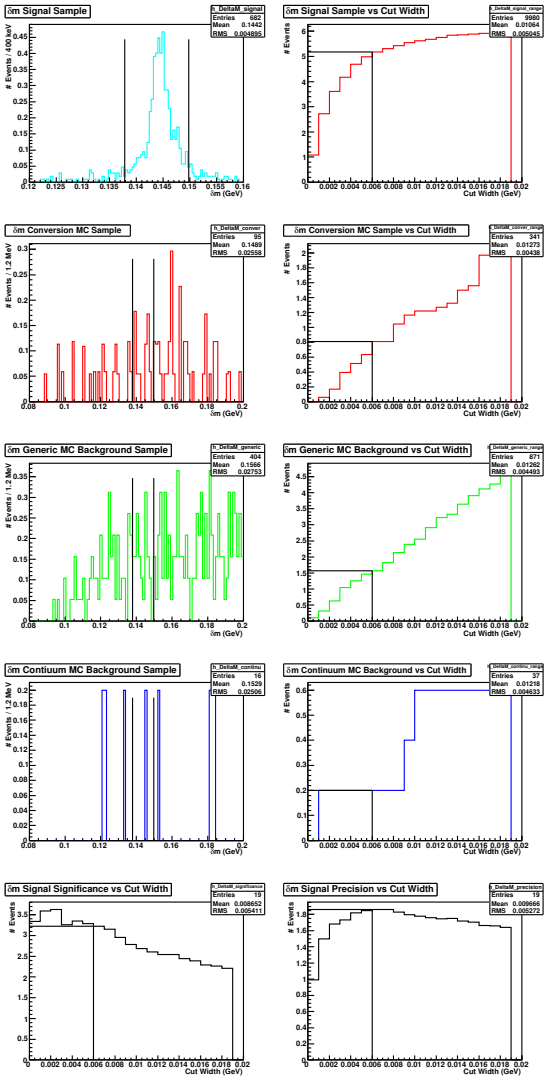

Figure A.36: δm, $K^+K^-\pi^+\pi^0$, electron-fit

Optimization plots for the selection criterion on the Δd_0 between the e^+e^- in the $D_s^+ \to K^+K^-\pi^+\pi^0$ decay mode. Plots on the left grouped as Fig. A.37 correspond to pion-fitted tracks in the simulated samples. Plots on the right grouped as Fig. A.38 correspond to electron-fitted tracks in the samples. The top left plots, for both samples, is the distribution of Δd_0 in the signal Monte Carlo sample. The top right plot graphs the signal MC sample accepted by the criterion as we vary the cut on the x-axis. For the pion-fitted samples on the left, the plots in the second and third rows correspond to the generic and continuum MC samples, respectively. For the electron-fitted samples on the right, the plots in the second, third and fourth rows correspond to the $D_s^{*+} \to D_s^+\gamma$, generic and continuum MC samples, respectively. For both sets of plots, the bottom left shows the significance of the signal over background. The bottom right plot shows the precision of the signal.

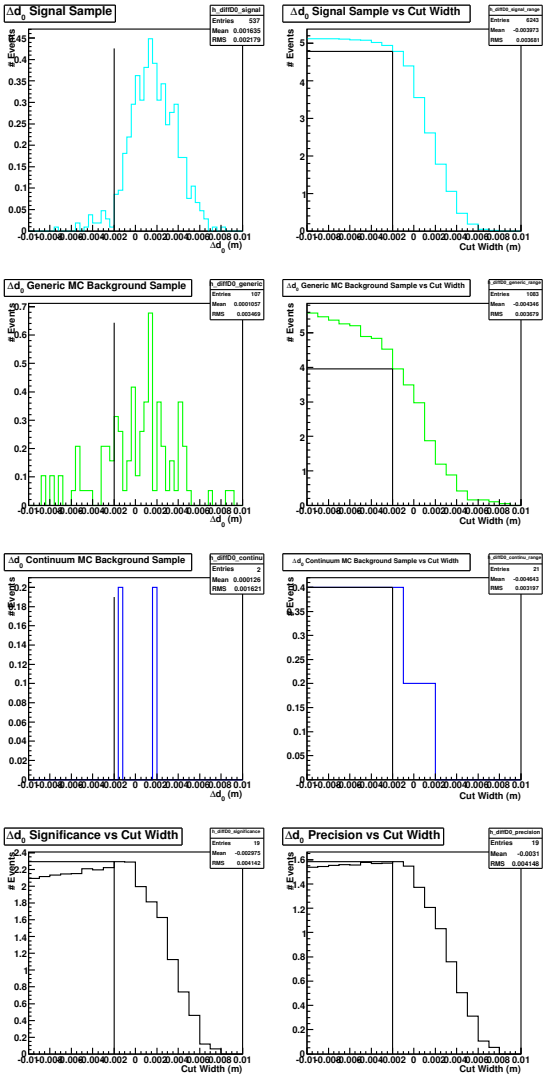

Figure A.37: Δd_0, $K^+K^-\pi^+\pi^0$, pion-fit

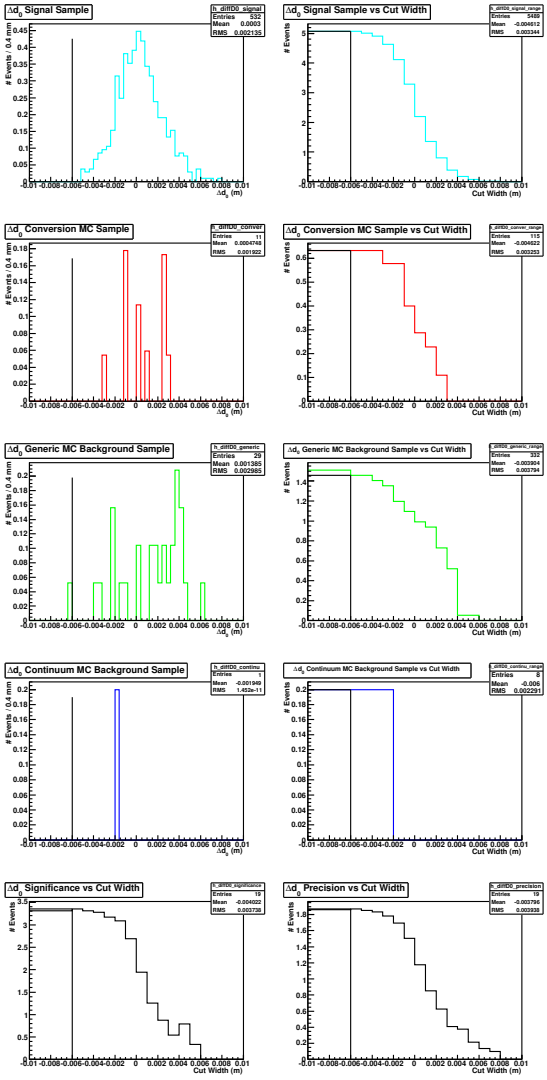

Figure A.38: Δd_0, $K^+K^-\pi^+\pi^0$, electron-fit

Optimization plots for the selection criterion on the $\Delta\phi_0$ between the e^+e^- in the $D_s^+ \to K^+K^-\pi^+\pi^0$ decay mode. Plots on the left grouped as Fig. A.39 correspond to pion-fitted tracks in the simulated samples. Plots on the right grouped as Fig. A.40 correspond to electron-fitted tracks in the samples. The top left plots, for both samples, is the distribution of $\Delta\phi_0$ in the signal Monte Carlo sample. The top right plot graphs the signal MC sample accepted by the criterion as we vary the cut on the x-axis. For the pion-fitted samples on the left, the plots in the second and third rows correspond to the generic and continuum MC samples, respectively. For the electron-fitted samples on the right, the plots in the second, third and fourth rows correspond to the $D_s^{*+} \to D_s^+\gamma$, generic and continuum MC samples, respectively. For both sets of plots, the bottom left shows the significance of the signal over background. The bottom right plot shows the precision of the signal.

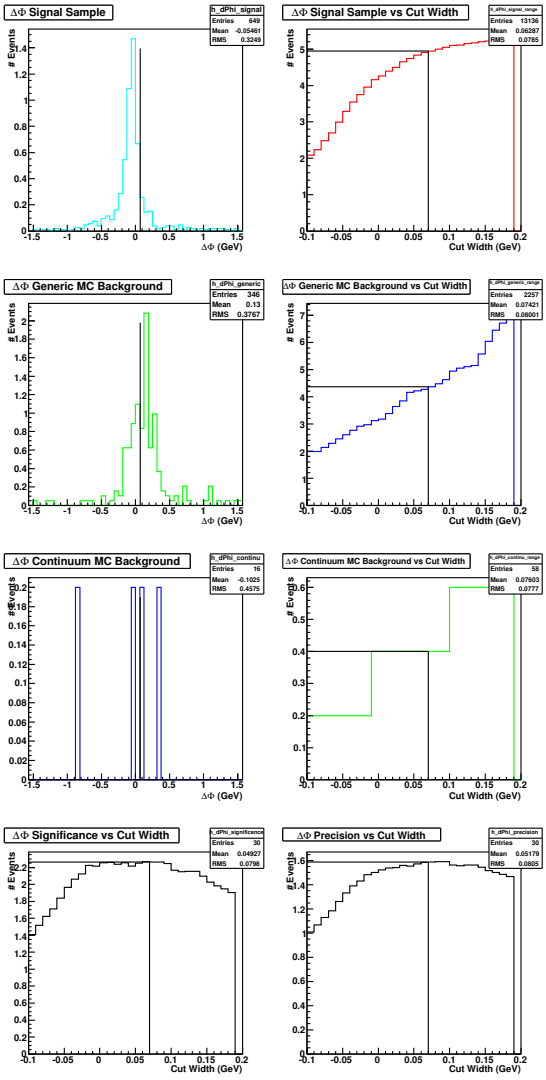

Figure A.39: $\Delta\phi_0$, $K^+K^-\pi^+\pi^0$, pion-fit

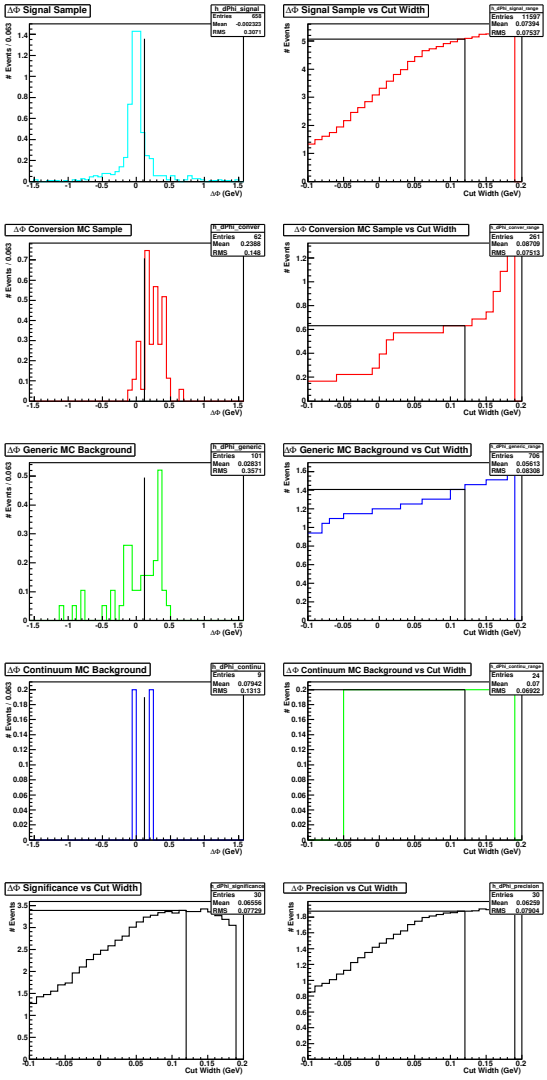

Figure A.40: $\Delta\phi_0$, $K^+K^-\pi^+\pi^0$, electron-fit

A.5 $D_s^+ \to \pi^+\pi^-\pi^+$

Optimization plots for the $m_{D_s^+}$ selection criterion in the $D_s^+ \to \pi^+\pi^-\pi^+$ mode. Plots on the left grouped as Fig. A.41 correspond to pion-fitted tracks in the simulated samples. Plots on the right grouped as Fig. A.42 correspond to electron-fitted tracks in the samples. The top left plots, for both samples, is the distribution of $m_{D_s^+}$ in the signal Monte Carlo sample. The top right plot graphs the signal MC sample accepted by the criterion as we increase the cut width plotted on the x-axis. For the pion-fitted samples on the left, the plots in the second and third rows correspond to the generic and continuum MC samples, respectively. For the electron-fitted samples on the right, the plots in the second, third and fourth rows correspond to the $D_s^{*+} \to D_s^+\gamma$, generic and continuum MC samples, respectively. For both sets of plots, the bottom left shows the significance of the signal over background. The bottom right plot shows the precision of the signal.

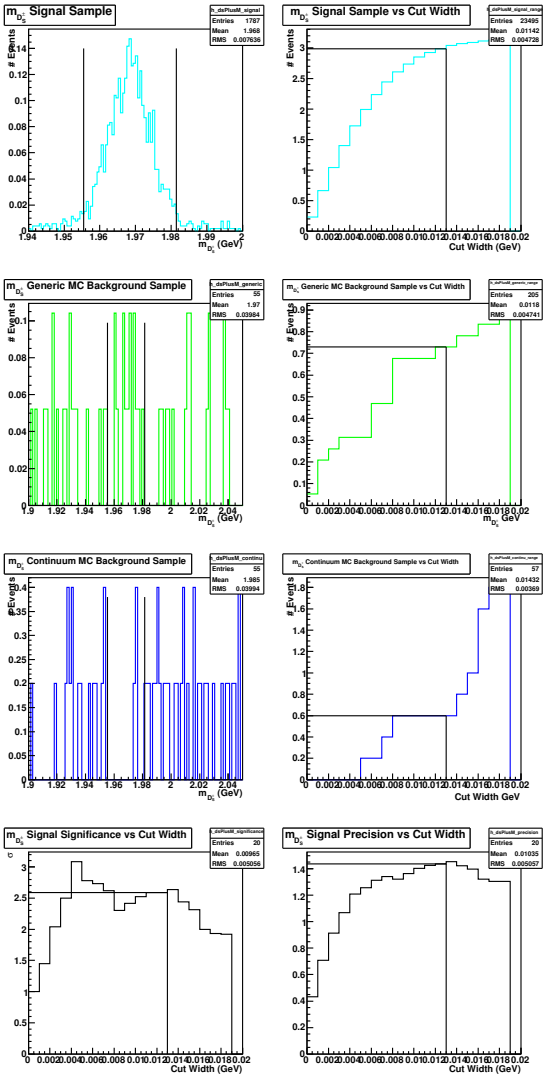

Figure A.41: $m_{D_s^+}$, $\pi^+\pi^-\pi^+$, pion-fit

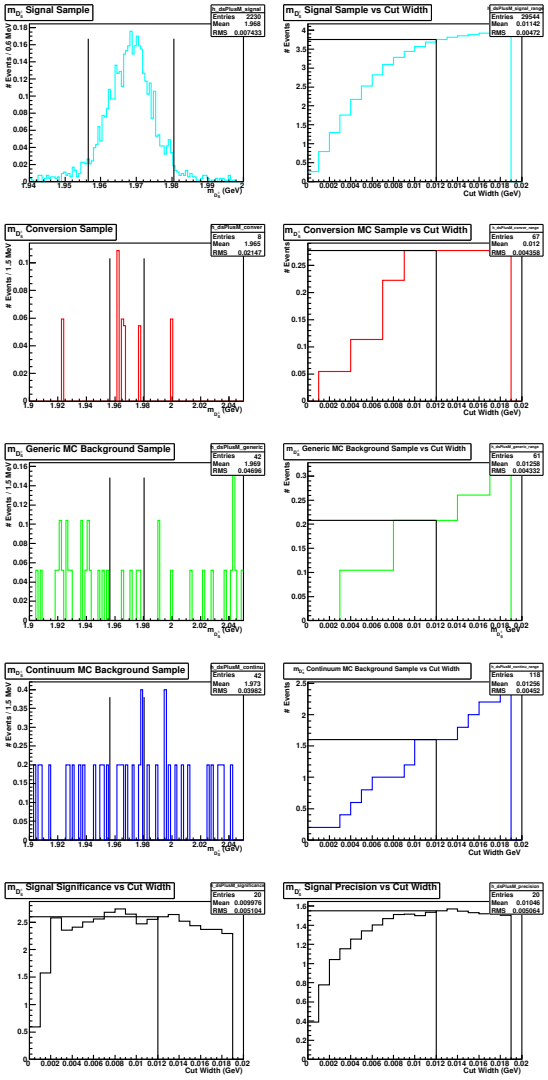

Figure A.42: $m_{D_s^+}$, $\pi^+\pi^-\pi^+$, electron-fit

Optimization plots for the m_{BC} selection criterion in the $D_s^+ \to \pi^+\pi^-\pi^+$ decay mode. Plots on the left grouped as Fig. A.43 correspond to pion-fitted tracks in the simulated samples. Plots on the right grouped as Fig. A.44 correspond to electron-fitted tracks in the samples. The top left plots, for both samples, is the distribution of m_{BC} in the signal Monte Carlo sample. The top right plot graphs the signal MC sample accepted by the criterion as we increase the cut width plotted on the x-axis. For the pion-fitted samples on the left, the plots in the second and third rows correspond to the generic and continuum MC samples, respectively. For the electron-fitted samples on the right, the plots in the second, third and fourth rows correspond to the $D_s^{*+} \to D_s^+\gamma$, generic and continuum MC samples, respectively. For both sets of plots, the bottom left shows the significance of the signal over background. The bottom right plot shows the precision of the signal.

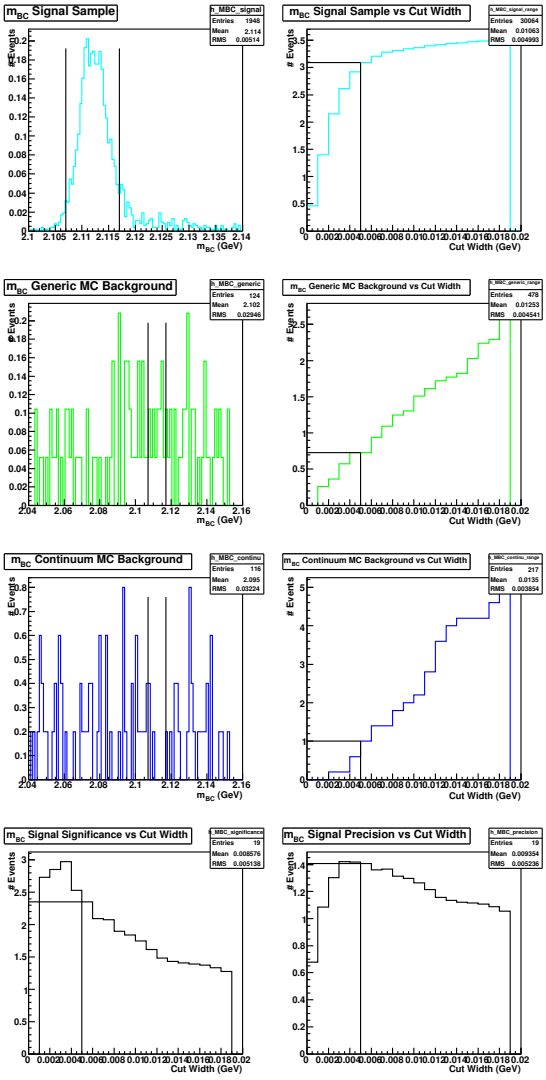

Figure A.43: m_{BC}, $\pi^+\pi^-\pi^+$, pion-fit

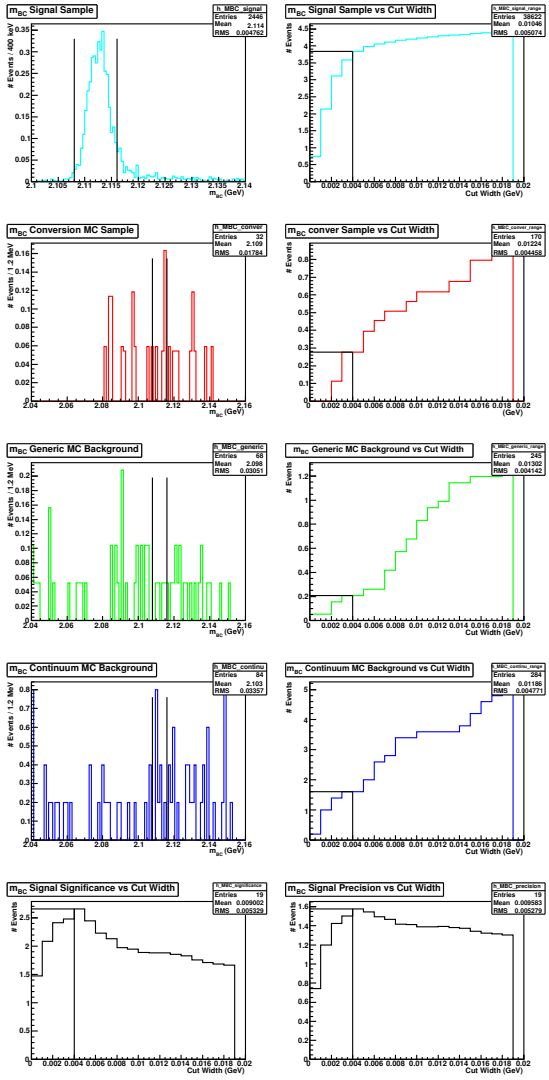

Figure A.44: m_{BC}, $\pi^+\pi^-\pi^+$, electron-fit

Optimization plots for the δm selection criterion in the $D_s^+ \to \pi^+\pi^-\pi^+$ decay mode. Plots on the left grouped as Fig. A.45 correspond to pion-fitted tracks in the simulated samples. Plots on the right grouped as Fig. A.46 correspond to electron-fitted tracks in the samples. The top left plots, for both samples, is the distribution of δm in the signal Monte Carlo sample. The top right plot graphs the signal MC sample accepted by the criterion as we increase the cut width plotted on the x-axis. For the pion-fitted samples on the left, the plots in the second and third rows correspond to the generic and continuum MC samples, respectively. For the electron-fitted samples on the right, the plots in the second, third and fourth rows correspond to the $D_s^{*+} \to D_s^+\gamma$, generic and continuum MC samples, respectively. For both sets of plots, the bottom left shows the significance of the signal over background. The bottom right plot shows the precision of the signal.

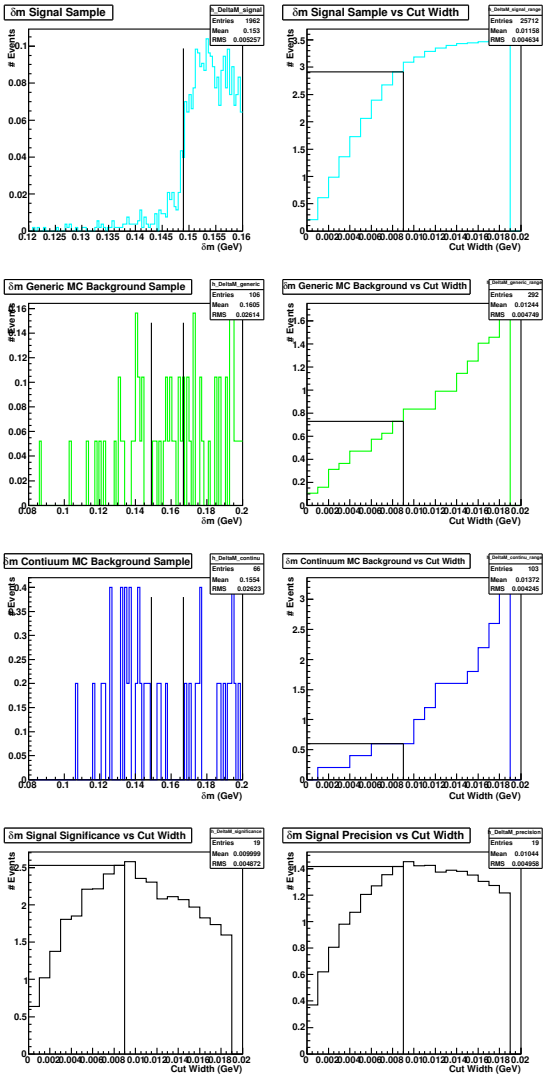

Figure A.45: δm, $\pi^+\pi^-\pi^+$, pion-fit

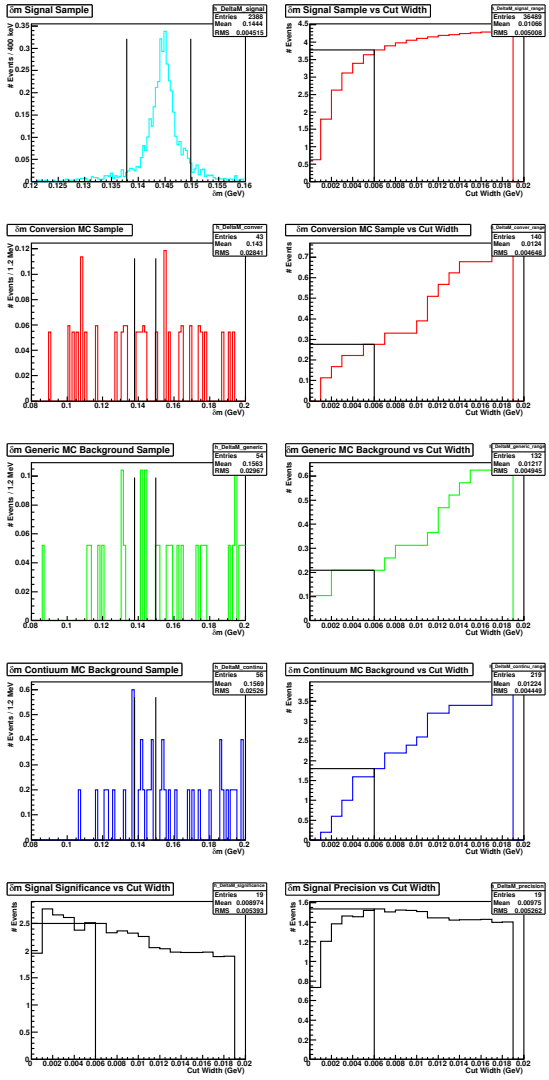

Figure A.46: δm, $\pi^+\pi^-\pi^+$, electron-fit

Optimization plots for the selection criterion on the Δd_0 between the e^+e^- in the $D_s^+ \to \pi^+\pi^-\pi^+$ decay mode. Plots on the left grouped as Fig. A.47 correspond to pion-fitted tracks in the simulated samples. Plots on the right grouped as Fig. A.48 correspond to electron-fitted tracks in the samples. The top left plots, for both samples, is the distribution of Δd_0 in the signal Monte Carlo sample. The top right plot graphs the signal MC sample accepted by the criterion as we vary the cut on the x-axis. For the pion-fitted samples on the left, the plots in the second and third rows correspond to the generic and continuum MC samples, respectively. For the electron-fitted samples on the right, the plots in the second, third and fourth rows correspond to the $D_s^{*+} \to D_s^+\gamma$, generic and continuum MC samples, respectively. For both sets of plots, the bottom left shows the significance of the signal over background. The bottom right plot shows the precision of the signal.

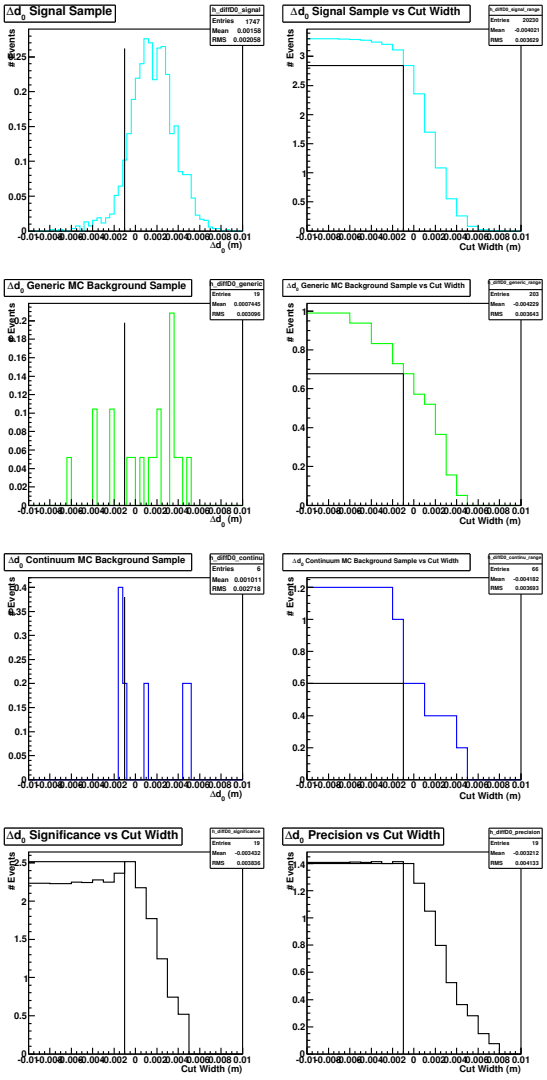

Figure A.47: Δd_0, $\pi^+\pi^-\pi^+$, pion-fit

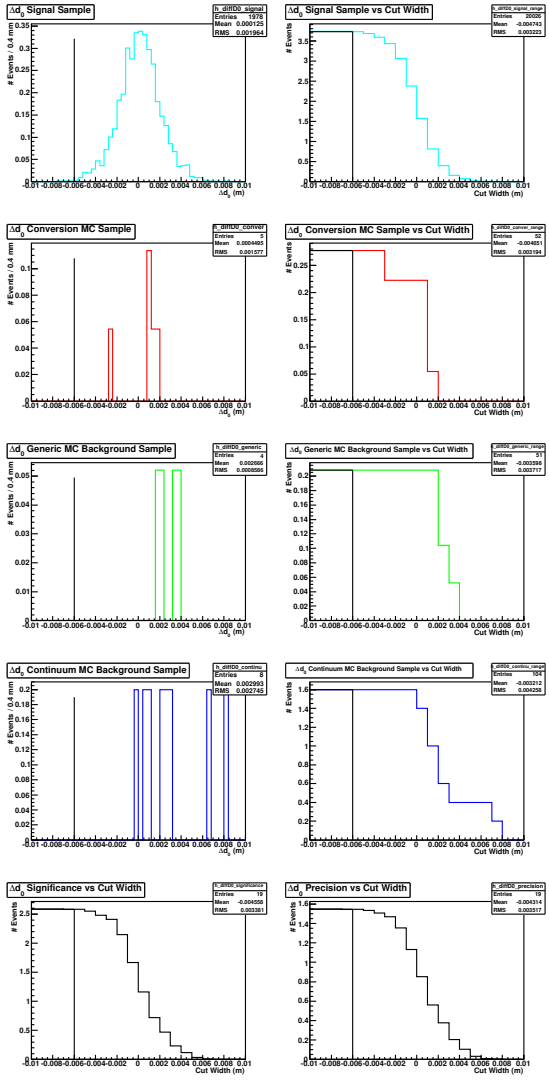

Figure A.48: Δd_0, $\pi^+\pi^-\pi^+$, electron-fit

Optimization plots for the selection criterion on the $\Delta\phi_0$ between the e^+e^- in the $D_s^+ \to \pi^+\pi^-\pi^+$ decay mode. Plots on the left grouped as Fig. A.49 correspond to pion-fitted tracks in the simulated samples. Plots on the right grouped as Fig. A.50 correspond to electron-fitted tracks in the samples. The top left plots, for both samples, is the distribution of $\Delta\phi_0$ in the signal Monte Carlo sample. The top right plot graphs the signal MC sample accepted by the criterion as we vary the cut on the x-axis. For the pion-fitted samples on the left, the plots in the second and third rows correspond to the generic and continuum MC samples, respectively. For the electron-fitted samples on the right, the plots in the second, third and fourth rows correspond to the $D_s^{*+} \to D_s^+\gamma$, generic and continuum MC samples, respectively. For both sets of plots, the bottom left shows the significance of the signal over background. The bottom right plot shows the precision of the signal.

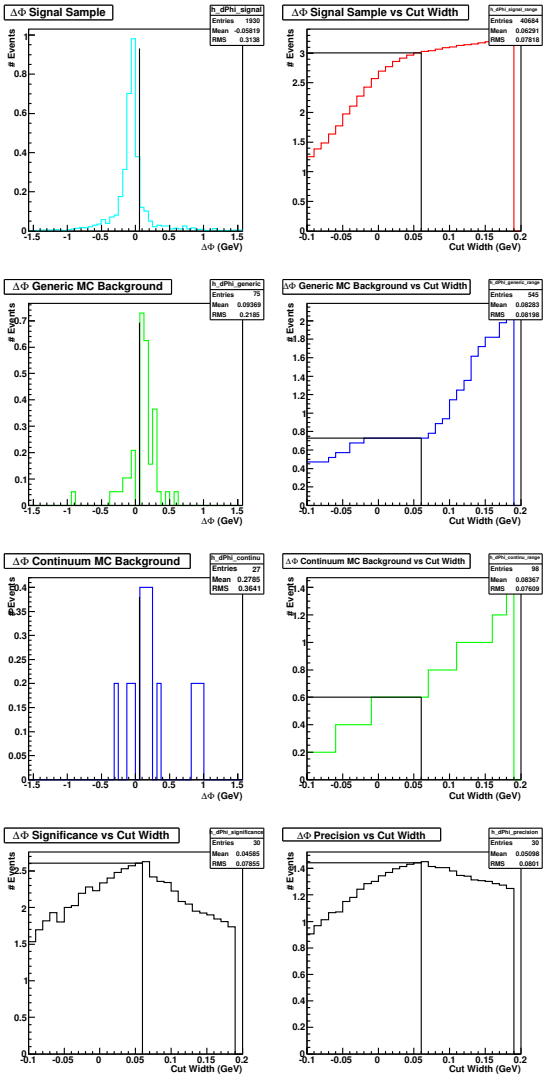

Figure A.49: $\Delta\phi_0$, $\pi^+\pi^-\pi^+$, pion-fit

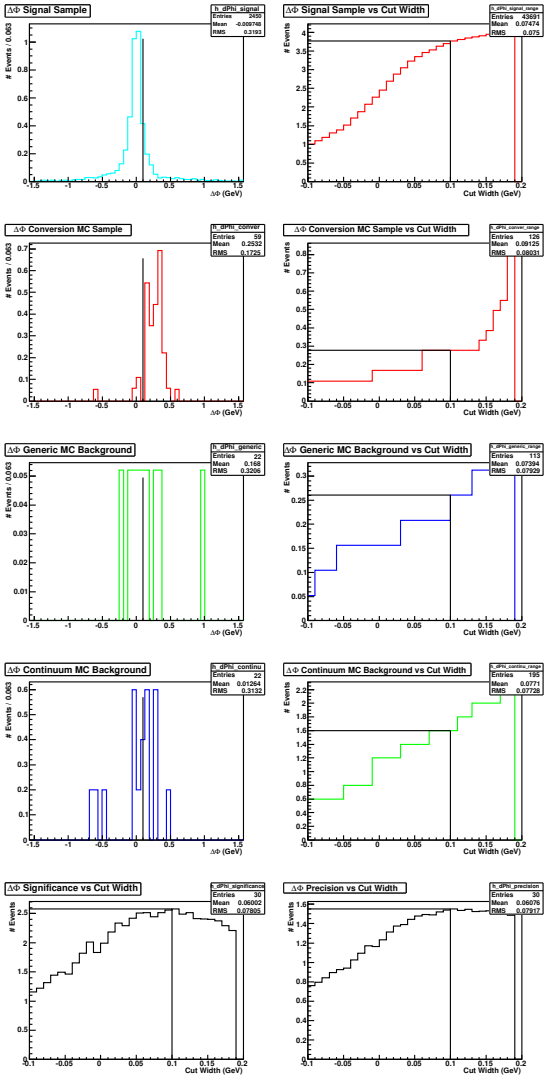

Figure A.50: $\Delta\phi_0$, $\pi^+\pi^-\pi^+$, electron-fit

A.6 $D_s^+ \rightarrow\rightarrow K^{*+}K^{*0}; K^{*+} \rightarrow K_S^0\pi^+, K^{*0} \rightarrow K^-\pi^+$

Optimization plots for the $m_{D_s^+}$ selection criterion in the $D_s^+ \to K^{*+}K^{*0}$ mode. Plots on the left grouped as Fig. A.51 correspond to pion-fitted tracks in the simulated samples. Plots on the right grouped as Fig. A.52 correspond to electron-fitted tracks in the samples. The top left plots, for both samples, is the distribution of $m_{D_s^+}$ in the signal Monte Carlo sample. The top right plot graphs the signal MC sample accepted by the criterion as we increase the cut width plotted on the x-axis. For the pion-fitted samples on the left, the plots in the second and third rows correspond to the generic and continuum MC samples, respectively. For the electron-fitted samples on the right, the plots in the second, third and fourth rows correspond to the $D_s^{*+} \to D_s^+\gamma$, generic and continuum MC samples, respectively. For both sets of plots, the bottom left shows the significance of the signal over background. The bottom right plot shows the precision of the signal.

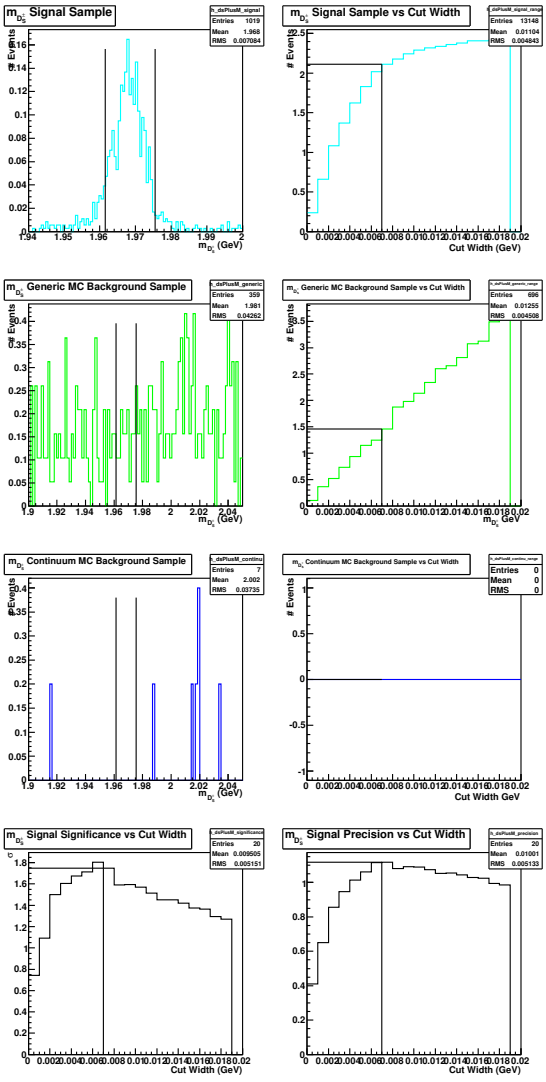

Figure A.51: $m_{D_s^+}$, $K^{*+}K^{*0}$, pion-fit

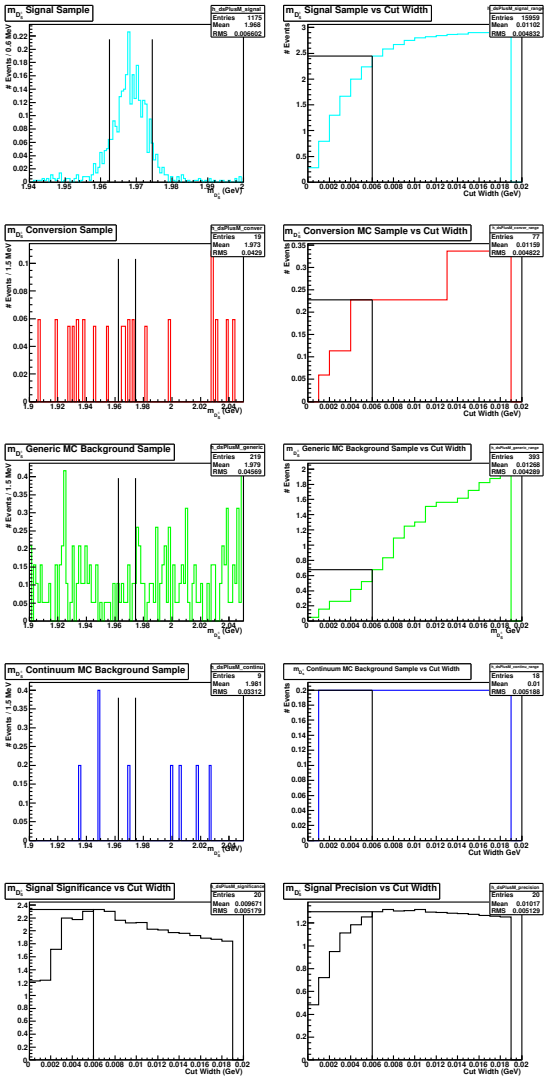

Figure A.52: $m_{D_s^+}$, $K^{*+}K^{*0}$, electron-fit

Optimization plots for the m_{BC} selection criterion in the $D_s^+ \to K^{*+}K^{*0}$ decay mode. Plots on the left grouped as Fig. A.53 correspond to pion-fitted tracks in the simulated samples. Plots on the right grouped as Fig. A.54 correspond to electron-fitted tracks in the samples. The top left plots, for both samples, is the distribution of m_{BC} in the signal Monte Carlo sample. The top right plot graphs the signal MC sample accepted by the criterion as we increase the cut width plotted on the x-axis. For the pion-fitted samples on the left, the plots in the second and third rows correspond to the generic and continuum MC samples, respectively. For the electron-fitted samples on the right, the plots in the second, third and fourth rows correspond to the $D_s^{*+} \to D_s^+\gamma$, generic and continuum MC samples, respectively. For both sets of plots, the bottom left shows the significance of the signal over background. The bottom right plot shows the precision of the signal.

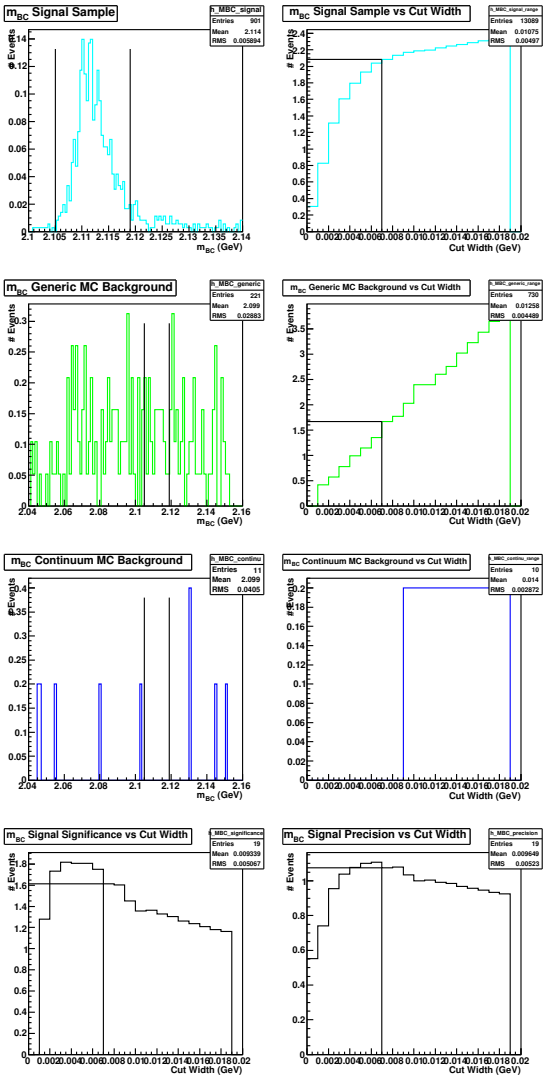

Figure A.53: m_{BC}, $K^{*+}K^{*0}$, pion-fit

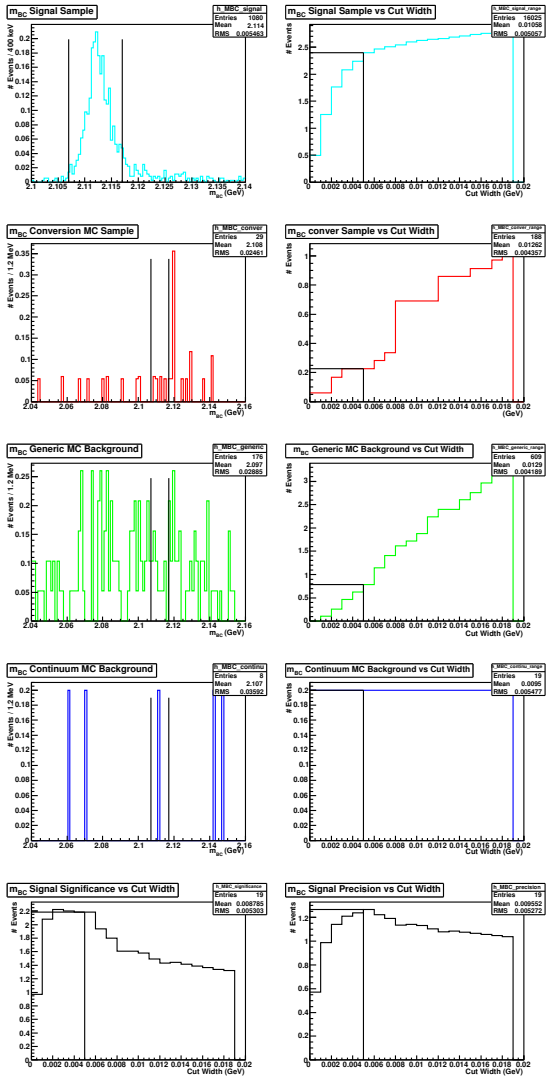

Figure A.54: m_{BC}, $K^{*+}K^{*0}$, electron-fit

Optimization plots for the δm selection criterion in the $D_s^+ \to K^{*+}K^{*0}$ decay mode. Plots on the left grouped as Fig. A.55 correspond to pion-fitted tracks in the simulated samples. Plots on the right grouped as Fig. A.56 correspond to electron-fitted tracks in the samples. The top left plots, for both samples, is the distribution of δm in the signal Monte Carlo sample. The top right plot graphs the signal MC sample accepted by the criterion as we increase the cut width plotted on the x-axis. For the pion-fitted samples on the left, the plots in the second and third rows correspond to the generic and continuum MC samples, respectively. For the electron-fitted samples on the right, the plots in the second, third and fourth rows correspond to the $D_s^{*+} \to D_s^+\gamma$, generic and continuum MC samples, respectively. For both sets of plots, the bottom left shows the significance of the signal over background. The bottom right plot shows the precision of the signal.

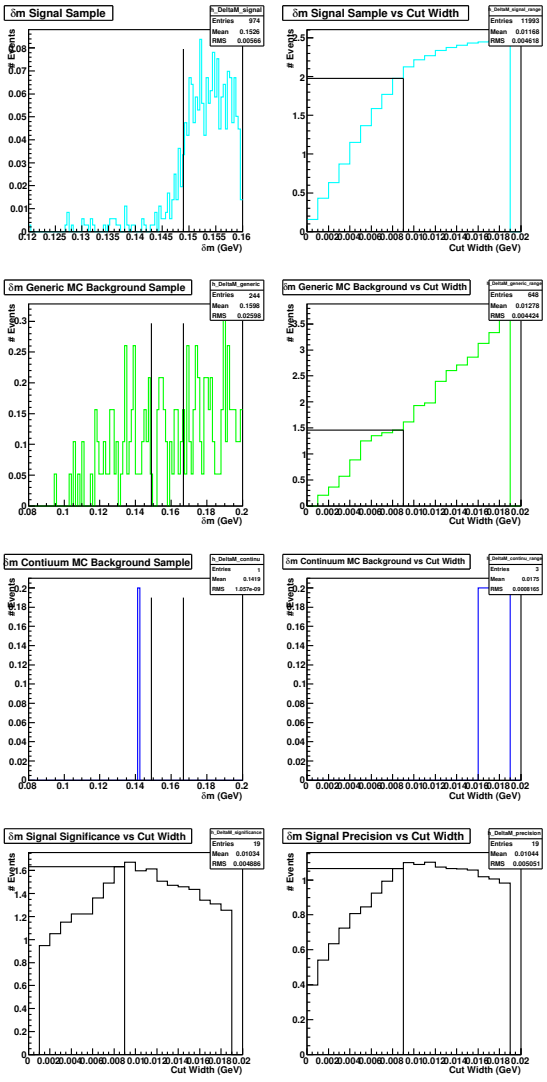

Figure A.55: δm, $K^{*+}K^{*0}$, pion-fit

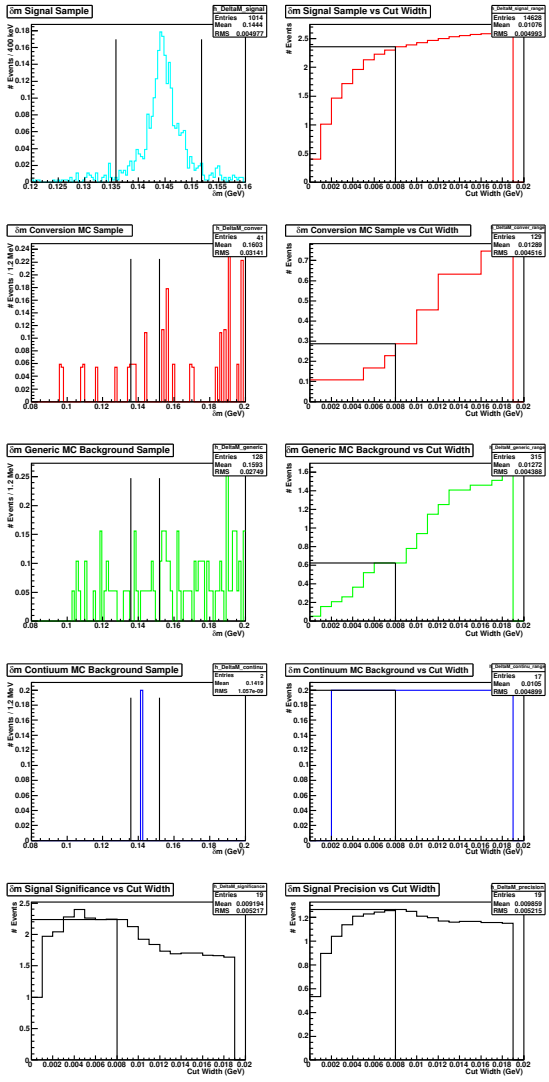

Figure A.56: δm, $K^{*+}K^{*0}$, electron-fit

Optimization plots for the selection criterion on the Δd_0 between the e^+e^- in the $D_s^+ \to K^{*+}K^{*0}$ decay mode. Plots on the left grouped as Fig. A.57 correspond to pion-fitted tracks in the simulated samples. Plots on the right grouped as Fig. A.58 correspond to electron-fitted tracks in the samples. The top left plots, for both samples, is the distribution of Δd_0 in the signal Monte Carlo sample. The top right plot graphs the signal MC sample accepted by the criterion as we vary the cut on the x-axis. For the pion-fitted samples on the left, the plots in the second and third rows correspond to the generic and continuum MC samples, respectively. For the electron-fitted samples on the right, the plots in the second, third and fourth rows correspond to the $D_s^{*+} \to D_s^+\gamma$, generic and continuum MC samples, respectively. For both sets of plots, the bottom left shows the significance of the signal over background. The bottom right plot shows the precision of the signal.

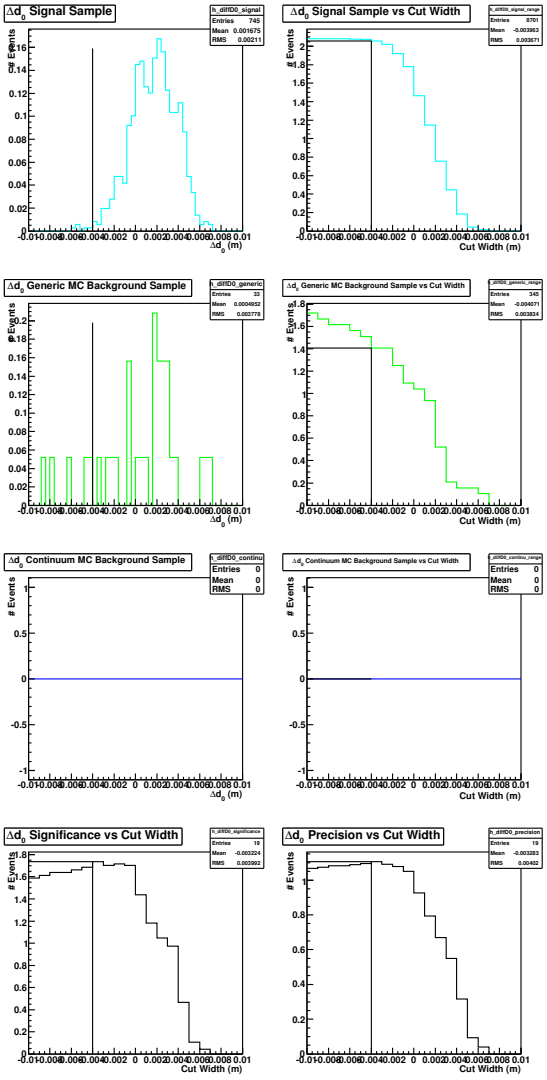

Figure A.57: Δd_0, $K^{*+}K^{*0}$, pion-fit

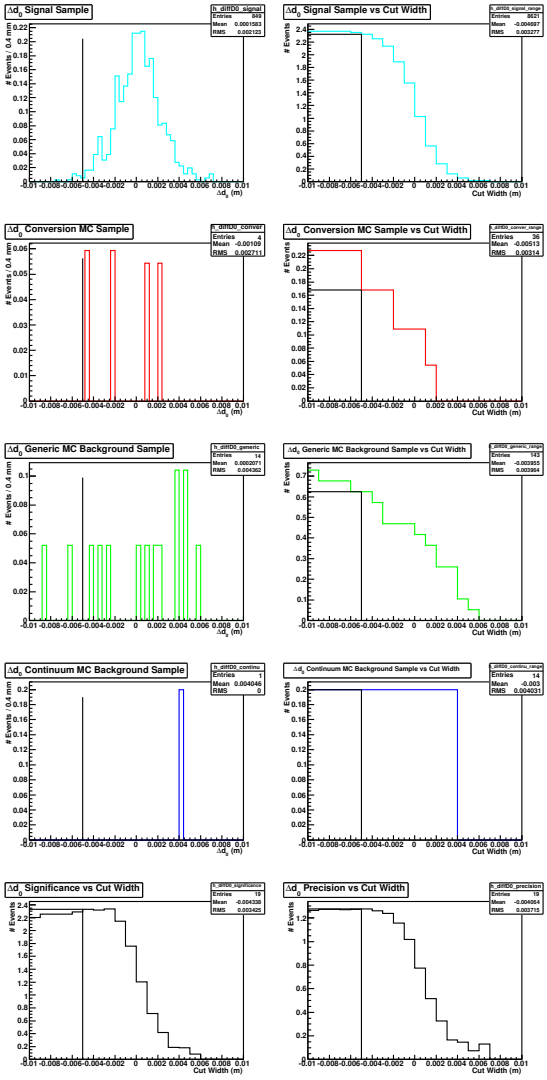

Figure A.58: Δd_0, $K^{*+}K^{*0}$, electron-fit

Optimization plots for the selection criterion on the $\Delta\phi_0$ between the e^+e^- in the $D_s^+ \to K^{*+}K^{*0}$ decay mode. Plots on the left grouped as Fig. A.59 correspond to pion-fitted tracks in the simulated samples. Plots on the right grouped as Fig. A.60 correspond to electron-fitted tracks in the samples. The top left plots, for both samples, is the distribution of $\Delta\phi_0$ in the signal Monte Carlo sample. The top right plot graphs the signal MC sample accepted by the criterion as we vary the cut on the x-axis. For the pion-fitted samples on the left, the plots in the second and third rows correspond to the generic and continuum MC samples, respectively. For the electron-fitted samples on the right, the plots in the second, third and fourth rows correspond to the $D_s^{*+} \to D_s^+\gamma$, generic and continuum MC samples, respectively. For both sets of plots, the bottom left shows the significance of the signal over background. The bottom right plot shows the precision of the signal.

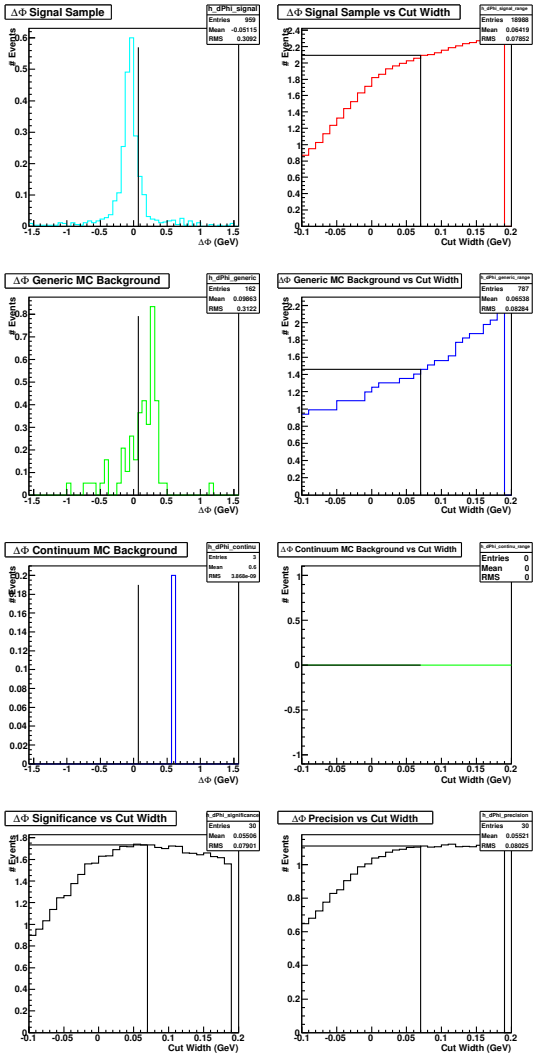

Figure A.59: $\Delta\phi_0$, $K^{*+}K^{*0}$, pion-fit

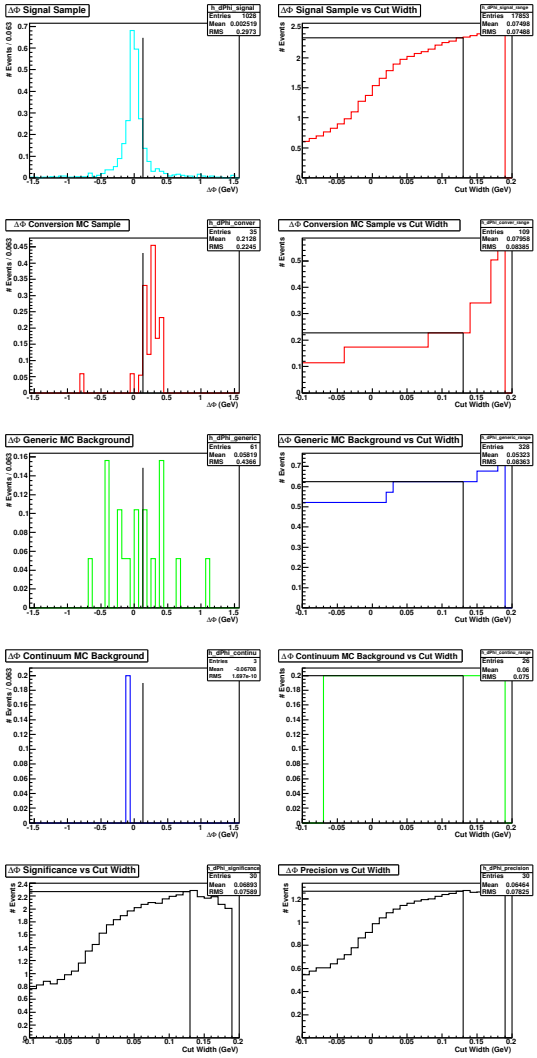

Figure A.60: $\Delta\phi_0$, $K^{*+}K^{*0}$, electron-fit

A.7 $D_s^+ \to \eta\rho^+; \eta \to \gamma\gamma; \rho^+ \to \pi^+\pi^0$

Optimization plots for the $m_{D_s^+}$ selection criterion in the $D_s^+ \to \eta\rho^+; \eta \to \gamma\gamma; \rho^+ \to \pi^+\pi^0$ mode. Plots on the left grouped as Fig. A.61 correspond to pion-fitted tracks in the simulated samples. Plots on the right grouped as Fig. A.62 correspond to electron-fitted tracks in the samples. The top left plots, for both samples, is the distribution of $m_{D_s^+}$ in the signal Monte Carlo sample. The top right plot graphs the signal MC sample accepted by the criterion as we increase the cut width plotted on the x-axis. For the pion-fitted samples on the left, the plots in the second and third rows correspond to the generic and continuum MC samples, respectively. For the electron-fitted samples on the right, the plots in the second, third and fourth rows correspond to the $D_s^{*+} \to D_s^+\gamma$, generic and continuum MC samples, respectively. For both sets of plots, the bottom left shows the significance of the signal over background. The bottom right plot shows the precision of the signal.

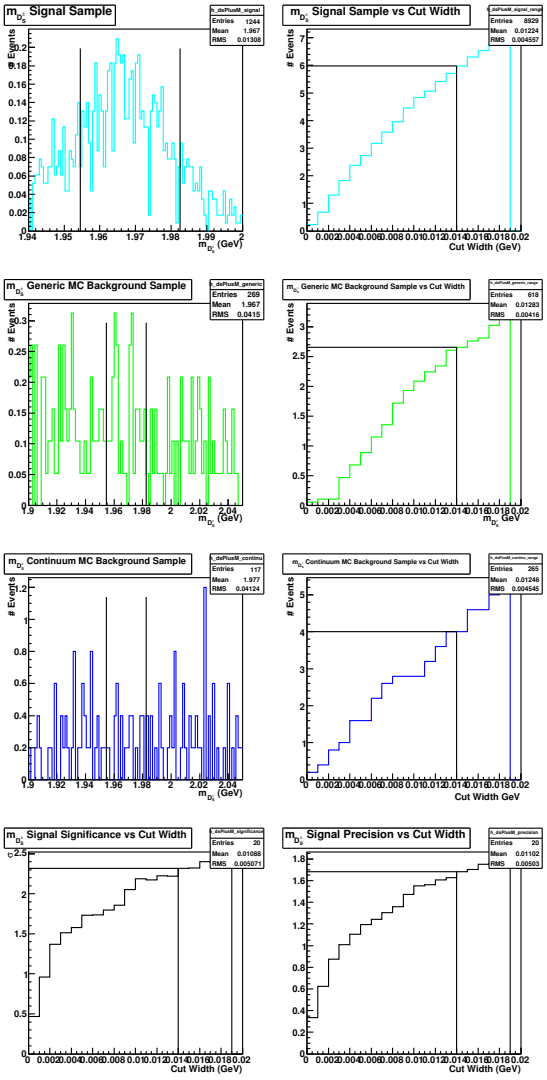

Figure A.61: $m_{D_s^+}$, $\eta\rho^+$, pion-fit

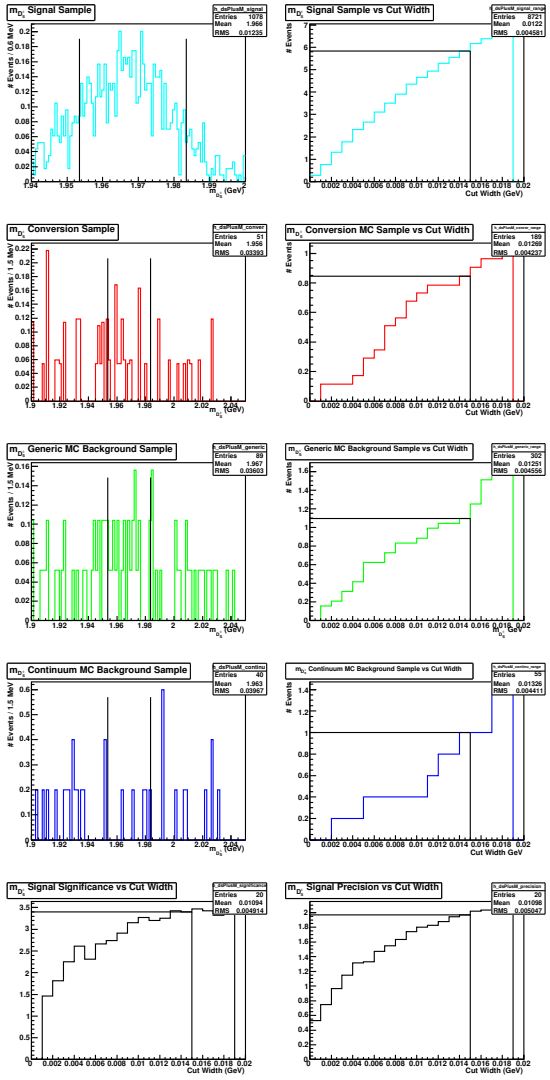

Figure A.62: $m_{D_s^+}$, $\eta\rho^+$, electron-fit

Optimization plots for the m_{BC} selection criterion in the $D_s^+ \to \eta\rho^+$ decay mode. Plots on the left grouped as Fig. A.63 correspond to pion-fitted tracks in the simulated samples. Plots on the right grouped as Fig. A.64 correspond to electron-fitted tracks in the samples. The top left plots, for both samples, is the distribution of m_{BC} in the signal Monte Carlo sample. The top right plot graphs the signal MC sample accepted by the criterion as we increase the cut width plotted on the x-axis. For the pion-fitted samples on the left, the plots in the second and third rows correspond to the generic and continuum MC samples, respectively. For the electron-fitted samples on the right, the plots in the second, third and fourth rows correspond to the $D_s^{*+} \to D_s^+\gamma$, generic and continuum MC samples, respectively. For both sets of plots, the bottom left shows the significance of the signal over background. The bottom right plot shows the precision of the signal.

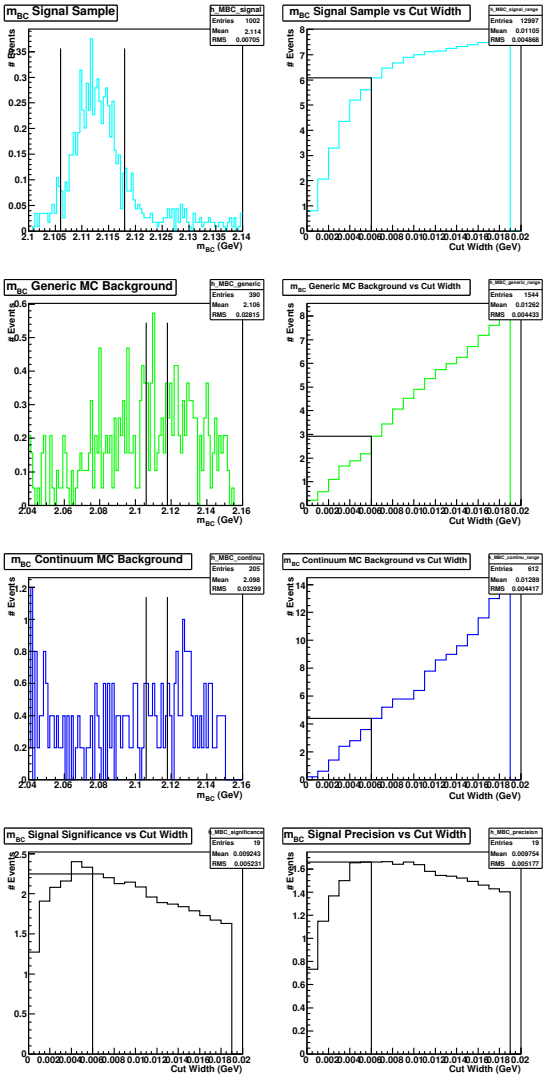

Figure A.63: m_{BC}, $\eta\rho^+$, pion-fit

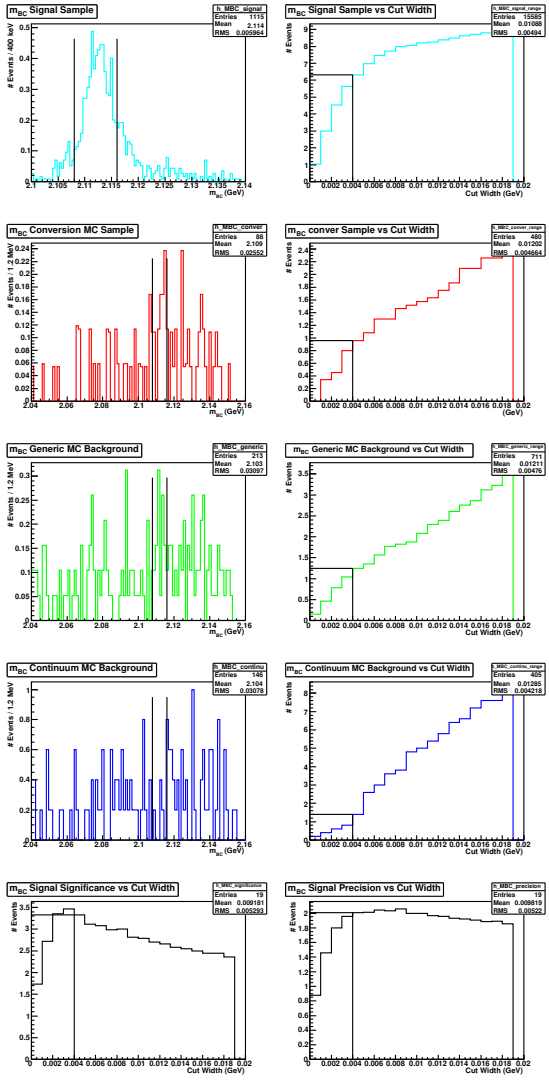

Figure A.64: m_{BC}, $\eta\rho^+$, electron-fit

Optimization plots for the δm selection criterion in the $D_s^+ \to \eta\rho^+$ decay mode. Plots on the left grouped as Fig. A.65 correspond to pion-fitted tracks in the simulated samples. Plots on the right grouped as Fig. A.66 correspond to electron-fitted tracks in the samples. The top left plots, for both samples, is the distribution of δm in the signal Monte Carlo sample. The top right plot graphs the signal MC sample accepted by the criterion as we increase the cut width plotted on the x-axis. For the pion-fitted samples on the left, the plots in the second and third rows correspond to the generic and continuum MC samples, respectively. For the electron-fitted samples on the right, the plots in the second, third and fourth rows correspond to the $D_s^{*+} \to D_s^+\gamma$, generic and continuum MC samples, respectively. For both sets of plots, the bottom left shows the significance of the signal over background. The bottom right plot shows the precision of the signal.

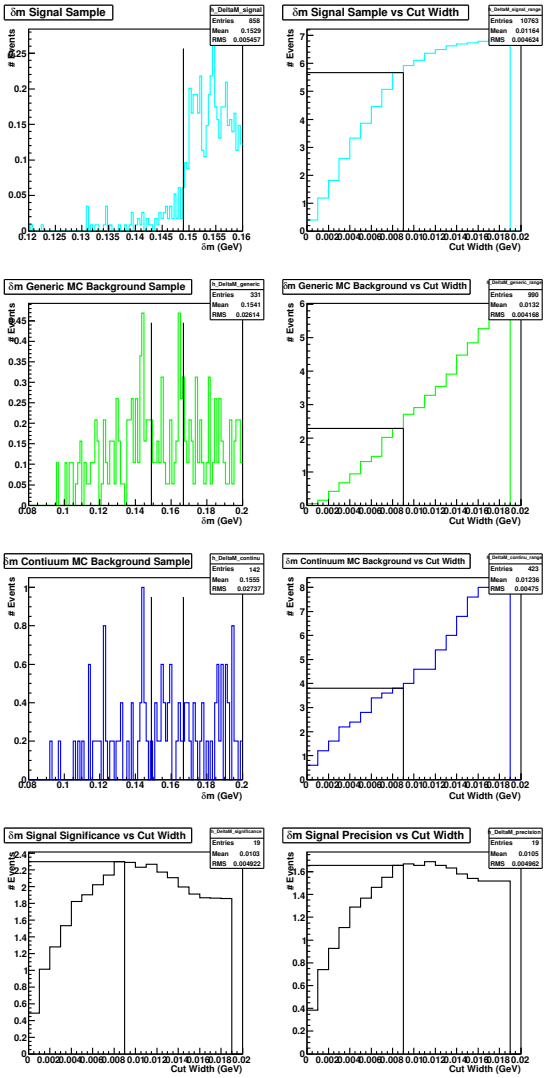

Figure A.65: δm, $\eta\rho^+$, pion-fit

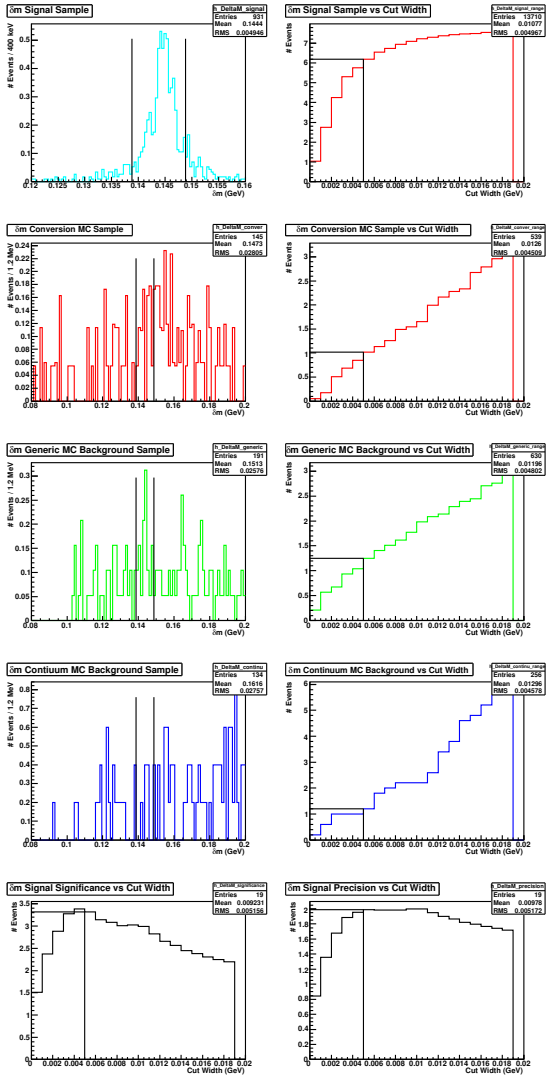

Figure A.66: δm, $\eta\rho^+$, electron-fit

Optimization plots for the selection criterion on the Δd_0 between the e^+e^- in the $D_s^+ \to \eta\rho^+$ decay mode. Plots on the left grouped as Fig. A.67 correspond to pion-fitted tracks in the simulated samples. Plots on the right grouped as Fig. A.68 correspond to electron-fitted tracks in the samples. The top left plots, for both samples, is the distribution of Δd_0 in the signal Monte Carlo sample. The top right plot graphs the signal MC sample accepted by the criterion as we vary the cut on the x-axis. For the pion-fitted samples on the left, the plots in the second and third rows correspond to the generic and continuum MC samples, respectively. For the electron-fitted samples on the right, the plots in the second, third and fourth rows correspond to the $D_s^{*+} \to D_s^+\gamma$, generic and continuum MC samples, respectively. For both sets of plots, the bottom left shows the significance of the signal over background. The bottom right plot shows the precision of the signal.

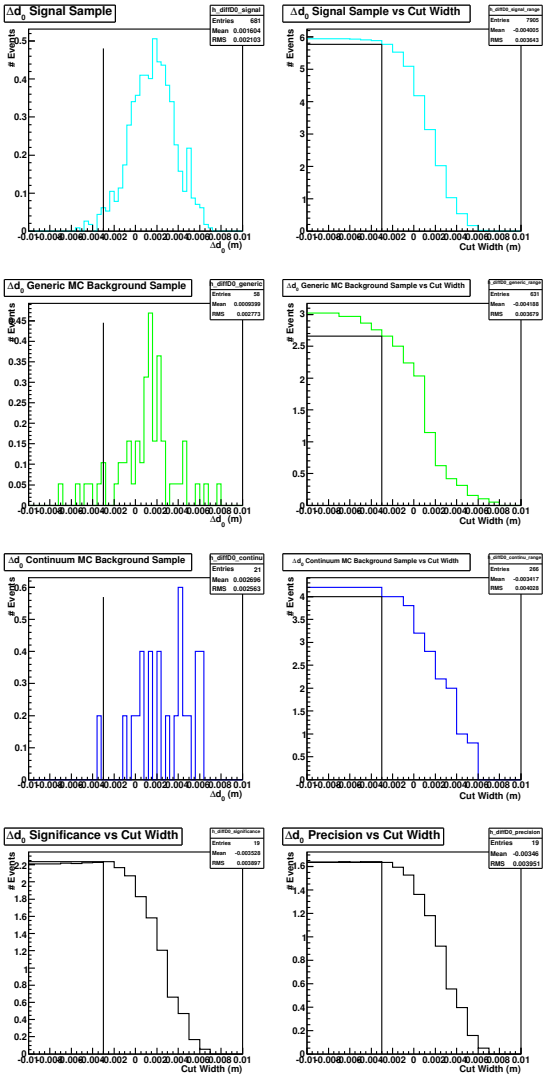

Figure A.67: Δd_0, $\eta\rho^+$, pion-fit

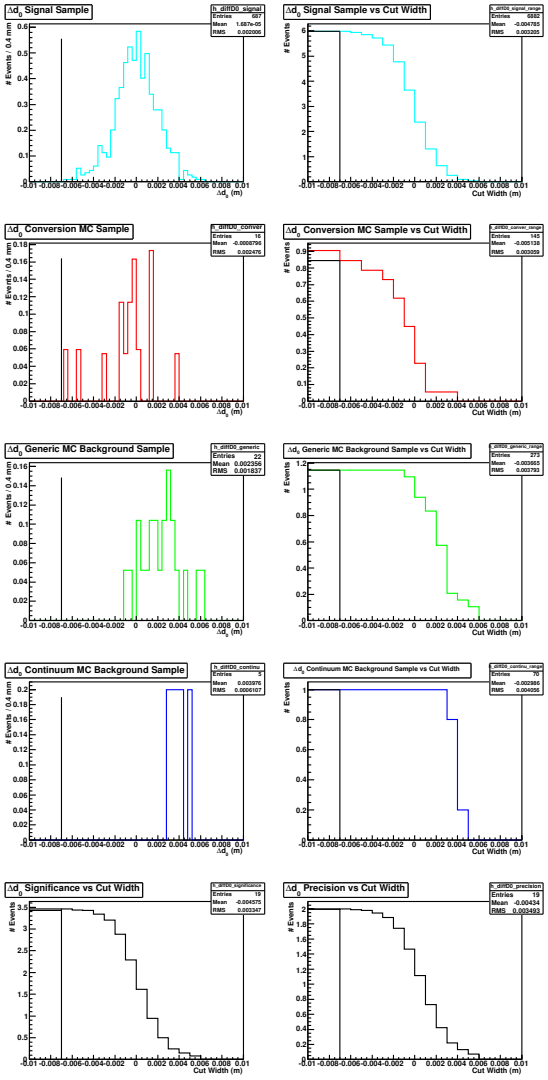

Figure A.68: Δd_0, $\eta\rho^+$, electron-fit

Optimization plots for the selection criterion on the $\Delta\phi_0$ between the e^+e^- in the $D_s^+ \to \eta\rho^+$ decay mode. Plots on the left grouped as Fig. A.69 correspond to pion-fitted tracks in the simulated samples. Plots on the right grouped as Fig. A.70 correspond to electron-fitted tracks in the samples. The top left plots, for both samples, is the distribution of $\Delta\phi_0$ in the signal Monte Carlo sample. The top right plot graphs the signal MC sample accepted by the criterion as we vary the cut on the x-axis. For the pion-fitted samples on the left, the plots in the second and third rows correspond to the generic and continuum MC samples, respectively. For the electron-fitted samples on the right, the plots in the second, third and fourth rows correspond to the $D_s^{*+} \to D_s^+\gamma$, generic and continuum MC samples, respectively. For both sets of plots, the bottom left shows the significance of the signal over background. The bottom right plot shows the precision of the signal.

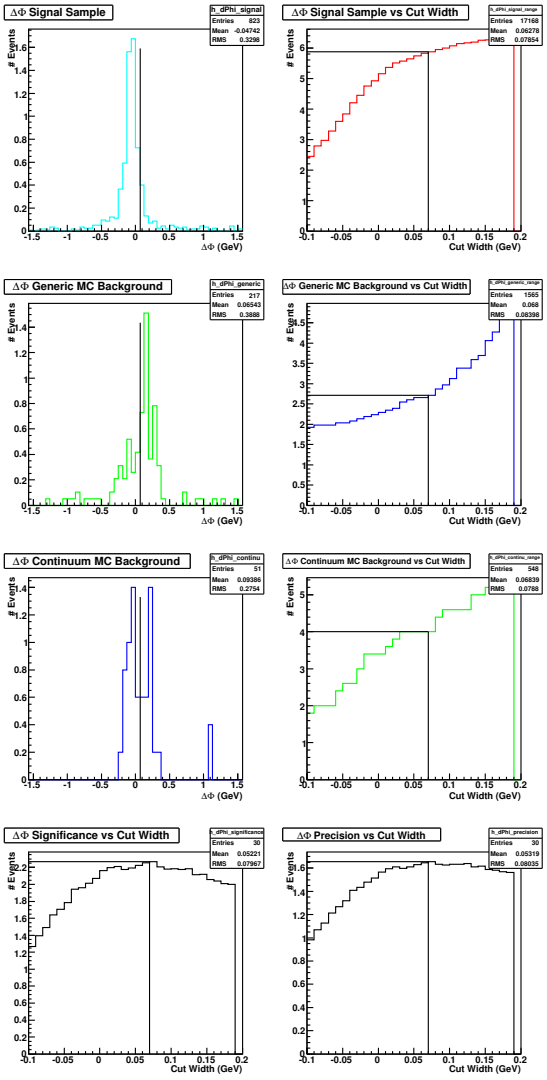

Figure A.69: $\Delta\phi_0$, $\eta\rho^+$, pion-fit

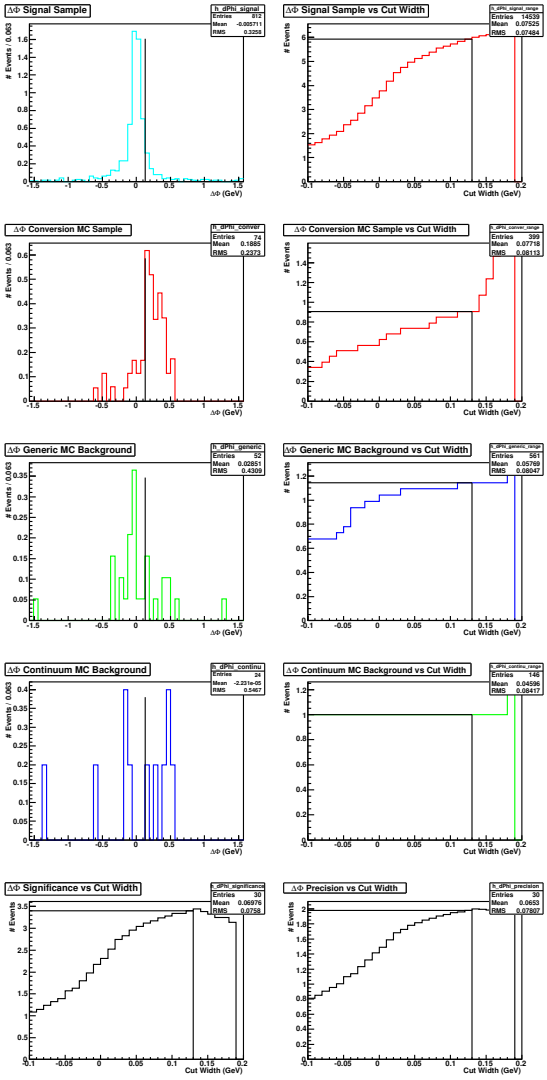

Figure A.70: $\Delta\phi_0$, $\eta\rho^+$, electron-fit

A.8 $D_s^+ \to \eta' \pi^+ ; \eta' \to \rho^0 \gamma$

Optimization plots for the $m_{D_s^+}$ selection criterion in the $D_s^+ \to \eta'\pi^+; \eta' \to \rho^0\gamma$ mode. Plots on the left grouped as Fig. A.71 correspond to pion-fitted tracks in the simulated samples. Plots on the right grouped as Fig. A.72 correspond to electron-fitted tracks in the samples. The top left plots, for both samples, is the distribution of $m_{D_s^+}$ in the signal Monte Carlo sample. The top right plot graphs the signal MC sample accepted by the criterion as we increase the cut width plotted on the x-axis. For the pion-fitted samples on the left, the plots in the second and third rows correspond to the generic and continuum MC samples, respectively. For the electron-fitted samples on the right, the plots in the second, third and fourth rows correspond to the $D_s^{*+} \to D_s^+\gamma$, generic and continuum MC samples, respectively. For both sets of plots, the bottom left shows the significance of the signal over background. The bottom right plot shows the precision of the signal.

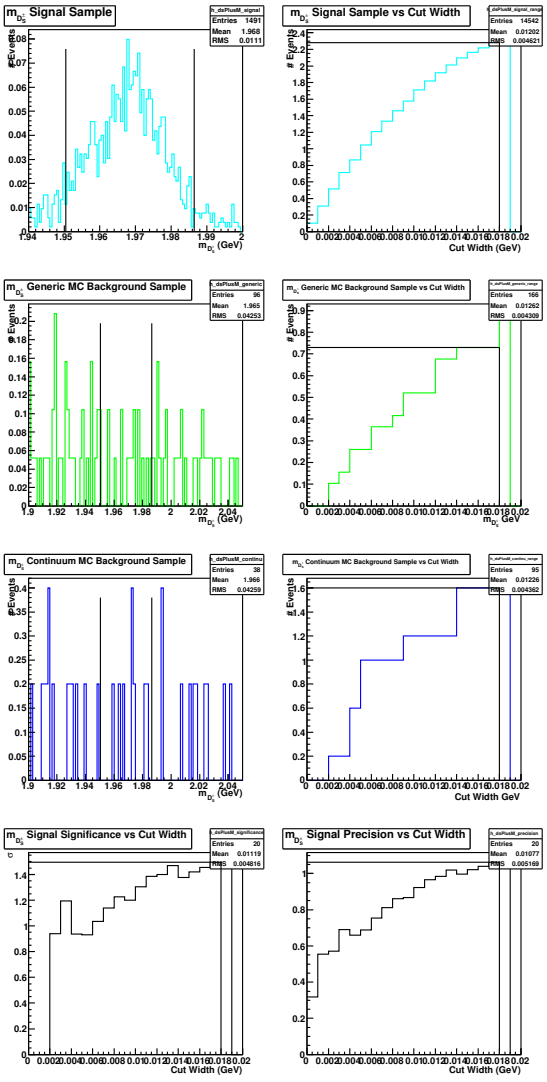

Figure A.71: $m_{D_s^+}$, $\eta'\pi^+; \eta' \to \rho^0\gamma$, pion-fit

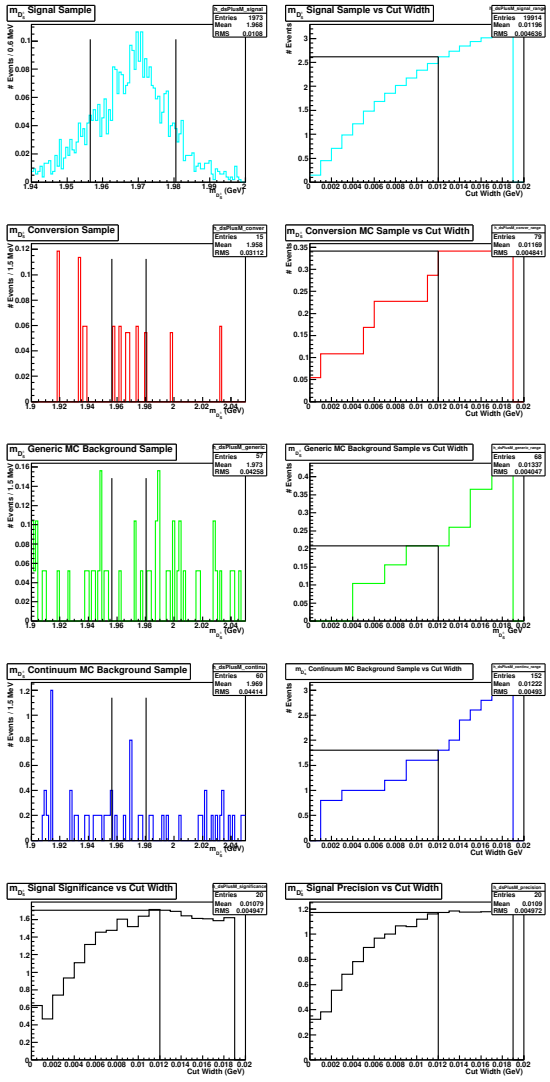

Figure A.72: $m_{D_s^+}$, $\eta'\pi^+; \eta' \to \rho^0\gamma$, e-fit

Optimization plots for the m_{BC} selection criterion in the $D_s^+ \to \eta'\pi^+; \eta' \to \rho^0\gamma$ decay mode. Plots on the left grouped as Fig. A.73 correspond to pion-fitted tracks in the simulated samples. Plots on the right grouped as Fig. A.74 correspond to electron-fitted tracks in the samples. The top left plots, for both samples, is the distribution of m_{BC} in the signal Monte Carlo sample. The top right plot graphs the signal MC sample accepted by the criterion as we increase the cut width plotted on the x-axis. For the pion-fitted samples on the left, the plots in the second and third rows correspond to the generic and continuum MC samples, respectively. For the electron-fitted samples on the right, the plots in the second, third and fourth rows correspond to the $D_s^{*+} \to D_s^+\gamma$, generic and continuum MC samples, respectively. For both sets of plots, the bottom left shows the significance of the signal over background. The bottom right plot shows the precision of the signal.

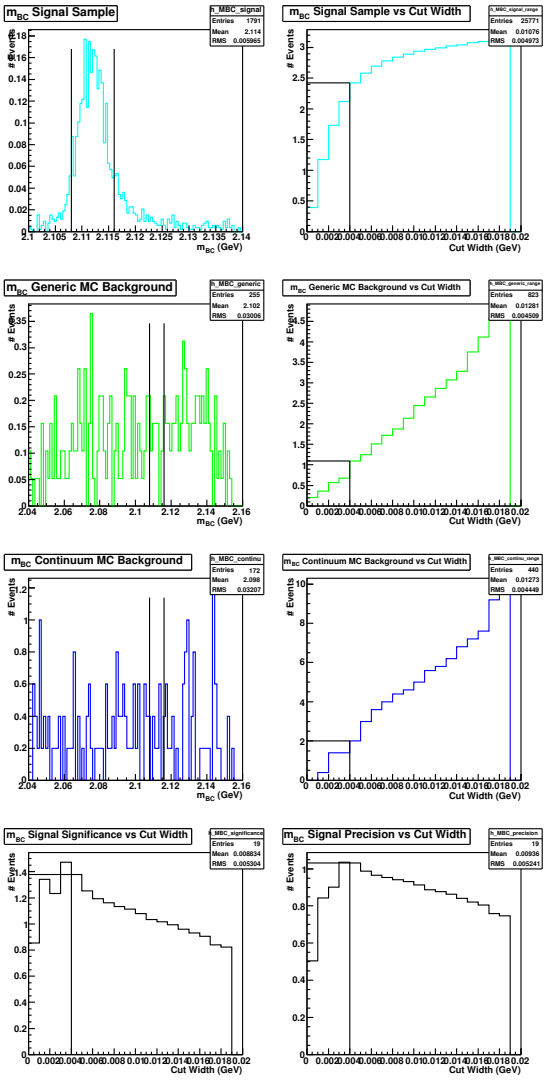

Figure A.73: $m_{BC}, \eta'\pi^+; \eta' \to \rho^0\gamma$, pion-fit

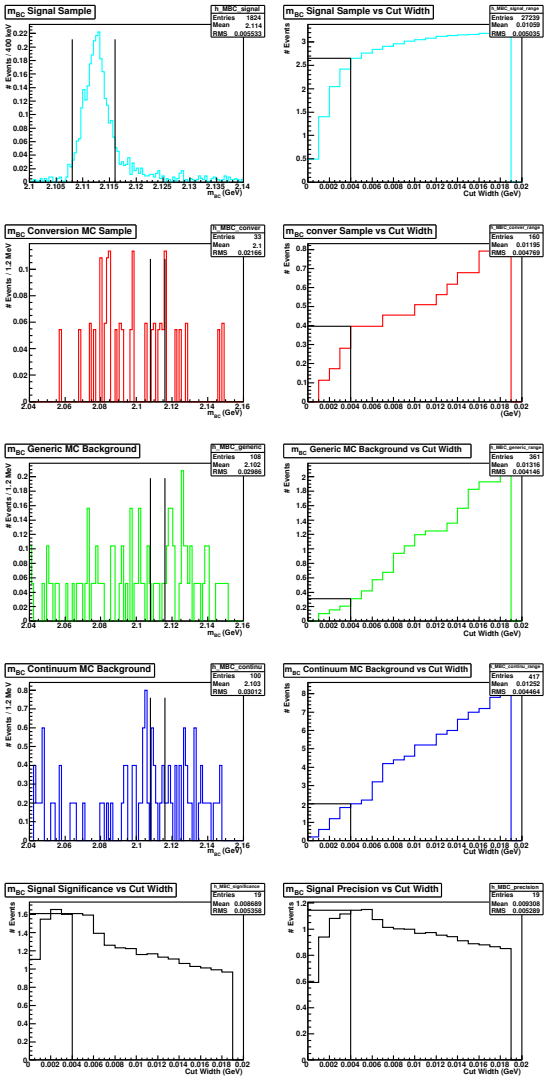

Figure A.74: $m_{BC}, \eta'\pi^+; \eta' \to \rho^0\gamma$, e-fit

Optimization plots for the δm selection criterion in the $D_s^+ \to \eta'\pi^+; \eta' \to \rho^0\gamma$ decay mode. Plots on the left grouped as Fig. A.75 correspond to pion-fitted tracks in the simulated samples. Plots on the right grouped as Fig. A.76 correspond to electron-fitted tracks in the samples. The top left plots, for both samples, is the distribution of δm in the signal Monte Carlo sample. The top right plot graphs the signal MC sample accepted by the criterion as we increase the cut width plotted on the x-axis. For the pion-fitted samples on the left, the plots in the second and third rows correspond to the generic and continuum MC samples, respectively. For the electron-fitted samples on the right, the plots in the second, third and fourth rows correspond to the $D_s^{*+} \to D_s^+\gamma$, generic and continuum MC samples, respectively. For both sets of plots, the bottom left shows the significance of the signal over background. The bottom right plot shows the precision of the signal.

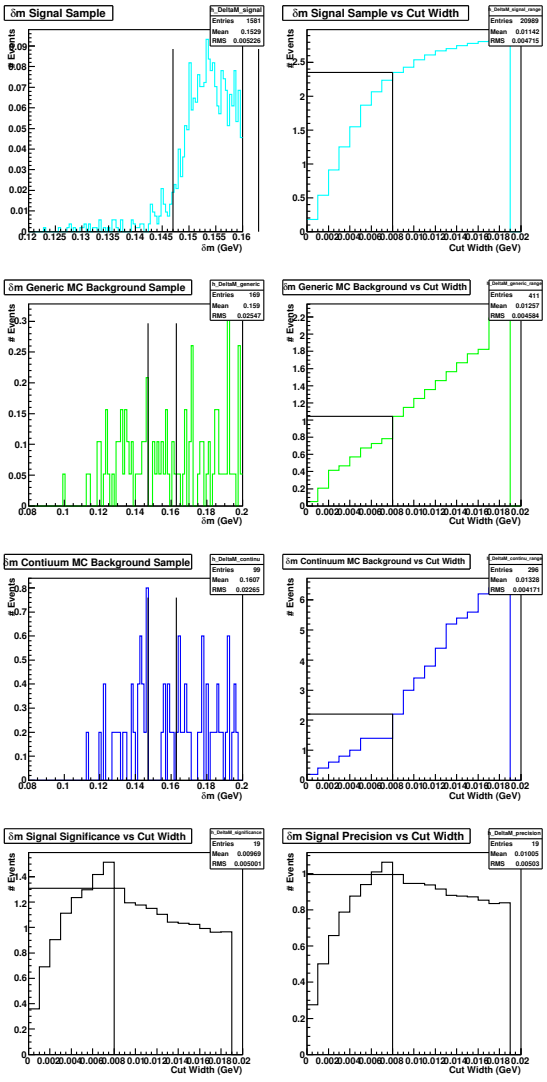

Figure A.75: δm, $\eta'\pi^+; \eta' \to \rho^0\gamma$, pion-fit

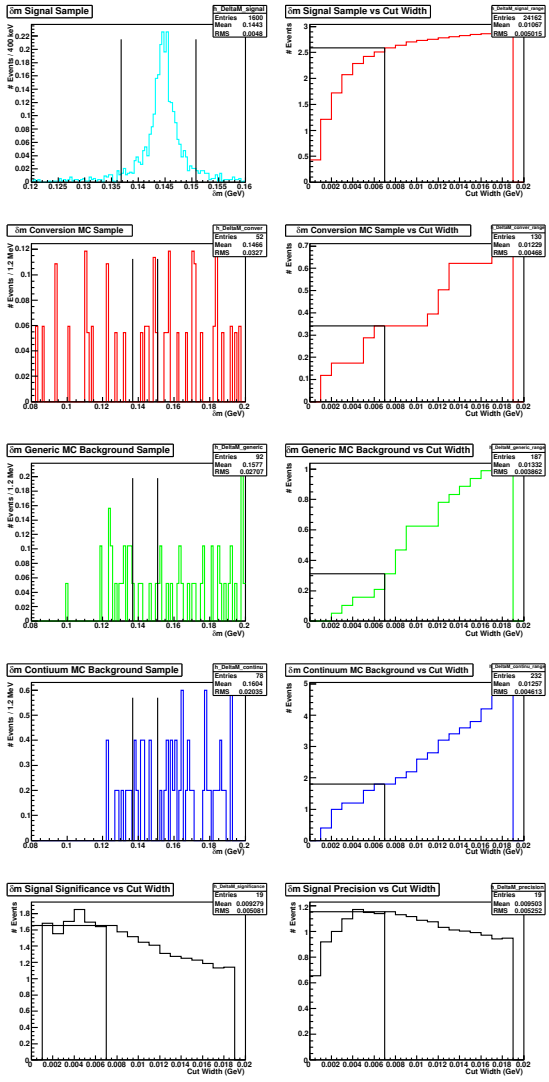

Figure A.76: δm, $\eta'\pi^+; \eta' \to \rho^0\gamma$, e-fit

Optimization plots for the selection criterion on the Δd_0 between the e^+e^- in the $D_s^+ \to \eta'\pi^+; \eta' \to \rho^0\gamma$ decay mode. Plots on the left grouped as Fig. A.77 correspond to pion-fitted tracks in the simulated samples. Plots on the right grouped as Fig. A.78 correspond to electron-fitted tracks in the samples. The top left plots, for both samples, is the distribution of Δd_0 in the signal Monte Carlo sample. The top right plot graphs the signal MC sample accepted by the criterion as we vary the cut on the x-axis. For the pion-fitted samples on the left, the plots in the second and third rows correspond to the generic and continuum MC samples, respectively. For the electron-fitted samples on the right, the plots in the second, third and fourth rows correspond to the $D_s^{*+} \to D_s^+\gamma$, generic and continuum MC samples, respectively. For both sets of plots, the bottom left shows the significance of the signal over background. The bottom right plot shows the precision of the signal.

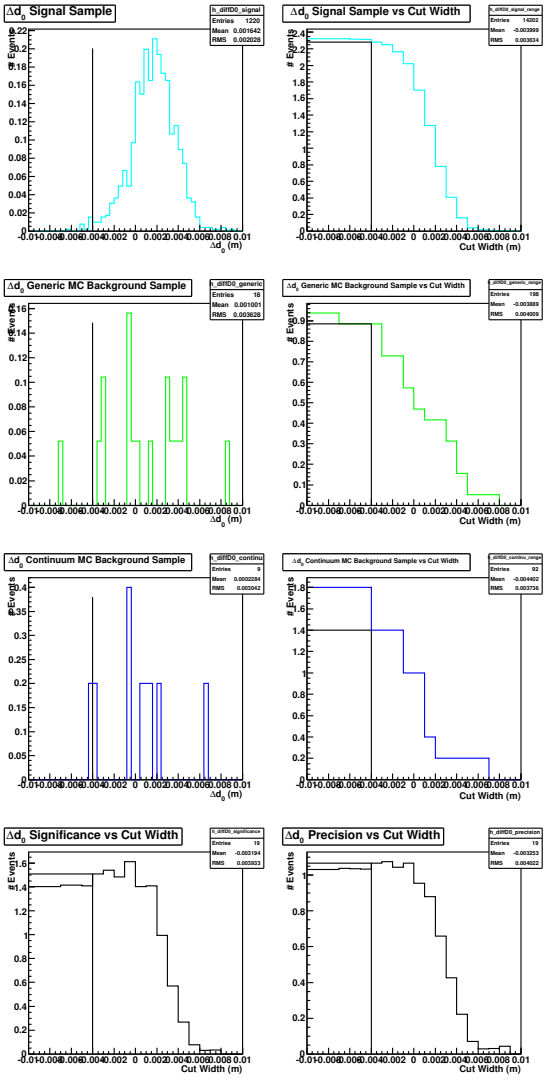

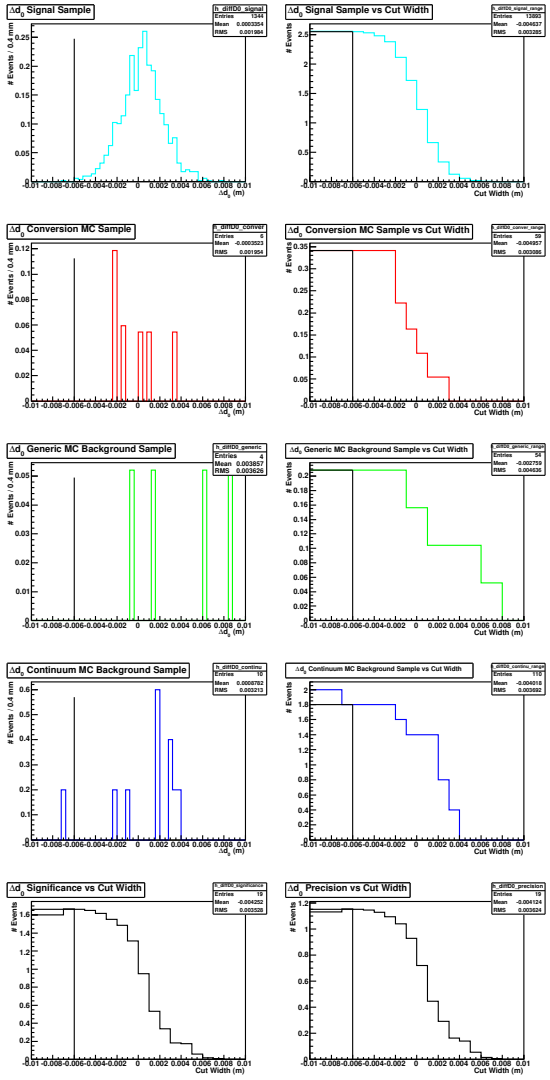

Figure A.77: Δd_0, $\eta'\pi^+; \eta' \to \rho^0\gamma$, pion-fit

Figure A.78: Δd_0, $\eta'\pi^+; \eta' \to \rho^0\gamma$, e-fit

Optimization plots for the selection criterion on the $\Delta\phi_0$ between the e^+e^- in the $D_s^+ \to \eta'\pi^+; \eta' \to \rho^0\gamma$ decay mode. Plots on the left grouped as Fig. A.79 correspond to pion-fitted tracks in the simulated samples. Plots on the right grouped as Fig. A.80 correspond to electron-fitted tracks in the samples. The top left plots, for both samples, is the distribution of $\Delta\phi_0$ in the signal Monte Carlo sample. The top right plot graphs the signal MC sample accepted by the criterion as we vary the cut on the x-axis. For the pion-fitted samples on the left, the plots in the second and third rows correspond to the generic and continuum MC samples, respectively. For the electron-fitted samples on the right, the plots in the second, third and fourth rows correspond to the $D_s^{*+} \to D_s^+\gamma$, generic and continuum MC samples, respectively. For both sets of plots, the bottom left shows the significance of the signal over background. The bottom right plot shows the precision of the signal.

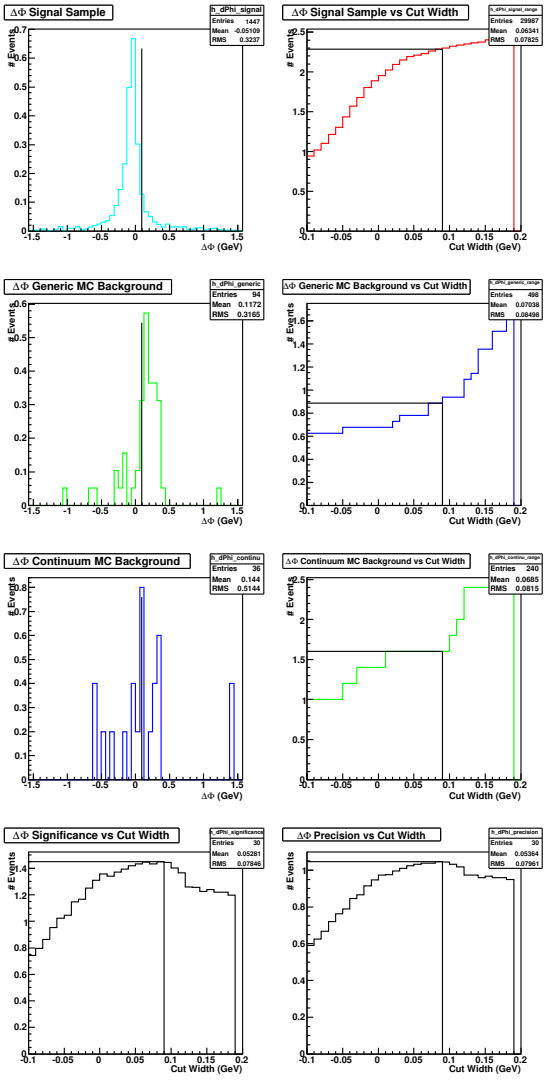

Figure A.79: $\Delta\phi_0$, $\eta'\pi^+; \eta' \to \rho^0\gamma$, pion-fit

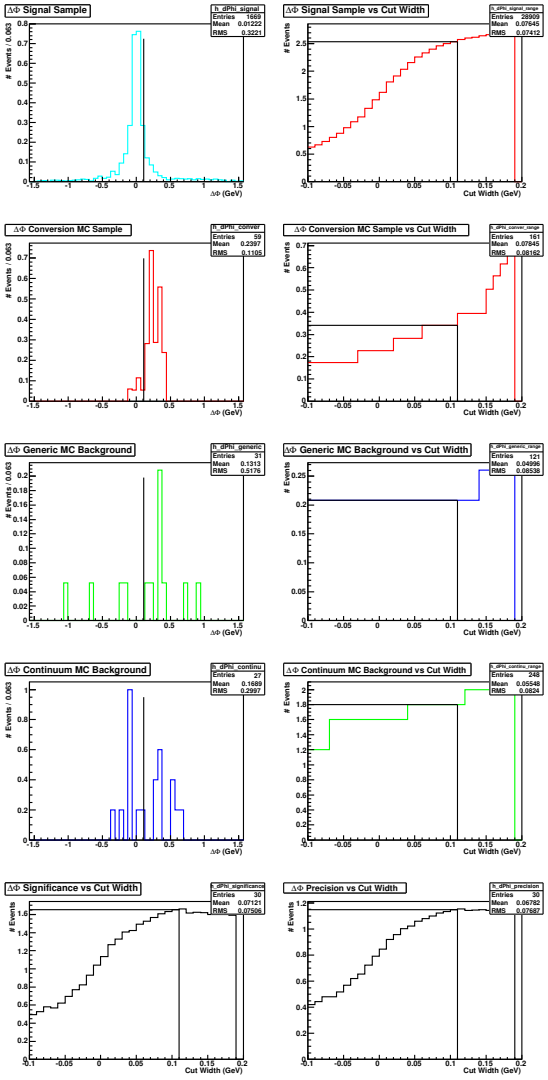

Figure A.80: $\Delta\phi_0$, $\eta'\pi^+; \eta' \to \rho^0\gamma$, e-fit

BIBLIOGRAPHY

[1] R. Abegg et al. Direct measurement of the branching ratio for the decay of the η meson into two photons. *Phys. Rev.*, D53:11–19, 1996.

[2] H. Albrecht et al. The Measurement of D_s^+ and D^+ meson decays into $\bar{K^{*+}}\bar{K^{*0}}$. *Z. Phys.*, C53:361–365, 1992.

[3] J. P. Alexander et al. Absolute Measurement of Hadronic Branching Fractions of the D_s^+ Meson. *Phys. Rev. Lett.*, 100:161804, 2008.

[4] C. Amsler, M. Doser, M. Antonelli, D.M. Asner, K.S. Babu, H. Baer, H.R. Band, R.M. Barnett, E. Bergren, J. Beringer, G. Bernardi, W. Bertl, H. Bichsel, O. Biebel, P. Bloch, E. Blucher, S. Blusk, R.N. Cahn, M. Carena, C. Caso, A. Ceccucci, D. Chakraborty, M.-C. Chen, R.S. Chivukula, G. Cowan, O. Dahl, G. D'Ambrosio, T. Damour, A. de Gouvła, T. DeGrand, B. Dobrescu, M. Drees, D.A. Edwards, S. Eidelman, V.D. Elvira, J. Erler, V.V. Ezhela, J.L. Feng, W. Fetscher, B.D. Fields, B. Foster, T.K. Gaisser, L. Garren, H.-J. Gerber, G. Gerbier, T. Gherghetta, G.F. Giudice, M. Goodman, C. Grab, A.V. Gritsan, J.-F. Grivaz, D.E. Groom, M. Grnewald, A. Gurtu, T. Gutsche, H.E. Haber, K. Hagiwara, C. Hagmann, K.G. Hayes, J.J. Hernndez-Rey, K. Hikasa, I. Hinchliffe, A. Hcker, J. Huston, P. Igo-Kemenes, J.D. Jackson, K.F. Johnson, T. Junk, D. Karlen, B. Kayser, D. Kirkby, S.R. Klein, I.G. Knowles, C. Kolda, R.V. Kowalewski, P. Kreitz, B. Krusche, Yu.V. Kuyanov, Y. Kwon, O. Lahav, P. Langacker, A. Liddle, Z. Ligeti, C.-J. Lin, T.M. Liss, L. Littenberg, J.C. Liu, K.S. Lugovsky, S.B. Lugovsky, H. Mahlke, M.L. Mangano, T. Mannel, A.V. Manohar, W.J. Marciano, A.D. Martin, A. Masoni, D. Milstead, R. Miquel, K. Mnig, H. Murayama, K. Nakamura, M. Narain, P. Nason, S. Navas, P. Nevski, Y. Nir, K.A. Olive, L. Pape, C. Patrignani, J.A. Peacock, A. Piepke, G. Punzi, A. Quadt, S. Raby, G. Raffelt, B.N. Ratcliff, B. Renk, P. Richardson, S. Roesler, S. Rolli, A. Romaniouk, L.J. Rosenberg, J.L. Rosner, C.T. Sachrajda, Y. Sakai, S. Sarkar, F. Sauli, O. Schneider, D. Scott, W.G. Seligman, M.H. Shaevitz, T. Sjstrand, J.G. Smith, G.F. Smoot, S. Spanier, H. Spieler, A. Stahl, T. Stanev, S.L. Stone, T. Sumiyoshi, M. Tanabashi, J. Terning, M. Titov, N.P. Tkachenko, N.A. Trnqvist, D. Tovey, G.H. Trilling, T.G. Trippe, G. Valencia, K. van Bibber, M.G. Vincter, P. Vogel, D.R. Ward, T. Watari, B.R. Webber, G. Weiglein, J.D. Wells, M. Whalley, A. Wheeler, C.G. Wohl, L. Wolfenstein, J. Womersley, C.L. Woody, R.L. Workman, A. Yamamoto, W.-M. Yao, O.V. Zenin, J. Zhang, R.-Y. Zhu, P.A. Zyla, G. Harper, V.S. Lugovsky, and P. Schaffner. Review of particle physics. *Physics Letters B*, 667(1-5):1 – 6, 2008. Review of Particle Physics.

[5] Bernard Aubert et al. Measurement of the branching ratios $\Gamma(D_s^{*+} \to D_s^+\pi^0)/\Gamma(D_s^{*+} \to D_s^+\gamma)$ and $\Gamma(D^{*0} \to D^0\pi^0)/\Gamma(D^{*0} \to D^0\gamma)$. *Phys. Rev.*, D72:091101, 2005.

[6] A. Beddall and A. Beddall. Measurement of the Dalitz-decay branching ratio of the π^0. *Eur. Phys. J.*, C54:365–370, 2008.

[7] Y. A. Budagov, S. Viktor, V. P. Dzhelepov, and P. F. Ermolov. Internal Conversion Pairs in the Decay of Neutral π Mesons. *Sov. Phys. JETP*, 11:755, 1960.

[8] A. Chen, M. Goldberg, N. Horwitz, A. Jawahery, P. Lipari, G. C. Moneti, C. G. Trahern, H. Van Hecke, M. S. Alam, S. E. Csorna, L. Garren, M. D. Mestayer, R. S. Panvini, Xia Yi, R. Giles, J. Hassard, M. Hempstead, K. Kinoshita, W. W. MacKay, F. M. Pipkin, Richard Wilson, H. Kagan, P. Avery, C. Bebek, K. Berkelman, D. G. Cassel, J. W. DeWire, R. Ehrlich, T. Ferguson, R. Galik, M. G. D. Gilchriese, B. Gittelman, H. Halling, D. L. Hartill, D. Herrup, S. Holzner, M. Ito, J. Kandaswamy, V. Kistiakowsky, D. L. Kreinick, Y. Kubota, N. B. Mistry, F. Morrow, E. Nordberg, M. Ogg, R. Perchonok, R. Plunkett, A. Silverman, P. C. Stein, S. Stone, D. Weber, R. Wilcke, A. J. Sadoff, S. Behrends, K. Chadwick, J. Chauveau, P. Ganci, T. Gentile, Jan M. Guida, Joan A. Guida, R. Kass, A. C. Melissinos, S. L. Olsen, G. Parkhurst, D. Peterson, R. Poling, C. Rosenfeld, G. Rucinski, P. Tipton, E. H. Thorndike, J. Green, R. G. Hicks, F. Sannes, P. Skubic, A. Snyder, and R. Stone. Evidence for the f meson at 1970 mev. *Phys. Rev. Lett.*, 51(8):634–637, Aug 1983.

[9] CLEO Collaboration. CLEO Yellow Book. *Internal*, 2001.

[10] D. Cronin-Hennessy et al. Measurement of Charm Production Cross Sections in e^+e^- Annihilation at Energies between 3.97 and 4.26 GeV. *Phys. Rev. D*, 80:072001, 2009.

[11] R. H. Dalitz. On an alternative decay process for the neutral π- meson, Letters to the Editor. *Proc. Phys. Soc.*, A64:667–669, 1951.

[12] R. Brun et al. Geant detector description and simulation tool. *CERN Program Library Long Writeup W5013*, 1993.

[13] S. L. Glashow, J. Iliopoulos, and L. Maiani. Weak interactions with lepton-hadron symmetry. *Phys. Rev. D*, 2(7):1285–1292, Oct 1970.

[14] Rob Kutschke. How and Why Wonder Book of CLEO Tracking Conventions. *CSN 94-334*, 1996.

[15] David J. Lange. The EvtGen particle decay simulation package. *Nuclear Instruments and Methods in Physics Research Section A: Accelerators,Spectrometers,Detectors and Associated Equipment*, 462(1-2):152 – 155, 2001.

[16] A. Lopez et al. Measurement of Prominent eta Decay Branching Fractions. *Phys. Rev. Lett.*, 99:122001, 2007.

[17] P. Naik et al. Measurement of the Pseudoscalar Decay Constant f_{Ds} Using $D_s^+ \to \tau^+\nu, \tau^+ \to \rho^+\bar{\nu}$ Decays. *Phys. Rev.*, D80:112004, 2009.

[18] Peter Onyisi and Werner Sun. Developments in $D_{(s)}$-Tagging. *CBX 06-11*, 2006.

[19] T. K. Pedlar et al. Charmonium decays to $\gamma\pi^0$, $\gamma\eta$, and $\gamma\eta'$. *Phys. Rev.*, D79:111101, 2009.

[20] A. Ryd et al. Tracking at CLEO. *CBX*, 2003.

[21] N. P. Samios. Dynamics of Internally Converted Electron-Positron Pairs. *Phys. Rev.*, 121:275–281, 1961.

[22] M. A. Schardt et al. A New Measurement of the Dalitz-decay branching ratio of the π^0. *Phys. Rev.*, D23:639, 1981.